Thermal Management of High Concentrating Photovoltaic System

Submitted by
Asmaa Rady Rashed Mariee Ahmed
to the
University of Exeter
as a thesis for the degree of
Doctor of Philosophy
in Renewable Energy
September 2021

I certify that all material in this thesis which is not my own work has been identified and that no material has previously been submitted and approved for the award of a degree by this or any other University.

Signature:……

This thesis is dedicated to…….

My loving Mother,

my Sisters

for their endless love, prayers, support, and advice,

and

my late Father whose words of encouragement still ring in my ears.

Abstract

Concentrated photovoltaic systems (CPV) have demonstrated the potential to achieve a high conversion power compared to conventional photovoltaic panels (PV) especially for areas with high solar irradiance. Under higher concentration ratios, solar cells can work at higher efficiencies by reducing the area of the solar cell and replacing it with optical components to collect the incident light more effectively. This is considered an efficient way to decrease the system cost without sacrificing the solar energy absorbed. However, the development of this emerging technology faces a number of challenges, one of them being the high temperature resulting from the increase in the concentration ratios. The solar cells may be subjected to damage if the temperature exceeds the limit recommended by the manufacturer.

This thesis investigates a number of innovative solutions for the development of high concentrator photovoltaics (HCPV) receivers. The work outlines the characteristics of the concentrator photovoltaic systems from different perspectives, the solar cell types, and optics classifications. The existing thermal management techniques, the advantages of nanotechnology in solar thermal applications, and the literature on the optical filters are also reviewed.

The thermal, electrical, and optical characterisations of the properties of the materials used in this research are introduced. The impact of the coolant type such as nanofluids, and heat sink design on the Multijunction (MJ) solar cell performance is investigated experimentally and theoretically. Water in comparison with the ethylene glycol and water mixture and syltherm oil using finned minichannel heat sink offers the best cell temperature uniformity. However, the highest outlet temperature is achieved using syltherm oil 800 especially for a concentration ratio above 1000 suns which is suitable for heat recovery applications that require a high temperature. Significant enhancement in the thermal conductivity of aluminium oxide/water and silicon dioxide/water nanofluids at different concentrations are measured in comparison with the distilled water. The thermal conductivity values were entered into COMSOL-Multiphysics software and the heat transfer effectiveness of the nanofluids was enhanced in comparison with water reaching 1.15 in the case of Al_2O_3/water at 5%, while in the case of using SiO_2/water it reached 1.11 using a finned channel

heat sink. Higher solar cell temperature uniformity is observed by using nanofluids in comparison with using water only as the maximum MJ solar cell temperature decreased by 3.6 °C at a concentration of 2000 suns in the case of using SiO_2/water.

The serpentine configuration has been investigated along with the straight channel heat sink for use in the HCPV applications. The centre inlet serpentine showed high electrical and thermal efficiencies until the concentration ratio of 2000 suns providing high-temperature uniformity and keeping the solar cell temperature below the recommended limit. The feasibility of using an infrared (IR) optical filter as a temperature regulator for the HCPV is explored. The IR filter successfully protects the single-junction solar cell from cracking and enhanced the cell efficiency by 180% at a solar irradiance of 400 W/m^2.

Detailed performance analysis of the focal spot area of the Fresnel Lens is presented to build a solid base of knowledge for higher concentration ratios. Uniform electrical and thermal distribution has been detected within the focal spot showing the highest measured power at the centre of the MJ cell of 2.5 W. The numerical results using the finite element method (FEM) are validated with the indoor experimental results of the test section replicating the experimental conditions in the laboratory. The effect of different working conditions is reported throughout the research. Although the MJ solar cell temperature was below the recommended limit, the temperature can be decreased even further if a high thermal conductivity thermal paste is utilised emphasizing its importance in reducing the temperature.

Acknowledgments

First, I would like to express my sincere gratitude and deepest appreciation to my Ph.D. supervisor Prof. Tapas Mallick for his constant endeavour, support, positive criticism, motivation, and immense knowledge. His guidance and obligation to attend our weekly meeting even during this difficult time of COVID-19 helped me to direct my research correctly. I heard one time that the Ph.D. is the beginning of the academic journey and I have been lucky to start it under his supervision.

I would like to thank Dr. Senthilarasu Sundaram for being in different moments attentive second supervisor. I also would like to thank Dr. Asif Tahir for his valuable comments and useful discussion during our group meetings. I extend my appreciation to Prof. Mohamed Abusara for his advice and kind words which encouraged me. I also owe thanks and appreciation to Prof. Yulong Ding, the director of the Birmingham Centre for Energy Storage, for hosting me and giving me the opportunity to conduct a part of my experimental work in his laboratory.

My sincere thanks go to Dr. Katie Shanks for the useful discussion we had, ideas to support my research, and her precious time to complete most of the experimental work. I would also acknowledge all the co-authors involved in the several publications. Special thanks extended to Dr. Anurag and Dr. Hasan for the stimulating discussions we had during our group meetings.

I would like to extend my thanks to Mr. James Yule at the University of Exeter. The experimental work would not be achieved without his technical expertise. I also owe thanks to the language team at the University of Exeter: Mr. Richard, Ms. Tess, and Ms. Isabel. I am thankful to all my colleagues and lab fellows at the University of Exeter-Penryn Campus “Solar Energy Group” for the great discussions we shared.

My appreciation goes to the Ministry of Higher Education and Scientific Research in Egypt, British Council, Newton-Mosharafa Fund, and Port Said University for giving me the opportunity to undertake my PhD study at the University of Exeter.

This thanks is extended to include the Egyptian Bureau for Cultural and Educational Affairs in London.

Last but not the least, my heartfelt gratitude goes to my family. A bouquet of thanks goes to mom, grandma, and sisters: Esraa, Walaa, and Radwa for their understanding, support, prayers, and unconditional love. Also, my little nieces Karma and Leen who have made me happy when I needed that. I am also obliged to thank all my friends here in the UK and in Egypt. My PhD experience would not have been the same without any of them.

Table of Contents

List of Figures

List of Tables

Abbreviations

1-D	One Dimension
2-D	Two Dimensions
3-D	Three Dimensions
AADAT	Azimuth-Altitude Dual-Axis Tracker
AC	Alternating Current
ADG	Achromatic Doublet on Glass
AM	Air Mass
App.	Application
a-Si	Amorphous Silicon
CdTe	Cadmium Telluride
CFD	Computational Fluid Dynamics
CIGS	Copper Indium Gallium Selenide
CIS	Centre Inlet Serpentine
CNT	Carbon Nanotubes
COVID-19	Coronavirus Disease 2019
CPC	Compound Parabolic Concentrator
CPV	Concentrated Photovoltaic
CR	Concentration Ratio
CRS	Central Receiver System
CSP	Concentrated Solar Power
DAPTC	Direct Absorption Parabolic Trough Collector
DASC	Direct Absorption Solar Collector
DBC	Direct Bonded Copper
DC	Direct Current
DNI	Direct Normal Irradiance
ECR	Effective Concentration Ratio
EES	Engineering Equation Solver
EG	Ethylene glycol
ETSC	Evacuated Tube Solar Collector
F	Finned Channel
F.F.	Fill Factor
FEM	Finite Element Method
FPSC	Flat Plate Solar Collector

FR	Fresnel Lens
GalnAs	Indium Gallium Arsenide
GalnP	Indium Gallium Phosphide
GCR	Geometrical Concentration Ratio
Ge	Germanium
GMRES	Generalised Minimal Residual
GNP	Graphene Nanoplates
HCPV	High Concentrated Photovoltaic
HCPVT	High Concentrated Photovoltaic Thermal
HSAT	Horizontal Single-Axis Tracker
IEC	International Electrotechnical Commission
IEEE	Institute of Electrical and Electronics Engineers
IR	Infrared
IRENA	International Renewable Energy Agency
LCOE	Levelized Cost of Electricity
LCPV	Low Concentrated Photovoltaic
LFR	Linear Fresnel Reflector
Max.	Maximum
MCPV	Medium Concentrated Photovoltaic
Min.	Minimum
MJ	Multijunction
MRL	Maximum Recommended Limit
MWCNT	Multiwalled Carbon Nanotubes
NIR	Near Infrared
NREL	National Renewable Energy Laboratory
OD	Optical Density
PASAT	Polar Aligned Single-Axis Tracker
PCM	Phase Change Materials
PDC	Parabolic Dish Collector
PDMS	Polymethyl Siloxane
PEC	Performance Evaluation Criterion
PG	Propylene Glycol
PMMA	Polymethyl Methacrylate
POE	Primary Optical Element
PPMS	Polyphenyl-Methylsiloxane

PTC	Parabolic Trough Concentrator
PV	Photovoltaic
PVP	Polyvinylpyrrolidone
Ref.	Reference
RPHS	Round Pin Heat Sink
SBS	Spectral Beam Splitting
SC	Straight Channel
SEM	Scanning Electron Microscopy
SFHS	Straight Fin Heat Sink
Si	Silicon
SIS	Side Inlet Serpentine
SOE	Secondary Optical Element
SoG	Silicon on Glass
SUT	Solar Updraft Tower
Temp.	Temperature
TSAT	Tilted Single-Axis Tracker
TTDAT	Tip-Tilt Dual-Axis Tracker
UHCPV	Ultra-High Concentrated Photovoltaic
USA	United States of America
UTC	U-tube Solar Collector
UV	Ultraviolet
VIS	Visible
Vol.	Volume
VSAT	Vertical Single-Axis Tracker
Wt.	Weight

Nomenclature

A	Area	m^2
C	Concentration	$\%$
c_p	Specific heat at constant pressure	$J/kg\ .K$
d	Diameter	mm
$\dot{E}$	Exergy rate	W
E_f	Effectiveness of heat transfer	
h	Heat transfer coefficient	$W/m^2.K$
H	Height	mm
I	Current	A
k	Thermal conductivity	$W/m.K$
l	length	mm
$\dot{m}$	Mass flow rate	kg/s
p	Pressure	Pa
P	Power	W
$\dot{Q}$	Heat rate	W
$\dot{q}$	Heat source	W/m^3
R	Resistance	K/W
Re	Reynolds number	
t	Thickness	mm
T	Temperature or Transmittance	K or $\%$
U	Velocity	m/s
V	Total domain volume or Voltage	m^3 or V
$\dot{V}$	Volume flow rate	m^3/s
W	Width	m
l	Geometrical Loss	

Greek symbols

Δ	Difference	
β	Temperature coefficient	$\%/K$
ε	Emissivity	
η	Efficiency	$\%$
μ	Dynamic viscosity	$Pa.s$

ξ	Exergy efficiency	%
ρ	Density	kg/m^3
σ	Stefan Boltzmann constant	$W/m^2.K^4$
φ	Volume fraction	%
ψ	Conversion factor	

Subscripts

a	Ambient
b	Bulk
bf	Base fluid
c	Channel
ceramic	Ceramic layer
conv	Convection
copper	Copper layer
eff	Effective
elec	Electrical
f	Fluid or Fin
fo	Focal
g	Geometrical
h	Hydraulic
h.s	Heat sink
heat	Waste heat
in	Input or inlet
Lens	Fresnel lens
light	Incident light
max	Maximum
MPP	Maximum power point
nf	Nanofluid
np	Nanoparticles
oc	Open circuit
opt	Optical
out	Outlet or output
rad	Radiation
ref	Reference
s	Solid or surface

sc	Solar cell or short circuit
th	Thermal or theoretical
tot	Total
w	Wall

List of Publications

[1] **A. Ahmed**, H. Baig, S. Sundaram, and T. K. Mallick, “Use of Nanofluids in Solar PV/Thermal Systems,” Int. J. Photoenergy, vol. 2019, pp. 1–17, Jun. 2019.

[2] **A. Ahmed**, K. Shanks, S. Sundaram, and T. K. Mallick, “Theoretical Investigation of the Temperature Limits of an Actively Cooled High Concentration Photovoltaic System” Energies, vol. 13, no. 8, p. 1902, Apr. 2020.

[3] M. Alzahrani, **A. Ahmed**, K. Shanks, S. Sundaram, and T. Mallick, “Optical losses and durability of flawed Fresnel lenses for concentrated photovoltaic application,” Mater. Lett., vol. 275, p. 128145, Sept. 2020.

[4] **A. Ahmed**, M. Alzahrani, K. Shanks, S. Sundaram, and T. Mallick, “Effect of using an infrared filter on the performance of a silicon solar cell for an ultra-high concentrator photovoltaic system” Mater. Lett., vol. 277, p. 128332, Oct. 2020.

[5] **A. Ahmed**, G. Zhang, K. Shanks, S. Sundaram, Y. Ding, T. Mallick, “Performance evaluation of single multi-junction solar cell for high concentrator photovoltaics using minichannel heat sink with nanofluids”, App. Therm. Eng., 115868, (2020).

[6] **A. Ahmed**, M. Alzahrani, K. Shanks, S. Sundaram, and T. Mallick, ”Reliability and Temperature Limits of the Focal Spot of a Primary Optical Component for an Ultra-High Concentrated Photovoltaic System”, CPV-17 AIP conference proceeding, 2021, Accepted.

[7] **A. Ahmed**, K. Shanks, S. Sundaram, T. Mallick, “Energy and exergy analyses of new cooling schemes based on a serpentine configuration for a high concentrator photovoltaic system”, App. Therm. Eng., 117528, (2021).

[8] M. Alzahrani, **A. Ahmed**, K. Shanks, S. Sundaram, and T. Mallick, “Optical Component Analysis for Ultrahigh Concentrated Photovoltaic System (UHCPV),” Sol. Energy, 2021.

[9] **A. Ahmed**, K. Shanks, S. Sundaram, T. Mallick, “A review on recent advances in concentrating photovoltaics systems”, In preparation.

[10] **A. Ahmed**, K. Shanks, S. Sundaram, T. Mallick, “Experimental and theoretical analyses of high concentrating photovoltaics system”, In preparation.

Chapter 1
Introduction

Renewable energy, especially solar and wind energy, has become the focus of unprecedented interest as a clean source for generating electricity. Solar energy is one of the world's most sustainable resources, capable of providing renewable and reliable energy to a wide range of locations. The amount of solar energy falling on the Earth in an hour is greater than what the whole planet's population consumes in one year [1]. Therefore, it is vital to develop an efficient technology to harness this energy capacity. In 2020, the installed capacity of the solar photovoltaics (PV) around the world reached 25.3% of the total renewable energy techniques according to the International Renewable Energy Agency (IRENA) [2] as shown in Figure 1. Solar photovoltaics is one of the most rapidly growing renewable energy sources, the power generated using solar photovoltaic technology increasing by 667,207 MW from 2010 to 2020 as presented in Figure 2.

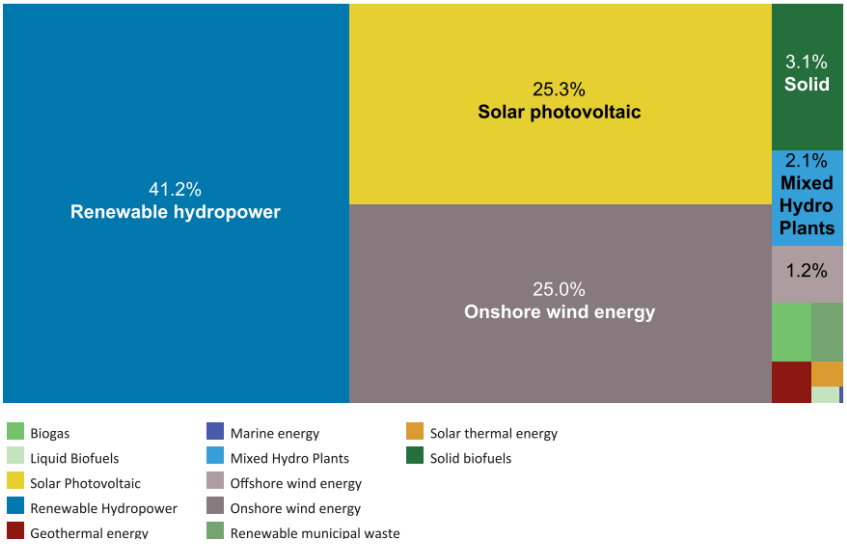

Figure 1 Renewable energy installed capacity in 2020 according to the International Renewable Energy Agency [2].

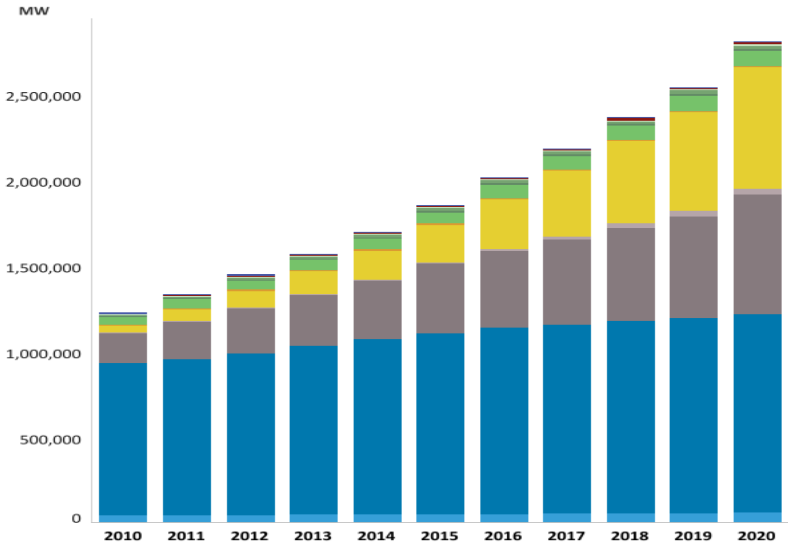

Figure 2 Global electricity generation/year from different renewable energy resources according to the International Renewable Energy Agency [3].

1.1 Concentrated photovoltaics is an emerging technology

Up to now, common photovoltaic (PV) panels available in the market convert between 15% and 20% of the incident energy into electricity, while a large portion is transformed into heat [4]. This motivated researchers to develop new technology which has the ability to convert more energy into electrical power. The key principle of concentrator photovoltaics (CPV) is the use of affordable and efficient optics that significantly reduce the solar cell area. This enables the use of high-performance small area multijunction solar cells (MJ) which offer a competitive levelized cost of electricity (LCOE) compared to concentrated solar power (CSP) and conventional flat-plate PV technology in high direct normal irradiance (DNI) regions [5].

The cell efficiency is defined as the ratio between the energy produced by the solar cell to the energy input from the sun. To date, the highest informed cell efficiency is 44.4% and 47.1% for 3-junction and 4-junction cells at 25 °C as reported by NREL [1]. However, the development of this type of technology faces several challenges such as the need for a durable material that can be sustained in outdoor conditions, high temperatures that affect the performance of the solar cell, and the thermal stresses that are created from the change of the solar irradiance throughout the day. Araki et al. [6] reported a rapid increase in the cell temperature at a concentration ratio of 500 suns as it can reach as high as 1400

°C if it is left completely insulated. Hence, to protect the solar cell from long-term degradation a typical maximum working temperature has been set as 110 °C such as in the cell used in this study by AZUR SPACE [7]. Therefore, designing an efficient thermal management system for the high concentrator photovoltaic system (HCPV) is essential to achieve high and stable performance.

1.2 Research aims and objectives

The aim of this research is to evaluate the performance of a high concentrating photovoltaic system using different thermal management approaches. This aim can be achieved through the following research objectives:

- Understand and develop a suitable model to investigate the thermal performance of the HCPVT using different designs and under different operating conditions. This includes gaining experience in the application of COMSOL-Multiphysics software to simulate the HCPVT system.
- Investigate the impact of using different heat sink designs, cooling fluids (including nanofluids), and optical filters on the HCPVT system performance to control the solar cell temperature. This is achieved by undertaking several parametric analyses to understand the impact of each factor on the system performance.
- Experimentally characterise the thermal, optical, electrical properties of the Al_2O_3/water and SiO_2/water nanofluids, Fresnel lens, IR optical filter, and solar cells, respectively. This is followed by conducting an indoor characterisation of the Fresnel lens focal spot area.
- Design and manufacture a prototype of the heat sink and full experimental setup along with conducting numerical validation for different cases to understand the thermal and electrical system performance of the HCPVT.

1.3 Research Methodology

1.3.1 Initial studies on the CPV thermal analysis

COMSOL-Multiphysics software is an efficient tool based on a finite numerical method that is utilised to perform the numerical modelling. The software is used to solve the coupled heat transfer and fluid flow partial differential equations to

perform the initial investigations of existing CPV designs and heat sinks and the obtained outcomes are validated against the theoretical and experimental studies in the literature.

1.3.2 Experimental characterisation

Experimental characterisation and analysis of the different materials used throughout the study are performed. This includes the thermal characterisation of the thermal conductivity of the nanofluids at different concentrations, optical characterisation of the optical components by measuring their efficiency to transmit a wide range of wavelengths, and electrical characterisation of the solar cells investigated throughout this research.

1.3.3 Numerical model development

Numerical 3-D models and workflow are developed to simulate the HCPVT system and conduct the thermal performance analysis. The simulated models consist of MJ solar cell and heat sink schemes. Some thermophysical properties of the investigated cooling media are entered into the software for greater accuracy. Different heat sink configurations and cooling media are investigated and compared, and several parametric studies are performed to investigate their impacts on the system performance.

1.3.4 Experimental investigations and numerical validations

Different experimental investigations are conducted to test the HCPVT performance. The feasibility of using IR filtering to thermally manage the system temperature is carried out using a Fresnel lens and IR filter under the solar simulator. Investigating the focal spot area of the Fresnel lens with and without utilising the MJ solar cell is conducted thermally and electrically. Then, the investigation of the heat sink test section utilised to thermally manage the solar cell temperature is carried out using an electric resistance heater as well as the MJ solar cell under the solar simulator. After that, numerical models for each case are built to simulate, validate, and analyse the test section using COMSOL software.

1.4 Contribution of the thesis to the field

Several approaches and parameters have been investigated in this research, all of which added significantly to the body of knowledge of the HCPV aiming to address the thermal management challenges, and can be summarised as follows:

- A comprehensive characterisation of the nanofluids and their classifications, applications, and future outlook as well as the parameters that affect their thermal conductivity have been identified.
- The impact of using different cooling media (distilled water, ethylene glycol and water mixture, and Syltherm oil) on the HCPV performance has been explored.
- The thermal characterisation of Al_2O_3/water and SiO_2/water has been carried out in terms of their thermal conductivity with the volume fraction and temperature.
- The impact of using nanofluids to thermally regulate the MJ cell temperature for a wide range of concentration ratios has been introduced.
- The influence of different heat sink configurations including finned heat sink, straight channel, side inlet serpentine, and centre inlet serpentine on the performance of the HCPV performance and cell temperature uniformity has been investigated.
- The feasibility of using IR filtering to regulate cell temperature has been explored under high concentration ratios.
- An exploration of the thermal and electrical performances of the focal spot area of the Fresnel lens has been introduced.
- An experimental investigation and numerical validation on the use of nanofluid on the Fresnel lens based HCPVT system performance from thermal and electrical perspectives have been studied.

1.5 Thesis Layout

The thesis is divided into 8 chapters, beginning with an introduction to the research project, progressing through technical analyses, and concluding with

findings and suggestions for future work. A brief summary of the content of each chapter is introduced below.

Chapter 1 of the thesis is an introductory chapter summarising the research background and motivation to undertake the current study. In addition, the aims and objectives are highlighted along with the research methodology conducted to investigate each part of the thesis. Finally, the contribution of each section to the field, as well as the thesis structure, are presented.

Chapter 2 of the thesis provides an overview of the basics of concentrating solar technologies with a special focus on concentrator photovoltaic systems (CPV), the advantages, and challenges of this technology in comparison with other techniques. This is followed by a review of the design principles, optics, and solar cells classifications. Also, a literature review of the thermal management systems including the use of the optical filters is addressed. The final part of the chapter presents the role of nanotechnology in solar thermal systems with a summary of its advantages and main challenges. The review includes the different research methodologies implemented in the previous studies including both the experimental and simulation works.

Chapter 3 introduces a comprehensive explanation of each of the instruments, devices, and materials used in the experimental investigation highlighting their working principles and specifications. In addition, the software packages used to undertake the theoretical investigation are described.

Chapter 4 concentrates on the detailed materials characterisation utilised in this research. This includes studying the optical, thermal, and electrical performance of these materials depending on their application. The optical characterisation is undertaken in terms of measuring the transmittance efficiency of the Fresnel lens and the IR optical filter, while the thermal characterisation is conducted in terms of thermal conductivity measurements of different working media with a comparison of the available empirical equations. The electrical characterisation of the solar cells is addressed in terms of the performance curves and fill factor.

Chapter 5 focuses on the numerical modelling development to carry out the thermal analysis of the HCPVT system. The physical models of the heat sink configurations along with the thermophysical properties of the materials and different working media are introduced. The governing equations of the coupled heat transfer and fluid flow and their boundary conditions are explained. Furthermore, different grid independence tests and validations studies are introduced.

Chapter 6 discusses the theoretical performance analysis of the HCPVT system and the impact of different cooling media as well as heat sink configurations. Different scenarios are investigated including the possibility of replacing the water, ethylene glycol/water mixture, and syltherm oil. Also, the impact of utilising nanofluids and their impact on the system performance is presented. The performance evaluation and feasibility of using different heat sink schemes are introduced.

Chapter 7 introduces different indoor experimental approaches to thermally regulate the temperature of a Fresnel lens based HCPVT system. Also, the description of each experimental setup is explained. The feasibility of using the IR optical filter is investigated to regulate the temperature of a silicon solar cell including evaluation of the electrical system performance. A comprehensive thermal, optical, and electrical analysis of the focal spot of the Fresnel lens is presented. Furthermore, experimental investigations of the impact of the heat sink configurations and heat transfer fluids are studied using uniform and nonuniform heat sources including the numerical validations of each case.

Chapter 8 presents the conclusions of all the achieved work throughout the thesis. Finally, the recommendations for future expansion of the work are listed.

Chapter 2
Background and literature review

2.1 Introduction

The aim of this chapter is to review the basic knowledge in relation to concentrator photovoltaic systems and their working characteristics. This includes their design principles and working conditions and an overview of the advantages and issues of the system. It also outlines different optics that have been utilised to date. Various thermal management methods that have been considered in the literature with reviews of the preceding studies have been highlighted in this chapter. The role of nanotechnology in solar thermal systems has been addressed in the last section.

2.2 Concentrated solar energy technologies

In general, concentrating solar energy is based on concentrating solar radiation to increase electricity generation. There are two main types of this technology: concentrating solar power systems (CSP) and concentrating photovoltaic systems (CPV). Both technologies have a number of common aspects as they both exploit concentrators to focus the incident light on the target object. In the case of CSP, the target object will be the thermal receiver, while for CPV it will be a photovoltaic solar cell. It is important to note that the working principle of the CPV system was driven from the CSP technology [8]. The classification and working criteria of each of these techniques will be reviewed in the following sections.

2.2.1 Concentrated Solar Power (CSP)

Concentrating solar power is a solar technology that uses mirrors or reflectors to concentrate the sun onto a thermal receiver. The fluid inside the receiver is heated using the power from the sun, this heat (solar thermal energy) is used to generate the power that drives the heat engine or steam turbine which is connected to an electric power generator for electricity production. The CSP technology is considered a promising option for power generation especially for areas of high direct normal irradiance (DNI). According to Shouman and Ezz [9], the solar thermal power locations can be divided according to their suitability into

excellent, good, suitable, and unsuitable regions. These zones are classified according to their daily and yearly direct solar irradiances as shown in Figure 3. The excellent zones are locations with direct normal irradiances above 6 kWh/m^2 of the daily total solar irradiance, while the unsuitable locations are areas that have a daily total solar irradiance of less than 3 kWh/m^2. The main concentrated solar power configurations are classified into three categories: point focus, line focus, and non-concentrated.

Point focus

Parabolic dish collector (PDC)

The PDC consists mainly of a reflective parabolic-shaped concentrator to concentrate the sunrays into a receiver that is mounted in the centre of the parabola to collect the heat. This receiver may be replaced by a Stirling engine that converts the thermal energy into mechanical form. This mechanical energy is converted into electrical power for electricity generation. The concentration ratio of this technology varies between 100 to 1000 suns and the operating fluid temperature can reach as high as 1500 °C.

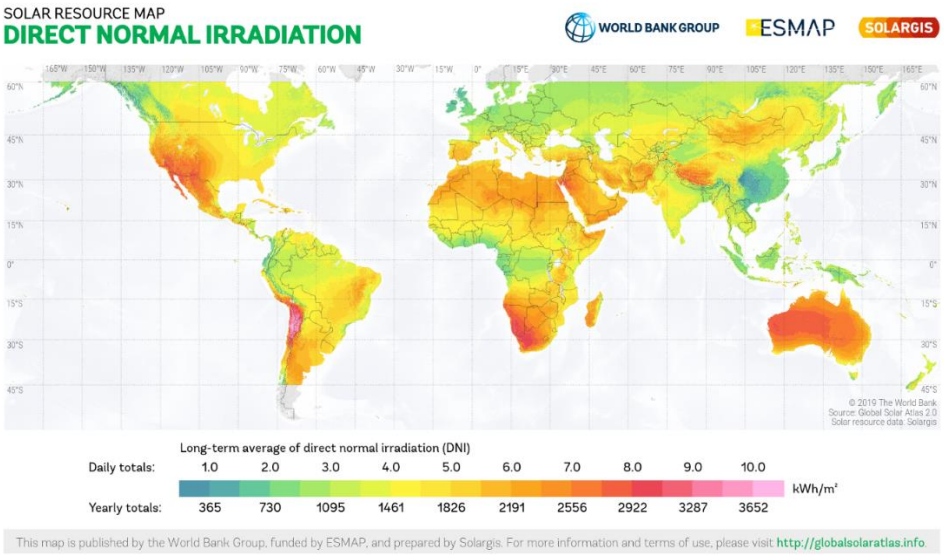

Figure 3 Direct normal irradiance distribution map [10].

Power tower or central receiver system (CRS)

This system comprises many heliostats (mirrors) where the sun rays are reflected by each of them into a central receiver fixed at the top of a tall tower. This receiver usually contains water or molten salt to work as a heat transfer fluid. After being heated by the reflected solar irradiance, the heat is transferred through a heat

exchanger where the water is converted into superheated steam. This steam drives a steam turbine that is connected to an electric generator at the bottom of the tower for electricity production. The concentration ratio can reach as high as 1500 suns by using this technology and the working medium temperature ranges between 300 and 2000 °C.

Line focus

Parabolic trough concentrator (PTC)

The PTC is composed of a concentrator made from a reflective material and a receiver (absorber). The function of the parabolic reflector is to concentrate the sunlight into the receiver which contains the heat transfer medium. The parabolic reflector is usually made from silvered acrylic. The absorber is placed in the focal point of the parabolic concentrator. Both the absorber and the reflector are moving in tandem to track the sun from sunrise to sunset. The working temperature range of the PTC usually varies from 20 to 400 °C and a concentration ratio of 15-45 suns [11].

Linear Fresnel reflector (LFR)

The LFR is comprised mainly of an absorber tube (receiver) as in the case of the PTC system, multiple rows of primary optics and one secondary optic (Figure 4b). The function of the primary reflectors is to concentrate a large amount of the incident solar irradiance into the secondary reflector which in turn reflects these rays to the absorber tube which increases the temperature of the heat transfer fluid. The heat transfer fluid working range for this technology fluctuates between 50 and 300 °C for a concentration ratio of 10 and 40 suns [11].

Non-concentrated

Solar updraft tower/ solar chimney (SUT)

This technology is based on the thermal engine concept. It mainly consists of solar air collectors, towers, and wind turbines. The air underneath a transparent roof is heated by the effect of high solar irradiance (the roof and the ground form a solar collector). When the air is heated, its density decreases which makes it lighter than the cold air. The hot air rises to the tower while the cold air comes from the outer premier of the solar collectors. In this way, this natural updraft is converted into mechanical energy by the wind turbine (based at the bottom of the tower) which is connected to an electric generator for electricity production. The

air temperature using this method increases by up to 35 °C which increases the air velocity updraft to about 15 m/s at full load [12].

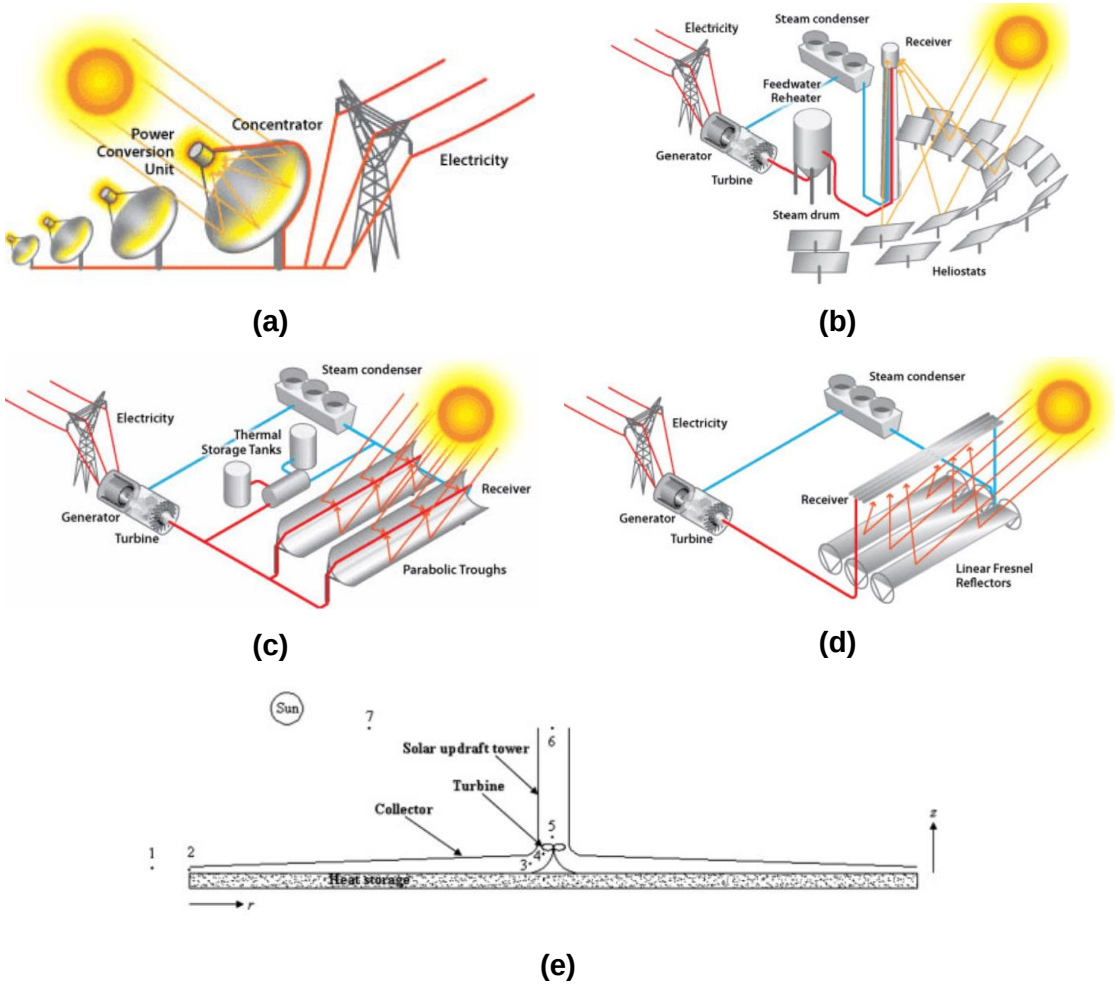

Figure 4 (a) Solar dish system (b) Solar power tower (c) Parabolic trough concentrator (d) Linear Fresnel reflectors, and (e) Solar updraft tower [13].

2.2.2 Concentrated Photovoltaic (CPV)

Concentrated photovoltaics (CPV) is a different kind to those mentioned above. The working idea of this system is based on concentrating the solar irradiance, by using cheap and efficient optical concentrators, on a small photovoltaic solar cell. This enables the use of high-performance small area multijunction solar cells (MJ) which offer a competitive Levelized Cost of Electricity (LCOE) compared to concentrated solar power (CSP) and conventional flat-plate PV technology in high direct normal irradiance (DNI) regions [5], especially for long-term usage. It is expected that the LCOE for the CPV system varies between 0.045 to 0.075 Euro/kWh by 2035 [14] as shown in Figure 5. Although the CSP is more flexible in comparison with the CPV technology, it is expected that the LCOE of the CSP

technology could hit 0.115 to 0.089 Euro/kWh by 2035 which is still higher than the CPV technology by about 53%.

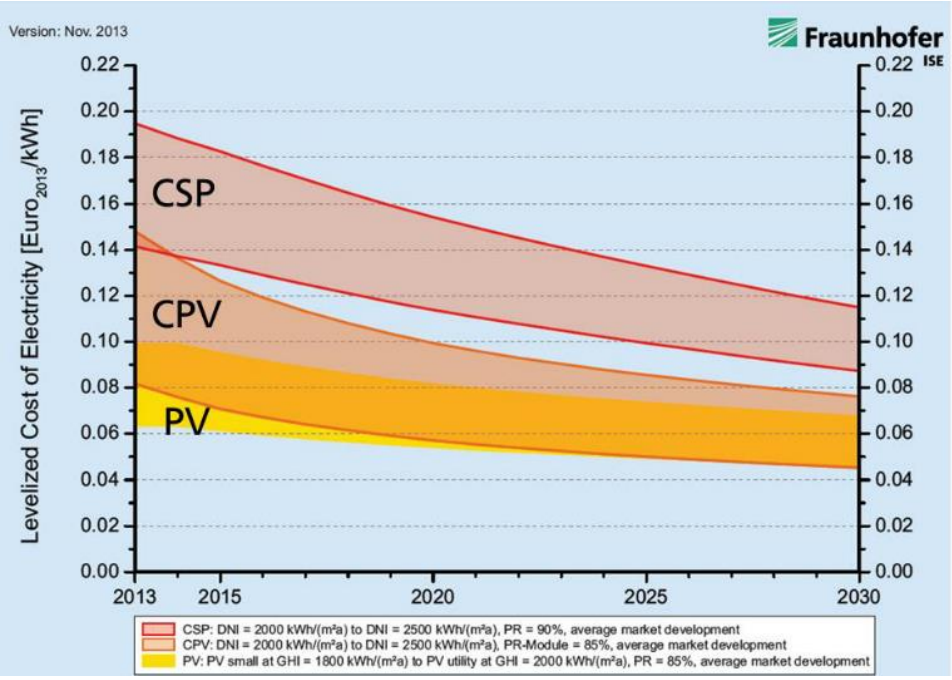

Figure 5 Comparison between the current and expected Levelized cost of different solar energy technologies until 2030 [14].

The PV solar cell is a semiconducting material that absorbs the light's photons and releases electrons. This process is defined as the photoelectric effect. This process does not require any mechanical power or chemical reactions. However, it depends mainly on the sun's movement. Therefore, one of the key criteria for this technology is using a highly accurate tracking device. The tracking accuracy requirements depend on the concentration ratio; for high and ultrahigh concentration ratios the two-axis tracking system is required, while for low concentration ratio one-axis may be sufficient. As the concentrated solar power technology, the CPV systems can be competitive only if they are in areas with high solar irradiances equal to or above 6 kWh/m^2/day [15]. Also, one of the advantages of the CPV over the CSP is that it can be scaled over a wide range from kW to GW depending on the required demand.

The CPV system can only concentrate the direct beam radiation but cannot use the diffused and filtered lights which occur due to cloudy, overcast, and polluted weather conditions. These lights have spectral discrepancies which can result in a mismatch between the produced electrical currents created within the series-connected p-n junctions in the Multijunction solar cells [16]. Due to the above

reasons, the CPV technology may fail to meet the power output expectations when the atmospheric conditions are below the standard.

2.2.2.1 CPV Classification

The CPV systems may be categorized according to their concentration ratios (CR), which is the ratio between the aperture area and the receiver area [17]:

1) Low concentrator photovoltaic (LCPV): CR<10 suns.
2) Medium concentrator photovoltaic (MCPV):10<CR<100 suns.
3) High concentrator photovoltaics (HCPV): 100<CR<2000 suns.
4) Ultra-high concentrator photovoltaics (UHCPV): CR>2000 suns.
Where every 1 sun is equal to 1000 W/m^2.

2.2.2.2 Advantages and challenges

The CPV systems have a wide range of advantages which can be described as follows:

1) High performance especially in areas with high direct normal irradiance.
2) Relatively low production cost due to the fact of using low amounts of semiconducting materials.
3) The production capacity of the system varied between kW to GW.
4) The waste heat from the system can be exploited for systems with high and ultrahigh concentration ratios that are actively cooled [15].
5) In comparison with silicon solar cells, they have a relatively low-temperature coefficient that makes them insensitive to the change in temperature and have an almost completely stable performance.
6) The tracking system allows stable energy generation throughout the day, especially for high concentration ratios.
7) Low environmental impact due to the use of small and non-toxic semiconducting materials.
8) The possibility of utilizing the land for other purposes such as agriculture in comparison with the CSP [18].

On the other hand, the technology still suffers from some limitations:

1) The HCPV can only concentrate the direct beam radiation in contrast to the LCPV which is able to make use of a small fraction of the diffuse radiation in addition to direct beam radiation.
2) The technology is only efficient and competent in areas with high normal irradiance. This limits its application, unlike the conventional flat-plate PV.
3) In the case of not using highly efficient optical components, the conversion efficiency, as well as the power output, will decrease significantly due to the optical losses.
4) The performance of the system depends mainly on the tracking system for high-energy production. Therefore, accurate tracking is one of the main requirements for a system's reliability.
5) The technology is still in the developing stage which increases the investment risk.

2.2.2.3 Solar cell

The solar cell is a device that is able to convert the energy from light into electricity when the light strikes a semiconductor surface. This process is called the photoelectric effect which was first discovered in 1839 by Alexandre Edmond Becquerel [19]. The absorption of light in semiconducting materials depends mainly on the bandgap concept. The bandgap can be defined as the distance between the conduction band and the valence band.

As shown in Figure 6, if the photon's energy is lower than the bandgap energy, it will not be absorbed and will pass through the semiconducting material. However, if the photon's energy is higher than the bandgap energy, it will be absorbed by the semiconducting material and will give this energy to electrons in the valence band to move up to the conduction band leaving a hole behind. In this respect, the access energy by the electron-hole pair will be wasted. The third scenario occurs when the photon energy is equal to the bandgap energy and will be absorbed proficiently with no excess heat.

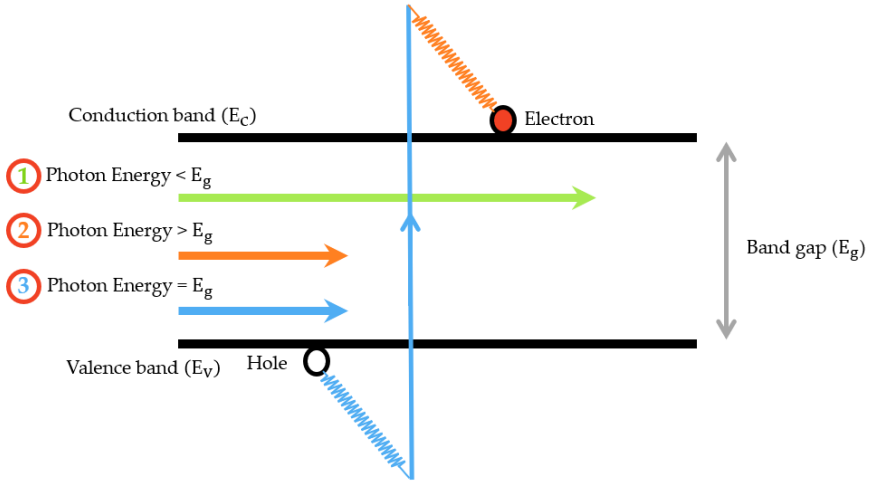

Figure 6 Electron-hole pair concept after illumination.

Figure 7 represents the electron-hole pair occurring in a PV cell. The upper-part (n-type) consists of semiconducting material that is doped with phosphorus, while the lower part (p-type) is doped with boron. When the n-type and p-type meet up it is called an n-p junction. The incident light produces an electron-hole pair (electron from p-region to the hole left in n-region), therefore the electrons flow from top to bottom which completes the circuit and generates electricity. This is a simplified version of the light to electricity conversion that occurs in silicon semiconductor photovoltaic cells [20].

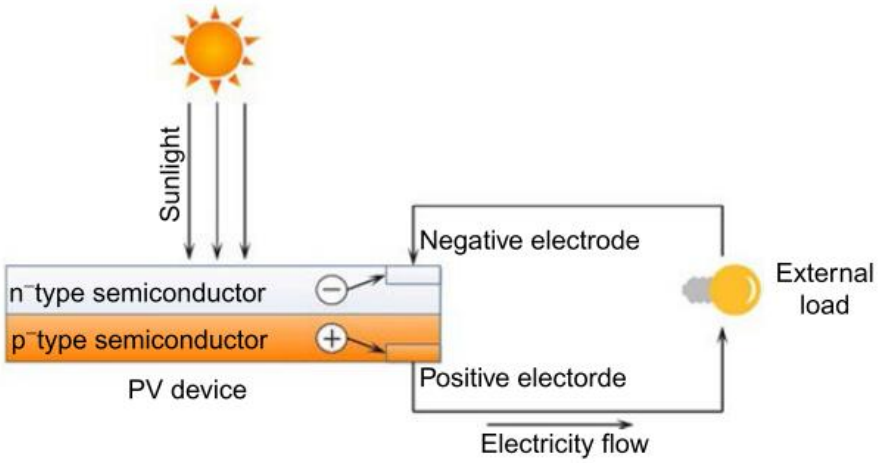

Figure 7 Cell principle operation [19].

The solar cells materials can be classified into three categories as introduced in Figure 8 as first, second, and third generations.

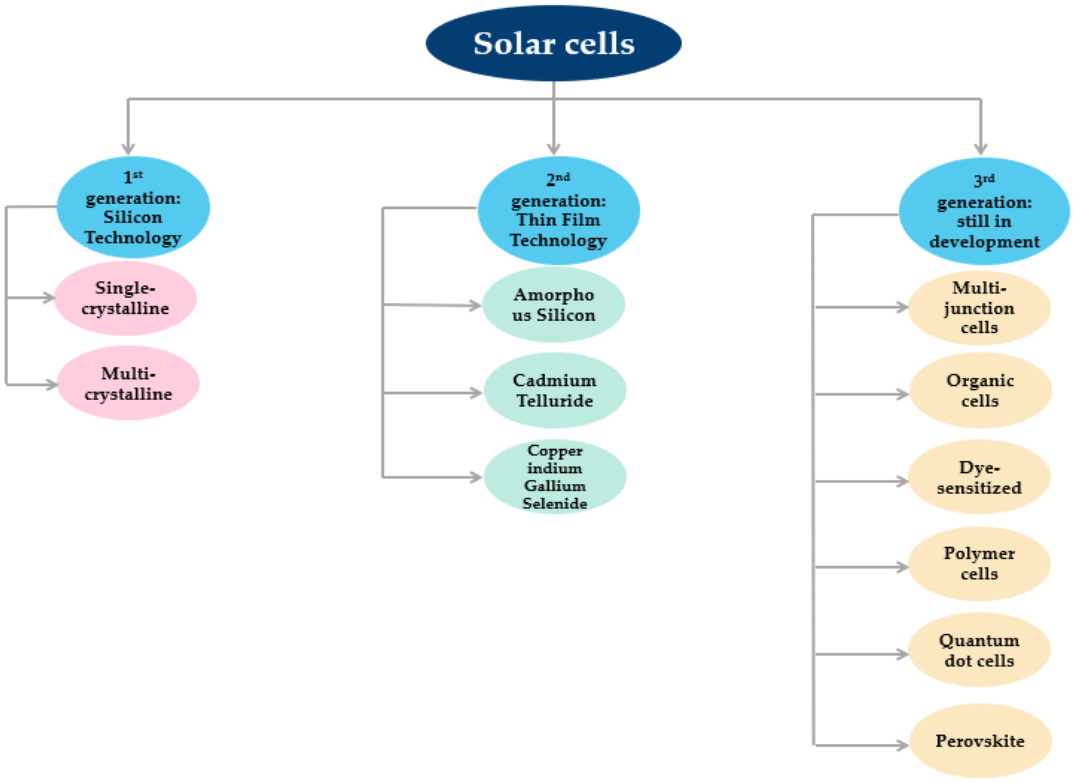

Figure 8 Solar cells classification.

First generation (wafer-based)

This type is dependent on silicon which is one of the most easily accessible materials on the Earth but not in pure form. Silicon dioxide accounts for 27.7% of the Earth's crust, it is the crust's second most abundant component. Therefore, to make it ready to use in the manufacturing process of the silicon solar cell, it should be passed through many processes. The silicon solar cells may be classified into single crystalline and multi-crystalline silicon solar cells.

Second generation (thin-film technology)

Due to the fragility of the wafer-based silicon solar cells, thin-film technology was developed to offer better performance with the flexibility option to the solar cells' technology (Figure 9). It also can be produced at large substrates with a low amount of material usage. Moreover, it has a high absorption coefficient, and the expected energy payback time is lower than the traditional silicon solar cells. There are three main types of thin-film solar cells: amorphous silicon (a-Si), cadmium telluride (CdTe), and copper indium gallium selenide (CIGS) solar cells. The highest recorded efficiencies according to NREL reached 14%, 22.1%, 2.6% for a-Si, CdTe, and CIGS, respectively [21]. As compared to the silicon type, the

fabrication process of these cells is considerably different. Many different approaches are implemented for every kind of cell, including vapor deposition, spin coating, electrolytic baths, and sputter processes. As compared to the silicon type, electrical connections are made on the back of the solar cells with an opaque coating, while the front of the solar cells is normally coated with a highly transparent conductive metal oxide.

Figure 9 Thin-film silicon solar cell [22].

Third generation (Emerging)

This type of technology is still in the development stage. The major types of this technology are Multijunction solar cell (used in the CPV), organic cells, dye-sensitized, polymer, quantum dot and perovskite solar cells. The motivation to create these devices is to achieve high conversion efficiency with the aim of avoiding the Shockley-Queisser limit if compared with the first and second-generation solar cells with the use of non-toxic materials and already available in abundance, low manufacturing cost and low energy payback time. The third-generation solar cells offer a solution for the huge losses that are created by using the single-bandgap solar cells. Another problem associated with the single bandgap cells is the inability to absorb photons that have energy lower than the specified bandgap (absorption losses), while the thermalization losses occur when the photons have energy higher than the bandgap energy of the material. These losses account for about half of the incident solar energy.

For a high concentration ratio (CR>100 suns), the multi-junction solar cell is the only reported technology that is able to withstand high solar irradiance and high temperature. On the other hand, silicon solar cells (c-Si) are reported to work at concentration ratios lower than 100 suns [5]. The multi-junction solar cells are a promising technology with a great number of advantages and still an active area of research. Multijunction cells (MJ) were originally utilized for space applications

due to their high conversion efficiencies required for this type of application in spite of their high manufacturing costs. In comparison to the conventional flat-PV, their costs are still higher but at the same time they can offer a wide range of advantages which is the reason for their utilization in the CPV market [23,24].

These cells are designed with multiple tandem layers (usually from two to five layers) that are stacked above each other and connected in series as shown in Figure 10. The semiconducting materials used are from the third and fifth element group in the periodic table [25]. The drive to design such kinds of cells is to achieve high conversion efficiency with minimum losses and a low-temperature coefficient to withstand high-temperature weather conditions. Several bandgap energies can be obtained by carefully tuning the compositions.

Figure 10 Schematic diagram of different multijunction solar cells made from III-V semiconducting materials.

Usually, the combinations of the sublayers follow the lattice constant principle. Every junction should have the same lattice constant as the other ones (with different bandgap energy) to avoid lattice mismatches which increase the conversion losses. Therefore, the triple-junction solar cell is composed of GaInP/GaInAs/Ge with a lattice constant of 5.65 [Aº]. The most common lattice-matched MJ solar cell is introduced in Figure 11.

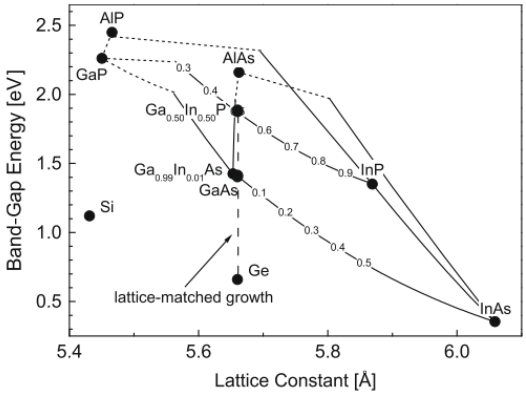

Figure 11 Lattice constants for the most common semiconducting materials [26].

The key concept of these cells is that the light photons with the larger wavelengths will be absorbed in the bottom layer, while the photons with the smaller wavelengths will be absorbed in the upper layer as introduced in Figure 12. To prevent current mismatch, which is considered a critical problem and requires a high manufacturing accuracy, the current produced by each cell should be equal to the smallest one within the currents generated by any other cell. Therefore, scaling each layer's thickness is of importance because the thinner the layer, the higher the produced current. The triple-junction cell is composed of three layers as follows:

- *Top layer indium gallium phosphide (GaInP):* This semiconducting material absorbs the ultraviolet and visible part of the solar spectrum. It has a bandgap energy of 1.86 eV.
- *Middle layer gallium arsenide (GaInAs):* Absorbs the near-infrared spectrum with a bandgap energy of 1.4 eV.
- *Bottom layer germanium (Ge):* The photons with the infrared spectrum are absorbed by using this sub cell. Also, it has a bandgap energy of 0.65 eV.

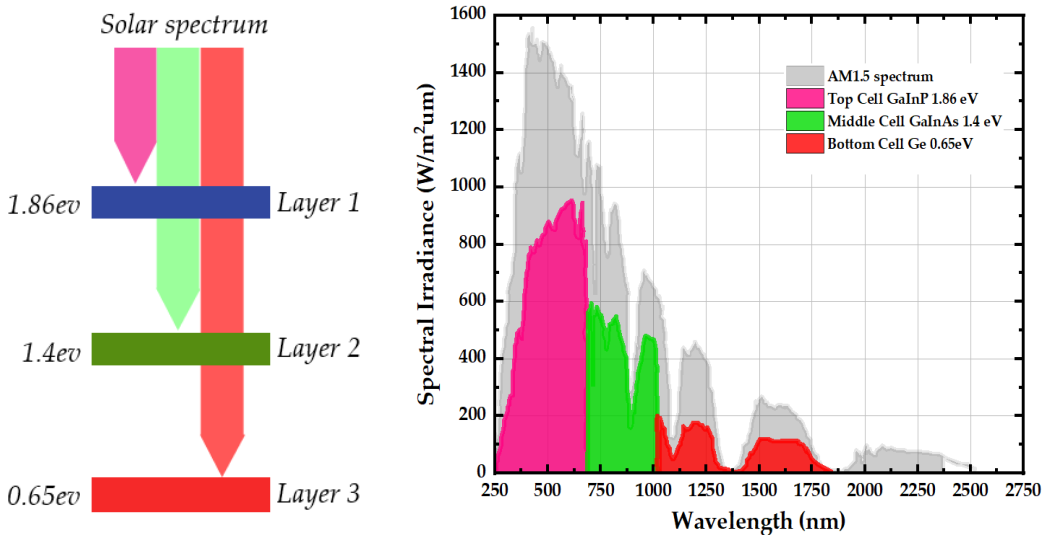

(a) **(b)**

Figure 12 (a) Spectrum splitting and (b) spectral irradiance for stacked configuration of a triple-junction solar cell.

The maximum theoretical efficiency as calculated by Fraunhofer ISE [27] varying with the number of the pn-junctions is plotted in Figure 13 for the reference spectrum AM1.5G (1 sun and ambient temperature of 25 °C) and AM1.5D (500 suns and ambient temperature of 25 °C). The maximum theoretical efficiency increases by increasing the number of the pn-junctions reaching 67.5% for the 5-

junctions solar cell under 500 suns. However, due to the thermalisation and absorptions losses, these values have not yet been achieved. However, according to the NREL report [15], the efficiency of MJ cells is increasing at a rate of about 0.5 to 1 percent per year [15]. The highest reported solar cell efficiencies for the single and multijunction solar cell are 36% (achieved at 38.1 suns) and 47.1% (6-junctions solar cell at 143 suns) respectively. Both have been produced and tested in NREL labs as illustrated in Figure 14. On the other hand, the enhancement in the silicon solar cell efficiency is still limited to 27% in comparison with the progress in the MJ solar cell. However, the reported module efficiencies of these solar cells have lower values as shown in Figure 15.

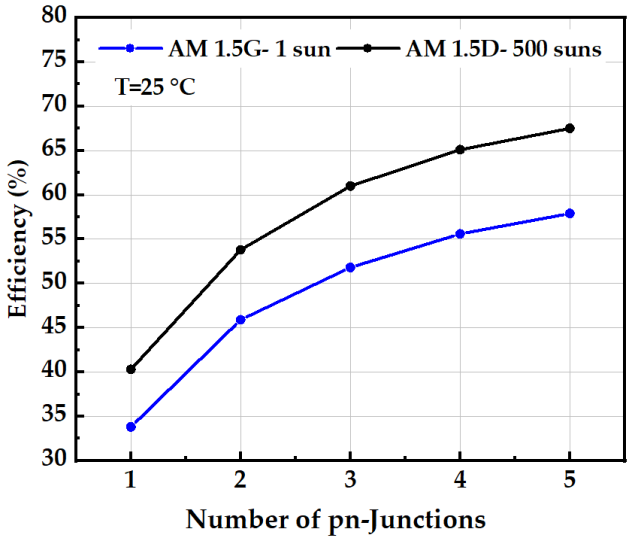

Figure 13 The maximum calculated theoretical efficiency of different pn-junction solar cells by Fraunhofer ISE measured at 1 sun (AM1.5G) and 500 suns (AM 1.5D) at 25 °C.

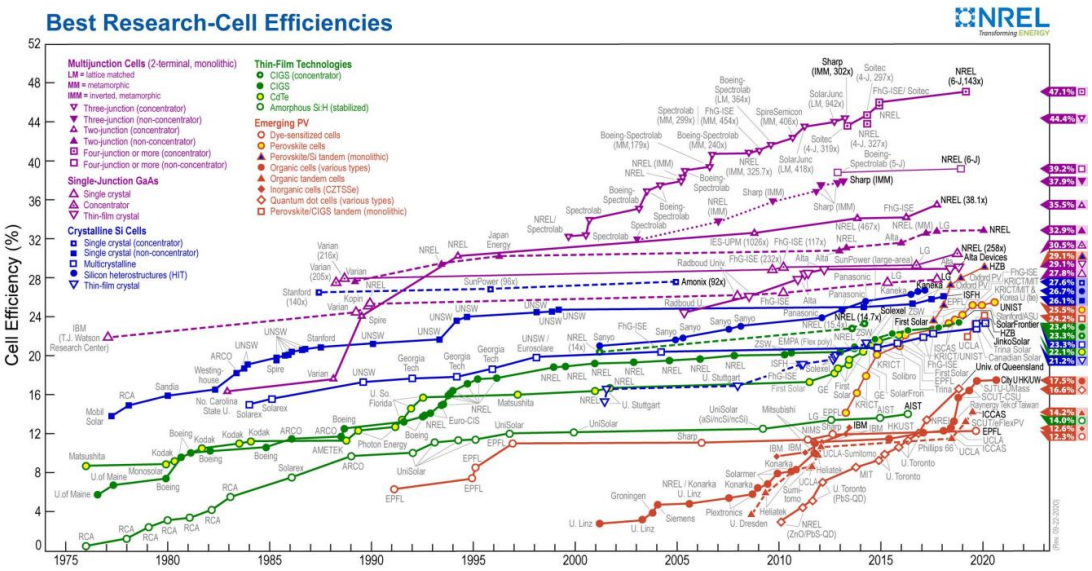

Figure 14 Different solar cells efficiencies as reported by NREL [28].

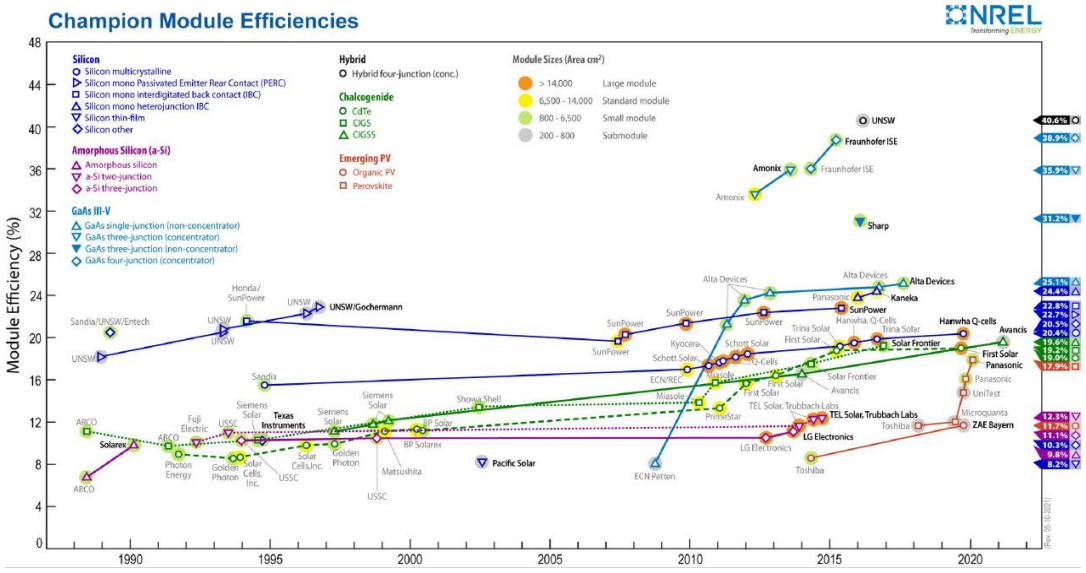

Figure 15 Different module efficiencies as reported by NREL [29].

In comparison to the first-generation solar cells, the MJ cell fabrication is very different. Each sub-layer is manufactured separately and then stacked on each other using a mechanical process [30]. The fabrication process is still expensive which makes this type inaccessible at present [31]. In addition to its high cost and limited availability, it also offers some dangerous environmental and health impacts as it contains gallium arsenide (GaInAs). This component is usually produced from gallium and arsenic or from the reaction of trimethyl gallium and trimethyl arsenic which are both toxic and cause severe health conditions which can be summarized as presented in Table 1.

Table 1 Health problems associated with different materials in MJ solar cell [32].

Material	Utilization	Health problems
Arsenic	GaAs manufacture	Poisonous and carcinogenic
Phosphine and Arsine	In the process of GaAs doping	Poisonous and work-related illnesses
Trimethyl gallium	In the process of manufacturing GaInAs	work-related illnesses

In many applications, a silicon sub-layer (Si) can replace the expensive Germanium layer (Ge) as a cheaper solution. However, this can create a number of problems to the solar cell, for example about 4% difference of the lattice constant [26], different thermal expansion, and lower conversion efficiency. Table 2 summarises a comparison between different semiconducting materials in terms of the thermal expansion and lattice constant.

Table 2 Different semiconducting materials properties [26].

Material	Bandgap energy (eV)	Thermal expansion coefficient (°C)	Lattice constant (A^o)
GaAs	1.4	5.7×10^{-6}	5.653
Ge	0.7	5.9×10^{-6}	5.646
Si	1.1	2.6×10^{-6}	5.431

The characteristics of the solar cell can be described in terms of current (I)-voltage (V) and power (P)-voltage graphs as seen in Figure 16. As introduced in the beforementioned graph, the I-V curve characterizes the change of the output voltage of the cell in relation to the current, while the P-V curve represents the variation of the produced power by the cell versus the cell's output voltage. These curves measure the ability of the cell to convert the incident illumination into electrical power.

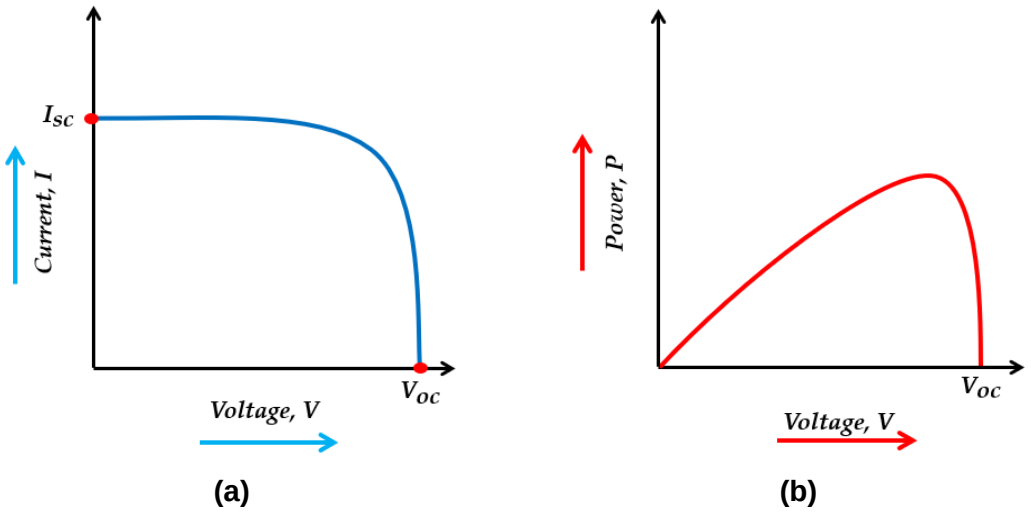

Figure 16 (a) Current-voltage curve (b) power-voltage curve of the solar cell.

Therefore, a number of important performance parameters should be defined. Firstly, short circuit current (I_{sc}), is defined as the maximum current flowing through the cell when the voltage drop is zero. The value of the short circuit current depends on other factors such as the cell area, the amount of the incident light, optical properties as well as the light spectrum. When the current through the cell becomes zero, the voltage reaches its maximum and this value is known as open-circuit voltage (V_{oc}). Since the power values at both the short circuit current and open-circuit voltage are zero, another parameter is introduced to measure the maximum power (P_{MPP}) produced by the solar cell which is called fill factor (F.F.). From Figure 17 and Eq. 2.1, the fill factor is the ratio between Area1 (the maximum power produced by the cell) to Area2 (the product of the short circuit current and open-circuit voltage). In other words, the fill factor measures the squareness of the solar cell's I-V curve.

$$F.F. = \frac{Area\ 1}{Area\ 2} = \frac{P_{MPP}}{I_{sc}\ V_{oc}} \tag{2.1}$$

$$P_{MPP} = I_{MPP}\ V_{MPP} \tag{2.2}$$

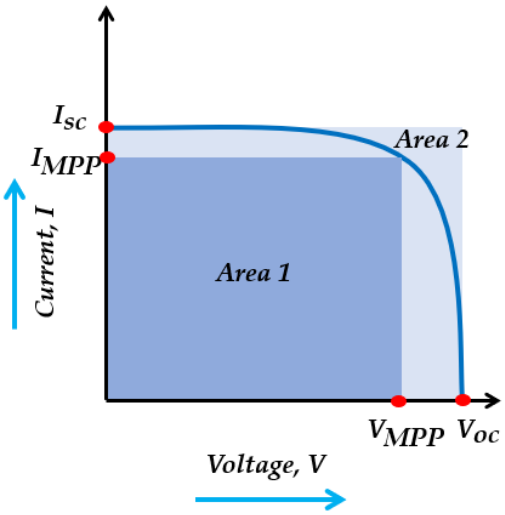

Figure 17 Solar cell fill factor.

2.2.2.4 Receiver assembly

The CPV receiver consists of one single solar cell or several solar cells that are arranged in columns and arrays (densely packed cell) that receive the focused sunlight passed through the optics as defined by IEEE [33]. Figure 18 differentiates between single and densely packed solar cells. Alternatively, IEC 62108 [34] defined the CPV receiver as a combination of the solar cell attached to a heat spreader, diode to reduce the electrical losses, and an optional secondary optical component that concentrates the incident solar radiation on the solar cell. The HCPVT system under investigation is a single point focus system that consists of a Fresnel lens and a CPV assembly as presented in Figure 19. The Fresnel lens is a cost-effective optic with high transmittance and can achieve high concentration ratios (more details will be presented in the next sections).

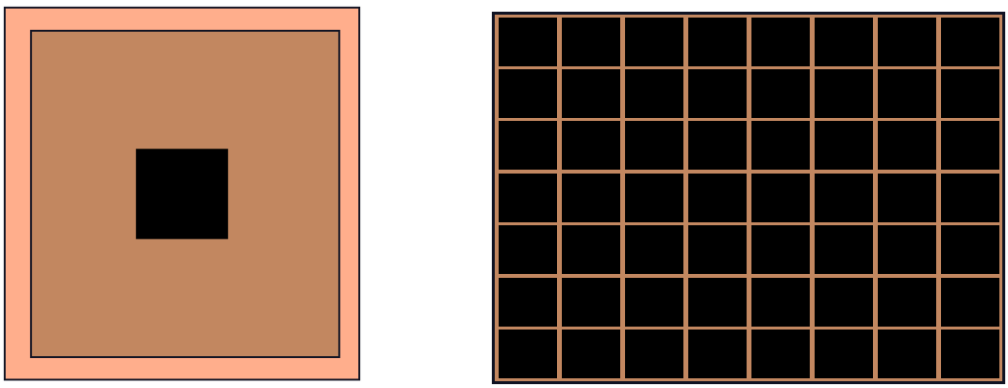

(a) **(b)**

Figure 18 (a) Single solar cell configuration and (b) Densely packed configuration.

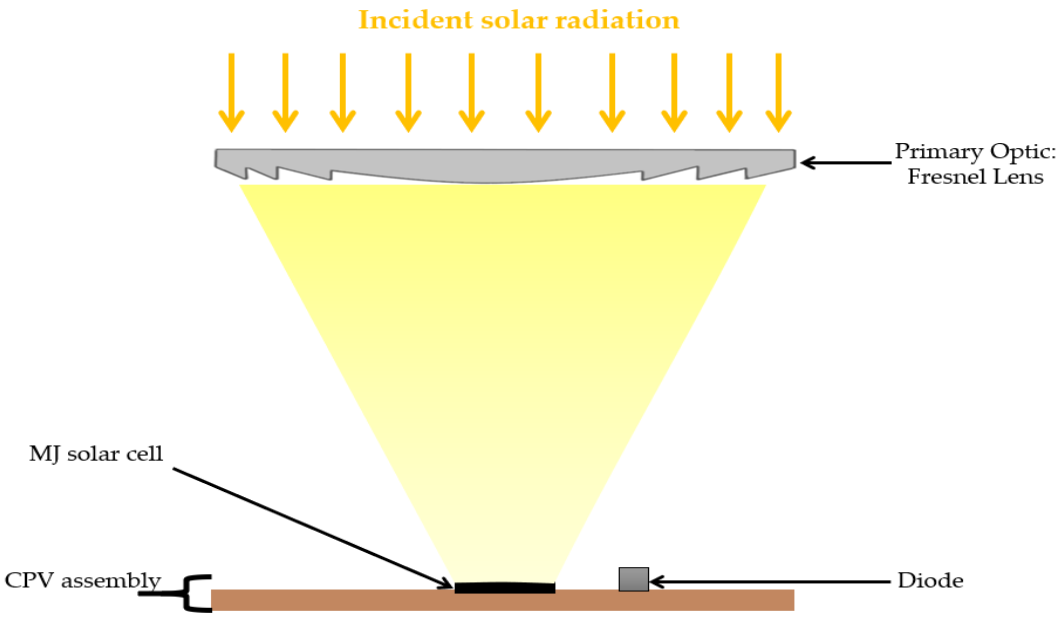

Figure 19 The HCPV system components.

2.2.2.5 CPV Optics

There are two ways to increase the electricity output from the system, either to increase the system size or by using concentrators to focus the sunlight on a small solar cell. The concentrator optics can be divided into two categories: imaging and non-imaging optics [35]. The first type projects a miniature image of the sun onto the solar cell as in, for instance, aspheric plano-convex lens (ex: Fresnel lens) or parabolic mirrors as presented in Figure 20 a and b, respectively. In the aspheric plano-convex lens, the incident sunlight is absorbed through it by refraction and concentrated in the focal point, while in the case of parabolic mirrors, the incoming rays are reflected and met in the focus [36]. Unlike imaging optics, the other kind does not produce an image of the light source, but it reflects the incident rays from the edges onto the edge of the solar cell and all the intervening rays can hit the target (known as the edge-ray principle) [37]. Therefore, this type focuses on maximizing the power transmission which in turn offers a high degree of freedom. A compound parabolic concentrator (CPC) or Kaleidoscope homogenizer can be considered an example of this kind of optics (Figure 20 c) [38].

I. Primary optical element (POE)

The primary optical elements used in the CPV systems can be categorized into two types: reflective and refractive optics.

- *Reflective POE*

High optical efficiencies can be obtained by using this type especially if it has high spectral reflectivity for a large number of wavelengths. In addition, they do not show chromatic aberration (the inability of a lens to concentrate all colours to the same point), unlike the refractive optics. Examples of this type are gold, silver, and aluminium coated mirrors. From Figure 21, one can see that the silver-coated shows the best reflectivity for a wide range of wavelength from 280 to 1800 nm [36]. The silver mirror is usually made by coating the glass, metal, or polymer with silver. After that, a layer of SiO_x is applied to protect the surface from humidity and corrosion. The optics used in Cassegrain, paraboloidal dishes/trough, flat reflector, and V-trough are reflective as introduced in Figure 22 [39–43].

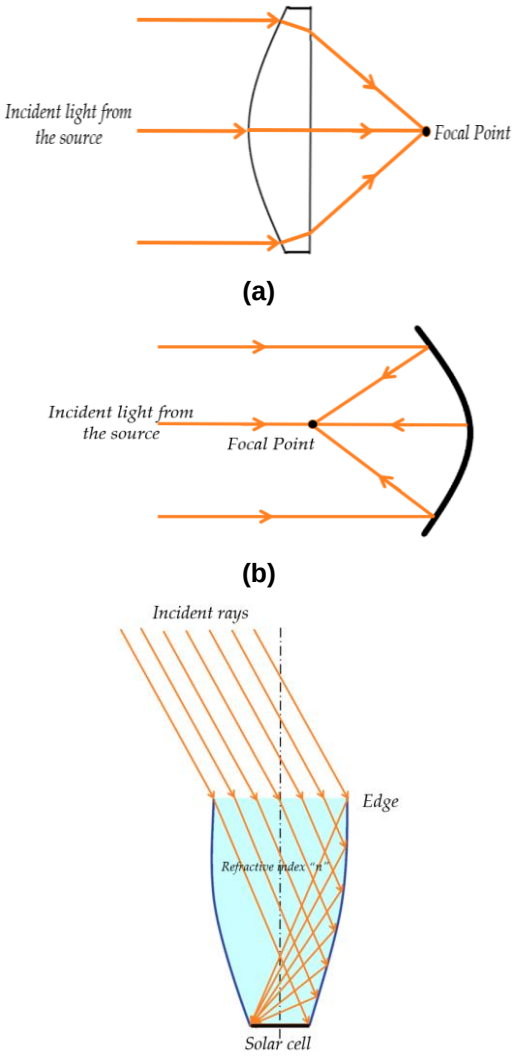

Figure 20 Imaging optics examples: (a) aspheric plano-convex lens and (b) paraboloidal mirrors, Non-imaging optics example: (c) compound parabolic concentrator.

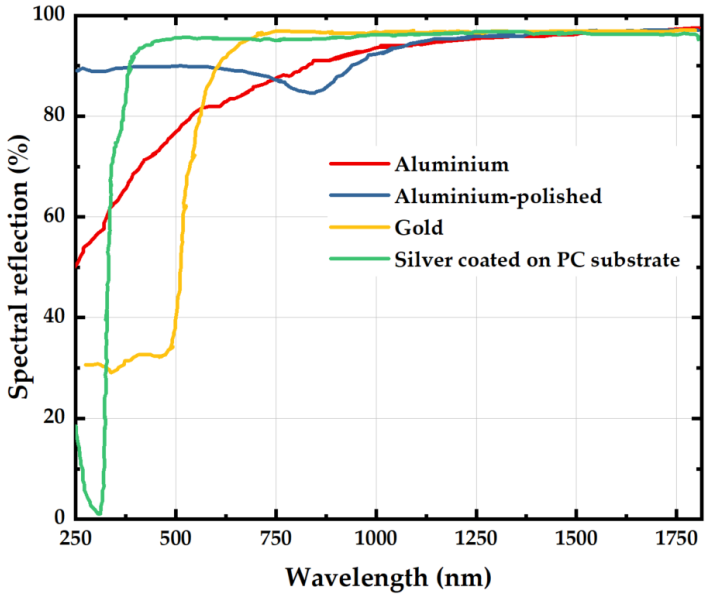

Figure 21 Spectral reflections with wavelength for the most common coated mirrors (aluminium, aluminium-polished, gold, silver coated on PC substrate).

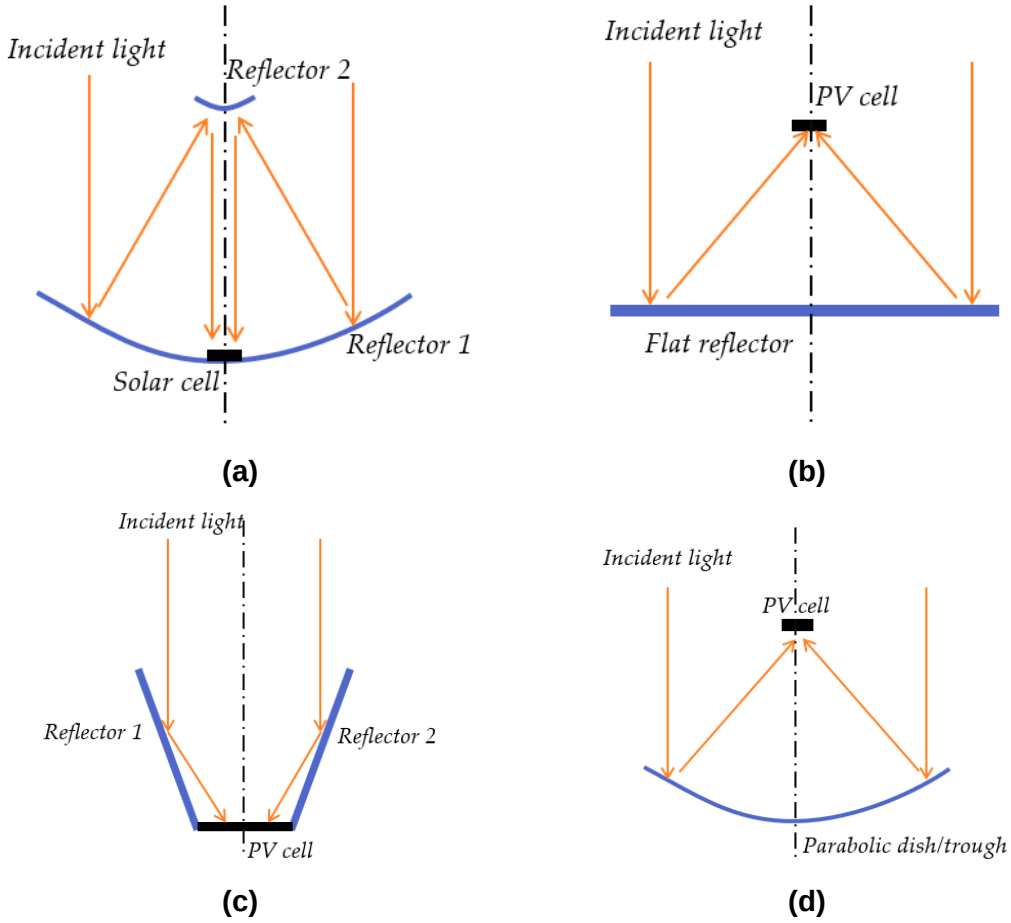

Figure 22 (a) Cassegrain configuration, (b) flat reflector, (c) V-trough, (d) parabolic dish/trough.

- *Refractive POE*

The area of the lenses arranged in arrays in one CPV single unit usually varies from 4 to 1000 cm^2 [38]. The full glass lenses are mechanically stable and have high transparency but at a high cost. Therefore, the Fresnel lenses that have been made from silicon on glass (SoG) and polymethyl methacrylate (PMMA) are introduced. Still, the losses due to the manufacturing and molding process need to be minimized to obtain higher optical efficiencies. From Figure 23, it can be seen that the transmission of the PMMA lens is much lower than the SoG at a certain wavelength (for example at 1125 nm, 1375 nm, and 1680 nm). This can lead to reduced power production from the solar cells due to the decrease in the transmitted solar radiation at these points. For example, for the four-junction solar cell where the bottom junction absorbs energy above 1120 nm, using a PMMA lens leads to a 12% reduction in the generated power as reported by Riesen et al. [44]. A slight reduction is observed in the higher wavelengths' regions in comparison with the previous type. Also, the glass substrate has mechanical stability and resistance to UV radiation in comparison to the PMMA lens. Besides, as mentioned above due to the possibility of chromatic aberration of the FR lens, the concentration ratio of a system may be limited to 1000 suns.

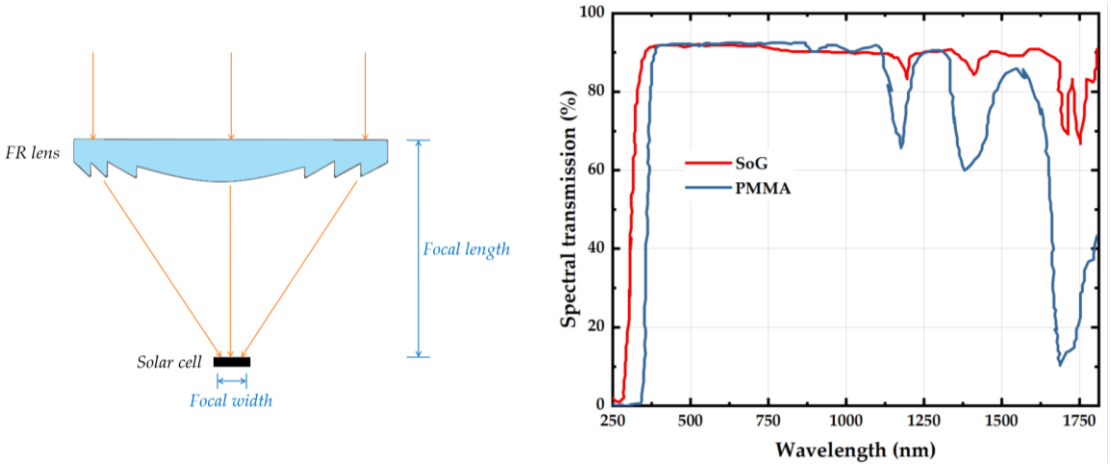

(a) **(b)**

Figure 23 (a) Schematic diagram of the FR lens showing the focal width and length, (b) Spectral transmission for lenses made from SoG and PMMA.

With respect to the SoG lens, the thermal expansion of silicon and glass is different which makes it essential to observe the effect of the lens's temperature on the optical efficiency. Also, the temperature affects the refractive index of the lens due to the possible shape deformation under higher concentration ratios [45].

Therefore, in a bid to maintain stable performance and high optical efficiency, Hornung et al. [46] developed an improved SoG Fresnel lens that is able to withstand high temperatures taking into account the expected deformation that can occur to the lens.

The improved lens offered an observed stable performance with an average improvement of 3% as presented in Figure 24 [46]. An achromatic doublet on glass (ADG) Fresnel lens has been developed by Languy et al. [47,48] aiming to overcome the losses from the ordinary Fresnel lens. This type incorporates the benefit of mirrors of being achromatic and plastic lenses that have a high tolerance of fabrication errors [49]. Also, the effect of temperature and lens shape due to deformation at high concentration ratios on the refractive index has been overcome [50]. This increases the maximum theoretical concentration ratio up to 5000 suns instead of 1000 suns using the single lens [47].

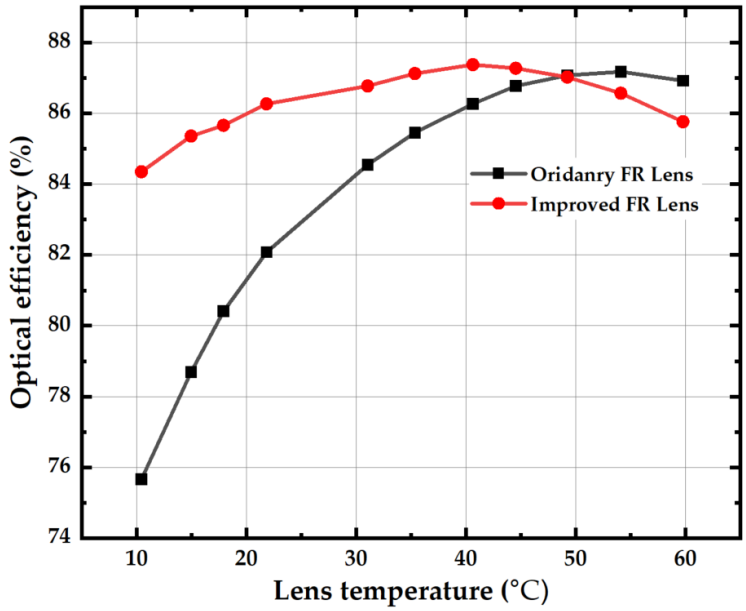

Figure 24 Change in the optical efficiency with lens temperature.

II. Secondary optical element (SOE)

The purpose of the SOE is to increase the concentration ratio, acceptance angle, and producing a homogenized radiation distribution on the surface of the solar cell [51]. Therefore, the solar cell fill factor can be enhanced, and electrical losses can be reduced [52]. In the case of SOE failure, the module is not destroyed but the optical efficiency and thus the power output will be decreased [53]. Usually, at the exit from the SOE, the effective concentration may vary between 300 to

1100 suns or higher than this [34]. The SOE can be classified into reflective and refractive SOEs.

- *Reflective SOE*

This type is made by bending the metal sheets such as aluminium with an addition of a silver layer to increase the reflectivity. Figure 25 shows a conical reflector surrounding the refractive optical component to increase the optical efficiency. Jaus et al. [54] investigated the performance of concentrator photovoltaic using two kinds of secondary optics which were reflective and refractive. A 40 mm × 40 mm Fresnel lens was used as a primary optical component to concentrate the incoming solar irradiance on a triple-junction solar cell. The authors concluded that the acceptance angle increased up to ±0.9°. Also, for a module consisting of 48 cells, an efficiency of 28.5% was achieved using reflective secondary optics.

(a) **(b)**

Figure 25 (a) Conical secondary reflective optic [54]*, (b) reflective secondary optic with legs mounted* [34]*.*

- *Refractive SOE*

These secondary optics are manufactured from materials that are fully translucent and UV-stable, usually made from silicon cones, moulded glass, or sintered in a Sol-gel process. The SOE is then glued to the solar cell using silicon glue-like polymethyl siloxane (PDMS) as it did not show degradation as reported by Victoria et al. [55] as in the other type of Polyphenyl-methylsiloxane (PPMS). Different designs of the concentrators are found in the literature such as revolved, crossed [56], compound [57], crossed V-trough [43], lens walled [58,59], polygon [60], square elliptical hyperboloid [61] (Figure 26). The most common type studied in the literature is the compound parabolic concentrator (CPC) as in Figure 27

[52]. Due to the high aspect ratio of the CPC, the concentration ratio is limited to 40 suns although it can reach as high as 42,000 suns theoretically for pure reflective optic [48].

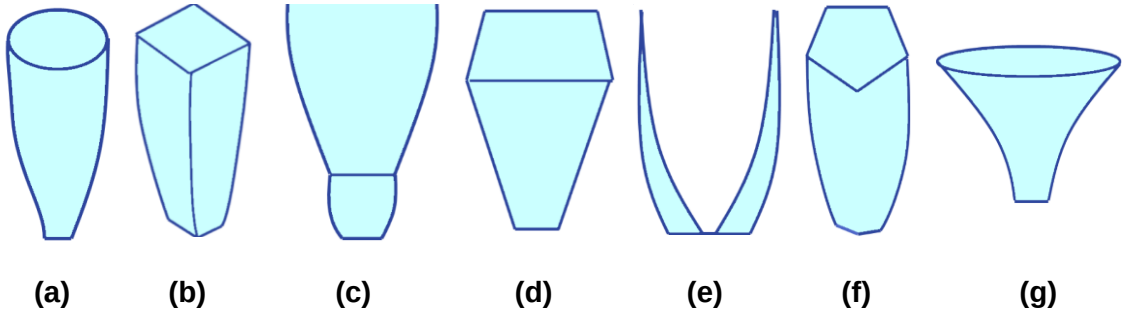

Figure 26 Different configurations of compound parabolic concentrator (a) revolved, (b) compound, (c) crossed, (d) crossed V-trough, (e) lens-Walled, (f) polygon, (g) square elliptical hyperboloid.

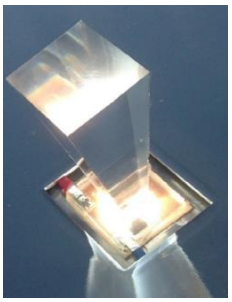

Figure 27 Refractive compound concentrator [52].

2.2.2.6 CPV thermal management systems

As previously mentioned, part of the incident solar radiation is converted into electricity, while the other part is converted into heat which increases the solar cell temperature. Up to 80% of the incident solar radiation on the solar cell may be lost as heat [62,63]. The rapid increase in the solar cell temperature has a negative impact on solar cell efficiency and its durability. Araki et al. [6] highlighted in their research that the temperature can reach 1400 °C for a CPV system with 500 suns if the system is kept insulated. Therefore, designing an adequate cooling system to extract the excess heat from the CPV is mandatory. To avoid the long-term degradation problems and the risk of melting the connections, the typical maximum working temperature limit for some solar cell types is set to 110 °C [7]. By integrating a heat dissipating system with the CPV, the overall efficiency (summation of the thermal and electrical efficiency) of the system can be raised. Figure 28 presents the energy balance system through the

CPVT module. The incident solar radiation is concentrated using the POE. Part of the total incident energy on the solar cell is lost as optical losses, while the remaining is converted into two forms. The first portion is transformed into electrical power, and the rest is converted into waste heat as this heat is removed by the heat sink [64].

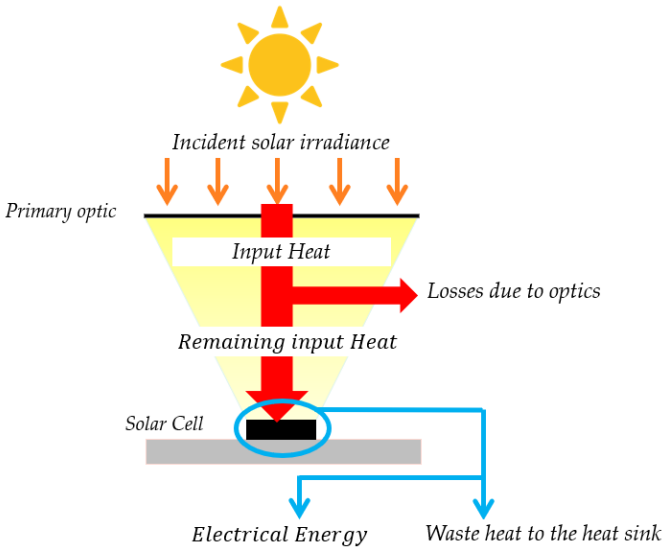

Figure 28 Energy balance diagram for the CPVT system.

Several cooling methods have been introduced in the literature to thermally manage the single solar cell and densely packed configurations. Royne et al. [65] discussed different cooling methods in their study. Generally, the heat extraction mechanisms can be classified into active, passive cooling systems, and by using optical filters [66–72]. Classification of the most common thermal management configurations are presented in Figure 29. The working idea of active cooling is based on using a pump to force the coolant to flow inside the pipe or a heat exchanger, while in the case of passive cooling the heat can be disposed to the ambient air by natural convection and radiation. Sometimes introducing passive cooling in a system can be not sufficient especially if the surface is exposed to high heat flux. On the other hand, using optical filters may offer a good option as they depend mainly on the working wavelength to be attenuated or transmitted. More information on the use of optical filters in solar systems is provided in section (c).

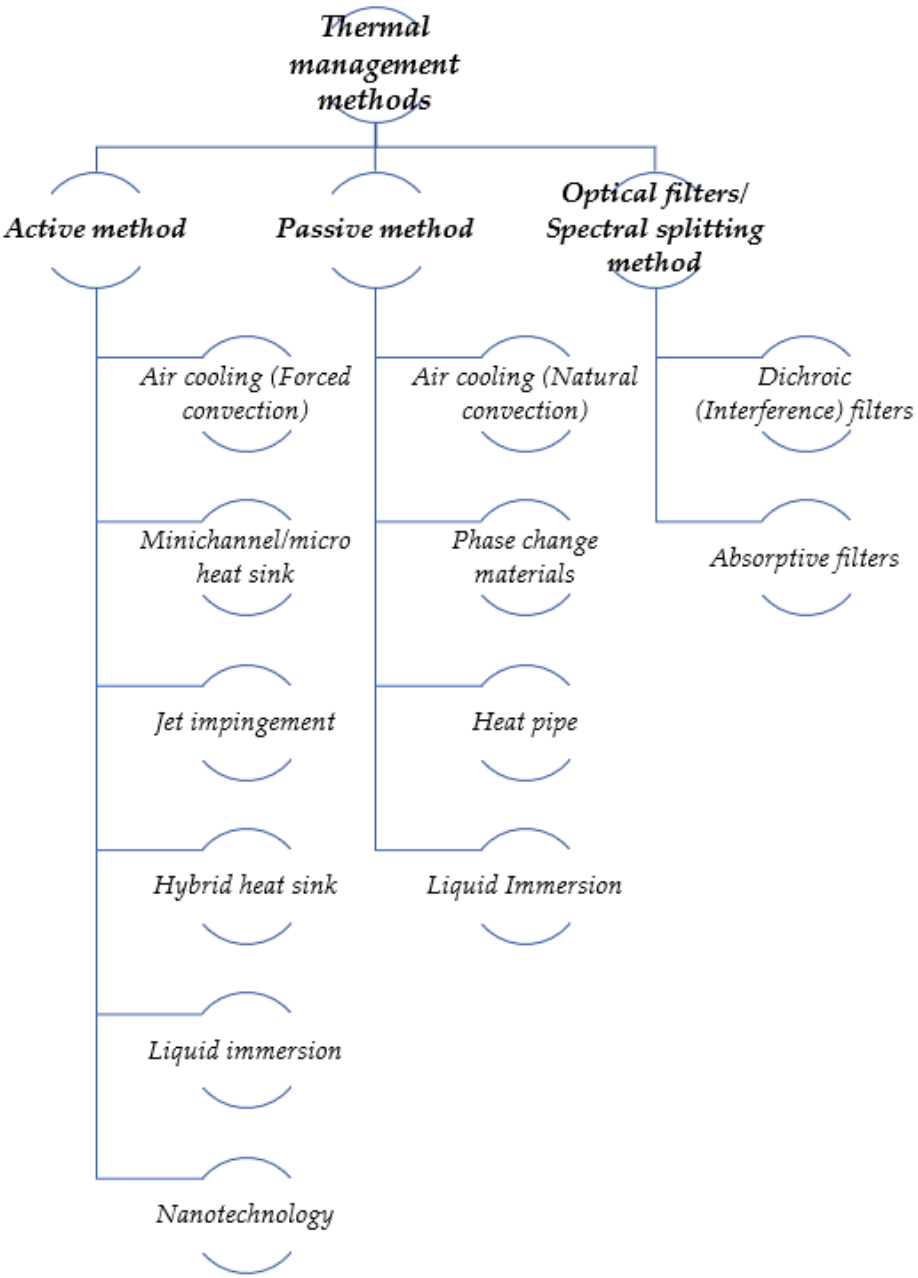

Figure 29 Thermal management methods classification.

I. Passive cooling methods

The passive cooling technique relies on extracting the heat from the heat source (solar cell) employing a heat spreader that is rejecting the heat to the environment (in the case of using air, Figure 30a and b) or to the phase change material or by submerging the cell in a dielectric liquid. Also, introducing a heat pipe is considered a passive method as it depends mainly on the natural convection process. The heat spreader is usually manufactured from either aluminium, copper, or silicon. The major benefit of passive cooling is that there is no pumping power required to remove the disposed heat. On the other hand, the constraints

of this method rely on the surrounding ambient temperature, wind velocity and direction, the design of the heat sink, and the incident solar irradiance.

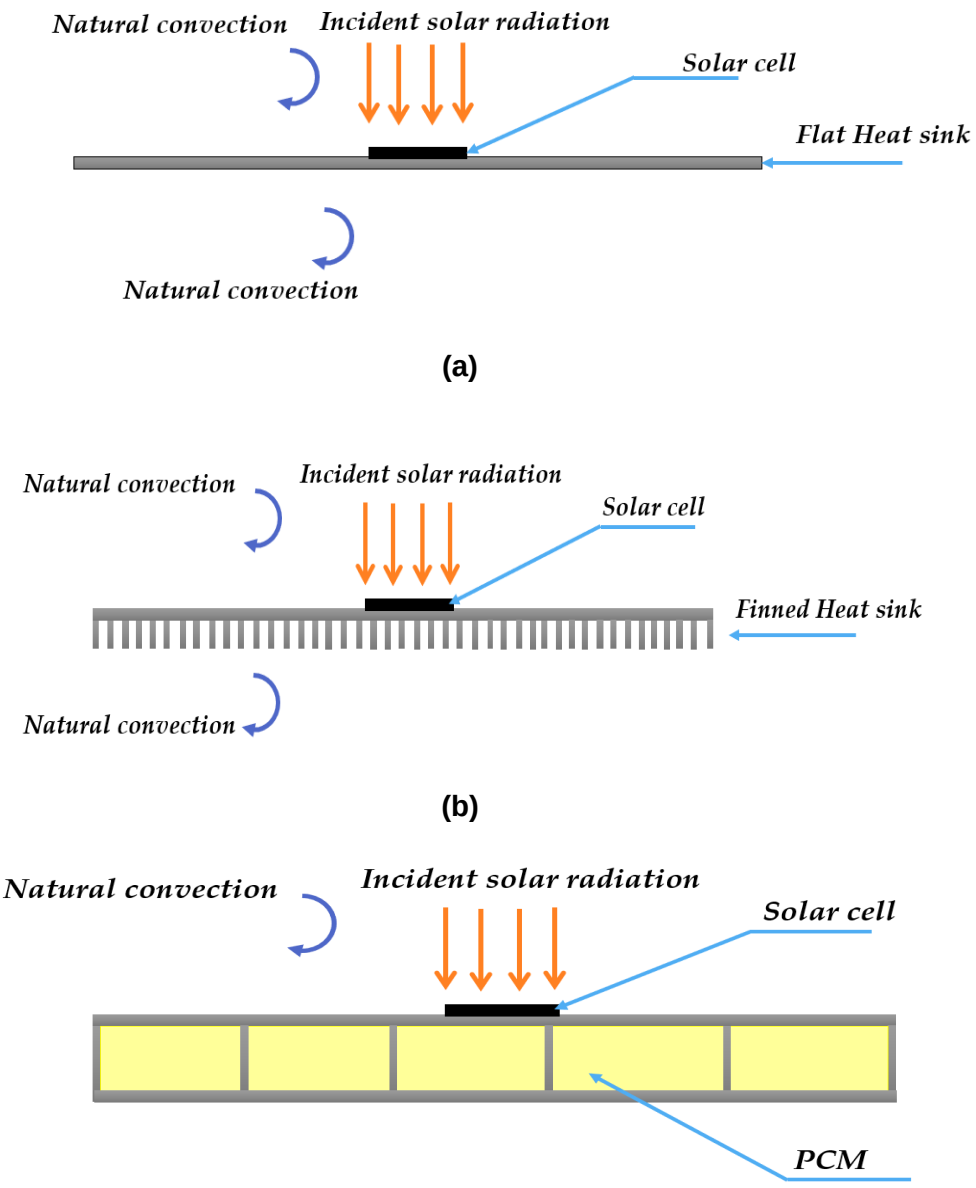

Figure 30 The most common passive cooling configurations in the literature (a) flat heat sink, (b) finned heat sink, (b) finned heat sink filled with PCM.

The area of the heat sink is usually calculated according to the following famous formula [73]:

$$A_{h.s}=A_{lens}=A_{cell}\ CR \tag{2.3}$$

Where $A_{h.s}$, A_{lens}, and A_{cell} are the heat sink, lens, cell areas, respectively. Many researchers have utilized this method for managing the temperature of the solar

cell. Valera et al. [74] studied numerically the effectiveness of a flat-plate aluminium heat sink for cooling several MJ solar cell sizes (0.25 mm × 0.25 mm, 0.5 mm × 0.5 mm, 1 mm × 1 mm, 3 mm × 3 mm) that were subjected to high concentration ratios varied between 2000 suns and 10,000 suns. The authors concluded that the heat sink was able to maintain average solar cell temperatures of 45 °C for 0.25 mm × 0.25 mm solar cell and 110 °C for 3 mm × 3 mm solar cell at a cell efficiency of 40% and concentration ratio of 10,000 suns.

Theristis and O'Donovan [75] investigated theoretically a 10 mm × 10 mm MJ solar cell assembly at a concentration ratio of 500 suns. The authors subjected the copper layer to a heat transfer coefficient varied between 1200 $W/m^2.K$ to 1600 $W/m^2.K$ which is considered the highest allowable value for passive cooling conditions as defined by Mudawar et al. [76]. At a heat transfer coefficient of 1200 $W/m^2.K$ and an ambient temperature of 25 °C and 45 °C the solar cell temperature reached 72 °C and 92 °C, respectively. Therefore, the CPV assembly at a concentration ratio of 500 suns and passive conditions can be thermally managed according to the authors.

Micheli et al. [77] studied a triple-junction solar cell that is exposed to a high concentration ratio using the passive cooling technique. The flat-plate heat sinks used were made from copper and aluminium, while the cell sizes tested ranged from 10 mm to 0.25 mm. The main aim of the study was to show the applicability and simplicity of cooling miniature solar cells using only the flat-plate heat sink. The results revealed that the aluminium heat sink withstood high concentrations reached 1000 suns for the cell size of 10 mm × 10 mm and was preferable over the copper because of its lower density and cost.

Another study by the same researchers [78] investigated the effectiveness of a micro-fins heat sink in terms of fin effectiveness and mass-specific heat transfer coefficient under passive cooling conditions. The authors analysed the results in terms of mass-specific heat transfer, the micro-fins showed a change of 50% in mass-specific heat transfer. Micro plate-fins were investigated for a high concentrator photovoltaic system working with a 3 mm × 3 mm MJ solar cell which was subjected to 500 suns and passive cooling conditions. The heat sink performance was tested under standard and worst-case conditions where the solar cell temperature reached 73 °C and 103 °C respectively. The feasibility of using a silicon heat sink for the application of the passive cooling method for high

concentrator photovoltaic was inspected by the same group [79]. The MJ solar cell was exposed to a concentration ratio of 500 suns. Different substrate materials to be used as a finned heat sink were examined. The findings showed that using a silicon wafer heat sink offered minimised thermal stresses.

Aldossary et al. [80] studied theoretically the performance of the high concentrator photovoltaic system (500 suns) based on 10 mm × 10 mm with passive cooling technique. The studied heat sinks were round pin heat sink (RPHS) and straight fin heat sink (SFHS). The length and depth of the heat sink were 90 mm by 90 mm, while the length of the fins was 50 mm. The system was able to keep the solar cell temperature at 65 °C and 85 °C using the SFHS and RPHS at an ambient temperature of 25 °C. The authors concluded that this system is not suitable for harsh climatic conditions as the ambient temperature may increase to 50 °C which could affect the cell temperature and durability.

Yupeng et al. [81] investigated experimentally and numerically the behaviour of a solar cell under a concentration of 100 suns. The system used was point focus using a small solar cell. The cell was replaced by a thin electric resistance heater which had the same dimensions as the solar cell and power to simulate the irradiance incident on the surface of the cell. The study compared the behaviour of the system under natural and forced convection conditions for different ambient temperatures. The temperature difference between the cell and the base was recorded as 38 °C. Abo-Zahhad et al. [82] investigated the performance of a single solar cell under passive cooling conditions by varying the heat transfer coefficient at the back surface of the copper layer from up to 1600 $W/m^2.K$ at a concentration ratio of 1500 suns. The authors reported that there was a significant enhancement in the solar cell temperature with the increase of the back-heat transfer coefficient.

The application of phase change materials (PCM) has been examined by several researchers as a heat extraction coolant for low concentrated photovoltaic systems (LCPV) [83,84]. The working principle depends on simultaneous absorption, melting, and releasing of heat as the temperature increases or reduces as shown in Figure 31. There are mainly three types of PCMs which include organic, inorganic, and eutectic mixture. The heat sink underneath the solar cell is usually filled with a PCM as introduced in Figure 30 to extract the excess heat from the back of the cell.

Manikandan et al. [85] examined theoretically the performance of the MJ solar cell included in an LCPV system. The concentration ratio varied from 3 to 10 suns. The heat recovery system presented in this study consisted of a finned heat sink that was filled with PCM (OM-32). The authors concluded that the PCM proved a good alternative of extracting the heat from the solar cell for the tested range of solar irradiances. The efficiency of the system reached 22% and 27% at concentration ratios of 3 and 5 suns, respectively. Another study was introduced by Zarma et al. [86] in which they considered using nanoparticles with phase change material for controlling the temperature of LCPV with a concentration ratio of 20 suns on a surface of a silicon solar cell. Through their theoretical study, they compared the performance of adding aluminium oxide, copper oxide, silicon dioxide nanoparticles to calcium chloride hexahydrate PCM. The authors found that adding nanoparticles to the PCM enhances the temperature uniformity of the cell which improves the electrical efficiency of the system.

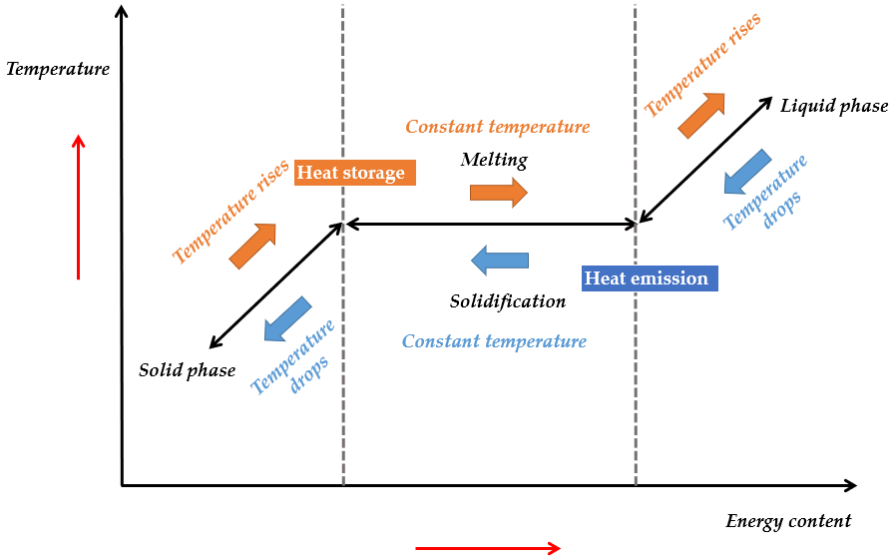

Figure 31 Working principle of phase change materials.

Emam et al. [87] evaluated a concentrator photovoltaic system performance using a PCM and water jacket. Different heat sink configurations were studied theoretically which included 2-D models for single, three, and five parallel cavities. The study showed that using the water jacket with the PCM enhanced the performance of the system in comparison with the system when using a PCM alone. At a concentration ratio of 20 suns, the silicon solar cell temperature reached 72 °C during the whole day and electrical efficiency of 17.7% was calculated during the daytime.

Another interesting technique is known as a heat pipe. Generally, the heat pipe consists of a working medium and wick structure as shown in Figure 32. Due to the heat gained through the evaporator section, the vaporized liquid is transferred to the condenser part to release its heat. This process is considered a natural convection process as the vapor moves naturally due to the density difference. Anderson et al. [88] conducted an experimental-theoretical study on integrating the heat pipe with the CPV system. The heat pipe was made from copper and its evaporator section was attached at the back of a single solar cell, while aluminium fins were attached to the condenser section as presented in Figure 32b for superior performance. The authors reported a temperature difference of 40 °C between the cell and ambient temperatures, while it reached 210 °C without a heat pipe at a concentration ratio of 400 suns.

Akbarzadeh and Wadowski [89] examined the impact of introducing a heat pipe into a CPV system with a designed concentration ratio of 20 suns. The authors reported that the solar cell temperature decreased to 46 °C which led to an increase in the electrical efficiency of 10%. Cheknane et al. [90] tested the performance of a heat pipe to reduce the temperature of a silicon solar cell for a concentrator photovoltaic at a concentration ratio of 500 suns. The heat pipe was made from copper and its performance was tested using two different working media: water and acetone. The results showed that the selection of the working medium depends mainly on the available temperature. However, the copper heat pipe maintained a reasonable temperature of the cell and enhanced its efficiency.

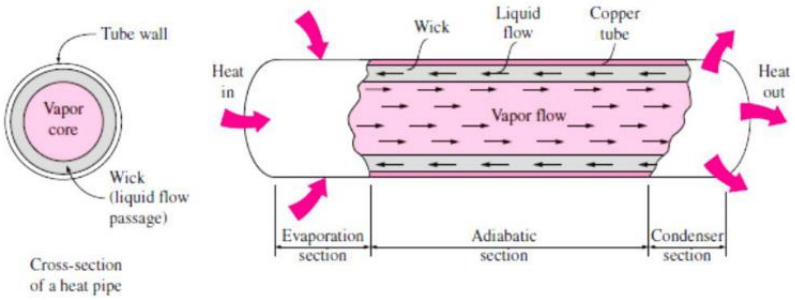

(a)

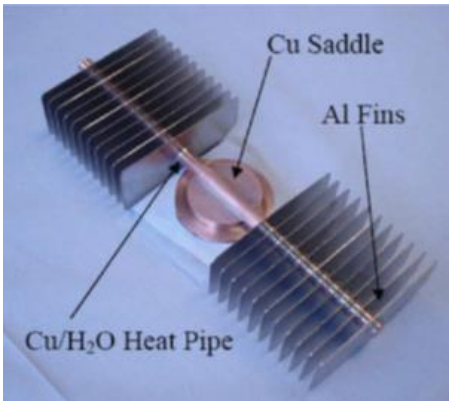

(b)

Figure 32 (a) Schematic representation of the heat pipe working principle [91]*, and (b) Copper heat pipe introduced by Anderson et al.* [88]*.*

Liquid immersion is another cooling method discussed in the literature. The method depends on immersing the solar cells in a circulating liquid which is usually dielectric to suppress the electric charges. As shown in Figure 33, the heat is transferred from both cell surfaces (the upper and bottom surfaces) in contrast to the conventional methods where the heat is only transferred from the back surface of the CPV. In another paper by Zhu et al. [92], it was reported that the silicon solar cell can reach as low as 45 °C and the heat transfer coefficient would be more than 3000 $W/m^2.K$. Therefore, higher cell efficiency was demonstrated using this technology.

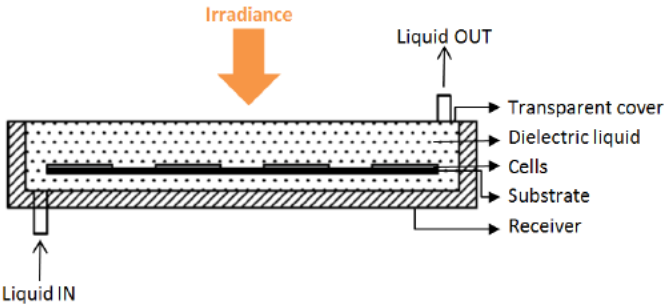

Figure 33 Schematic diagram of liquid immersion technology [93].

Xing et al. [94] suggested submerging a single MJ solar cell in dimethyl silicon oil with a thickness varying between 1 to 30 mm in an experimental study for a concentration ratio of 500 suns. The study revealed that the silicon oil increased the efficiency and power output from the cell from 19.556 W and 39.567% to 20.083 W and 40.572% at an oil thickness of 1 mm. Han et al. [95] compared the performance of different liquid media on the behaviour of a concentrator silicon solar cell. The compared media were deionized water, isopropyl alcohol, dimethyl silicon oil, and ethyl acetate. The performance of the solar cell was tested for concentration ratio varying from 10 to 30 suns. An increase in the electrical efficiency by 8.5% to 15.2% was observed when the layer thickness was 1.5mm. Increasing the thickness further to 9 mm led to a reverse impact on the electrical performance. A further investigation was carried out by Kang et al. [96] by submerging dense array MJ solar cells in a phase-change liquid (ethanol). The system was designed for concentration ratios between 219.8 and 398.4 suns. The experimental results showed that this method was able to keep the cell temperature in the range between 87.3 °C and 88.5 °C.

II. Active cooling methods

As mentioned earlier, the active cooling method depends on circulating the heat transfer medium through the system to guarantee a sufficient reduction in the system's temperature. This type provides efficient heat dissipation when the passive techniques are ineffective. There are several heat extraction mechanisms that can be categorized as an active cooling system such as using fans to blow the heat off the target surface which is a form of forced convection process. In addition, forcing the coolant to flow through the channels of the heat sink and sometimes liquid immersion process requires increasing the fluid

velocity to maintain a fixed temperature through the operation are other types of active method.

Al-Amri and Mallick [97] conducted a theoretical study to thermally analyse the performance of a triple-junction solar cell working under different concentration ratios varying from 100 to 200 suns. An aluminium plate was attached at the back surface of the cell with a thickness of 1.5 mm. Forced air cooling was examined to reduce the solar cell's temperature during the operation. The findings revealed that although the temperature reduced by 50%, the proposed thickness should be reduced to 0.5 mm for concentration ratios between 200 and 345 suns. Another study by the same researchers [98] introduced the effect of non-uniform illumination in the case of using triple junction for a concentration ratio of 100 suns.

The active cooling method using air was investigated for solar cell temperature mitigation. The results showed that although the solar cell temperature reduced by 20%, this technique is ineffective for higher concentration ratios under the tested circumstances. Sabry [99] conducted a theoretical study for a concentrator photovoltaic system with a multijunction solar cell. The concentration ratio varied from 100 suns to 500 suns. The solar cells were attached to the top of a copper tube with water flowing inside. The results showed that the cell temperature reached 370 K with an 8 mm copper tube and a concentration ratio of 500 suns. In addition, there was significant reduction of the solar cell temperature with the increase in the convection heat transfer coefficient.

Radwan et al. [100] conducted a 1-D theoretical study on the performance of LCPV based silicon solar cell to study the effect of a straight microchannel heat sink. At a concentration ratio of 40 suns and Reynolds number of 100, the maximum cell temperature reached 41 °C while the electrical efficiency of the silicon cell was 18.5%. Overall, the authors reported that there was a significant enhancement in the system performance with an increase in the Reynolds number.

Aldossary et al. [80] investigated theoretically an active cooling system that consists of a straight channel heat sink with a 10 mm × 10 mm MJ solar cell. The fluid used in modelling was water and a high concentration ratio of 500 suns was assumed in the calculations. The authors indicated that the system was able to

maintain the solar cell temperature at 60 °C with a slight increase in the ambient temperature in comparison with the case of using passive cooling technique. Reddy et al. [101] examined the performance of an HCPV system for a densely packed configuration solar cell. The area of the studied module was 120 mm × 120 mm. The results showed that only 0.2% of the produced power is used for pumping for an HCPV system with 1.5 kW.

Multilayer heat sinks have been discussed in the literature for the application in the CPV and electronic devices [102,103]. Yang and Zuo [104] investigated experimentally an LCPVT system with three silicon solar cells connected in series exposed to a concentration ratio of 28 suns. The authors examined a multi-layered manifold with a microchannel to maintain the cell temperature in the safe operating range. The cell temperature decreased from 44.1 °C to 20.4 °C by increasing the mass flow rate. The calculated heat transfer coefficient reached 8235.84 $W/m^2.K$, while the maximum observed pressure drop was 3 kPa.

Al Siyabi et al. [105] considered a 500 suns HCPVT system based on a multi-layered microchannel heat sink. They reported a solar cell temperature of 54 °C using four layers of the heat sink. Ali et al. [106] studied densely packed MJ solar cells that were subjected to a concentration ratio of 1000 suns. The authors investigated the effect of using a converged divergent heat sink on the system performance. The findings showed that the counter-current converged divergent heat sink was able to reduce the temperature non-uniformity by 17.7% compared with the current flow pattern.

Another study by the same researchers [107] discussed the performance of a four quadrants mini channel heat sink for densely packed configuration exposed to the concentration ratio of 1000 suns. The results showed that the average cell temperature achieved by the parallel cases was lower than that of the counter flow configurations. A further paper concerned with the performance of the densely packed solar cells was introduced by Tan et al. [108]. They theoretically studied the behaviour of 1800 suns HCPV. The average temperature of the CPV receiver varied from 91 °C to 104 °C which increased by decreasing the flow rate.

Awad et al. [109] investigated the use of an impingement jet to mitigate the temperature of a silicon solar cell in an LCPV system as the concentration ratio varied from 5 to 20 suns. The authors provided the system with a heat spreader

for additional enhancement and water was provided as a working medium in this research. A temperature of 87 °C was observed with an electrical efficiency of 14.3%. The authors reported that the heat spreader helped to reduce the temperature of the cell by about 4 °C. Barrau et al. [110,111] investigated the use of a jet impingement and microchannel for densely packed solar cells subjected to concentration ratios varying from 415 to 1905 suns. The proposed design was able to achieve a low thermal resistance of 2.18×10^{-5} K.m^2/W and provided a tolerable temperature distribution for the solar cells. Additionally, Abo-Zahhad et al. [112] discussed theoretically the performance of a single MJ cell at a concentration ratio of 1000 suns using a hybrid impingement jet and microchannel heat sink. The study revealed that the lowest achieved temperature of 55 °C and temperature nonuniformity of 5.8 °C occurred at a mass flow rate of 50 g/min.

Sun et al. [113] explored the CPV system behaviour by submerging the silicon solar cells in dimethyl silicon oil as a temperature management method. 9.1 suns were concentrated on mono-crystalline solar cells. The experimental results showed that this technique was able to maintain the temperature of the solar cell in the range between 20 °C and 31 °C at a solar intensity of 910 W/m^2, a liquid inlet temperature of 15 °C and a maximum Reynolds number of 13602. Also, Kang et al. [114] investigated the impact of this method on densely packed solar cells for a high concentrator photovoltaic. Two mounting structures of the cells were examined: with fins and without fins. The results showed that the silicon oil mitigated the solar cell temperature as the highest temperature recorded was 77 °C at a flow velocity of 0.5 m/s. Other studies related to the use of nanofluids will be introduced in section 2.3.

III. Optical filters/ Spectral beam splitting (SBS)

As discussed in the previous sections, there are many ways to dissipate the excess temperature of the solar cell whether it is multi-junction or silicon solar cells. One way is to use optical filters or spectral beam splitting filters (SBS) for the CPV system. This can allow the cell's temperature to be reduced significantly. The basic concepts of this technology and its applications in solar systems will be reviewed in the following sections.

The solar spectral irradiance wavelengths vary from 300 nm to 4000 nm as shown in Figure 34a which is partially transformed to electrical power when a solar cell is utilized. This is limited by the spectral response of the solar cell that is used in the solar module as discussed previously. For the single junction (silicon) solar cell, the spectral response ranges from about 300 nm to 1000 nm, while in the case of the multijunction solar cell the spectrum response extends to 1800 nm. These wavelengths fall in the range of the visible light and part of the infrared radiation as presented in Figure 34.

The main working idea of the optical filter is controlling the amount of the passing solar irradiance to prevent the solar cell overheating [115]. This can be achieved by transmitting the selected wavelengths through these devices which are located in the light path. The efficiency (transmittance) of the optical filters to transmit the desired wavelength is measured by the spectrophotometer. Another parameter that must be considered is called optical density (OD) which describes the amount of energy blocked by the filter. The following formula is used to calculate this factor:

$$\mathrm{OD} = -\log\left(\frac{T}{100\%}\right) \tag{2.4}$$

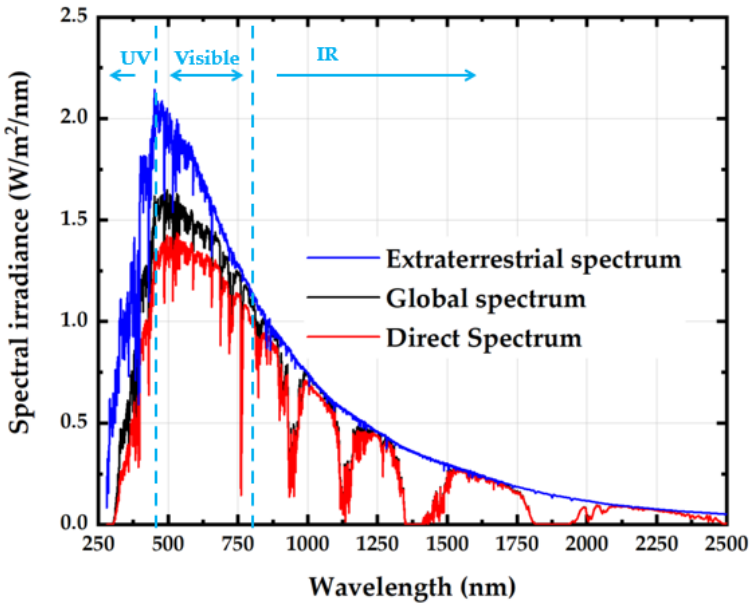

(a)

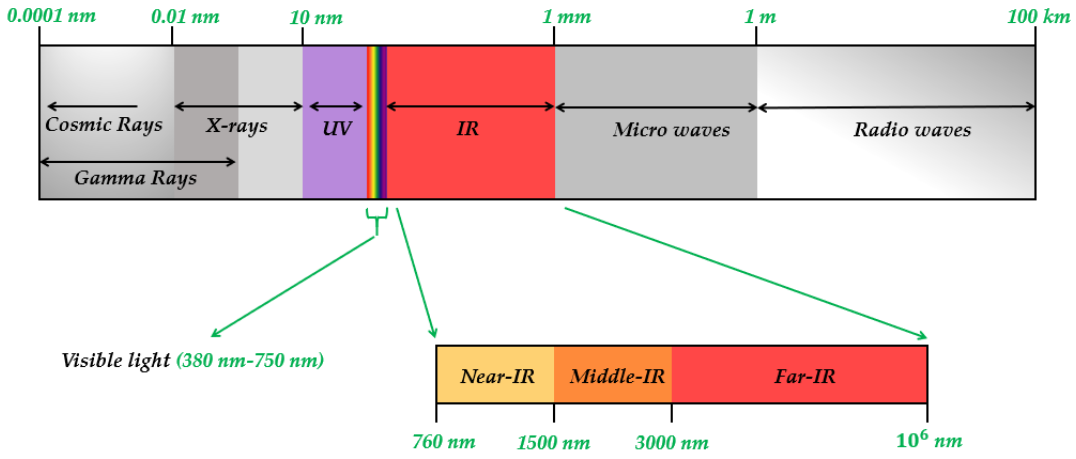

(b)

Figure 34 (a) Variation of the Extra-terrestrial (AM0), Global (AM1.5G), and Direct (AM1.5D) spectral irradiances with the wavelength, and (b) electromagnetic spectrum distribution.

The optical filters or the spectral splitting devices can be classified in many different ways. The majority of researchers agree that it can be classified into two main categories: absorptive and dichroic (interference) filters [116]. Figure 35 differentiates between the two types. Absorptive filters imply that a certain portion of wavelengths is absorbed, while the rest is transmitted into the solar cell. This type is usually made from dyed glass or pigmented gelatine which holds the previously mentioned properties. Also, it can be made from inorganic and organic

compounds. The durability and stability of this type make it more advantageous than the other types.

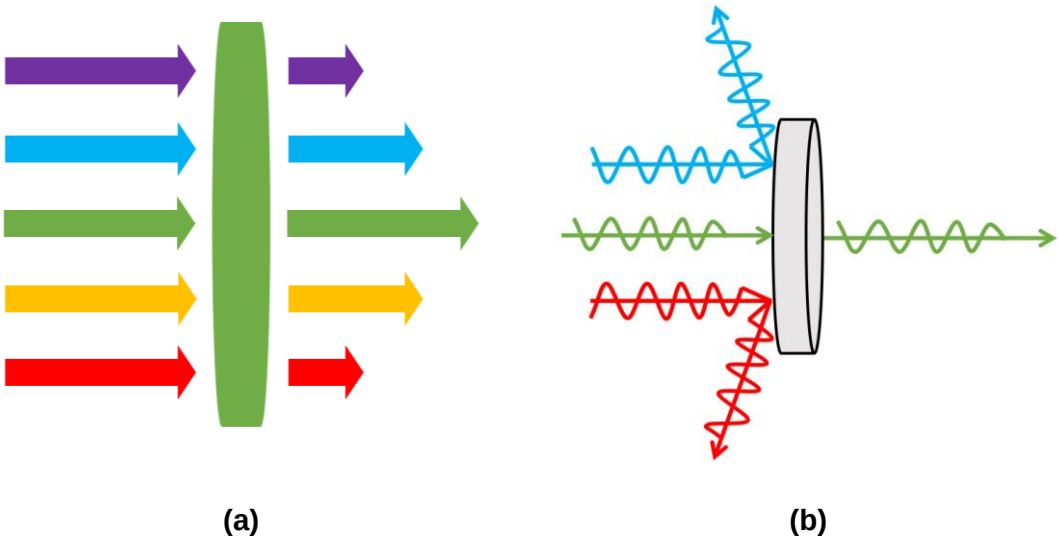

Figure 35 Working principle of the (a) Absorption and (b) Dichroic filters.

On the other hand, dichroic filters are based on the interference principle. This type can also be called a reflective or thin-film filter. They are usually made by coating a glass substrate using optical layers. The working idea of this type is when the incident light strikes the surface of the filter it is split into two beam components of different wavelengths. The desired light components will be transmitted to the solar cell, while the interfered component is reflected into the environment. There are mainly four kinds of dichroic filters: long-pass, band-pass, short-pass, and band-blocking filters as displayed in Figure 36. The long and short-pass filters can work as cold and hot mirrors respectively as they are able to transmit or attenuate the near-infrared and infrared radiation. A hot mirror is a filter that passes the visible and UV light, while attenuates the IR radiation. The cold mirror reflects the visible and UV radiation while permitting the IR wavelengths.

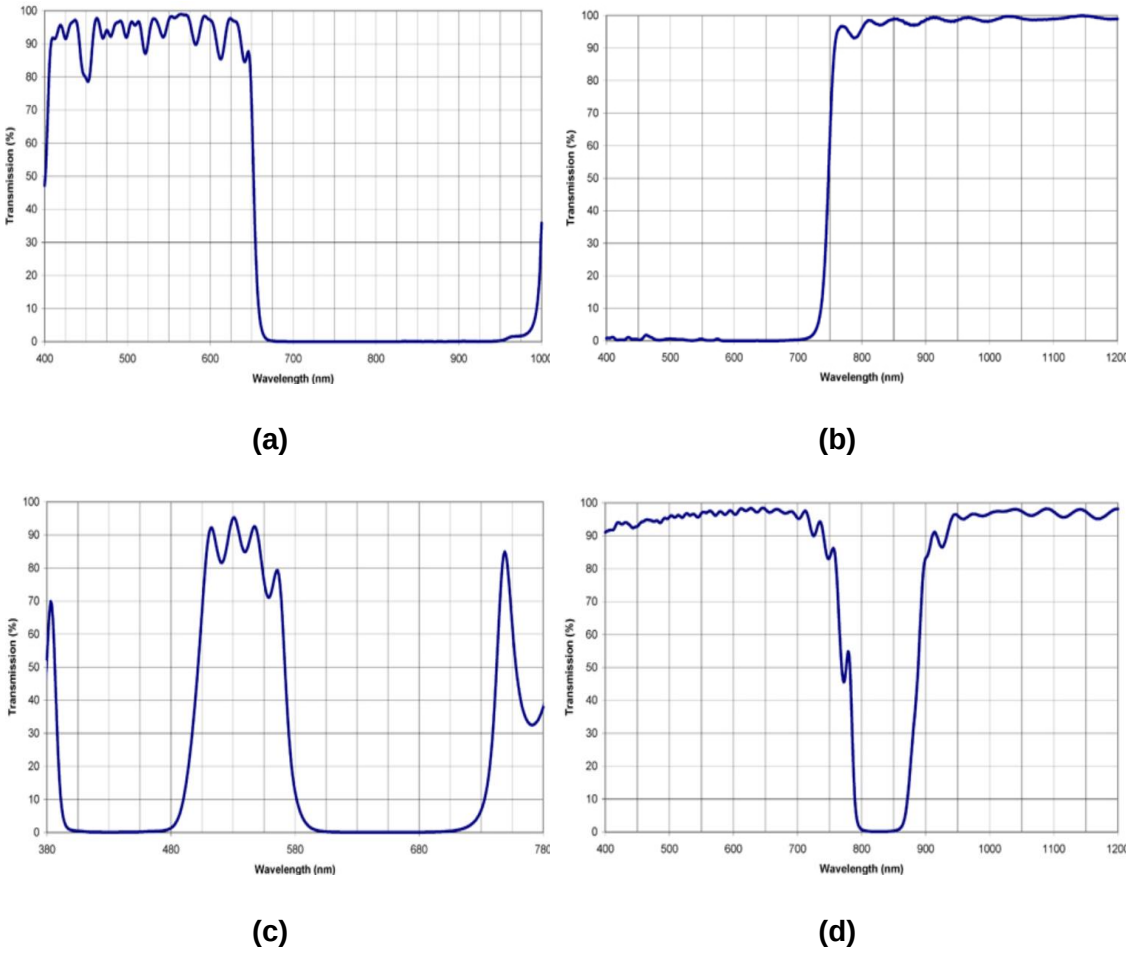

Figure 36 Difference between (a) short-pass, (b) long-pass, (c) band-pass, and (d) band-block filters, adapted from: [117].

Likewise, the band-pass and band-blocking filters have a certain working range of the wavelengths that can be transmitted or reflected by using the suitable filter. An example of the band-pass type is a monochromatic filter which only permits a narrow scale (a single colour) of the wavelengths [118]. Another example is the infrared filter which can be subcategorized into infrared-passing filters, infrared cut-off filters, and mid-infrared filters. Firstly, the infrared-passing filters allow the infrared wavelengths to pass whilst blocking the visible light range (ex. Infrared camera). Conversely, the infrared-cut off filters block/reflect the infrared wavelengths from passing into the targeted object but allow the visible light to pass. The mid-infrared filters block the unwanted portion of the infrared light that causes heating to the targeted object. There are also the ultraviolet filters that obstruct the ultraviolet radiation if it is a UV-blocking filter or allow the ultraviolet light to pass which is known as UV-passing filters.

A number of researchers have presented different studies related to the use of the interference filter with the concentrated solar energy technology to gain an enhancement in the total conversion efficiency. Jiang et al. [119] studied theoretically a two-stage parabolic trough concentrating photovoltaic system as presented in Figure 37 using ray-trace simulation. As shown in the graph, the reflected light by using the mirror is concentrated on the beam filter which is reflected again onto the cell with the heat sink underneath it. Therefore, the beam filter blocks the unwanted wavelength from passing through the solar cell and the remainder is used as a heat source for the fluid inside the receiver tube. They reported that by using the suggested system, the heat load on the surface of the solar cell can be reduced by 20.7%, while about 11% of the total incident can be recovered by the receiver.

Another theoretical study by Hu et al. [120] discussed the performance of the linear Fresnel reflector using a filter that is coated with a thin layer of Nb_2O_3/SiO_2. The incident light on the linear concentrator is concentrated on the surface of the filter. Part of this light passes through the filter to the solar cell while the other is reflected into a thermal receiver which contains the heat transfer fluid. The theoretical modelling showed that the electrical efficiency of the system reached 12% and about 30% of the incident light can be converted into useful thermal energy. Another study was presented by the same researchers [121] incorporating a dual-axis tracking system which enhances the system design as the total efficiency of the system reached 36.3%, while the total exergetic efficiency reached 26.5% and 25.6% at a temperature of 25 °C and 50 °C respectively which was higher in comparison with standalone CPV system.

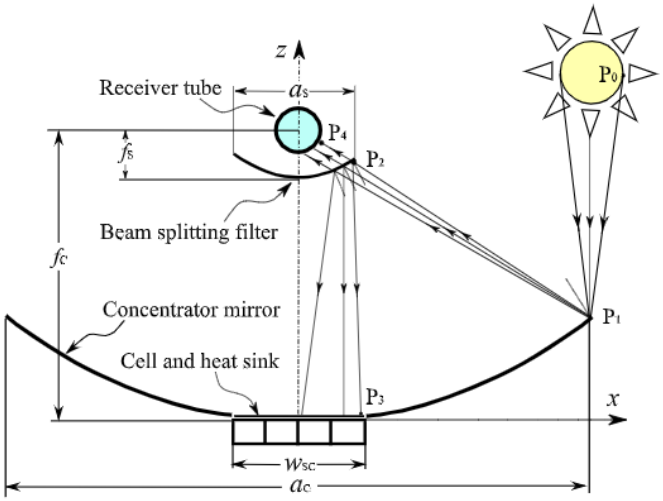

Figure 37 Two stage parabolic trough concentrating photovoltaic system using a beam splitter filter [119].

Lasich et al. [122] considered a system that consisted of a 1.5 m parabolic dish and flux modifier which has the ability to block the unwanted IR wavelengths and deliver only the necessary solar flux to the solar cell as well as decreasing the tracking accuracy needed for the system. In addition to that, a heat sink was implemented into a system to achieve a temperature of 50 °C for a GaAs solar cell, a light guid, and a Gregorian/Cassegrainian lens as a secondary concentrator as shown in Figure 38. The working principle of the system is when the incident light is concentrated by the dish concentrator, it is reflected again into the concentrator lens and by using the flux modifier the concentrated rays can find their path through the light guide to the receiver. This heat is to be used as thermal energy for heating purposes. The experimental results showed that the total cogeneration efficiency of the system reached 31.8% and thermal efficiency of 13.4% at a temperature of 1100 °C which can be used to produce super-heated steam. Kandilli and Kulahli [122] studied a theoretical system composed of dish concentrators and a thermal receiver by introducing two filters of cold and hot mirrors. The obtained energy and exergy efficiencies were 7.3% and 1.16% respectively due to the calculated optical losses.

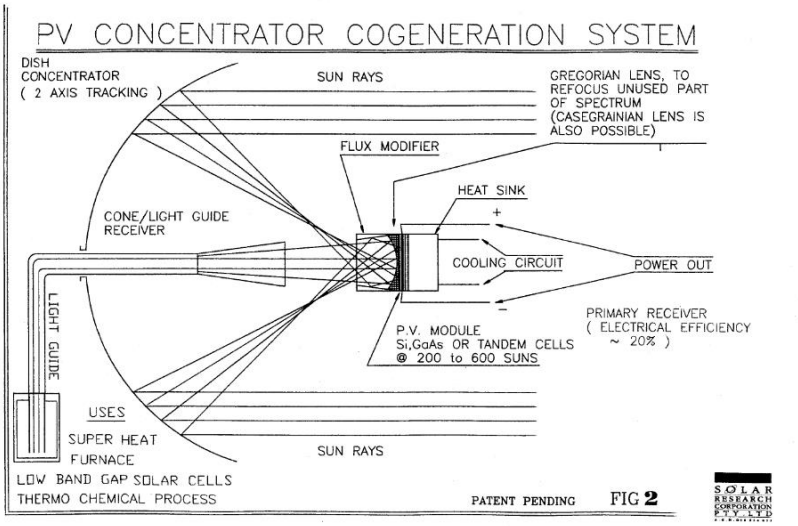

Figure 38 Parabolic dish concentrator with IR filter for both electricity production and heating purposes [122].

All the discussed works above have a similar working idea which depends on filtering/splitting the concentrated light that is reflected from the concentrators before reaching the solar cell. This process is known as a pre-concentrated method. However, to date few studies have been introduced in the literature about the effectiveness of these filters experimentally. Another approach has been analysed by a few researchers that is termed a “pre-split method”. In this concept, the filter is attached to the mirrors/concentrators or in the front of the glass which is simpler than the other methods. Ulavi et al. [123] proposed a theoretical study for the pre-split technique to be used in a CPC system. As described in Figure 39, the interference IR filter is made from cadmium telluride and is attached at the back of the CPC concentrators. In this way, the incident light can be split into two beam components. The IR component is concentrated into the thermal receiver, while the visible light fraction is absorbed by the filter. The results showed that an increase in the produced energy reached 20% , while the thermal efficiency was 31%.

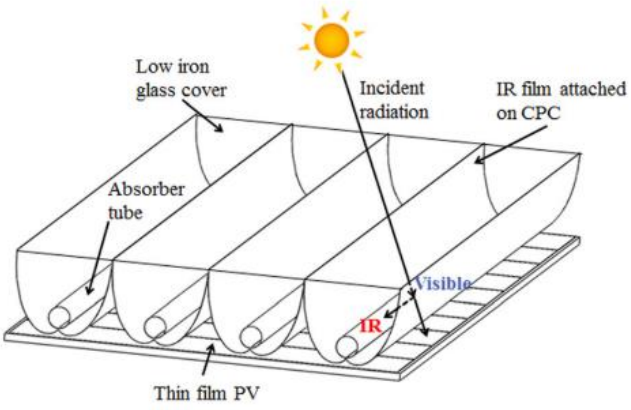

Figure 39 Pre-split CPV system designed by Ulavi et al. [123].

Khoshdel et al. [124] investigated the impact of plasmonic cross-shaped nano-antennas as a band-block filter by introducing metallic nanoparticles to protect the cell from the ultraviolet (UV) and infrared (IR) radiations. They reported that this type obstructed 79.6% and 65.2% of the incident UV and IR radiations for a wavelength from 300 to 400 nm and 1100 to 1800 nm. Sudhakar et al. [125] studied the impact of using different filter colors on the performance of solar panels in terms of current, power, and efficiency. Although all the tested filters reduced the efficiency of the solar panel, the red filter showed the highest performance of the tested colors.

One of the major defects of applying an absorptive liquid filter to be used in the CPVT systems is the absence of indecomposable liquids with suitable absorption solar spectra [126]. Therefore, in their survey, Looser et al. [123] introduced possible undecomposable heat transfer fluids and nanoparticles to be used as an absorptive filter. Despite a few studies having covered the use of this kind of filter in CPVT applications, they concentrated mainly on theoretical investigation and optical measurements of the liquid filter. Taylor et al. [127,128] conducted a theoretical study on using metallic-shell/dielectric-core (silica) particle nanofluids. These nanoparticles are Au/SiO_2, Ag/SiO_2, and Al/SiO_2 as well as the Ag nanoparticles. The performance of the system was enhanced after using this nanofluid-based optical filter in comparison with a conventional fluid optical filter (thermal oil or water).

Jing et al. [129] conducted an experimental-theoretical study to analyse the use of the SiO_2/water nanofluids with particle size varying from 5 nm to 50 nm to be used as an optical filter. The theoretical study of the system showed that the

exergetic efficiency was enhanced by 7% at a concentration ratio of 40 suns. The combined interference and absorptive liquid filters were considered by Mojiri et al. [130,131]. The concentrated light passed firstly to the thermal receiver which contained the absorptive fluid. The fluid worked as a short pass filter with a cut-off wavelength of 1200 nm. After that, the transmitted light portion passed to the interference filter before focusing on the silicon solar cell. The coated interference filter is a long pass filter that reflected all the wavelengths lower than 600 nm and permits the rest to pass.

2.2.2.7 Tracking systems

The CPV system can achieve an optimum performance if the system is held perpendicular to the solar radiation direction. Therefore, to reach the optimum concentration and electricity production, it is extremely important to achieve a precise position in relation to the sun [132]. This can be completed through a tracking system on which the CPV system is loaded. So, the CPV system can follow the sun's motion from East to West and its path from North to South. The tracking system offers an efficient solution to overcome the power losses according to Lambert's cosine law which states that the solar intensity is proportional to the cosine of the incident angle (Figure 40).

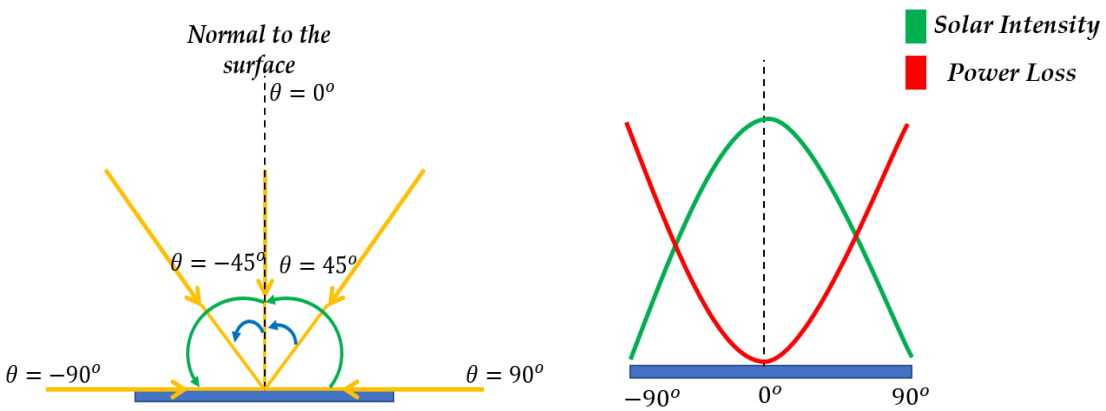

Figure 40 (a) Representation of the incident angle, and (b) Schematic diagram of the relation between the solar intensity, power loss, and incident angle according to Cosine's law.

The tracking is usually achieved through a mechanical motion. Tracking systems can be classified in many different ways [133]. The most common classification

is by the degree of freedom into single-axis and double-axis trackers. When the surface rotates around one axis, it is called a single-axis tracker and can be classified into four types as seen in Figure 41. Horizontal single-axis tracker (HSAT) and vertical single-axis tracker (VSAT) are tracking systems that use the East-West axis and North-south axis respectively to trace the sun's motion. On the other hand, the motion of the tilted single-axis tracker (TSAT) depends on setting the axis of rotation to be parallel to the earth's rotation axis. The polar-aligned single-axis tracker (PASAT) has a tilted axis of rotation aligned to the polar star. Dual-axis methodology is categorized into two types as introduced in Figure 42. The first type is called the tip-tilt dual-axis tracker (TTDAT) which could track two motions from East to the west (horizontal) and from north to south (Vertical). The other type is the azimuth-altitude dual-axis tracker (AADAT) which tracks the sun's path in four directions as it is mounted on a ring with rollers that are fixed to the ground.

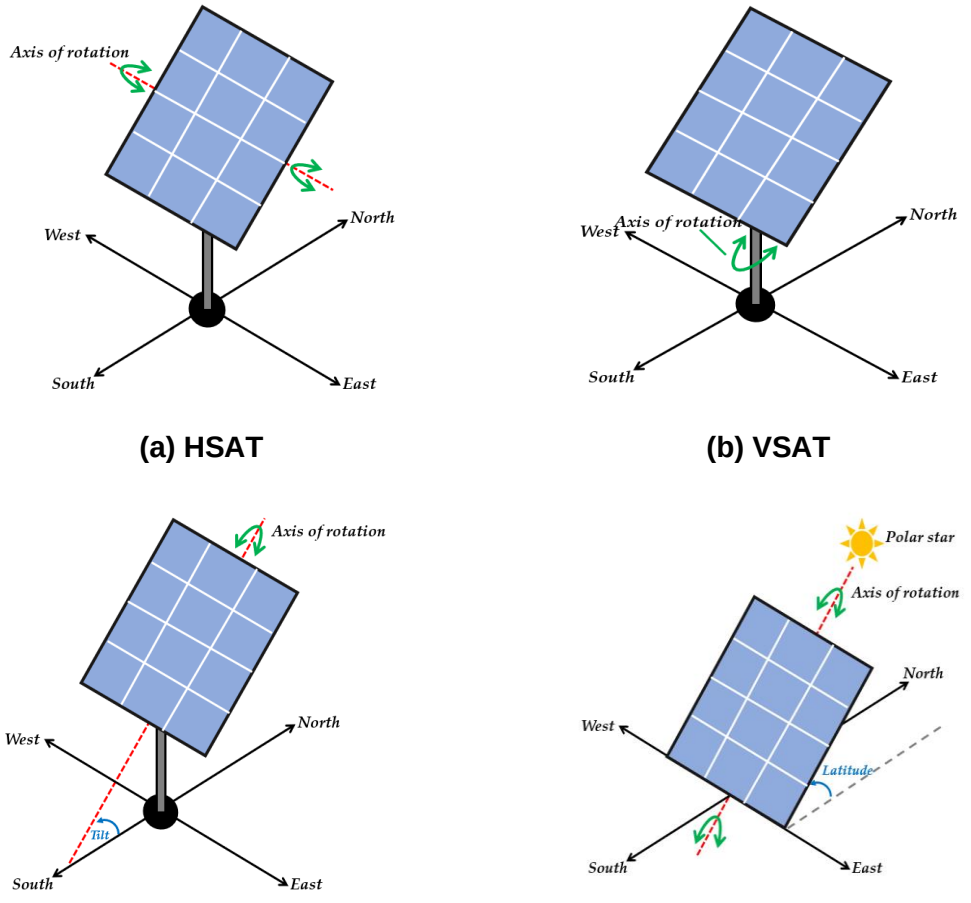

Figure 41 Single-axis trackers types.

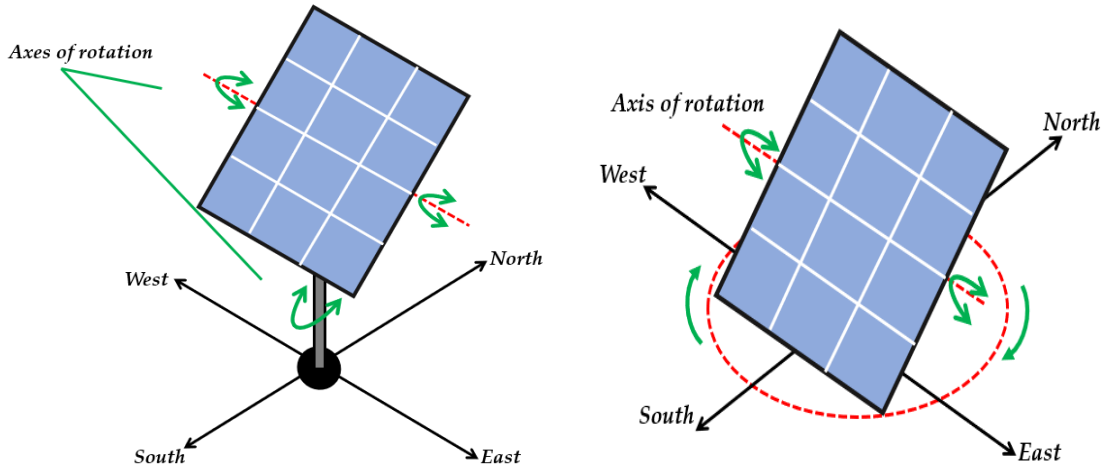

(a) TTDAT **(b) AADAT**

Figure 42 Dual-axis trackers types.

2.3 Nanotechnology

2.3.1 Introduction

Nanotechnology is a multidisciplinary field that combines science, engineering, and technology at a nanoscale [134]. There is a wide range of applications where nanotechnology can participate, for instance: material science, medicine and biology, and engineering (Figure 43). In the solar energy field, nanotechnology can positively participate by replacing the working medium with nanofluids or by using different kinds of nanoparticles for the manufacturing process of the solar cells. Nanofluid is a new type of heat transfer fluid that allows more heat to be removed from the solar system. Through the coming sections, different aspects and applications in solar systems will be covered and reviewed in detail.

2.3.2 Nanofluid definition

Nanofluid has been defined in different ways in the literature but many researchers agree that it is a mixture of nanoparticles, which have a diameter ranging from 1 to 100 nm, dispersed efficiently in a base fluid [135–140]. These base fluids can be water, refrigerants, glycols, or thermal oils [137,138,141]. By using nanofluid, the heat transfer through the fluid can be enhanced as well as the thermal performance of the whole system [142].

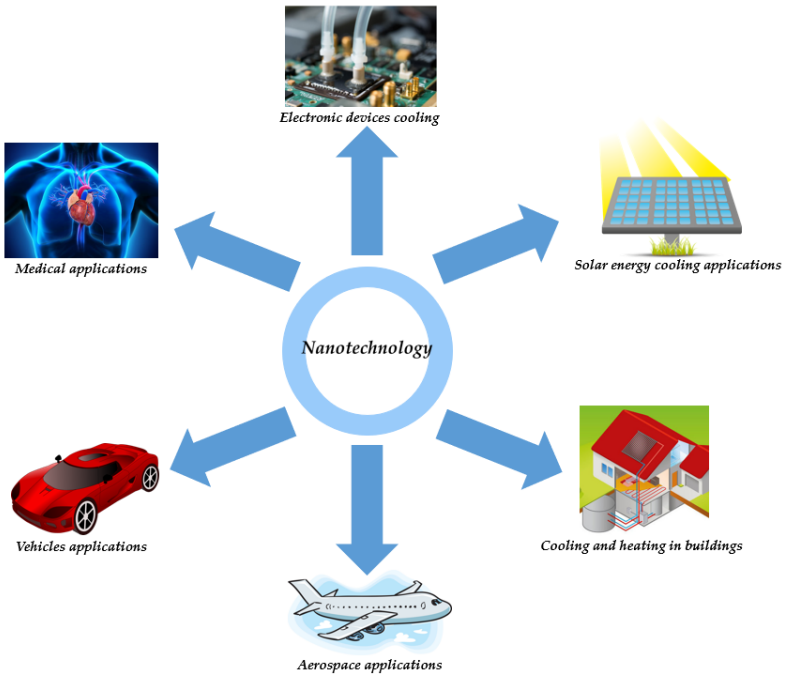

Figure 43 Applications of nanotechnology in different fields.

2.3.3 Nanoparticles classification

Nanoparticles can be classified as shown in Figure 44 [135,138,143] into metal-based, carbon-based, and nanocomposites. The metal-based nanoparticles can be further divided into two groups; metals (Al, Fe, Cu…etc) and metal oxides which are a chemical compound of metal and oxygen (TiO_2, Cu_2O, ZnO,…etc). The carbon-based nanoparticles can be categorized into three types; fullerenes (a molecular form of carbon C_n where n>20) [144], carbon nanotubes which are carbon allotropes with a cylindrical nanostructure, and graphene which is carbon with a two-dimensional allotropic form. The final group is nanocomposites, which are a particularly distinctive type of nanoparticles. This category consists of two dissimilar types of particles with diameters less than 100 nm [145]. These nanocomposites may be classified into a ceramic matrix, metal matrix, and polymer matrix.

These types of nanoparticles can boost the thermal properties of the base fluid as they have high thermal conductivity. This thermal conductivity can enhance the overall performance of the system which leads to a decrease in the operating cost [136,146–148]. Moreover, nanofluids can work as optical filters for the photovoltaic cells as they can catch all of the redundant solar energy that is not useful for PV working range as well as reducing the cells' temperature [136,149].

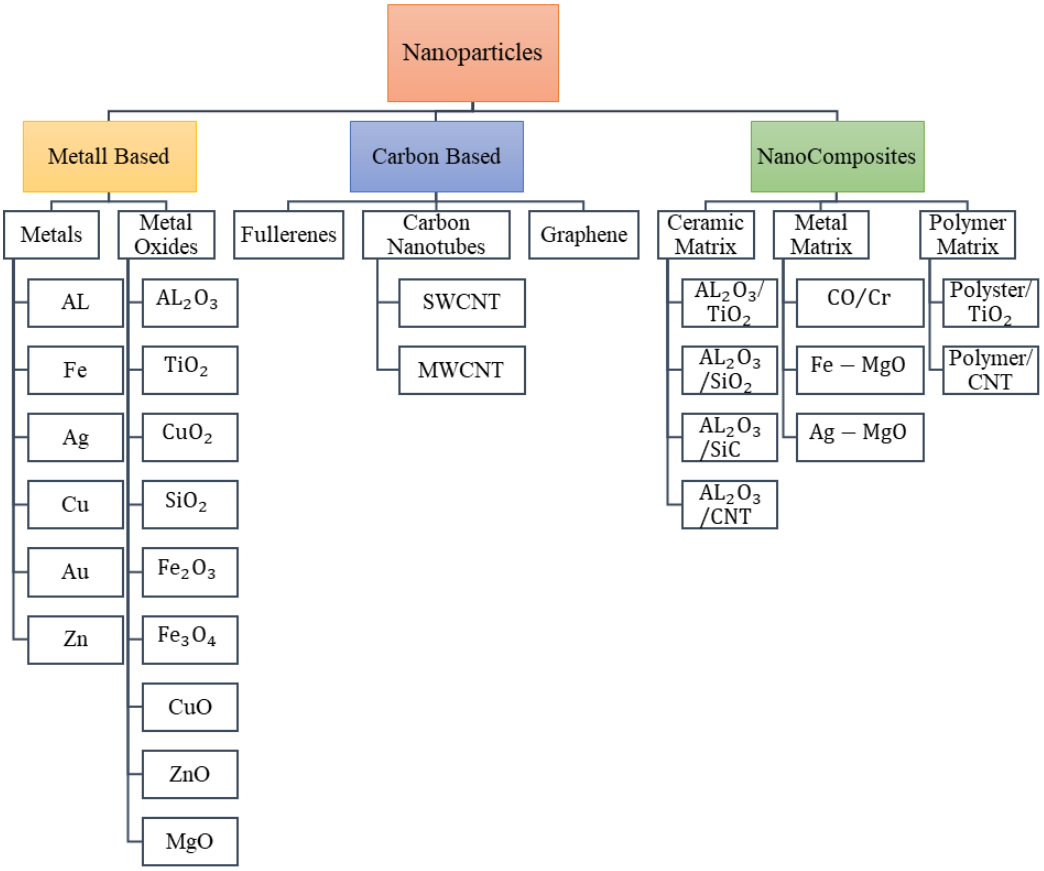

Figure 44 Nanoparticle's classification and types.

2.3.4 Advantages and challenges

Nanofluids have some advantages and limitations which are discussed as follows:

Advantages

- Improving the heat transfer coefficient of the working fluid by raising its thermal conductivity [138,150].
- Allowing the fluid to convey high amounts of thermal energy by raising the density and specific heat product [138].
- Boosting the heat transfer between the fluid and receiver [138].
- Enhancing both the thermal and electrical efficiencies of the PV system.
- Lowering the absorber temperature, therefore, protecting the material.

Challenges

Although nanofluids enhance the heat transfer phenomena, there are several challenges to their implementation:

- The high cost of production and preparation [150,151].
- Using nanofluids may lead to high operating cost due to the increase in the pump work [138,139,152,153].
- Sometimes when the operating conditions of the system are by natural convection and exposed to high temperature, the nanoparticles could agglomerate and show an unstable behaviour (ex. heat pipe) [154]. Figure 45a shows a Scanning Electron Microscopy (SEM) image of CuO nanoparticles agglomerated during experiments which have a negative effect on the performance of the system [155]. There are several methods to avoid nanoparticles agglomeration as reported in the literature whether by adding surfactants or by subjecting the nanofluids into sonication which can break down the nanoparticles agglomeration [156,157].
- Nanoparticles can cause erosion and corrosion to the metallic components of the system or even clog the flow passages [151]. Celata et al.[158] stated that the erosion depends on the pipe's material. They undertook experiments on two tube types: stainless steel and copper. They noticed that by using stainless steel tube, there was no erosion when using water or nanofluids in contrast to copper tube where the erosion was uniformly distributed through the tube.
- Many authors state that nanoparticles may have some toxic effects on the environment and human health [159,160].

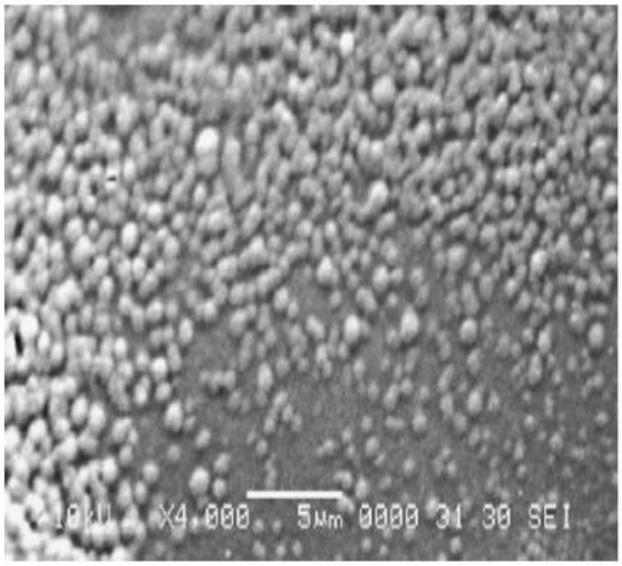

Figure 45 Scanning Electron Microscopy (SEM) image of agglomerated CuO nanoparticles.

2.3.5 Nanofluid preparation

In order to ensure significant performance, nanofluids need a successful preparation step to achieve stability of the suspended particles within the base fluid as well as their uniformity [161]. There are two ways to prepare nanofluids:

Single-step method

In this process, the dispersion and production of nanoparticles occur in the same step. This method can be carried out either by physical or chemical means [162]. In the physical method, the Ultrasonic Aided Submerged Arc System is used for the synthetisation of nanoparticles. The electrical energy generated from titanium electrodes which are merged in the dielectric liquid is used to melt the nanoparticles and vaporizes the deionized water. After this, in the vacuum chamber, the nanofluid, which is the mixture of the melted nanoparticles and deionized water, is formed [163,164]. On the other hand, the chemical method depends on adding a reducing agent to the mixture of nanoparticles and base fluid followed by stirring and heating [164].

Two-step method

In this method, the nanoparticles are prepared as a first stage and then mixed with the base fluid by using high shear or ultrasound methods. Table 3 indicates the advantages and drawbacks of both the single and two-step methods. In order

to ensure that the nanoparticles are stable inside the base fluid, different techniques have been introduced in the literature. Firstly, by using ultrasonication process, this approach is appropriate for nanofluid volumes from 0.2 to 2000 ml and produces a nanofluid with high stability and is considered the most popular method for preparation [164]. This process can be classified into either direct or indirect ultrasonication.

Direct sonication means that the mixture is in direct contact with the ultrasonic probe or horn. In this process, the required amount of both the nanoparticles and base fluid are weighed, then added into a vessel. The mixture should be stirred with a very thin metal rod for 1 minute followed by direct ultrasonication for 30 to 45 minutes. However, if the nanofluid is prepared by using the ultrasonic bath or pulsed ultrasonic, this process will be categorized as in-direct sonication. In this case, the mixture of nanoparticles and host fluid are kept inside a vessel which is immersed into a bath. Through this bath, the ultrasonic pulsations are transferred. This method is not preferable for high viscous-based nanofluids [165].

Unlike the ultrasonication process, high-pressure homogenizer is considered the most effective method for nanofluid preparation. However, this technique suffers from some disadvantages; huge size and weight, high cost, and limited processing capacity at a time (5-50 mL) [166]. Another mixing procedure is known as a mechanical stirrer (overhead stirrer) which can mix large volumes up to 20 L. However, It is not an effective way to avoid particle agglomeration if compared with other treatment methods [166]. In addition to the previous techniques, a shaker (disperser) is suitable for nanofluid preparation at ambient conditions. In addition, this is highly efficient for mixing nanoparticles with refrigerants to form the nanofluids. This mixture is called nano-refrigerant. Also, it can be useful for gaseous and low-temperature fluids.

Table 3 Advantages and disadvantages of single and two-step method [161,162].

Property	**Single-step method**	**Two-step method**
Stability	✓(high level)[167]	✓(achieved by adding reactants and surfactants) [168]
Avoiding Agglomeration	✓(Low level)	✓

Avoiding Storage and Transportation	✓	–
Simple	–	✓
Large quantity produced	–	✓
Particle uniformity	–	✓
Quick process	–	✓
Dispersion	✓(Totally)	✓(Partially)

2.3.6 Use of nanotechnology in PVT systems

This section presents the studies carried out in the field of solar thermal photovoltaics using different kinds of nanoparticles. Figure 46 summarizes the working idea of using a nanofluid to cool down a solar cell subjected to solar radiation. Using this type of cooling medium with PV systems allows the extraction of heat to be used in other thermal applications. Moreover, decreasing the PV cell's temperature leads to higher electricity generation.

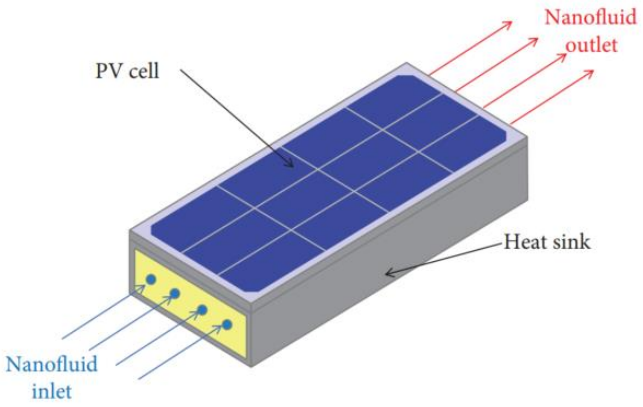

Figure 46 Schematic diagram of photovoltaic solar thermal system (PV/T) with nanofluid as a cooling medium.

A number of authors, such as Manikandan and Rajan [169], considered this technique in their research. They carried out an experimental study to evaluate the performance of sand-propyleneglycol-water nanofluid and its applicability in the solar energy field. The two-step method used to prepare this nanofluid, and the stability (thermal conductivity) was measured over 6 months. The measurements showed that the thermal conductivity changed only by 0.002 W/m.K which represents merely a 0.5% change in its value. Further, the authors conducted a comparison between the Sand-PG-water nanofluid and PG-water in

terms of the enhancement in the collection efficiency of solar energy. The experiments showed a higher temperature rate in the case of Sand-PG-water (0.5 vol.%) than in that of using only PG-water. In addition, for the volume fraction of 2 vol.% of nanoparticles, the enhancement in the collection efficiency reached 16.5%.

Silicon carbide (SiC) has been an attractive type of nanoparticles for a number of researchers. Al-Waeli et al. [170] provided experimental research on enhancing the performance of the PVT system using nanofluid (SiC/water). The authors tested several concentrations of nanoparticles (1, 1.5, 2, 3, 4 wt.%). They prepared the nanofluid using an ultrasonic shaker bath which showed significant stability of the nanofluid when examined over 6 months. The results revealed that the thermal conductivity of the working medium improved up to 8.2%. In addition, adding 3 wt.% of SiC led to a promising enhancement in both the electrical and thermal efficiencies by 24.1 and 100.19%, respectively.

Another experimental study was conducted by Al-Waeli et al. [171] where they built a novel design of PVT system, in which a tank was connected to it was filled with phase change material mixed with nanoparticles (SiC), to store the heat rejected from the system. This tank was able to exchange the heat from the fluid pipe inside it. The same tube was passed in the back of the PVT system to extract the heat from it. The fluid passing through this tube was nanofluid (SiC-water), to benefit from its ability to extract more heat. Adding nanoparticles to the PCM enhanced the charging and discharging processes. The nanoparticles volume fraction tested 0%, 1%, 2%, 3%, and 4%. The results showed that the new system enhanced the electrical current from 3.69 to 4.04 A and the electrical efficiency increased from 8.07 to 13.32% when compared to the conventional system.

Metal Oxide nanoparticles have shown significant results when used with different base fluids. Sardarabadi and Fard [172] presented a numerical and experimental study of a photovoltaic thermal system cooled by different types of nanoparticles and water as a base fluid flowing through copper tubes in the back of the PV. A schematic diagram of the system is shown in Figure 47. These nanoparticles were as follows; Al_2O_3, TiO_2, ZnO. The experimental and numerical findings showed that, TiO_2/water and ZnO/water enhanced the electrical efficiency more than the Al_2O_3/water. Regarding the thermal efficiency,

ZnO/water exhibited significant values if compared with the two other types. In addition, they studied the effect of increasing the mass fraction of ZnO from 0.05 to 10% by weight. While the thermal efficiency increased by four times, the temperature reduced by only 2% and the electrical efficiency by 0.02%.

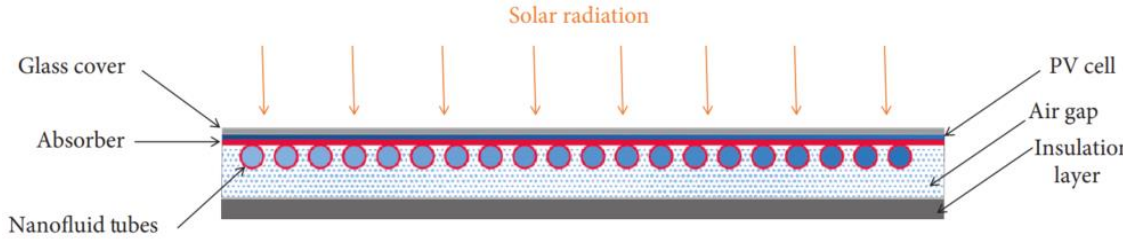

Figure 47 Schematic diagram of the PV/T system working on nanofluids.

Khanjiari et al. [173] performed a CFD analysis of a PVT system using Ag/water and Alumina/water nanofluids. The results exhibited that the efficiency, as well as the heat transfer coefficient, were increased by raising the nanoparticle volume fraction. The heat transfer coefficient at φ=5% for Alumina/water nanofluid increased by 2% with increasing the inlet velocity from 0.03 to 0.23 m/s. On the other hand, the heat transfer coefficient in the case of using Ag/water nanofluid was higher and varied from 28 to 45%. The thermal efficiency of using Alumina/water and Ag/water rose by 3 and 10%, respectively when the volume fraction increased from 1 to 10%. In addition, the enhancement in the electrical efficiency of Ag/water was greater than Alumina/water.

Hussein et al. [174] conducted an experimental investigation on the effect of using Al_2O_3/water as a cooling medium for PVT system by applying forced convection. Different concentrations of Al_2O_3/water were applied (0.1, 0.2, 0.3, 0.4, and 0.5%). The authors concluded that at a concentration of 0.3%, the temperature dropped significantly to 42.2 °C and the electrical efficiency rose to 12.1%. On the other hand, increasing the concentration ratio higher than this value caused raising the temperature again to 52.2 °C while the electrical efficiency declined to 11.3%.

Elmir et al. [175] presented a simulation study for a one-way channel in the backside of the PVT system, the flow inside this channel was nanofluid Al_2O_3/water (φ=0 to 10%). The solar cells were made from silicon and the inclination angle was set at 30°. The authors used Brinkman and Wasp models to predict the physical properties. The results revealed that using nanofluid

enhanced the heat transfer rate in the system and imposing low values of Reynolds number (Re=5) boosted the heat transfer rate by 27% at (φ=10%).

Rejeb et al. [176] introduced experimental and numerical studies of a PVT system cooled by several types of nanofluids. The authors tested different types of nanoparticles (Al_2O_3 and Cu) at several concentrations (0.1, 0.2, and 0.4 wt.%) with different base fluids (water and ethylene glycol), on the electrical and thermal efficiencies of the system. The results confirmed that the performance (thermal and electrical efficiencies) of water as a base fluid is more effective than ethylene glycol. The numerical model used to predict the annual electricity production for three different cities: Lyon (France), Mashhad (Iran), and Monastir (Tunisia). In addition, Cu/water showed higher electricity output for the three different cities reaching 791 kWhr/m^2 in Monastir.

Nada et al. [177] presented an experimental study using Al_2O_3 nanoparticles (d_{np}=20 nm) with Rt_{55} paraffin wax for enhancing the efficiency of a photovoltaic system. The authors built three modules; the first one was the reference module, a PCM layer was integrated into the backside of the PV for the second configuration, and in the third one PCM layer with nanoparticles was used. All of the modules were tested under Egyptian climatic conditions from 8 AM to 6 PM. A mechanical stirrer was used to mix the PCM with 2 vol.% the nanoparticles. The findings showed that by using PCM and nanoparticles, the efficiency improved by 13.2% and the temperature declined by 10.6 °C while, in the case of using PCM only, the efficiency boosted by 5.7% and the temperature decreased by 8.1% only.

Sardarabadi et al. [178] conducted an experimental study on the effect of using SiO_2/water as a coolant in a PVT system. The mass fractions used were 1 and 3% by weight. The overall efficiency rose by 3.6 and about 7.9% for the cases 1 and 3 wt.%, respectively if compared with using pure water only. In addition, the highest increase in both thermal and exergetic efficiency was observed at 3 wt.% (12.8 and 24.31%, respectively).

Michael and Iniyan [179] carried out an experimental study by adding a thin copper sheet instead of a Tedlar layer to the silicon cell and used CuO/water as a cooling medium to enhance the performance of the system. The nanofluid was at a 0.05% volume fraction. The authors tested the electrical and thermal

efficiencies of the system with and without glazing. They found that the thermal efficiency when using glazing and nanofluid was enhanced by about 45% in comparison with water only, while the electrical efficiency reduced by roughly 3%. The authors attributed this reduction to the need for a new heat exchanger with higher effectiveness.

Ghadiri et al. [180] introduced an experimental study of cooling a PVT system by using ferrofluid (Fe_3O_4/water). The authors studied the effect of different mass concentrations (1 and 3 wt.%) as well as changing the solar radiation (600 and 1100 W/m^2) on the overall efficiency and exergy rate. In addition, the performance of the ferrofluid was investigated under constant and magnetic fields. The findings confirmed that ferrofluid enhanced the overall efficiency by about 76% at 3 wt.% if compared with using distilled water only. On the other hand, this value can be improved by 3% and the exergy rate by about 46% if the system is accompanied by an alternating magnetic field of 50 HZ.

A Comparison between silicon carbide and metal oxide nanoparticles has been introduced by Al-Shamani et al. [181]. The scholars experimentally investigated the cooling performance of a PVT system by using three different types of nanoparticles; SiO_2, TiO_2, and SiC with distilled water as a base fluid. These nanofluids were prepared by the two-step method, where the nanofluids were prepared by dispersing the nanoparticles in the distilled water by using an ultrasonic device. The efficiency of the system and thermophysical properties of the nanofluids were tested outdoor under the Malaysia tropical climate conditions. The thermophysical properties (ρ, v, and k) were tested under various concentrations (0.5 to 2 wt.%). The researchers observed that the viscosity of all the nanofluids declined by raising the temperature from 25 to 60 °C the opposite of the thermal conductivity. In addition, SiC had the highest photovoltaic thermal efficiency (81.73%) and electrical efficiency (13.52%) of the three types.

A Carbon-based nanoparticle has been used by Hjerrild et al. [149]. They introduced an experimental and numerical model of a spectrally tailorable optical filter, synthesized from nanofluids (Ag/SiO_2 with 0.026 wt.% and CNT in water) placed between the light source and the solar cell. These two types of nanoparticles were selected because of their high absorptivity of light. Also, CNT can enhance the heat transfer rate which allows more heat extraction. The findings showed that the combined efficiency was boosted by 30% if compared

to the conventional model where the electrical efficiency increased by about 6.6%.

2.3.7 Use of nanotechnology in CPVT systems

In contrast to the conventional photovoltaic systems concentrated photovoltaic use concentrators or mirrors as shown in Figure 48 to focus the sunlight on highly efficient solar cells. Thus, both electrical and thermal efficiencies could increase if nanotechnology is adopted in the system.

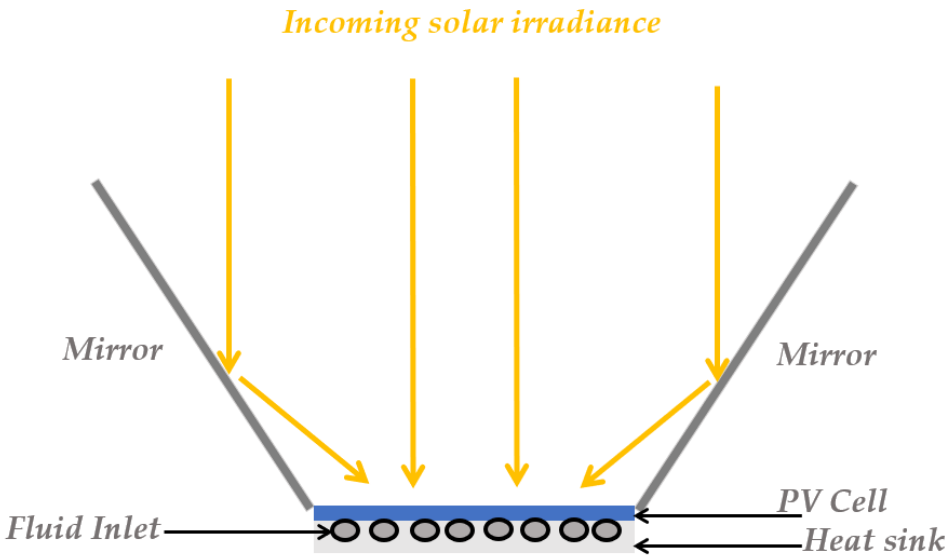

Figure 48 Schematic diagram of concentrated photovoltaic thermal systems.

Very little research has been carried out into using nanofluid as a cooling medium on the CPVT systems. Hassani et al. [182] carried out numerical studies on two concentrated PVT system designs. The first one (D-1) had two separate channels, one channel for the optical nanofluid and the other channel for the thermal nanofluid. The second design was a double pass channel (D-2). The optical nanofluid consisted of Ag (d_{np}=10 nm) nanoparticles dispersed in Therminol VP-1 which is suitable for high-temperature applications and has the ability to absorb the long wavelength, while Ag can absorb the short wavelength. The thermal nanofluid is from Ag and suspended in water. The authors concluded that the overall efficiency showed a sharp increase for GaAs and Si at a solar concentration of 160 and 100 suns when the volume fraction grew from 0.001% to 1.5%. In addition, the study recommended that using two different types of fluids in a separate channel design is more efficient than the other designs.

Rahbar et al. [183] presented mathematical modeling of a system consisting of a parabolic trough concentrator with the concentrated photovoltaic system working on Ag/water to run an Organic Rankine Cycle. The analytical solution of the 1-D model was carried out by using Engineering Equation Solver (EES). The nanofluid was used as a cooling fluid for the CPVT as well as an optical filter to extract only the useful solar spectrum for the concentrated photovoltaic system. The authors concluded that adopting nanofluid as a working medium with CPVT system had a great influence on the electrical, thermal, and overall efficiencies (1.8%, 3.3%, and 5.1%, respectively at CR=13.05 compared to CPV). This effect appeared after raising the concentration ratio higher than 7.

Metal oxide nanoparticles have attracted the attention of some scientists due to their stability and affordability. Xu and Kleinstreuer [184] introduced a numerical 1-D study of the effect of (Al_2O_3/water) nanofluid on the cooling of a low concentrated silicon solar cell by using Maxwell's model for thermal conductivity. The results showed that nanofluids were efficient in cooling the solar cell. In addition, the researchers stated that using diathermic oil instead of water will give better performance for other thermal applications. In general, they agreed that nanofluids increased both the electrical and thermal efficiencies of the system.

Another study by Xu and Kleinstreuer [185] in which they presented another mathematical study (2-D modeling) on the effect of using Al_2O_3/water as a cooling medium for a photovoltaic straight channel exposed to highly concentrated solar intensity. The channel was subjected to heat conduction and turbulent nanofluid convection. The influence of changing nanoparticle volume fraction (0 to 4%), Reynolds number at the inlet (3000 to 70000), inlet nanofluid temperature (15 to 45 °C) and different channel height (2 to 14 mm) on the performance of the system were studied. The study was conducted by using ANSYS-CFX 14 (control volume method). The results showed that the cell efficiency increased by raising the volume fraction and reducing the inlet nanofluid temperature. In addition, the authors observed that the maximum efficiency obtained was 20% at a concentration ratio of 200 suns, inlet Reynolds number at 30,000, and channel height 10 mm.

Srivastava and Reddy [186] studied different configurations of parabolic trough concentrator (PTC) with a compound parabolic collector. In addition, they

discussed the effect of using a different number of cells as well as various types of fluids; Al_2O_3/water, Syltherm 800, Therminol VP1, and Therminol VP59. The study was carried out by using SIMPLE solver in Fluent 16.1. It was concluded that using CPC had a negligible effect on the performance of the system, the cooling rate at a concentration of 6% being lower than at 0% and 1%. The authors attributed this to agglomeration. In addition, the maximum thermal output was achieved by using Syltherm 800 which was 2592.42 W, while the highest electrical output (692.2 W) was observed by using Al_2O_3/water at a concentration of 1%. Lelea, et al. [187] introduced a theoretical 2-D study by using ANSYS-Fluent on cooling CPVT straight microchannel by using Al_2O_3/water at different nanoparticles diameters (28 nm and 47 nm) and concentrations (1%, 3%, and 5%). A single-phase model was used to evaluate the kinematic viscosity and thermal conductivity. The authors claimed that the maximum temperature, in the case of using φ=5%, was lower than in the case of water only.

Zarma et al. [86] built a mathematical 2-D model using ANSYS 19.0 to examine the performance of CPVT using PCM (Calcium Chloride Hexahydrate) with different types of nanoparticles; Al_2O_3, CuO, and SiO_2. The nanoparticles were examined at different concentrations, 1 wt.% and 5 wt.%.The mixture of PCM and nanoparticles were in a rectangular container at the back surface of the solar cell with dimensions of; Height=125 mm and Length = 100 mm. The results of the numerical study revealed that the maximum performance achieved was by using Al_2O_3 at a concentration of 5 wt.%. where the electrical efficiency was 8%, and the temperature uniformity was 12 °C. In addition, the authors stated that using nanoparticles with PCM improved the heat transfer rate by increasing the thermal conductivity of the mixture.

Yazdanifard et al. [188] presented a mathematical study of using TiO_2/water as a working medium for a parabolic trough concentrator integrated with the concentrated photovoltaic receiver of a silicon solar cell. The mathematical equations were solved by using MATLAB software. The effect of increasing the volume fraction and flow regime was introduced. The results revealed that, in the case of laminar flow, when the volume fraction of the nanoparticles increases, both kinematic viscosity and thermal conductivity of the nanofluid rise. Therefore, at a constant mass flow rate, the Reynolds number decreased, which caused the heat transfer coefficient to develop. Hence, the photovoltaic temperature

declined, the opposite of the case of turbulent flow. As a result of all of the above, there were greater increases in the thermal, electrical, and total efficiencies in the case of laminar more than in turbulent flow.

Menbari et al. [189] experimentally and numerically studied the effect of using CuO/water as a nanofluid on the performance of direct absorption parabolic trough collector (DAPTC). The numerical and experimental results showed that the thermal efficiency of the system improved by increasing the nanoparticles volume fraction from 0.002 to 0.008% as it rose from 18 to 52%. In addition, the authors stated that it enhanced the performance by increasing the flow rate from 20 to 100 L/hr.

Bellos and Tzivanidis [190] conducted mathematical research by using Solidworks flow simulation to perform optical, thermal, and flow studies about the effect of using syltherm 800/copper oxide on the performance of the CPVT with parabolic trough concentrator, a cross-section of the studied receiver is shown in Figure 49. The absorber was made from PV silicon cell of a width of 100 mm, while the receiver aperture area was 10 mm^2.The authors studied the effect of changing the inlet temperature (25 to 200 °C), and the nanofluid flow rate (300 to 720 L/hr) on the flow properties. The study concluded that using nanofluid improved the electrical, thermal, and total efficiency. In addition, there was a slight enhancement in the thermal efficiency after 540 L/hr. The maximum thermal, electrical, and total efficiencies at an inlet temperature of 100 °C and flow rate of 540 L/hr, were 46.84%, 6.60%, and 2.08%, respectively which were greater than the values achieved by using pure oil only.

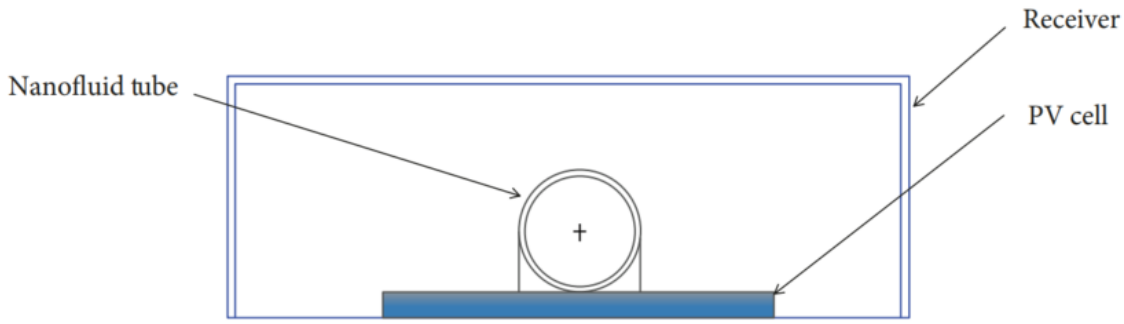

Figure 49 Cross-section of the studied receiver.

An et al. [191] presented an experimental study using Cu_9S_5 nanofluid as an optical filter in concentrating PVT as shown in Figure 50. This Oleylamine solution

consists of Cu_9S_5 nanoparticles dispersed in Oleylamine ($C_{18}H_{37}N$). The particle diameter ranged from 50.5 to 73.7 nm and the average diameter was 60.2 nm. In addition, three different concentrations of the nanofluid were used (22±1.1,44.6±2.2,89.2±4.5 ppm). The results revealed that increasing the particle concentration had a great influence on the performance of the system. Moreover, the maximum efficiency achieved by using this nanofluid at a high concentration was 34.2% which was higher than that without an optical filter (17.9%).

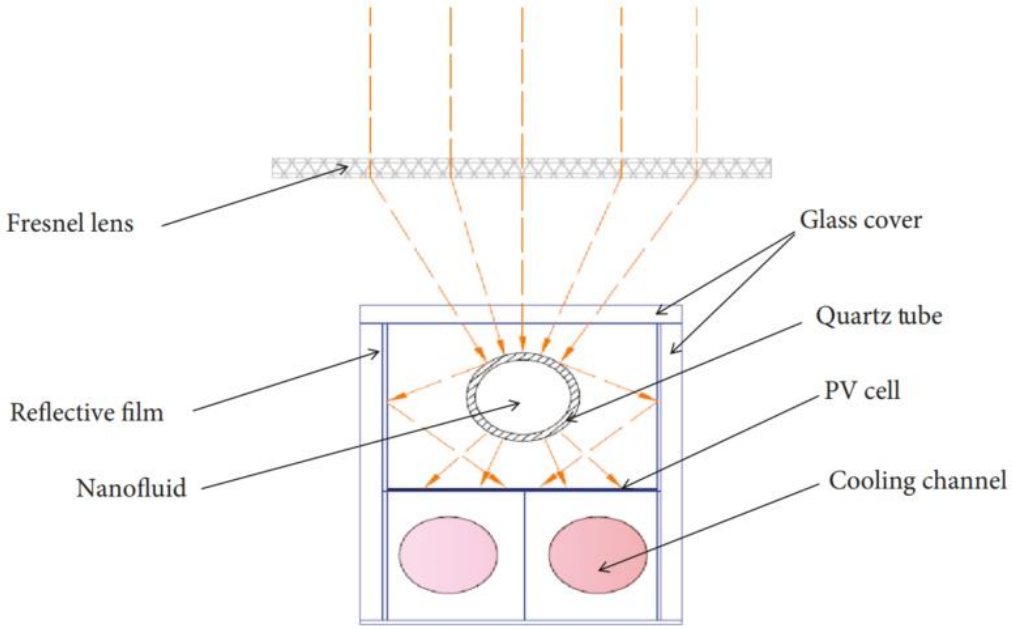

Figure 50 Schematic representation of the concentrated photovoltaic thermal system studied by An et al.

Radwan et al. [192] mathematically studied the effect of using Al_2O_3 and SiC nanoparticles with water on the cooling of a LCPV system based on silicon solar cell. A 2-D study for straight channel heat sink was carried out by using ANSYS Fluent 16.2. The diameter of both Al_2O_3 and SiC was 20 nm, the concentration varied from 1% to 4%, and the Reynolds number from 10 to 100. The authors stated that the performance of the LCPV system was improved by using SiC/water than in the case of Al_2O_3/water. In addition, a significant decrease in the cell temperature was observed by increasing the volume fraction of both types of nanofluids.

This research was followed by 3-D modeling using ANSYS 17.2 to study the effect of using the same nanoparticles on the performance of a straight microchannel heat sink within an LCPV [193]. Compared to Al_2O_3/water, SiC/water showed better performance in terms of cell temperature uniformity, net

electrical power of the solar cell, and electrical efficiency. In addition, the authors agreed that 4% of SiC caused a decrease in the maximum local solar cell temperature compared with pure water.

2.3.8 Other studies dealt with nanofluids as a working medium

Due to the benefits of nanofluids over conventional options, various scientists have conducted several studies to examine the performance of direct absorption solar collector (DASC), flat plate and u-tube solar collectors (FPSC& UTSC) and evacuated tube solar collector (ETSC). Otanicar et al. [194] presented experimental and numerical studies on the effect of using different nanoparticles (Graphite sphere-based, carbon nanotube-based, and silver sphere-based), as a cooling medium, on a direct absorption solar collector (DASC). These nanoparticles were tested with water at a range of volume fractions and particle sizes. The authors concluded that graphite nanoparticles can increase the collector efficiency by only 3% if compared with the conventional flat surface absorber if the volume fraction is equal to 5%. On the other hand, by using silver nanoparticles the efficiency enhanced by 5%, while by using CNT a small difference can appear. After a volume fraction of 5%, the efficiency began to decrease slightly.

Kang et al. [195] experimentally evaluated the performance of both the flat plate and U-tube solar collectors if the nanofluid is used (Al_2O_3/water) under several volume concentration (0.5,1,1.5%) and nanoparticle size (20,50,100 nm). Regarding the flat plate solar collector, the efficiency increased to 72.4% when using the nanofluid instead of water at a volume fraction of 1% and nanoparticle size 20 nm. This value was the maximum if compared with those at nanoparticle size 50 and 100 nm. In addition, the efficiency of the flat plate solar collector increased by 3.5% if compared with the U-tube solar collector after use Al_2O_3/water. Therefore, the solar collector's performance was enhanced when the particle size decreased. Further, the authors concluded that the maximum efficiencies for both the flat plate and U-tube solar collectors occurred at 1% volume fraction.

Yousefi et al. [196] experimentally studied the effect of using MWCNT/water as a nanofluid for absorbing heat from the flat-plate solar collector (FPSC). The effect of several parameters was studied on the performance of the flat plate solar

collector; MWCNT weight fraction (0.2% and 0.4%), using surfactant of Triton, nanofluid mass flow rate ranged from (0.0167 to 0.05 kg/s). The Triton X-100 was added to the nanofluid in the ratio of 1:350 in order to achieve the maximum dispersion. Also, the two-step method was applied using 400S Ultrasonic model for 30 minutes and the mixture was stable for up to 10 days. In comparison with water, the nanofluid enhanced the heat transfer in the flat plate solar collector and boosted the thermal efficiency by using the chemical surfactant. Moreover, the maximum thermal efficiency was achieved at 0.05 kg/s and fraction weight of 0.4%.

Kiliç et al. [197] introduced an experimental study on the impact of using TiO_2/water with a concentration of 2 wt.% on the effectiveness of the flat plate solar collector. The authors used the two-step method to prepare the nanofluid, using surfactant -Triton X100- at a concentration of 0.2 wt.% to keep the prepared nanofluid stable and avoid agglomeration. After that, they exposed the mixture to an ultrasonic bath. The maximum achieved instantaneous efficiency of the collector by using this nanofluid was 48.672% whereas it was only 36.204% by using water only.

Verma et al. [198] investigated the influence of using two different hybrid fluids; (80% MgO+20% MWCNTs)/water, and (80% CuO+20% MWCNTs)/Water on the performance of a flat plate solar collector. The diameters of CuO and MWCNT nanoparticles were 42 nm, and 7 nm, respectively. The concentration of the samples were 0.25, 0.5, 0.75, 1, 1.25, 1.5, and 2 vol.%. Both of the hybrid fluids were prepared by using the two-step method. Initially, the mixture of CuO/water and MgO/water at maximum concentration were prepared by using deionized water. After that, MWCNT was added in the solution, followed by ultrasonic agitation, and then ultrasonic bath for 2 hr. The authors stated that both the energetic and exergetic efficiencies of MgO (71.54%, and 70.55%, respectively) hybrid nanofluid were much greater than that in the case of CuO hybrid fluid (70.63%, and 69.11%, respectively).

Chougule et al. [199] introduced experimental research on using carbon nanotubes CNT/water at a concentration of 0.15 vol.%, diameter of 10-12 nm, and length of 0.1-10 μm. The idea of the research was to examine this type of nanofluid inside copper heat pipe as a cooling method for flat plate collectors. The authors studied the performance of the system under several conditions;

changing the collector angle with a fixed position, and activating the tracking mechanism of the collector. They found that the best performance (45%) was at a tilt angle of 31.5°.

Ghaderian and Sidik [200] performed experimental research to examine the effect of using Al_2O_3/distilled water on the performance of the evacuated tube solar collector (ETSC). The volume fractions used were 0.03 and 0.06% (particle diameter of 40 nm) and the volume flow rate range of the nanofluid studied was from 20 to 60 L/hr. The authors prepared the nanofluid by using the two-step method which showed good stability over the following 7 days. The maximum average efficiency was achieved by using Al_2O_3/distilled water as a working medium was 58.65% at 0.06% volume fraction and flow rate of 60 L/hr, which was considered a very high value if compared with using water only (22.85%).

Iranmanesh et al. [201] carried out experimental research on using Graphene nanoplatelets GNP/distilled water as a working fluid inside the evacuated tube solar collector. The mass fractions tested were 0.025, 0.05, 0.075, 0.1 wt.% at volume flow rate of 0.5, 0.1, and 1.5 L/min. The authors prepared the nanofluid by using an ultrasonication probe without any surfactants which showed good stability for the following three months after the initial preparation. The experiments revealed that the maximum efficiency of the collector occurred at nanoparticles concentration of 0.1 wt.% and a volume flow rate of 1.5 L/min. This value was 90.7% which was greater than that of using distilled water only (54.81%).

Liu et al. [202] experimentally investigated the efficiency of the evacuated tube solar collector which was integrated with a compound parabolic concentrator (CPC) by using CuO/water with a concentration of 1.2 wt.% and a diameter of 50 nm. The nanofluid was prepared by using the two-step method, by suspending the nanofluid on the water followed by oscillating it in an ultrasonic bath. The performance of the system was enhanced by using nanofluid by 12.4% at an air outlet temperature 160 °C whereas, the maximum efficiency achieved was 57.6% at an air outlet temperature of merely 130 °C.

Mahendran et al. [203] experimentally examined the influence of using TiO_2/water on the performance of the evacuated tube solar collector. The outdoor tests took place in Malaysia where the daily solar isolation reached 900 W/m^2. The

nanoparticles' diameter was 30 to 50 nm and volume fraction concentration of 0.3%. Preparation of the nanofluid was conducted by using the two-step method; the authors used a mechanical stirrer for 2 hours in order to ensure that the mixture was homogenous. The maximum efficiency achieved by using nanofluid was 73% which was higher than the case of using water only by 16.67% where the volume flow rate was 2.7 L/min.

Hussain et al. [204] undertook an experimental study on the effect of using two different types of nanofluids Ag (d_{np}=30 nm)/water, and ZrO_2 (d_{np}=50 nm)/water on the evacuated tube solar collector efficiency. The nanoparticles were at different concentrations; 0, 1, 3, and 5 vol.% and different mass flow rates of 30, 60, and 90 L/hr.m^2. The two-step method was used for preparing the nanofluid; after dispersing the nanoparticles in distilled water, ultrasonic mixing was applied using surfactant but the mixture remained stable for 4 hours. The authors claimed that the efficiency of the solar collector achieved by using Ag/water was 21.05% at 5 vol.% and 90 L/hr.m^2 which was considered higher than in the case of using ZrO_2/water. Therefore, the Ag/water achieved better performance than ZrO_2/water.

Kaya et al. [205] examined experimentally the performance of an evacuated U tube solar collector working with ZnO (d_{np}=30 nm)/ethylene glycol and pure water. The base fluids used were 50% ethylene glycol and 50% pure water, the nanofluid tested was at a volume concentration of 1%, 2%, 3%, and 4%, and three different mass flow rates (0.02, 0.03, 0.045 kg/s). A surfactant agent polyvinylpyrrolidone (PVP) was added to the mixture of the base fluid (EG+water). Thereafter, the magnetic stirring was enabled to ensure that the nanofluid was homogeneous. The authors noted that the maximum efficiency (62.87%) of the solar collector was achieved at a volume concentration of 3% and a mass flow rate of 0.045 kg/s.

Tong et al. [206] studied the influence of using multi-walled carbon nanotube (MWCNT) nanoparticles with water on the performance of an enclosed type evacuated tube solar collector. The nanofluid was prepared by using the two-step method (gum arabic with 0.25 wt.% concentration as a surfactant, followed by probe sonication). The efficiency of the system was tested under concentration volume of 0.06 to 0.24 vol.% and mass flow rate of 0.01 kg/s. The theoretical and

experimental results revealed that the heat transfer coefficient was enhanced by 8% by using nanofluid at 0.24 vol.%.

Ozosy and Corumlu [207] experimentally determined the efficiency of a thermosyphon heat pipe evacuated tube solar collector by using Ag/water as a working medium in the heat pipe. The nanofluid used was at a concentration of 20 ppm and prepared by using the two-step method. Firstly, the electrolysis method was applied to the mixture of silver and pure water. Secondly, the authors used Tannic Acid as a surfactant. The volumetric flow rate of the nanofluid was 0.18 L/min. The results revealed that the solar collector efficiency rose between 20.7% and 40%. A conclusion for all the above studies about nanotechnology is introduced in the following table.

Table 4 Conclusion of the previous studies.

App.	Nano particles	Base fluid	C	d_{np} nm	k mW/m.k	Method	Stability	Parameters Studied					Ref.
								k	μ	η_{th}	η_{elec}	$\eta_{overall}$	
PV/T	SiC	Water	1–4 wt.%	45–65	370–490	Two step method (ultrasonic shaker)	Up to 6 months	✓	✓	✓	✓	✓	[170]
	SiC	Water	0–4 vol.%	45–65	370–490	Two step method (ultrasonic shaker)	Up to 6 months	✓	✓	✓	✓	✓	[171]
	SiC	PCM											
	Al_2O_3	Water	0.2 wt.%	20	40	Two step method (ultrasonic vibrator)	Up to two days	–	–	✓	✓	–	[172]
	TiO_2			10–30	8.9								
	ZnO			10–25	13								
	Ag-SiO_2	Water	0.026 wt.%	6–13	–	Two step method (ultrasonic bath followed by probe)	–	–	–	✓	✓	✓	[149]
	CNT												
	SiO_2	Water	1, 3 wt.%	11–14	–	Two step method	Up to ten days	–	–	✓	✓	✓	[178]

					(ultrasonic processor)							
Ag / Al_2O_3	Water	1–12 vol.%	50	–	Numerical Study (CFD)	–	✓	–	✓	✓	✓	[173]
Al_2O_3	Water	0.1–0.5 vol.%	30	–	–	–	–	–	✓	✓	–	[174]
Fe_3O_4	Water	1, 3 wt.%	45	–	Two step method (ultrasonic mixing)	At least one month	–	–	✓	✓	✓	[180]
Al_2O_3 / Cu	Water/Ethylene Glycol	0.1–0.4 wt.%	–	40 / 401	Two step method (ultrasonic mechanism)	–	–	–	✓	✓	–	[176]
CuO	Water	0.05 vol.%	75	–	Two step method (ultrasonicator)	From one (Triton X-100) to 3 days (SDBS surfactant)	✓	✓	✓	✓	✓	[179]
SiO_2 / TiO_2	Water	0.5-2 wt.%	–	–	Two step method	–	✓	✓	✓	✓	✓	[181]

	SiC					(ultrasonic device)							
	Al_2O_3	Water	0.02 wt.%	–	–	–	–	–	–	✓	✓	✓	[208]
	Al_2O_3	Water	0–10 vol.%	–	–	Numerical Study	–	–	–				[175]
LCPVT	Al_2O_3 / SiC	Water	4 vol.%	20	–	2D-Numerical Study (CFD)-straight heat sink &Si cell	–	–	–	✓	✓	–	[192]
	Al_2O_3 / SiC	Water	4 vol.%	20		3D-Numerical Study (CFD)-straight heat sink &Si cell	–	–	–	✓	✓	–	[193]
	Al_2O_3	Water	5 vol.%	38.4	–	1D-Numerical Study (CFD)-straight heat sink &Si cell	–	✓	–	✓	✓	✓	[184]
	Al_2O_3	Water	1-5 vol.%	13-47	–	1D-Numerical Study (CFD)-straight heat sink &Si cell	–	–	–	✓	–	–	[187]

	Al_2O_3	Water	4 vol.%	38.4	–	2D-Numerical Study (CFD)- straight heat sink &Si cell	–	–	–	Temp.	–	–	[185]
CPV/SBS	Ag	Therminol VP–1	0.001-1.5 vol.%	10	–	Numerical Study	–	–	–	✓	✓	✓	[182]
	Cu_9S_5	Oleylamine ($C_{18}H_{37}N$)	0.001-1.5 vol.%	60.2	–	Ultrasonic Washer (before each test)	–	✓	–	✓	✓	✓	[191]
PTC	CuO	Syltherm 800	5 vol.%	–	–	Numerical Study (CFD)	–	✓	✓	✓	✓	✓	[190]
	Al_2O_3	Water	0- 6 vol.%	–	–	Numerical Study (CFD)	–	✓	–	✓	✓	✓	[186]
	Ag	Water	6-13 vol.%	–	–	Numerical Study (CFD)	–	–	–	✓	✓	✓	[183]
	TiO_2	Water	4 vol.%	21	–	Numerical Study	–	✓	✓	✓	✓	✓	[188]
DAPTC	CuO	Water	0.002-0.008 vol.%	<100	–	Two step method (ultrasonic probe with	Stable through the exp.	–	–	✓	–	–	[189]

						Sodium Hexa Meta Phosphate surfactant							
DASC	Graphite Ag CNT	Water	0-1 vol.%	30 20-40 6-20	–	Two step method (Sonication with sodium dodecyl-sulfate surfactant)	–	–	–	✓	–	–	[194]
FP&UTSC	Al_2O_3	Water	0.5-1.5 vol.%	20-100	–	–	Up to one week	–	–	✓	✓	–	[195]
	MWCNT	Water	0.2-0.4 wt.%	10-30	–	Two step method (ultrasonic probe) and (adding Triton X-100)	Up to 10 days	–	–	✓	–	–	[196]
	TiO_2	Water	0.2 wt.%	44	–	Two step method (ultrasonic processor	–	–	–	✓	–	–	[197]

						Bandelin Sonorex Super RK514H) with Triton-X 100							
	MgO+MWCNT (80:20) CuO+MWCNT (80:20)	Water	0.25-2 vol.%	7-42	–	Two step method (ultrasonic bath)	–	✓	✓	✓	✓	–	[198]
	CNT	Water	0.15 vol.%	10-12	3.47	Chemicals followed by ultrasonic bath (two step method)	15 hr	–	–	✓	–	–	[199]
ETSC	Al_2O_3	Water	0.03-0.06 vol.%	40	36	Two step method (Adding Triton-X 100 followed by ultrasonic probe	Up to one week	✓	–	✓	–	–	[200]
	GNP	Water	0.025-0.1 wt.%	5-10	–	Two step method (ultrasonic	Up to three months	✓	✓	✓	–	–	[201]

					probe) without surfactants							
CuO	Water	1.2 wt.%	50	–	Two step method (ultrasonic bath)	–	–	–	✓	–	–	[202]
TiO_2	Water	0.3 vol.%	30-50	8.4	Two step method (followed by mechanical stirrer)	–	–	–	✓	–	–	[203]
Ag	Water	1-5 vol.%	30	429	Two step method (followed by ultrasonic mixing)	Up to 4 hrs	–	–	✓	–	–	[204]
ZrO			50	22.7								
ZnO	EG/water (50:50)	1-4 vol.%	30	27.2	Two step method (followed by magnetic stirrer)	–	–	–	✓	–	–	[205]

	MWCNT	Water	0.06-0.24 vol.%	–	3000	Two step method (ultrasonic probe) followed by adding gum Arabic for stability	–	✓	✓	✓	–	–	[206]
	Ag	Water	20 ppm	60	–	Two-step method (followed by adding Tannic acid as a reducing agent)	one year under observation	–	–	✓	–	–	[207]

2.3.9 Thermophysical properties of nanoparticles and base fluids

This section introduces the thermophysical properties of both nanoparticles and base fluids that have been used in the literature. These thermophysical properties include density, specific heat, and thermal conductivity (Table 5).

Table 5 Nanoparticles and base fluids properties as stated in the literature.

Nanoparticle/base fluid type	**Density, ρ_{np} (kg/m^3)**	**Specific Heat, $c_{p,np}$ (J/kg.K)**	**Thermal Conductivity, k_{np} (mW/m K)**	**Ref.**
Alumina (Al_2O_3)	3960	773	40	[209,210]
Aluminium (Al)	2700	904	237	[210]
Carbon Nanotube (CNT)	1350	—	3000	[210]
Copper (Cu)	8940	385	401	[210]
Copper Oxide (CuO)	6000	551	33	[210]
Graphite (C)	2160	701	120	[210]
Silicon (Si)	2320	714	148	[210]
Silicon Carbide (SiC)	3370	1340	150	[210]
Silicon dioxide (SiO_2)	3970	765	3970	[211]
Titanium Carbide (TiC)	4930	711	330	[210]
Titanium dioxide (TiO_2)	4230	692	8.4	[210]
Cuprous Oxide (Cu_2O)	6320	42.36 J/mole.K	76.5	[211]
Graphene Oxide (GO)	1910	710	1000	[211]
Iron Oxide (Fe_2O_3)	5250	650	20	[212]
Single-walled carbon nano tubes (SWCNTs)	2100	841	6000	[213]
Multi-walled carbon nano tubes (MWCNTs)	2100	711	1500	[214]
Ag+MgO nanocomposite	7035	554.5	242	[215]
Fe_3O_4+MWCNTs nanocomposite	4845.4	680.66	509.14	[214]
Pure water	997.1	4179	0.613	[176,209]
Ethylene glycol	1113.2	2470.2	0.258	[176,216]
Engine oil	870	2012	0.142	[217]

As stated earlier, the idea behind using nanoparticle within the base (host) fluid is to increase the thermal conductivity of the carrying fluid which leads to boosting the heat transfer phenomenon through the system. Therefore, in this section, we discuss some important parameters that have a significant influence on the thermal conductivity of the nanofluid as mentioned in the published studies:

Nanoparticle volume concentration

Nanoparticle volume concentration has a significant influence on the enhancement of the thermal conductivity of the nanofluid. Several studies have proven that increasing the volume fraction up to 5% [159] can increase the thermal conductivity for example as reported by Iranmanesh et al. [198] and Verma et al. [195].

Temperature

Increasing the temperature has a considerable effect on boosting the thermal conductivity of the nanofluid which has been revealed by Lee et al. [218], Al-Waeli et al. [170], Verma et al.[198], Qiu et al. [219], and Iranmanesh et al. [201] as the opposite of the behaviour shown for viscosity. Nevertheless, Bellos and Tzivanidis [190] in their recent research using CuO/syltherm oil 800 confirmed that the thermal conductivity of the nanofluid decreased by increasing the temperature.

Particle size

Nanofluid consists of base fluid and nanoparticles which have a diameter of less than 100 nm. Therefore, it is preferred to use nanoparticles with small sizes to achieve a better enhancement in thermal conductivity as well as in heat transfer. Kang et al. [195] discussed the effect of increasing the nanoparticles' diameter on the efficiency of the flat plate solar collector. The results revealed that using a particle size of d_{np}=20 nm boosted the efficiency compared with d_{np}=50 nm, and 100 nm.

Base fluid type

There are several types of base fluids, as stated above. Xie et al.[220] observed that using base fluid with low thermal conductivity is more efficient than using fluids with high thermal conductivity. In contrast, Rejeb et al. [176] argued that using water (as a base fluid) which has higher thermal conductivity than ethylene glycol led to great

enhancement in the thermal conductivity for the same nanoparticle and operating conditions.

Nanoparticle shape

Many researchers have studied the effect of the nanoparticle shape on fluid performance and its thermal conductivity [221]. Murshed et al. [222] studied two geometrical configurations of TiO_2 nanoparticle; cylindrical shape (d_{np}=10 nm, L=40 nm) and spherical shape (d_{np}=15 nm). The experimental results showed that the cylindrical shape achieved greater improvement in thermal conductivity. Figure 51 shows a comparison of thermal conductivity improvement when using differently shaped nanoparticles these include blades, platelets, cylinders, bricks, and spheres. It was found that the best thermal conductivity is achieved when using blades. The scientists attributed this to the large heat transfer area of the particles which conducts the heat through the fluid.

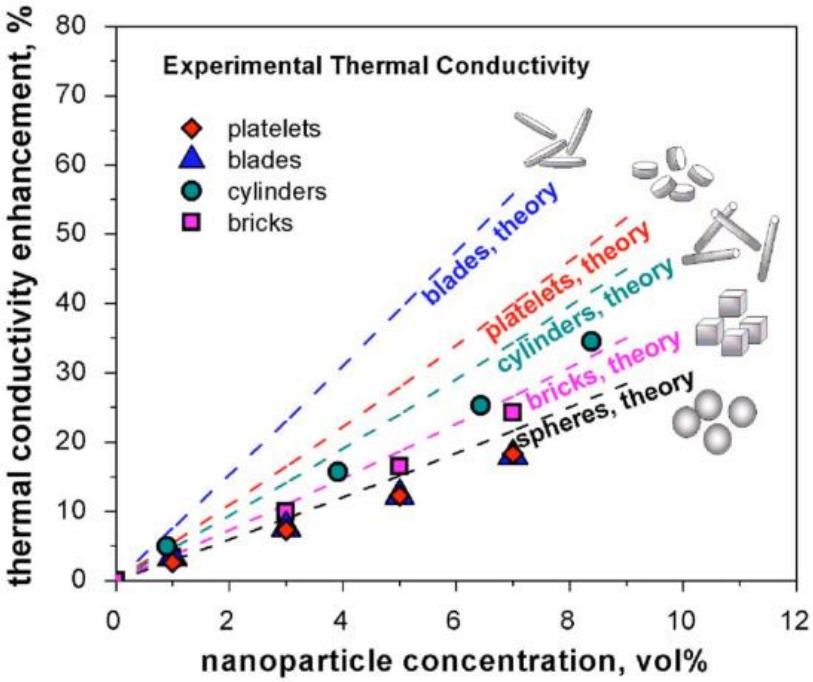

Figure 51 Effect of nanoparticles shape on the thermal conductivity of alumina nanofluid at different values of volume fractions [221].

Surfactants

The function of adding a surfactant or an additive is to prevent the agglomeration and sedimentation of the nanofluid and improve its stability. For example, these surfactants or additives can be sodium hexa meta phosphate [189], sodium dodecyl-sulfate [194], Triton-X 100 [197], or sodium dodecylbenzene sulphonate [179]. However, using a specific type of surfactant depends on the type of both the nanoparticle and base fluid [223].

2.4 Conclusion

This chapter discussed a number of relevant topics concerning the current Ph.D. research. In addition, a range of previous studies related to these areas were considered. In the first section, a comprehensive review of the concentrated solar energy technologies was introduced. This includes their working criteria, advantages, and limitations of each type. In respect of the concentrated photovoltaic (CPV), the solar cell and optics classifications were reviewed.

From the review, it can be noted that concentrator photovoltaics offers a promising future for electricity production and can outperform conventional flat-plate photovoltaics for areas with high solar irradiances. This is due to the reduction in the amount of semiconducting materials and the use of highly efficient optics. However, this technology suffers from several challenges such as the increase in the cell temperature which reduces the electrical efficiency and the power output.

Therefore, the thermal management systems introduced in the previous studies were reviewed in the next section including active and passive cooling techniques. From this section, it can be seen that the active cooling method offers an efficient and reliable solution for the high concentration systems, unlike the passive technique.

The second topic discussed in this chapter was optical filters. A review of their classifications, working principles, and previous studies related to the applications of this technology was provided. The main idea of this method is attenuating the unwanted wavelengths, which causes the increase in the cell temperature, from passing to the cell, while allowing the useful wavelengths. This can protect the solar cell and at the same time increase the electricity production.

In the last part of this review, the use of nanotechnology in solar thermal systems was introduced. Also, nanoparticles, nanofluids definitions, and their preparation methods were reviewed, and the advantages and limitations of this technology were discussed. Nanofluid works as a good heat transfer fluid as the use of the nanoparticles raise the thermal conductivity of the medium increasing its ability to absorb more heat which enhances the system efficiency. Therefore, using this medium may offer a great advantage to the HCPV system and regulates its temperature.

In light of the above discussion, it can be argued that the need for an efficient HCPV cooling system is of great importance. There is a lack of in-depth research on the application of nanofluids in high concentrator photovoltaic systems with multijunction solar cells from the theoretical and experimental points of view using uniform and non-uniform heat sources. Also, using experimentally measured thermal conductivity values for the pure water and nanofluids along with the computational modelling for more accuracy has not been studied to date. A limited number of heat sink configurations have been introduced in the literature, but finned minichannel and serpentine-based heat sinks have not yet been investigated.

Therefore, investigating these techniques will be an important contribution to the CPV field. It is also notable that the temperature distribution in the focal spot of the Fresnel lens has not been experimentally studied yet along with the thermal and electrical performance of the HCPV system in case of any misalignment occurs between the receiver and the lens.

Also, the literature review shows a lack of experimental research on the use of optical filters especially with Fresnel lens-based systems as most of the work conducted through the literature was theoretical. Therefore, an experimental investigation on the applicability of using optical filters as a cooling method will be an important contribution to the CPV temperature regulation systems. Therefore, to understand each of the previously mentioned methods, it is important to conduct a full study that includes both theoretical and experimental investigations which will be introduced by this research.

Chapter 3
Instruments, materials, and methods

3.1 Introduction

This chapter provides a comprehensive description of the instruments, materials, and software utilised throughout the present work. A list of the key equipment employed during the experimental investigation is presented in section 3.2 providing a detailed description of each piece of equipment and its working characteristics. A number of these instruments were used to analyse the optical, thermal, and electrical properties of the materials. In section 3.3, a record of the most common laboratory materials related to solar cells and working fluids are introduced. Finally, the software packages that were adopted for the design and modelling of the current work are described in section 3.4.

3.2. Instruments

3.2.1 Spectrophotometer

For the measurement of the optical properties, a Perkin Elmer Lambda 1050 UV/Vis/NIR, USA spectrophotometer was used as presented in Figure 52. The instrument is able to evaluate the transmittance, absorptance, and reflectance of the materials for a wide range of wavelengths. The wavelengths vary between 175 nm and 3300 nm with a degree of accuracy that could reach as low as 0.5 nm [224]. The light source of the device comes from deuterium and tungsten halogen lamps. The working idea of the device depends on the passing light through many filters and a monochromator before reaching the sample which is placed in a sample holder. The measurements of the transmittance and absorptance are completed with regard to the air, unlike reflectance which is measured in respect of a calibrated reflective surface. This white surface could be Labsphere SRS-99-020 AS-01161-060 with wavelengths between 250 nm and 2500 nm and a reflectance of 99%. The maximum and minimum operating temperature ranges are 35 °C and 15 °C, respectively. The Perkin Elmer Lambda 1050 UV/Vis/NIR device used a PMT, InGaAs, and PbS 3-detector module.

Figure 52 Perkin Elmer Lambda 1050 UV/Vis/NIR spectrophotometer.

3.2.2 Solar Simulator

A WACOM super solar simulator (AAA+ WXS-210S-20, AM1.5G from Wacom Electric Co. Ltd., Japan), as shown in Figure 53a, was used as a source for high collimated illumination. The irradiance area dimensions are 300 mm × 300 mm, and the Xenon lamp is a 2000 W short arc with an angle of ±3°. The maximum solar intensity used in the experiment was 1000 W/m^2 constant irradiance, while the lowest solar intensity provided by this device reached 400 W/m^2. The solar intensity, non-uniformity, and instability at 1 sun are within ±2% and ±1% respectively at an air mass of 1.5G [225]. The device is working on a three-phase AC 15A, 50/60 Hz, 200 V with an error of ±10% that is connected to the device as shown in Figure 53b. To maintain an appropriate working temperature for the solar simulator, the device is supplied by an exhaust cooling fan for the lamp which is the source of heat. To control the solar irradiance from the solar simulator, the instrument is provided with a GmbH Helicon device [226]. This device is able to control the lamp intensity by using the Helicon software. The solar spectrum given by the solar simulator in comparison with the AM1.5 irradiance is introduced in Figure 53c for wavelengths of 300 nm to 2000 nm.

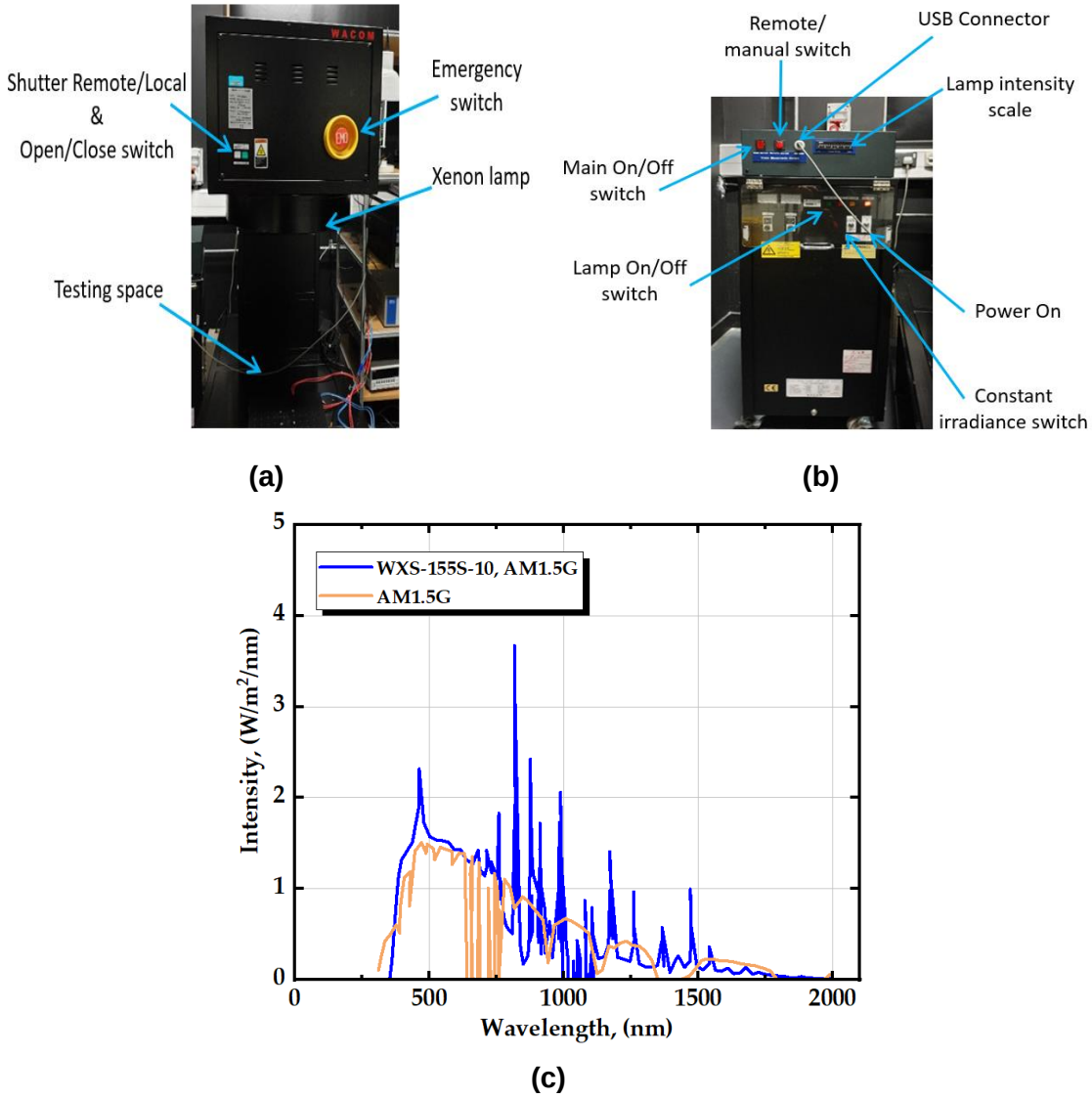

Figure 53 (a) WACOM solar simulator, (b) simulator power unit, (c) solar spectrum of the WACOM solar simulator for AM1.5 spectrum and AM1.5 irradiance.

3.2.3 I-V Curve Tracer

An EKO I-V curve tracer (Figure 54a) was used to measure the current and voltage of single and multijunction solar cells. This was achieved by varying the electrical load by sweeping the current and voltage values. The device is connected to both the solar simulator and the PC. The software used to complete the measurement is MP-160i as shown in (Figure 54b). Through the software, the rated current and voltage of the measured solar cell were inputted to obtain the I-V curve of the tested solar cell [227]. Other values can be obtained by using the software such as open circuit voltage, short circuit current, fill factor and maximum power. Table 6 introduces some important characteristics of this device.

(a) **(b)**

Figure 54 (a) EKO I-V curve tracer, (b) MP-160i software interface for MJ solar cell.

Table 6 Characteristics of EKO I-V curve tracer [227].

Variable	Value	Unit
Input current	10	A
Input voltage	300	V
Input power	300	W
Accuracy	±0.5%	

3.2.4 Thermal Conductivity Meter

For the measurement of the fluids' thermal conductivity, a LAMBDA 01/L thermal conductivity measuring system from Flucon Fluid control GmbH was employed [228]. The measuring method is based on transient hot wire theory. The system consists of the main unit which is connected to a probe as shown in Figure 55a. The probe is contained in a vessel with a capacity of 40 ml of the sample as presented in Figure 55b. The probe is attached to a temperature sensor for measuring the temperature of the fluid and a fine wire for measuring the thermal conductivity of the medium. In order to heat the vessel which contains the fluid inside, a temperature control system can be used, or a water bath (MultiTemp III) as shown in Figure 55c. The system's characteristics and details are introduced in Table 7.

(a) **(b)**

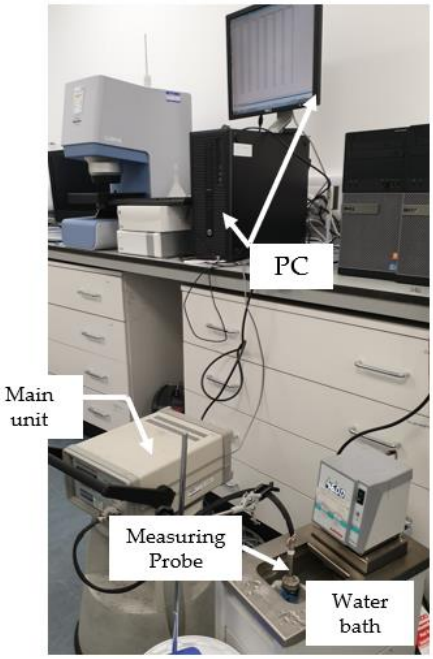

(c)

Figure 55 (a) Lambda thermal conductivity meter [228]*, (b) thermal conductivity Prob.* [228]*, (c) experimental setup used for measuring the thermal conductivity.*

Table 7 Characteristics of LAMBDA thermal conductivity meter [228]*.*

Parameter	**Value**	**Unit**
Sample vessel diameter	36	mm
Sample vessel length	100	mm
Temperature range	–50 to 300	°C
Temperature measurement	PT100	
Temperature accuracy	±0.1	°C
Thermal conductivity range	10–2000	W/m.K
Measurement accuracy	±1%	

3.2.5 Water Bath

A MultiTemp III water bath from Amersham Biosciences (Figure 56) was utilised to provide the heating and cooling requirements for the experimental setup with a bath volume of 3 litters [229]. The details and characteristics are introduced in Table 8.

Figure 56 MultiTemp III water bath.

Table 8 MultiTemp III Water bath characteristics.

Parameter	**Value**	**Unit**
Temperature range	-10 to 90	°C
Temperature accuracy	<±0.1	°C
Heating capacity	800	W
Cooling capacity	265	W

3.2.6 Power supply unit

For the power supply to both the pump and the heater, a TTi-EX354RD dual power supply (Figure 57) was used throughout the experiment. A maximum power output of 280 W can be delivered with a voltage output range of 0 to 35 V with an accuracy of ±0.3% and current output varies from 0 to 4 A with an accuracy of ±0.6% [230].

Figure 57 TTi-EX354RD dual power supply-280 W.

3.2.7 Thermocouple welding instrument

For fine wire thermocouple welding, a LAB FACILITY instrument (Figure 58) was utilised. The maximum power supply varies between 110 to 120 Vac.

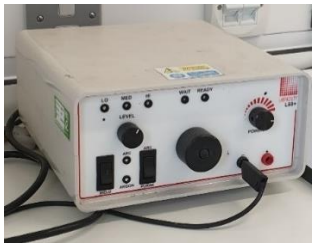

Figure 58 Lab facility thermocouple welder.

3.2.8 Soldering station

A Weller soldering station-WD 1000 (Figure 59) with a 120 V power unit was exploited for soldering the solar cells' electrical terminals.

Figure 59 Weller soldering station.

3.2.9 Magnetic stirrer

For providing a sufficient mixing for the nanofluids, a Stuart hotplate magnetic stirrer (Figure 60) was provided for that function. The mixing was completed with the help of mixer stir bars. The maximum heating temperature of this instrument is 325 °C and the stirrer speed is in the range between 100 and 2000 rpm [231].

Figure 60 Stuart Magnetic Stirrer.

3.2.10 Ultrasonicator

The ultrasonication process for nanofluids was used in order to ensure enough mixing for the nanofluids used. This was accomplished using a Hilsonic ultrasonicator cleaner (Figure 61) for 30 minutes. This process can be classified as an indirect mixing process as the mixture of nanoparticles and base fluid is kept inside a vessel which is immersed into a bath. Through this bath, the ultrasonic pulsations are transferred.

Figure 61 Hilsonic ultrasonicator cleaner.

3.2.11 Pump

A peristaltic pump is used to pump the fluid through the experimental setup as introduced in Figure 62a. This is type is a positive displacement pump and also known as a roller pump. The fluid is confined in an elastic tube inside the pump casing as shown in the schematic diagram in Figure 62b. The pump is supplied with 3 roller rotors and the gear motor has a maximum voltage and current of 12 V and 1.5 A, respectively [232]. The maximum flow rate to be handled is 0.562 L/min. The power input to the pump is controlled by using the DC power supply and the pump is grounded for electrical safety. There are two types of tube materials used with the pump: verderprene and silicon.

(a) **(b)**

Figure 62 (a) VERDERFLEX peristaltic pump contained within a case manufactured in ESI workshop, (b) schematic diagram of the working idea of the peristaltic pump [233].

3.2.12 Flow meter

For flow rate measurements, a Parker variable area flow meter (Figure 63) was utilised throughout the experiment. The measuring range varies between 0.07 L/min to 0.55 L/min. The accuracy of the flow meter is ±2%, while the repeatability limit is within ±1% as detailed by the manufacturer [234]. Furthermore, to verify the measurement accuracy using the flow meter, it was calibrated with a glass beaker and a stopwatch before the start of the experiments. The maximum difference between the two methods was less than 4.3%.

Figure 63 Parker variable area flow meter.

3.2.13 Temperature measurements

Temperature measurement methods can be classified into contact and contactless methods. The contact method is conducted by using thermocouples whereas the contactless method uses Infrared thermography. Thermocouples are usually made from two different conducting materials which are combined at one end. Due to the difference in temperature between the two junctions of the thermocouples, a thermoelectric effect is created. There are several types of

thermocouples: K, T, E, J, N, S, R, and B each type varying in terms of characteristics and working limit. On the other hand, infrared thermography is considered a non-contact real-time technique where the device is not in contact with the heated or cooled surfaces [235]. By using an infrared thermal camera, two-dimensional thermal images can be produced with the minimum and maximum temperatures of the captured scene.

3.2.13.1 Temperature loggers and thermocouples

Two temperature loggers were used throughout the experimental investigation: the Pico logger (Figure 64a) (USB-TC-08) with temperature range varying from –270 °C to 1820 °C with an accuracy of the measurements of ±0.2% [236] and the EXTECH temperature meter (Figure 64b) with temperature range (–100 °C to 1300 °C) and accuracy of ±0.4% [237]. These loggers work with several types of thermocouples, for example: B, E, J, K, N, R, S, and T. The thermocouples used in this research are K as it has a suitable working range (–75 °C to 250 °C). Different sizes were used: 0.075 mm, 0.2 mm, and 1mm.

For the inlet and outlet fluid temperatures size 1 mm was selected and for the solar cell and heater surfaces size 0.2 mm was chosen. On the other hand, for measuring the temperature between the heat sink and the CPV assembly, size 0.075 mm was preferred. All these thermocouples were calibrated before starting the measurement at water freezing (0 °C) and boiling (100 °C) temperatures. The accuracy of the calibration was ±0.2 °C which is satisfactory to be used in the experimental investigation.

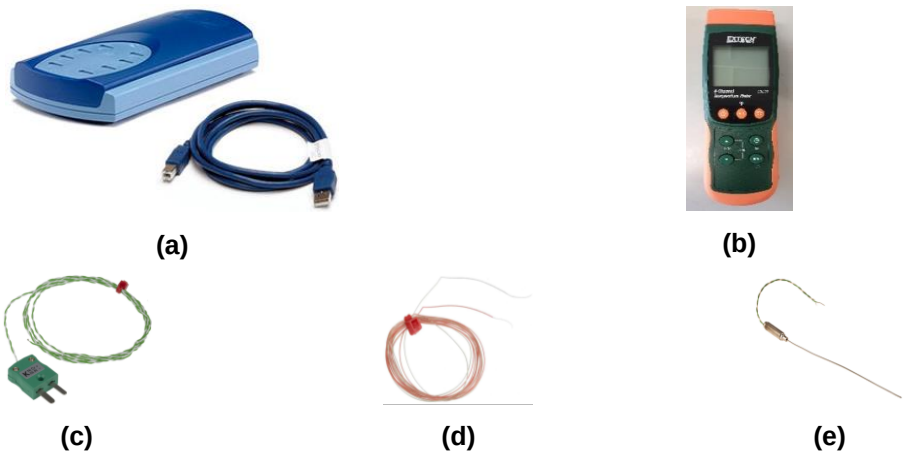

Figure 64 (a) Pico temperature logger, (b) EXTECH temperature meter, (c) K-type thermocouple 0.2 mm, (d) K-type thermocouple 0.075 mm, (e) K-type thermocouple 1 mm.

3.2.13.2 Infrared thermal camera

An FLIR infrared thermal camera-T425 (Figure 65) was used to capture thermal images for the experiments by creating 2D pictures. Several input details should be entered in the camera such as emissivity, distance from the object, and ambient temperature. The working temperature range varies between −20 °C to 1200 °C and the resolution is 320×240 pixels both of which offer great potential to show sufficient details of the scene with an accuracy of ±2.0% [238].

Figure 65 FLIR IR camera.

3.3. Materials

3.3.1 Multijunction solar cell

The solar cell used in this research is a triple-junction solar cell manufactured by AZUR Space. The cell consists of three layers (GaInP/GaInAs/Ge) which are stacked above each other. The thickness of the MJ solar cell is 190 µm with an active area of 100 mm^2. The cell's maximum efficiency achieved at 25 °C and concentration ratio of 500 suns is 39%. The effect of concentration ratio and temperature on the cell's performance is introduced in Figure 66.

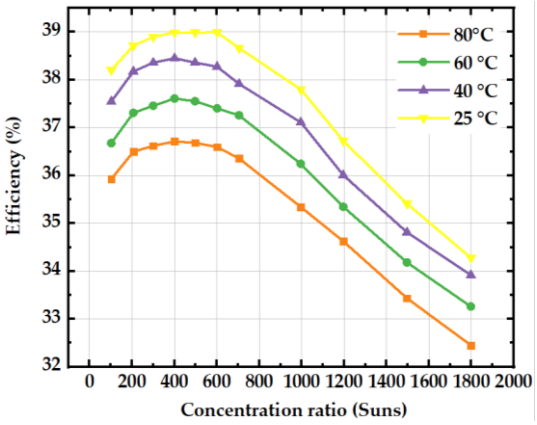

Figure 66 AZUR Space MJ solar cell Efficiency curve as a function of concentration ratio and temperature [239].

3.3.2 CPV assembly

The CPV assembly used in this research is introduced in Figure 67. The (GaInP/GaInAs/Ge) solar cell is mounted on a direct bonded copper (DBC). The DBC consists of two layers of copper with a thickness of 0.25 mm and a layer of ceramic that is sandwiched between them. This layer has a thickness of 0.32 mm. Two parallel 10 A silicon Schottky diodes are mounted on the upper copper layer.

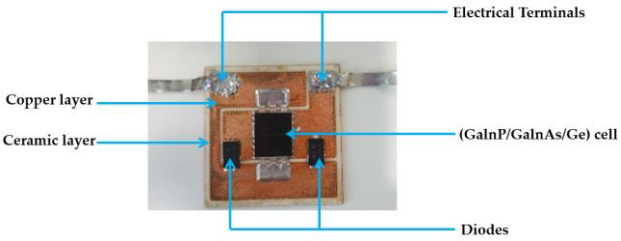

Figure 67 AZUR SPACE CPV assembly.

3.3.3 Silicon solar cell

A single-junction silicon solar cell was used in this research for the investigation of the effectiveness of the infrared filter. The dimensions of the silicon solar cell used is 5.1 cm × 5.1 cm as introduced in Figure 68. The maximum efficiency, power output, current, and voltage of this cell are 17%, 0.43 W, 0.86 A, and 0.5 V, respectively [240].

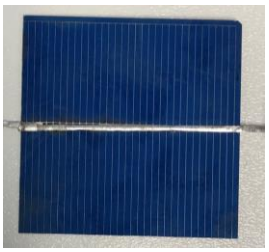

Figure 68 Single junction silicon solar cell.

3.3.4 Cooling mount

For providing cooling facilities to the solar cells through the experimental investigation, a Temperature Stabilised Vacuum Chuck Controller-Bentham VC-TE-20 (Figure 69) was utilised for extracting the heat from the bottom surface of the solar cell. The cooling mount dimensions are 20 cm × 20 cm × 1.5 cm. It can provide a wide range of cooling temperatures (the tested water temperature varies between 10 °C to 25 °C).

Figure 69 Bentham VC-TE-20 cooling mount.

3.3.5 Electric power resistor

A power resistor (10 mm × 10 mm) (Figure 70) to simulate the heat flux on the surface of the solar cell was employed. The maximum power output from this resistor is 35 W as provided by Bourns [241] and the power was supplied through the DC power supply by varying the current and the voltage to give the desired power according to Eq. 3.1. The tested power output fluctuates between 5 W to 35 W.

$$P = I\,V \tag{3.1}$$

Figure 70 Thick film heater.

3.3.6 Heat sink paste

To attach the power resistor and MJ solar cell to the heat sink, a metal oxide paste was applied. The function of this paste is also to provide electrical isolation. The thermal conductivity of the grease is 2.9 W/m.K and the working temperature range varies between –40 °C and 200 °C [242].

3.3.7 Fresnel lens

A non-chromatic Orafol Fresnel lens (Figure 71) made from silicon on glass (SoG) was utilised for concentrating the solar irradiance. The given dimensions of the SoG lens are 23 cm by 23 cm which is the inlet aperture area of the light and thickness of 3.5 mm. SOG Fresnel lenses are typically manufactured by moulding a thin silicon layer onto a glass plate [34].

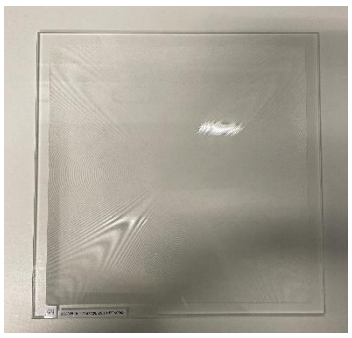

Figure 71 Silicon on glass Fresnel lens.

3.3.8 Infrared filter

A KG1 Infrared optical filter from Bentham was utilised throughout the investigation (Figure 72). The heat absorbing filter is 5.1 cm × 5.1 cm made from glass and is working as an IR cut-off filter. The filter provides high transmittance in the visible light range, while attenuates the IR wavelengths from passing to the cell.

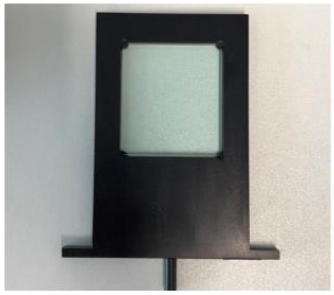

Figure 72 IR optical filter.

3.3.9 Nanofluids

The tested nanofluids were aluminium oxide with water (Al_2O_3/water) and silicon dioxide with water (SiO_2/water). These nanofluids were obtained from Sigma Aldrich at high concentrations (20 wt.% and 40 wt.% in H_2O, respectively) [243,244]. They were diluted to give different concentrations. To ensure enough mixing, stirring on a hot plate magnetic stirrer was carried out followed by ultrasonication for 30 min.

3.4. Methods

3.4.1 CAD Tools

Two applications were employed in this research. For illustrations and 2D drawings, AutoCAD software was used, while for the simulations and 3D models Solidworks software was selected. Solidworks offers a simple user interface for drawing the 3D designs in comparison with the geometry interface offered by COMSOL-Multiphysics software. In addition, the lengths and angles of the specified geometry can be easily modified. The software can be linked to COMSOL-Multiphysics through a live link which provides flexibility to modify different drawing parameters that can be used during the parametric study.

3.4.2 COMSOL-Multiphysics software

COMSOL-Multiphysics software is a program that is based on the finite element method (FEM) to solve a range of physics problems. The conjugated heat transfer and fluid flow interfaces have been exploited for modelling the high concentrator photovoltaic thermal systems (HCPVT) using 3D geometries. Therefore, different fluid parameters and heat transfer can be analysed. In order to solve the specified problem, geometry should be designed and drawn using the software itself or with the aid of external software such as AutoCAD and Solidworks. Each volume should be defined as either solid or fluid along with its material type.

The boundary conditions step should be defined to solve the partial differential equations of the heat transfer and fluid flow. Following this, a suitable mesh type and size should be allocated for each physics. Through this software, the user is able to choose the type of the study, for example, stationary, time-dependent, or parametric sweep…. etc. The equations are solved iteratively using an iterative solver called the Generalised Minimal Residual (GMRES). The residuals of the mass and energy equations should be less than the relative tolerance (10^{-3}) that was set in the solver. To have an appropriate representation of the results a post-processing step is very important. Different planes and cross-sections for the temperature, velocity distribution, and other parameters can then be produced.

3.5 Experimental errors

The difference between the measured and true values is referred to as experimental error. In terms of the solar simulator, the solar intensity of the device is within ±2% at 1 sun and air mass of 1.5G, while the accuracy of the current-voltage curve tracer is within ±0.5%. Another key parameter is thermal conductivity which is an important thermophysical property that measures the ability of the fluid to conduct heat. The accuracy of the lambda instrument as reported by the manufacturer is within ±1%. The thermal conductivity measurements were repeated three times which gave an accuracy of ±1.5%. The temperature accuracy of the water bath is <±0.1 °C, while it is ±2% in the case of the flow meter with a repeatability limit of ±1%.

Furthermore, to verify the measurement accuracy using the flow meter, it was calibrated with a glass beaker and a stopwatch before the start of the experiments. The maximum difference between the two methods was less than 4.3%. In terms of the temperature measurements, before starting the measurement, both the thermocouples and the IR camera were calibrated with two temperatures points; boiling water (100 °C) and liquid-ice water (0 °C). Against a mercury thermometer, they gave differences of ± 0.2 °C and ± 2.0 °C, respectively. A clear sight from the IR camera to the setup was guaranteed with an angle of incidence of 30^{o} between the camera and the perpendicular to the measured surface.

3.6. Conclusion

A list of different types of equipment, materials, and software packages that were employed in this study have been introduced in this chapter. The instruments were used for the transmittance, thermal conductivity, and electrical features measurements were presented, including an overview of their working characteristics of each of them. In addition, each component of the experimental setup that was used through the investigation was described in more detail. Also, the methods that were employed for the temperatures and flow rate measurements were described. The characteristics of both the multijunction and silicon solar cells were detailed as well as the dimensions and the properties of the Fresnel lens. In terms of designing and modelling the current work, several software packages were utilised and described in the final section of the chapter.

Chapter 4
Optical, thermal, and electrical characterisation of materials associated with concentrating photovoltaics

4.1 Introduction

The aim of this chapter is to provide a detailed experimental investigation of the optical, thermal, and electrical performance of the materials used in this research to ensure the system performs adequately. The optical characterisation (Section 4.2) was carried out in terms of the transmittance efficiency of the Fresnel lens and the infrared filter, while the thermal characterisation (Section 4.3) included an investigation of the thermal conductivity of the considered base fluid and nanofluids. Finally, an electrical analysis (Section 4.4) was undertaken with reference to current, voltage, and produced power.

4.2 Optical characterisation

In order to understand the behaviour of an optical system, optical characterisation should take place. The optical properties of an object reveal information about how much light can be transmitted, reflected, and absorbed through it. Therefore, before starting the experimental measurements, measurements of both the Fresnel (FR) lens and infrared (IR) filter transmittance were conducted. The transmittance measurements were completed by using the spectrophotometer under a wide range of wavelengths. The transmittance can be defined as the ratio between the light escaped through the optical element to the light on the surface of the object.

4.2.1 Characterisation of the Fresnel lens

To analyse the system performance more accurately, the transmittance measurement of the SoG FR Lens was undertaken. The measurement was carried out using a PerkinElmer LAMBDA 1050+ UV/Vis/NIR spectrophotometer for the wavelength between 250 nm and 2000 nm. The values of the SoG FR Lens transmittance along with solar spectral irradiance with the wavelength are

plotted in Figure 73. It is important to note that a large portion of the solar irradiance can pass through the FR lens for the corresponding wavelengths. Higher values of transmittance were observed through the measured wavelengths as the average total transmittance reached about 91%.

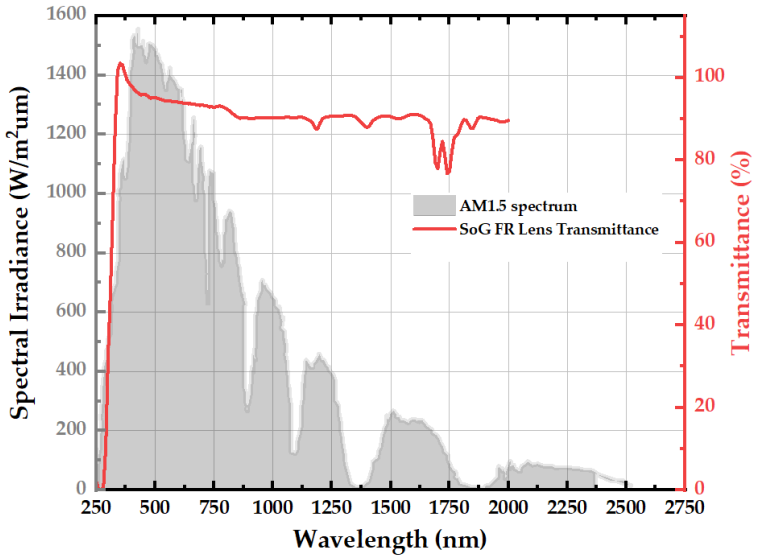

Figure 73 Variation of the SoG FR lens transmittance and solar spectral irradiance with the wavelength.

4.2.2 Characterisation of the Infrared filter

The function of the IR filter in this research was to work as an interference filter as it blocks the unwanted wavelengths which cause heating and damage to the cell. The IR filter transmittance measurement and optical density calculations against the wavelength are introduced in Figure 74. The measurements of the transmittance were undertaken for the wavelength range between 250 to 2000 nm. As can be seen from the graph, the highest transmittance value (85%) was observed between wavelengths 300 nm and 550 nm, while the average transmittance was calculated as 19% over the whole range of the wavelength. The optical density of the IR filter was calculated and plotted against the wavelength as shown in Figure 74b. It can be seen that the maximum calculated optical density value reached 1.4, while an average optical density of 0.73 is estimated from wavelength of 940 nm to 2000 nm which indicates a high ability of the IR filter to attenuate the irradiance in the IR region.

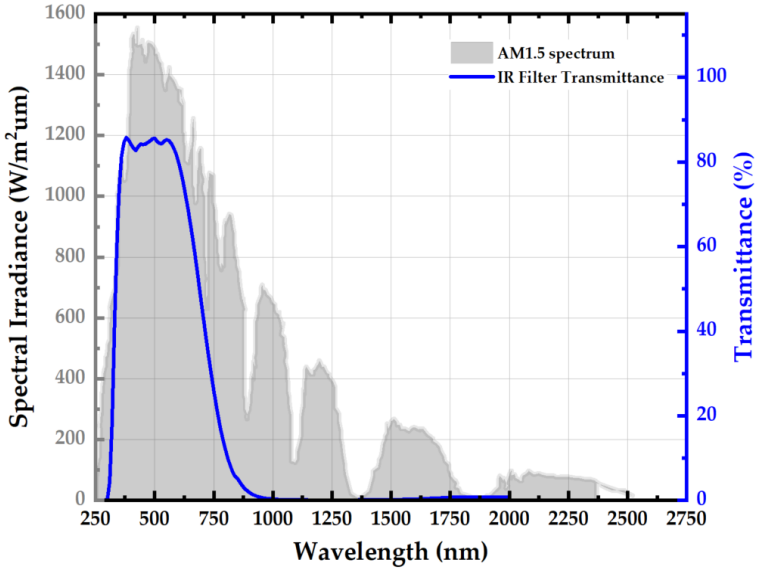

(a)

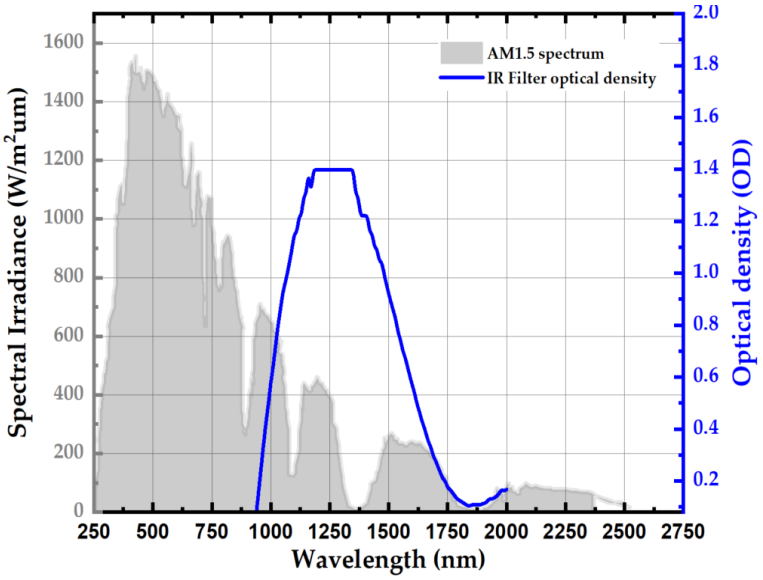

(b)

Figure 74 Variation of the IR filter (a) transmittance and (b) optical density and solar spectral irradiance with the wavelength.

4.3 Thermal characterisation

The objective of carrying out a thermal characterisation for the working media was to assess their thermal conductivity which is an important thermophysical property in the heat extraction mechanism. Thermal conductivity measures the ability of the medium to conduct heat and can be defined as the ratio between the heat transferred through a unit thickness due to the change in a temperature gradient. The measurements were undertaken using a Lambda 01/L thermal conductivity meter for the distilled water and nanofluids. The tested nanofluids' samples are Al_2O_3/water and SiO_2/water which were purchased from Sigma

Aldrich as reported in the previous section. To date, the thermal conductivity values of these nanofluids have not been reported. Therefore, the measurements of these nanofluids will be discussed in the next section to confirm their ability to conduct heat. All the measurements have been repeated three times and the uncertainty of the measurements did not exceed ±1.5%.

4.3.1 Thermal conductivity measurements of distilled water

The thermal conductivity measurements of the distilled water were carried out as a function of temperature. This is to ensure the accuracy of the thermal conductivity meter before testing the nanofluids. The tested temperature range varied between 25 °C to 45 °C with incremental steps of 5 °C. As shown in Figure 75, there was a notable enhancement in the thermal conductivity by 6.6% as the fluid temperature rose from 25 °C to 45 °C. This can be attributed to the enhancement of the collision of the atoms which improves the heat transport criteria.

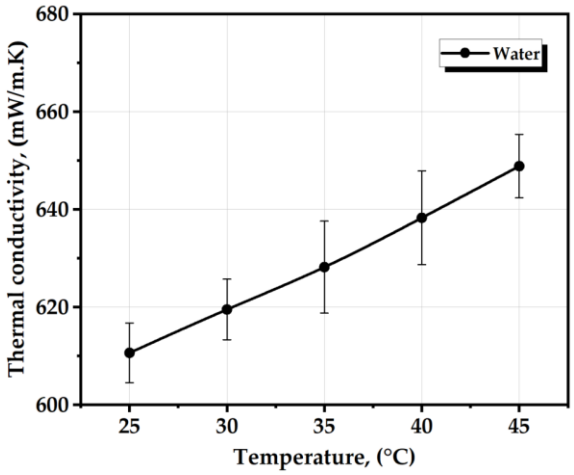

Figure 75 Variation of the experimentally measured thermal conductivity of water with temperature.

4.3.2 Thermal conductivity measurements of aluminium oxide/water

Thermal conductivity measurements of Al_2O_3/water nanofluid at volume fractions of 2.5% and 5% with the change in temperature are introduced in Figure 76. It is significant that the increase in the volume fraction from 2.5% to 5% leads to a noticeable enhancement in the experimentally measured thermal conductivity. For a volume fraction of 2.5%, the thermal conductivity increased from 655.5 mW/m.K to 692 mW/m.K which corresponds to temperatures 25 °C and 45 °C, respectively. This means that the nanofluid conductivity improved by 5.6% due to

the increase in the temperature. Similar behaviour was noticed at a volume fraction of 5% as the highest measured thermal conductivity reached as high as 750 mW/m.K, while the lowest value (706 mW/m.K) was observed at 25 °C. The improvement in the measured quantities at a high-volume fraction was due to the increase in the quantity metallic nanoparticles which helps to transport more heat through the base fluid. Also, in comparison with the water values from the previous section, adding nanoparticles at a volume fraction of 5% enhanced the thermal conductivity by 15.5% at a temperature of 45 °C.

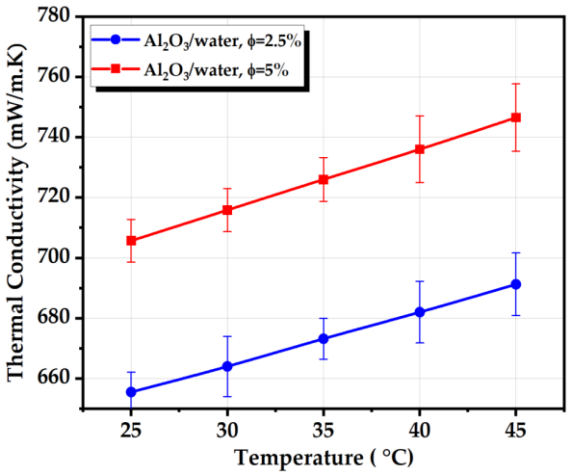

Figure 76 Variation of the experimentally measured thermal conductivity of aluminium oxide/water with temperature.

4.3.3 Thermal conductivity measurements of silicon dioxide/water

Figure 77 presents the experimental thermal conductivity measurement of the SiO_2/water nanofluid at volume fractions 2.5 and 5% for a temperature range from 25 °C to 45 °C. By increasing the temperature and volume fraction, a large augmentation of the thermal conductivity was noticed as it increased by 3.1% by increasing the volume fraction to 5%. The highest thermal conductivity was 693 mW/m.K at a temperature of 45 °C and a concentration of 5%. Since the silicon dioxide nanoparticles have lower thermal conductivity values in comparison with the aluminium oxide nanoparticles, the measured thermal conductivity of the silicon dioxide nanofluids was lower. However, adding silicon dioxide nanoparticles at a concentration of 5% enhanced the water conductivity by 7%.

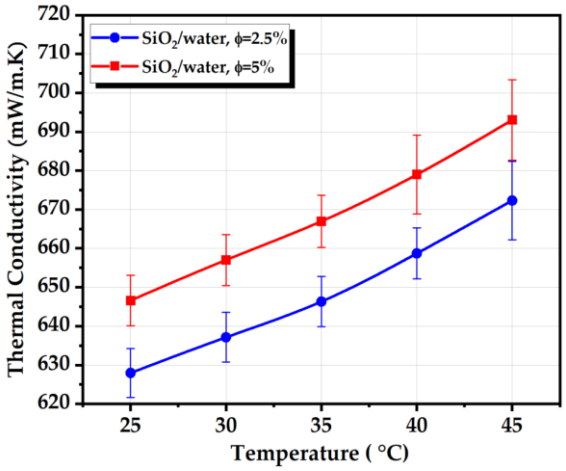

Figure 77 Variation of the experimentally measured thermal conductivity of silicon dioxide/water with temperature.

4.3.4 Comparison with the theoretical model

The measured thermal conductivity values were compared with the Hamilton and Crosser relation [245] as it is expressed by:

$$k_{nf}=\left(\frac{k_{np}+(n-1)\,k_{bf}-(n-1)\,\varphi\,(k_{bf}-k_{np})}{k_{np}+(n-1)\,k_{bf}+\varphi\,(k_{bf}-k_{np})}\right)k_{bf} \qquad (4.1)$$

where k_{nf}, k_{np}, and k_{bf} are the thermal conductivity of the nanofluid, nanoparticles, and base fluid, while n and φ are the shape factor and volume fraction, respectively. Figure 78 a and b show the comparison between the experimentally obtained data and the calculated values for both Al_2O_3/water and SiO_2/water nanofluids, respectively. The comparison was carried out at different temperatures and volume fractions. Although the experimental thermal conductivity values for Al_2O_3/water are in good agreement with the theoretical results, the measured thermal conductivity of the SiO_2/water showed higher enhancement in comparison with the theoretical values especially at high temperatures. In addition, it is significant that the thermal conductivity increases markedly with the temperature at different concentrations which is in agreement with the literature.

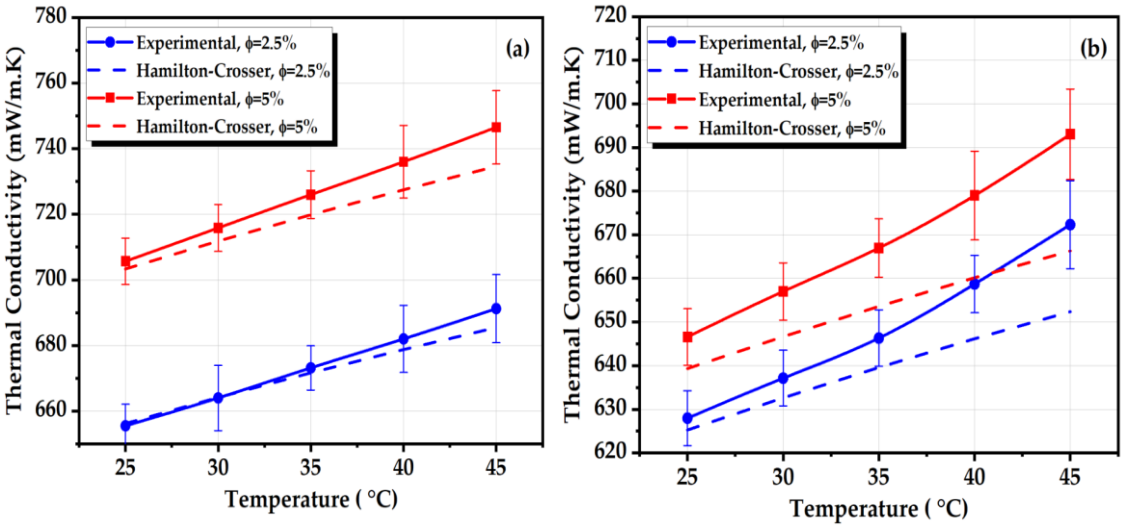

Figure 78 Comparison between the measured thermal conductivity and the results calculated the by Hamilton-Crosser model at different temperatures and volume fractions for (a) Al_2O_3/water (b) SiO_2/water respectively.

4.4. Electrical characterisation

To evaluate the electrical performance of the measured cells, a preliminary investigation was carried out for both the multijunction (MJ) solar cell assembly and silicon (Si) solar cell. The test was conducted under the solar intensity of 1000 W/m^2 using the solar simulator and the I-V tracer. The resulting values from the test were the short circuit current (I_{sc}), open-circuit voltage (V_{oc}), maximum power (P_{MPP}), maximum power current (I_{MPP}) , maximum power voltage (V_{MPP}) and fill factor (F.F.).

4.4.1 Multijunction solar cell assembly characterisation

One of the advantages of using the MJ solar cell is the ability to absorb a wide range of solar irradiance as shown in Figure 79. The absorbance band for the MJ solar cell is from ≈300 nm to 1800 nm. The photons energy with shorter wavelengths is absorbed in the upper layer, while the longer wavelength is transmitted to the lower layer. This enables the absorption of a wide range of incident solar irradiance on the cell, which increases its conversion efficiency.

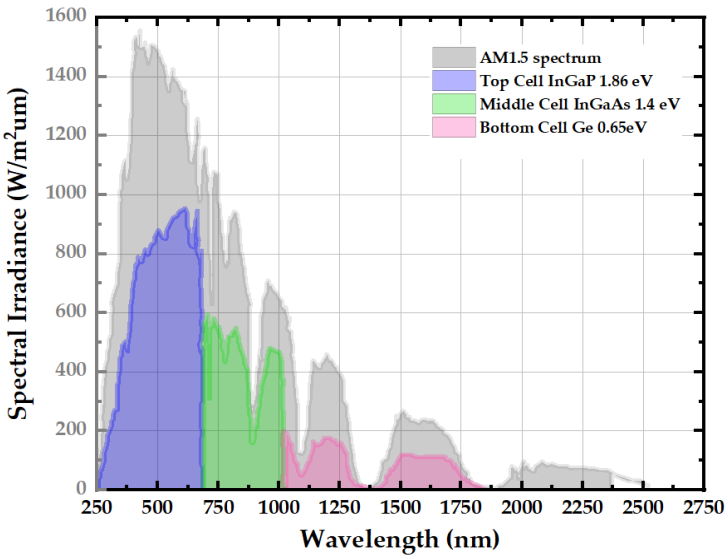

Figure 79 Variation of both Multijunction solar cell spectrum response and solar spectral irradiance with the wavelength.

Figure 80 a and b show the variations of both the current and power of the MJ solar cell with the voltage under one sun. The short circuit current had a value of 12.1263 mA while the open-circuit voltage reached 2084 mV. Also, the calculated maximum power produced by the cell at this solar intensity as shown from the graph and Table 9 is 15.8 mW. On the other hand, the fill factor reached as low as 0.622 which can be predicted from Figure 80 a .

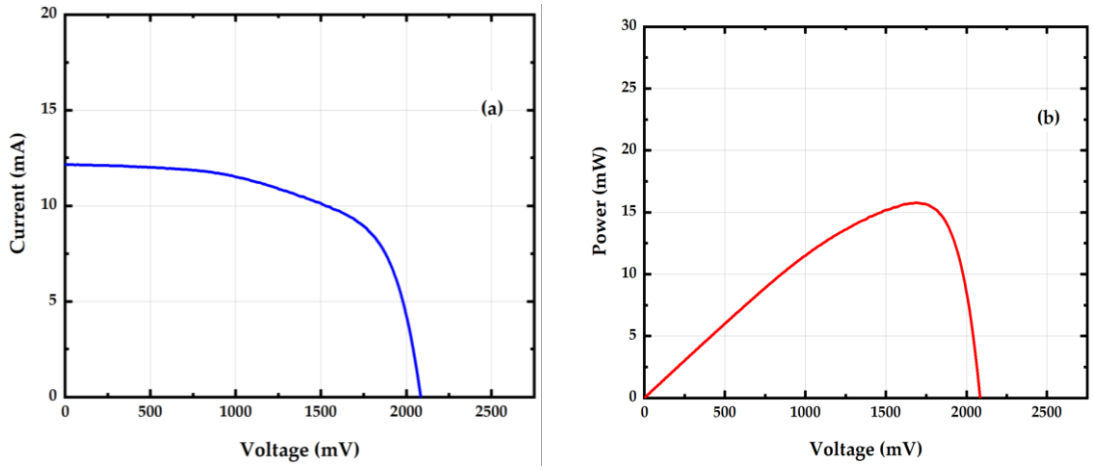

Figure 80 Variation of (a) current and (b) power with voltage for MJ solar cell under one sun.

Table 9 Tested MJ solar cell electrical characteristics under one sun.

Variable	Value	Unit
I_{sc}	12.163	mA
V_{oc}	2084.392	mV
P_{MPP}	15.757	mW
I_{MPP}	9.297	mA
V_{MPP}	1694.803	mV
F.F.	0.622	

4.4.2 Silicon solar cell characterisation

In contrast with the MJ solar cell, the absorbance range of the Si solar cell varies between ≈300 nm to 1100 nm (Figure 81). This allows the absorbance of a limited portion of the high spectral irradiance which limits its efficiency in comparison to the MJ solar cell.

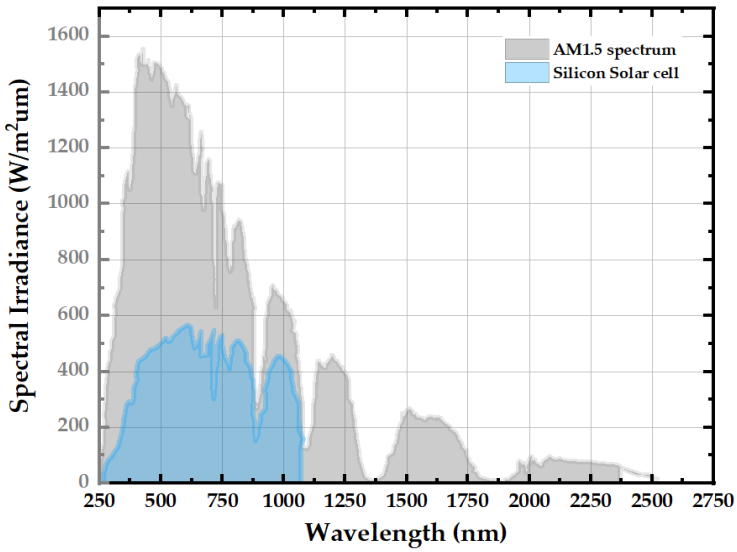

Figure 81 Variation of both Si solar cell spectrum response and solar spectral irradiance with the wavelength.

Measurements of both the I-V and P-V curves of the Si solar cell are introduced in Figure 82. A good fill factor was noticed during the measurement reaching 0.735 as introduced in Table 10 in comparison to the measured MJ solar cell. This is related to the fact that the MJ solar cell has an optimum performance under a concentration of 500 suns in comparison with the Si solar cell. Both the short circuit current and the open-circuit voltage were 958.167 mA and 612.053 mV, respectively. A lower value of open-circuit voltage was noticed in comparison to the MJ solar cell which can be attributed to the high series resistance which

causes a huge drop in the voltage. The maximum power reached as high as 430.85 mW, which is about 28 times higher than that of the MJ cell. On the other hand, the maximum power current and voltage reached 884.216 mA and 487.268 mV, respectively.

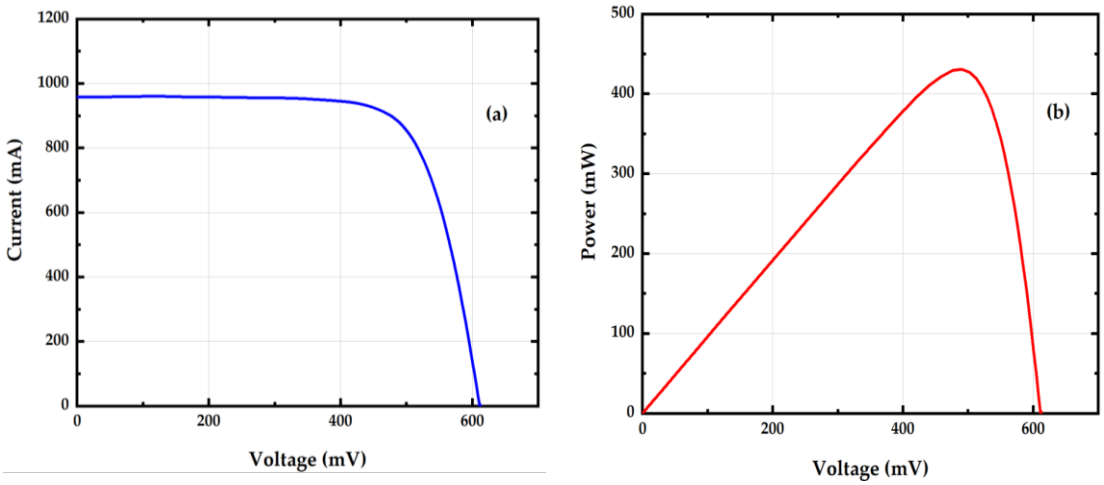

Figure 82 Variation of (a) current and (b) power with voltage for Si solar cell.

Table 10 Tested Si solar cell electrical characteristics.

Variable	Value	Unit
I_{sc}	958.167	mA
V_{oc}	612.053	mV
P_{MPP}	430.85	mW
I_{MPP}	884.216	mA
V_{MPP}	487.268	mV
F.F.	0.735	

4.5 Conclusion

A comprehensive evaluation of different materials properties was introduced in this chapter including an optical, thermal, and electrical experimental investigation. Firstly, in terms of optical properties, both the Fresnel lens and the infrared filter were examined using a spectrophotometer for transmittance efficiency measurements. The Fresnel lens had a high transmittance through a wavelength range from 300 nm to 2000 nm, except for two dips appearing at wavelengths of 1600 nm and 1750 nm. The average transmittance through the whole range was equal to 92%. In terms of the infrared filter, the measurement was undertaken from wavelengths from 250 nm to 2000 nm. A high optical

efficiency of about 85% was noticed from wavelengths 300 nm to 600 nm, while the average transmittance through the whole range was calculated to be 19%.

In addition, the thermal conductivity of the base fluid (distilled water), Al_2O_3/water, and SiO_2/water at different concentrations were demonstrated. The experimental measurements were carried out as a function of temperature and volume fraction. Overall, there was a significant enhancement in the measured thermal conductivity figures with an increase in temperature. In terms of water, the thermal conductivity increased by about 6.6% by increasing the temperature from 25 °C to 45 °C.

Regarding aluminium oxide/water, there was a notable enhancement with both the temperature and volume fraction as the thermal conductivity reached 750 mW/m.K. For silicon dioxide/water, the thermal conductivity reached 693 mW/m.K at a volume fraction of 5%. Good agreement between the Hamilton Crosser model and the measured values was observed especially at lower temperatures. At higher temperature values, the evaluated thermal conductivity of the SiO_2/water showed higher enhancement in comparison with the theoretical values. This can be attributed to the reason that the theoretical model does not depend on temperature.

Besides the optical and thermal characterisation, electrical evaluation of the electrical parameters of the MJ and Si solar cells were presented. The experimental measurements of the current, voltage, power and fill factor were tested under the solar intensity of 1 sun using the solar simulator and the I-V tracer. A higher fill factor and short circuit current were observed for the silicon solar cell in comparison with the MJ solar cell as the latter is designed for optimum performance at 500 suns. On the other hand, a lower open short circuit current was detected for the Si solar cell due to the high series resistance.

Chapter 5
Modelling of different heat sink configurations for concentrating photovoltaics system

5.1 Introduction

This chapter discusses the numerical modelling used in this research. This includes the physical models that will be studied in the subsequent chapter, in addition to their theoretical equations. The governing equations namely the partial differential equations of heat transfer and fluid flow and their boundary conditions are explained. In the second section, the thermophysical properties of the fluids used throughout the study are presented, while the last section introduces the grid independence tests and validations studies for the numerical modelling.

5.2 Mathematical approach

5.2.1 Physical models and theoretical analysis

Figure 83a presents a schematic diagram of the HCPV module which consists mainly of several Fresnel lenses which concentrate the incident solar irradiance on small MJ solar cells, while Figure 83b introduces the energy balance through the HCPVT system. Part of the total incident energy (Q_{in}) on the MJ solar cell is lost as optical losses ($Q_{opt,out}$) , while the remaining ($Q_{opt,in}$) is converted into two forms. The first portion is transformed into electrical power ($P_{sc,elec}$), and the rest is converted into waste heat ($Q_{sc,heat}$). This heat is removed by the coolant through the heat sink. The idea of using fins in the system is to allow more heat to be extracted. The MJ solar cell consists of three layers; germanium (Ge), indium gallium phosphide (GaInP), indium gallium arsenide (GaInAs). Their thermal properties and dimensions are presented in Table 11 and Table 12.

The temperature of the solar cell has been calculated by using the trial and error method [82,105,246]. This method is based on assuming the solar cell efficiency is equal to the reference efficiency in the first simulation. Then, after calculating the new cell temperature, new solar cell efficiency is obtained from Eq. 5.1 and inputted again into the software. This process is repeated until the difference between two consecutive iterations has reached ≤ 0.1 °C.

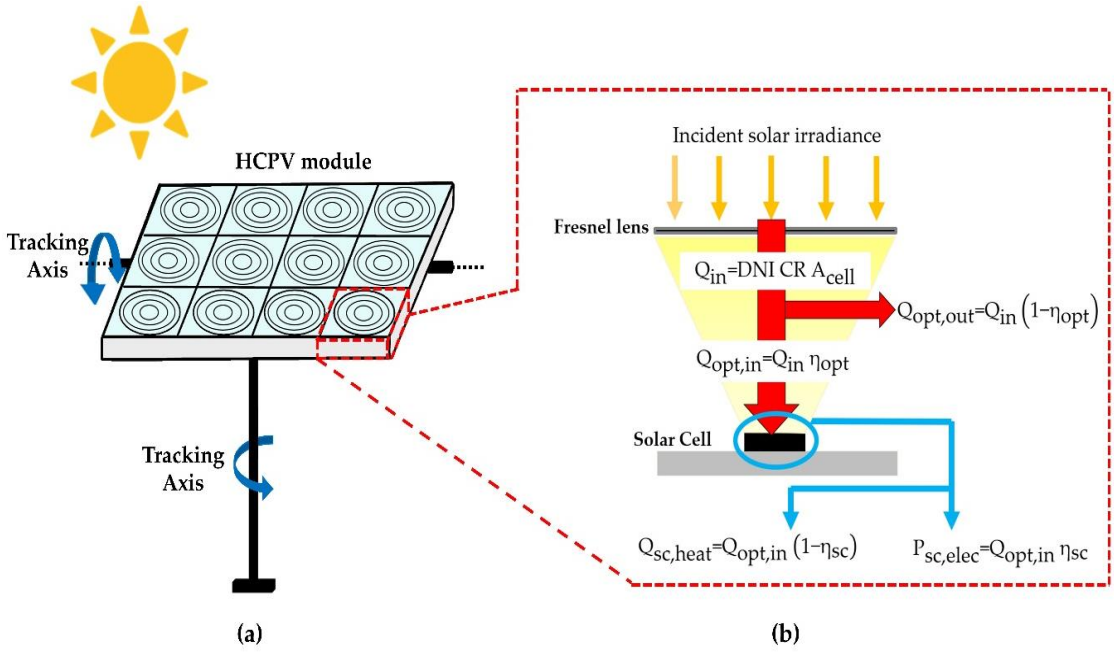

Figure 83 Schematic diagram of (a) the HCPV module and (b) the heat balance of the HCPV system.

$$\eta_{sc}=\eta_{ref}\left(1-\beta_{ref}\left(T_{sc}-T_{ref}\right)\right) \quad (5.1)$$

where β_{ref} is the temperature coefficient of the MJ solar cell and is equal to 0.047 %/K as provided by the manufacturer [7] and T_{ref} is the reference temperature of the solar cell which is equal to the ambient temperature 25 °C. The input heat, Q_{in}, to the system can be calculated from the following relation:

$$Q_{in}=DNI\ CR\ A_{cell} \quad (5.2)$$

Due to the optical losses, the actual heat incident on the solar cell can be calculated from the following relation:

$$Q_{opt,in}=Q_{in}\ \eta_{opt} \quad (5.3)$$

where η_{opt} is the optical efficiency of the system and is assumed to be 80% in the calculations [35,74]. The input optical power is converted into two types of energies, the first is the electrical power which can be calculated by the following relation:

$$P_{sc,elec}=Q_{opt,in}\ \eta_{sc} \quad (5.4)$$

The other is the waste heat to the finned mini-channel heat sink:

$$Q_{sc,heat}=Q_{opt,in}\left(1-\eta_{sc}\right) \quad (5.5)$$

The thermal energy to be carried by the fluid, Q_{th}, is equal to:

$$Q_{th}=\dot{m}\ c_{p,f}\left(T_{f,out}-T_{f,in}\right) \quad (5.6)$$

Hence, the thermal efficiency can be calculated thus:

$$\eta_{th}=\frac{Q_{th}}{Q_{opt,in}} \quad (5.7)$$

The pumping power of the fluid can be calculated from the following relation:

$$P_{pump}=\dot{V}\,\Delta p \quad (5.8)$$

Therefore, the useful electrical power produced from the system:

$$P_{useful,elec}=P_{sc,\ elec}-P_{pump} \quad (5.9)$$

The electrical efficiency of the system can be calculated as follows:

$$\eta_{elec}=\frac{P_{useful,elec}}{Q_{opt,in}} \quad (5.10)$$

Then, the overall efficiency of the HCPVT:

$$\eta_{overall}=\frac{Q_{th}+P_{useful,elec}}{Q_{in}} \quad (5.11)$$

Table 11 Dimensions of different layers of the HCPVT.

Number	Layer	Length (mm)	Width (mm)	Thickness (mm)
1	GaInP	10	10	0.07
1	GaInAs	10	10	0.07
1	Ge	10	10	0.07
2	Copper I	27	25	0.25
3	Ceramic	29	27	0.32
2	Copper II	29	27	0.25
4	Aluminium	29	27	6

Table 12 Material thermophysical properties of HCPVT [80,247].

Layer	Specific heat, c_p (J/kg.K)	Thermal conductivity, k (W/m.K)	Density, ρ (kg/m^3)	Emissivity, ε
GaInP	370	73	4470	0.9
GaInAs	550	65	5316	
Ge	320	60	5323	
Copper	385	400	8700	0.05
Ceramic	900	27	3900	0.75
Solder	150	50	9000	
Aluminium	900	160	2700	
SiO_2	765	1.4	2220	
Al_2O_3	745	40	3970	

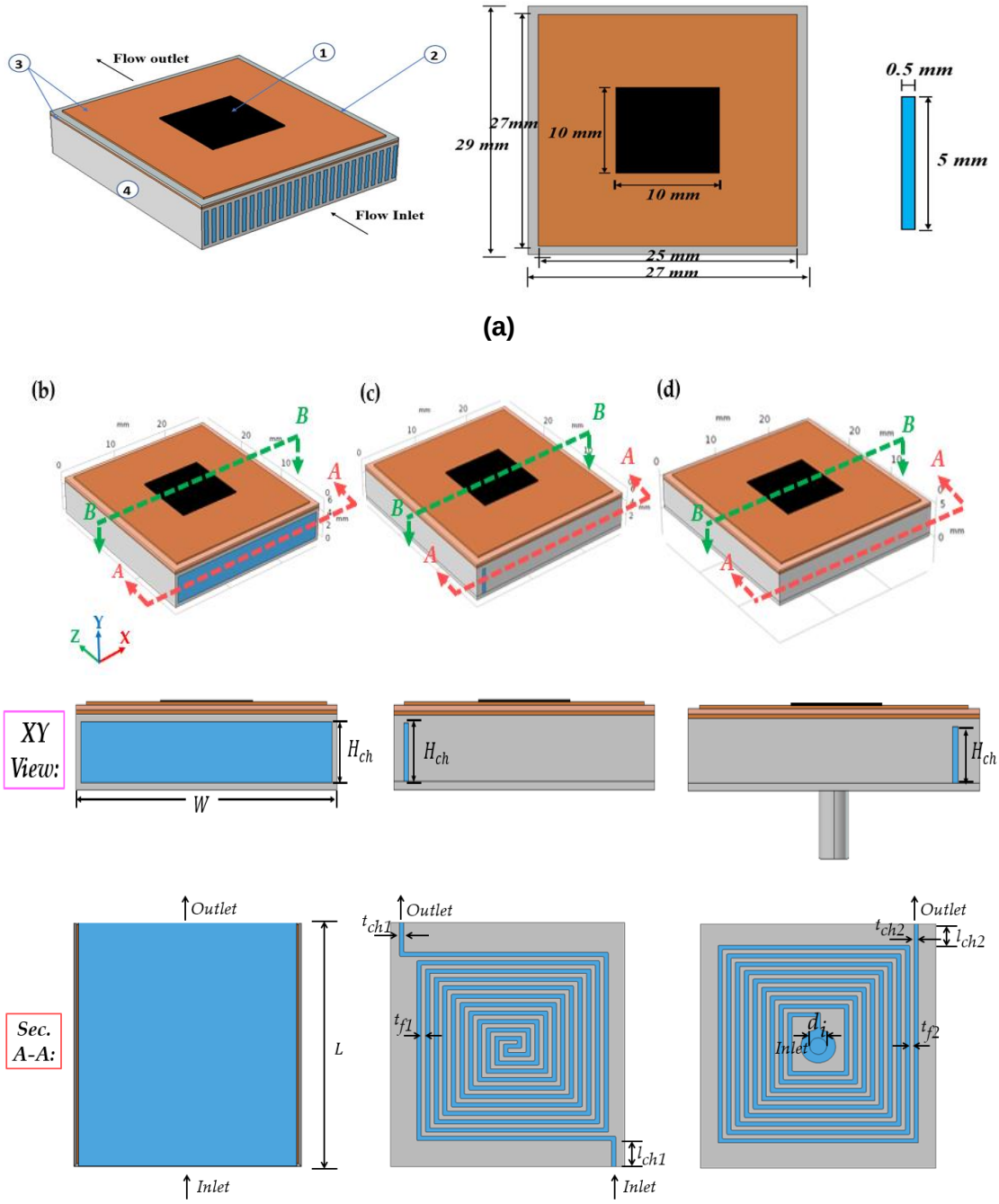

Figure 84 3D computational domains for (a) finned, (b) straight channel, (c) side inlet serpentine, (d) centre inlet serpentine. (1) MJ solar cell, (2) copper layers, (3) ceramic layer, (4) aluminium heat sink.

Four configurations of minichannel heat sink (Figure 84) have been considered in this research which are finned (F), straight channel (SC) , side inlet serpentine (SIS), and centre inlet serpentine (CIS) minichannel heat sinks. The 3D computational domains shown in Figure 84 are solved by COMSOL-Multiphysics [248]. This software discretizes the computational domain with a free tetrahedral mesh. The partial differential equations of the fluid and heat transfer are solved

iteratively using the Finite Element Method (FEM) by an iterative solver called Generalised Minimal Residual method (GMRES). The relative tolerance of this stationary solver is set to be 10^{-3}. The detailed dimensions of the considered heat sinks are presented in Table 13.

Table 13 Detailed dimensions of the considered heat sinks.

Parameter	**Value (mm)**	**Parameter**	**Value (mm)**
L	27	t_{f1}	0.5
W	29	d_{in}	2
W_c	0.5	H_c	5
H_{ch}	3	t_{ch2}	0.5
l_{ch1}	3	l_{ch2}	3
t_{ch1}	0.5	t_{f2}	0.5

In terms of nanofluid modelling, there are a number of studies that compared the results of the two-phase model with the homogenous single-phase model for calculating the thermophysical properties of the nanofluids [249]. As an example of these studies, Keshavarz Moraveji and Esmaeili [250] presented a comparison between the two and single-phase models, where no significant differences in the results were identified. Therefore, the homogenous single-phase model was considered in the calculations. For the calculation of Reynolds number:

$$Re=\frac{\rho_{nf}\, D_h\, U_{in}}{\mu_{nf}} \tag{5.12}$$

where the hydraulic diameter of the rectangular channel, D_h can be calculated from the following relation:

$$D_h = \frac{2\, W_c\, H_c}{(W_c+H_c)} \tag{5.13}$$

The heat transfer coefficient through the heat sink, h can be defined as follows:

$$h=\frac{q}{(T_w-T_b)} \tag{5.14}$$

where T_w and T_b are the temperature of the solid-fluid interface and bulk temperature, respectively. The overall thermal resistance of the heat sink can be calculated from the following relation:

$$R_{th}=\frac{T_{s,max}-T_{f,in}}{Q_{sc,heat}} \tag{5.15}$$

where $T_{s,max}$ is the maximum surface temperature of the heat sink. There are two factors to be considered to evaluate the efficacy of using the nanofluids in the system. The first is the heat transfer effectiveness (E_f) which is the ratio of the heat transfer coefficient in the case of using nanofluid to the heat transfer coefficient in the case of using base fluid (water) at the same Reynolds number [251].

$$E_f = \frac{h_{nf}}{h_{bf}} \tag{5.16}$$

The second factor is Performance Evaluation Criterion (PEC) which is the ratio of the useful heat gained from the system by using nanofluid to the pumping power. If the ratio between the PEC of nanofluids is higher than that of water, that's mean that the enhancement in heat transfer rate is higher than the increase in the pumping power.

$$PEC = \frac{Q_{th}}{P_{pump}} \tag{5.17}$$

5.2.2 Governing equations and boundary conditions

COMSOL-Multiphysics software [248] has been chosen to solve the 3D partial differential equations of the conjugate heat transfer and fluid flow. This finite element (FEM) software can discretize the 3D computational domain using a free tetrahedral mesh. Also, this software allows the partial differential equations to be solved iteratively using an iterative solver called Generalised Minimal Residual method (GMRES) with a relative tolerance set to 10^{-3}. Figure 85 indicates the boundary conditions implemented to the current HCPVT system which are as follows:

- The MJ solar cell receives uniformly focused high concentrated solar irradiance ranging from 500 suns to 2000 suns.
- The heat source of the HCPVT system is the germanium layer [252].
- As shown in Figure 85, mixed natural convection (h=15 W/m^2.K) [105] and radiation heat losses are considered for the top surfaces of: MJ solar cell, copper, and ceramic layers.
- Adiabatic conditions are applied to the sides and the back surface of the heat sink.
- Laminar, steady, and incompressible conditions have been assumed for the fluid flow inside the heat sink.

- The body force and viscous dissipation effects have been ignored.
- The fluid enters the channel at the ambient temperature which is assumed to be T_{in}=25 °C.
- An atmospheric outlet for the fluid pressure at the exit has been considered.

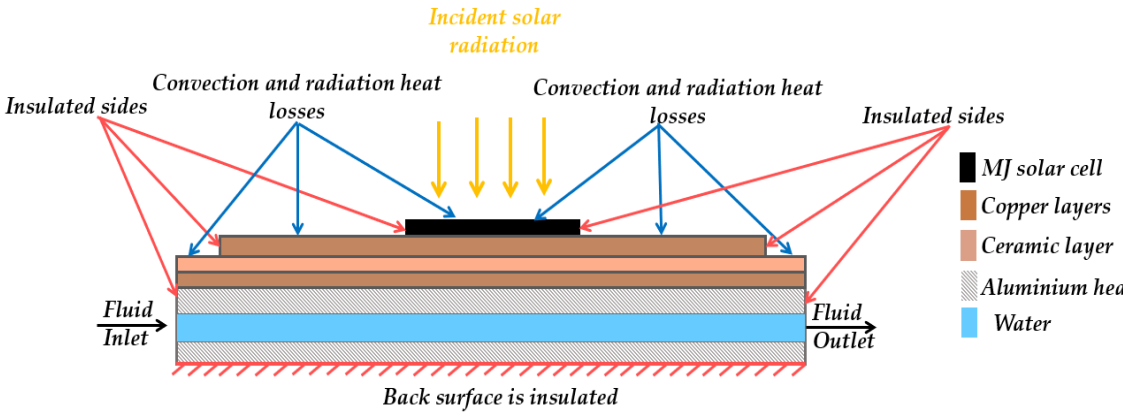

Figure 85 Schematic diagram of the implemented boundary conditions of the HCPVT system.

The rate of heat conduction in the solid domain may be described as follows:

$$\vec{q}=-k\nabla T \tag{5.18}$$

Then, the energy conversion law at steady state for the domain of the MJ solar cell:

$$-\nabla\left(\frac{k\nabla T}{A}\right)+\dot{q}=0 \tag{5.19}$$

The volumetric heat generation through the volume of germanium sublayer (V) can be expressed as follows [74,75,105,253]:

$$\dot{q}_{Ge}=\frac{Q_{sc,heat}}{V} \tag{5.20}$$

The heat transfer at the top surface of the MJ solar cell can be expressed by the following equation:

$$-k_{GaInP}\left(\frac{\partial T_{GaInP}}{\partial y}\right)=\left(q_{conv}+q_{rad}\right)_{GaInP\rightarrow a} \tag{5.21}$$

Then, for both the copper and ceramic layers, the heat balance equations:

$$-k_{copper}\left(\frac{\partial T_{copper}}{\partial y}\right)=\left(q_{conv}+q_{rad}\right)_{copper\rightarrow a} \tag{5.22}$$

$$-k_{ceramic}\left(\frac{\partial T_{ceramic}}{\partial y}\right)=\left(q_{conv}+q_{rad}\right)_{ceramic\rightarrow a} \tag{5.23}$$

The heat transfer equations for convection and radiation [74]:

$$q_{conv}=h\ (T_s-T_a) \tag{5.24}$$

$$q_{rad}=\varepsilon\ \sigma\ (T_s^4-T_a^4) \tag{5.25}$$

The conduction heat transfer for the heat sink can be expressed as:

$$\nabla.(k_{h.s}\nabla T_{h.s})=0 \tag{5.26}$$

The continuity equation for the fluid domain:

$$\nabla.(\rho_f\vec{U})=0 \tag{5.27}$$

The momentum equation:

$$\vec{U}.\nabla(\rho_f\vec{U})=-\nabla p+\nabla(\mu_f\nabla\vec{U}) \tag{5.28}$$

The energy equation:

$$\vec{U}.\nabla(\rho_f\, c_{p,f}T)=\nabla.(k_f\nabla T) \tag{5.29}$$

5.2.3 Exergy analysis

Exergy analysis is often used to evaluate the exergy efficiencies. It also, measures the maximum possible energy that can be produced during the process when the entropy is at its maximum. This is another method to evaluate the system performance by allowing the exergetic losses to be identified. This could, therefore, contribute to potential system improvements [254]. The exergy efficiency can be defined as the ratio of the utilized and the supplied exergy. Therefore, the thermal exergy efficiency can be calculated from the following relation [255]:

$$\xi_{th}=\frac{\dot{E}_{th}}{\psi_s\,\dot{Q}_{in}} \tag{5.30}$$

The thermal exergy rate is evaluated using the following equation [256,257]:

$$\dot{E}_{th}=\dot{m}\ c_{p,f}\left\{(T_{f,out}-T_{f,in})-(T_a+273)\,ln\left(\frac{T_{f,out}+273}{T_{f,in}+273}\right)\right\} \tag{5.31}$$

$$\psi_s=1-\frac{T_a}{T_{sun}} \tag{5.32}$$

On the other hand, electrical exergy efficiency is estimated from the following relation:

$$\xi_{elec}=\frac{\dot{E}_{elec}}{\psi_s\,\dot{Q}_{in}} \tag{5.33}$$

The electrical exergy rate is usually considered to be equal to the electrical power produced [255]:

$$\dot{E}_{elec} = P_{useful,elec} \quad (5.34)$$

Thus, the total exergy efficiency of the system which is the sum of the thermal and electrical exergy efficiency can be represented by the following relation:

$$\xi_{tot} = \xi_{elec} + \xi_{th} \quad (5.35)$$

5.3 Thermophysical properties of the fluids used

5.3.1 Water

The thermophysical properties of water (base fluid) are calculated using the following relations for density (ρ_f) specific heat ($c_{p,f}$), thermal conductivity (k_f), and dynamic viscosity (μ_f), respectively [137].

$$\rho_f = -0.003\ T_f^2 + 1.505\ T_f + 816.781 \quad (5.36)$$

$$c_{p,f} = -0.0000463\ T_f^3 + 0.0552\ T_f^2 - 20.86\ T_f + 6719.637 \quad (5.37)$$

$$k_f = -0.000007843\ T_f^2 + 0.0062\ T_f - 0.54 \quad (5.38)$$

$$\mu_f = 0.00002414 \times 10^{\left(\frac{247.8}{T_f - 140}\right)} \quad (5.39)$$

5.3.2 Ethylene glycol/ mixture 60:40

In the case of ethylene glycol and water mixture (60:40), the following equations have been used [258]:

$$\rho_f = -0.0024\ T_f^2 + 0.958\ T_f + 1014.297 \quad (5.40)$$

$$c_{p,f} = -0.00000489\ T_f^3 - 0.00475\ T_f^2 + 5.893\ T_f + 1641.327 \quad (5.41)$$

$$k_f = -0.00000302\ T_f^2 + 0.00238\ T_f - 0.09 \quad (5.42)$$

$$\mu_f = 0.00001202 \times 10^{\left(\frac{453.4}{T_f - 122}\right)} \quad (5.43)$$

5.3.3 Syltherm Oil 800

The thermophysical properties of the Syltherm oil 800 have been adapted from Loikits data [259]. These data include variation of specific heat capacity and density againist temperature as presented in Figure 86, while the change in the thermal conductivity and viscosity with temperature is shown in Figure 87. It can be seen that the specific heat is the only property which increases with temperature, while the other properties decrease significantly as the temperature increases.

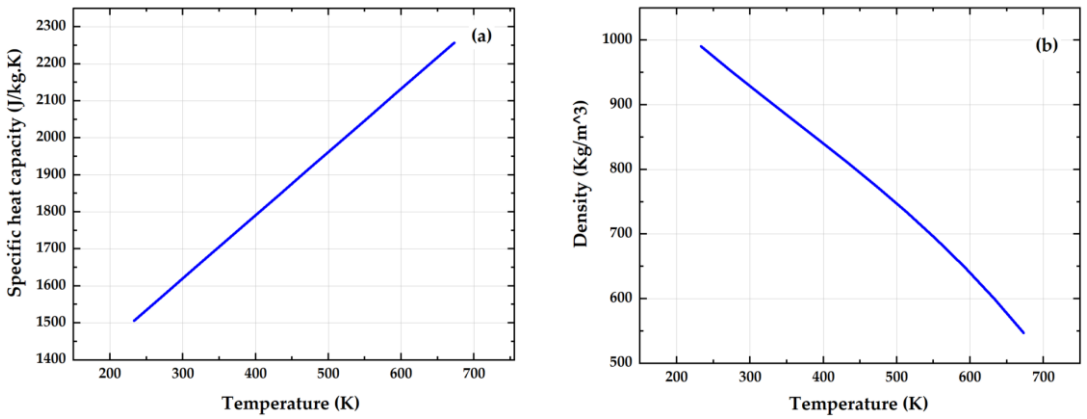

Figure 86 Variation of (a) specific heat capacity, and (b) density with temperature for sylthern oil.

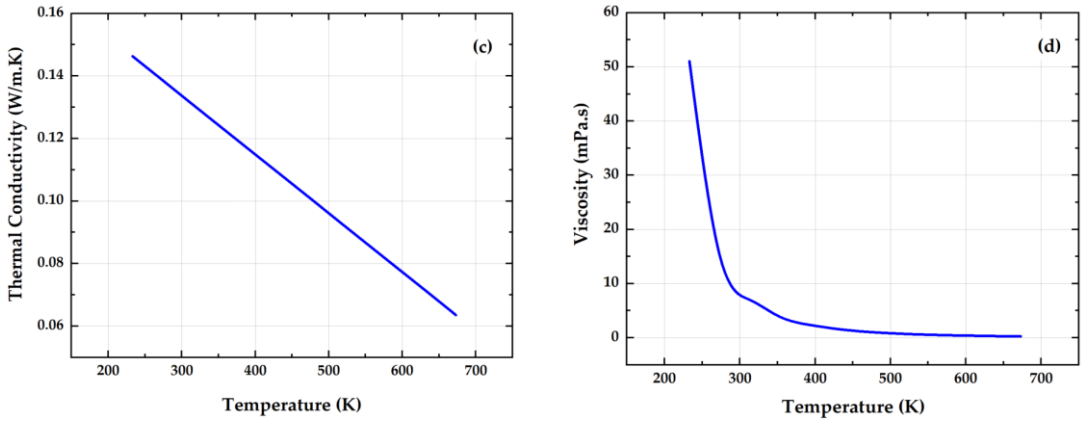

Figure 87 Variation of (a) thermal conductivity, and (b) viscosity with temperature for sylthern oil.

5.3.4 Nanofluids single phase model

The investigated nanoparticles are aluminium oxide (Al_2O_3) and silicon dioxide (SiO_2). These nanoparticles are affordable and easily accessible. The volume fractions (φ) used in the calculations are 2.5% and 5%. For the calculations of the thermophysical properties of the nanofluids, Das et al. [260] relation has been used for the density (ρ_{nf}). Khanafer et al. [261] equation has been considered in the calculations of the specific heat ($c_{p,nf}$). In addition, the thermal conductivity (k_{nf}) has been measured experimentally (next section) and the results have been compared with Hamilton and Crosser [245] model by considering the spherical shape of the nanoparticles, while for viscosity (μ_{nf}) calculations Brinkman relation [262] has been considered.

$$\rho_{nf} = (1-\varphi)\,\rho_{bf} + \varphi\,\rho_{np} \qquad (5.44)$$

$$c_{p,nf}= \frac{\rho_{bf}\,(1-\varphi)\,c_{pbf}+\rho_{np}\,\varphi\,c_{p,np}}{\rho_{nf}} \tag{5.45}$$

$$k_{nf}=\left(\frac{k_{np}+(n-1)\,k_{bf}-(n-1)\,\varphi\,\left(k_{bf}-k_{np}\right)}{k_{np}+(n-1)\,k_{bf}+\varphi\,\left(k_{bf}-k_{np}\right)}\right)\,k_{bf} \tag{5.46}$$

$$\mu_{nf}=\frac{\mu_{bf}}{(1-\varphi)^{2.5}} \tag{5.47}$$

5.4 Numerical solution

To check the effectiveness of the model, several steps were carried out. First, the quality of the built mesh was checked ensuring that the solution did not depend on the mesh element size. After that, a validation study was undertaken. The importance of this step is to ensure that the current solution can predict the same results of the selected models as the literature. After running the current model, the residuals from the continuity and energy equations were estimated to ensure that they have values lower than the relative tolerance set in the software and fulfilled the energy balance equation.

5.4.1 Grid independence test

For the finned minichannel heat sink, the number of mesh elements varied from 0.2×10^6 to 1.9×10^6. The study was undertaken in terms of the maximum temperature of the solar cell and the relative error between the previous and the current values as introduced in Figure 88. The maximum temperature has constant value for the grid element between 1.5×10^6 to 1.9×10^6. In addition, the error is decreased significantly with an increase in the number of the mesh elements. Therefore, the most suitable number of elements in terms of accuracy and calculation time has been considered (1.5×10^6) and a relative error of 0.07%, the generated mesh is presented in Figure 88. In addition, for CIS configuration the number of mesh elements have been increased from 1.9×10^5 to 4.1×10^6 until the variation in the temperature is decreased significantly as introduced in Figure 89. The number of mesh elements has been selected based on solution accuracy and consumed computational time. Therefore, 1.86 million mesh elements have been chosen with a relatively small error and lower computational time.

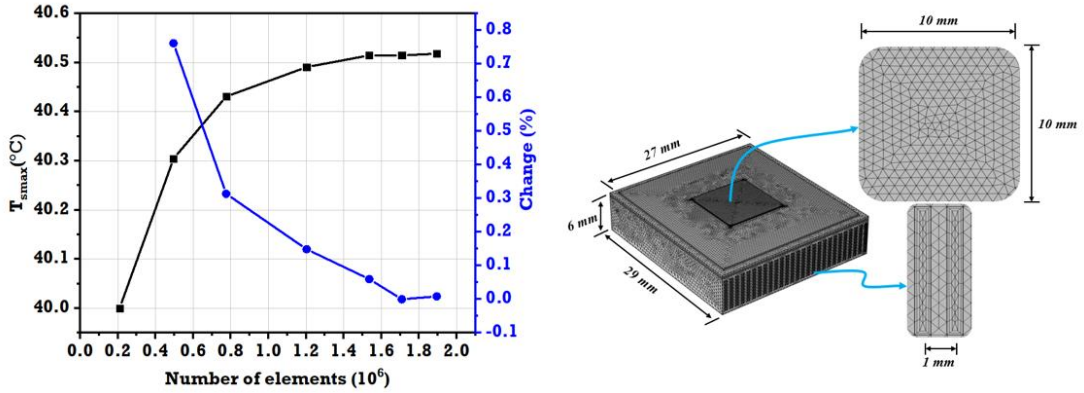

Figure 88 Mesh independence study for maximum solar cell temperature for 10 mm × 10 mm MJ solar cell at a concentration ratio of 500 suns by using water at Re=11.

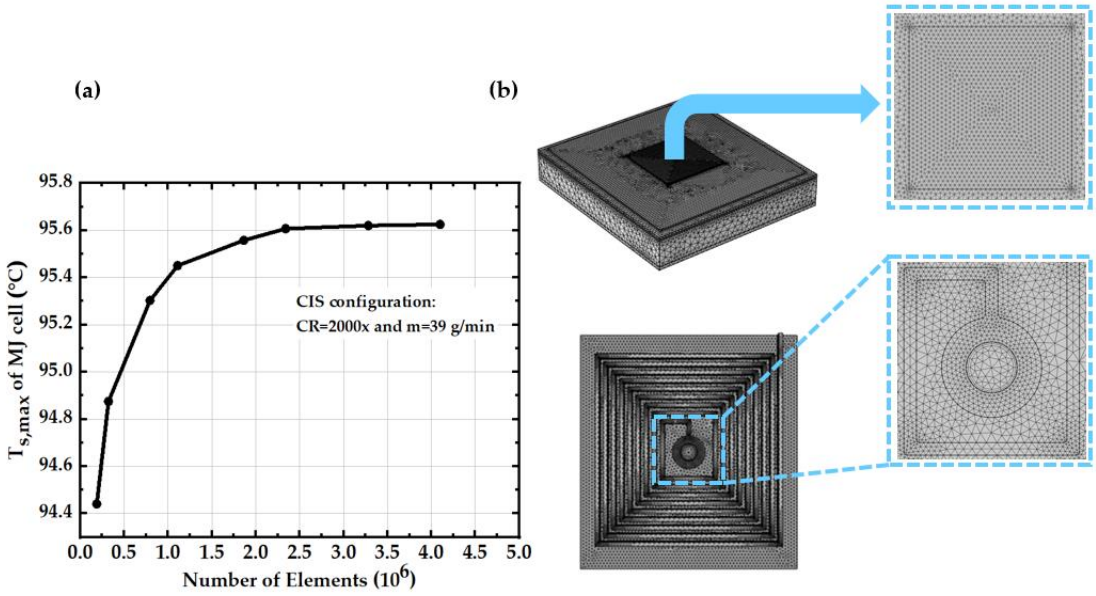

Figure 89 (a) Mesh independence analysis in terms of maximum solar cell temperature, (b) Meshing of the CIS configuration at CR=2000 suns and $\dot{m}$=39 g/min.

5.4.2 Validation study

5.4.2.1 CPV assembly Validation

Several models have been considered for the verification step to ensure the validity of the current results. Firstly, the results of Theristis et al. [75] and Al Siyabi et al. [105] have been compared for the HCPVT for the same physical modules dimensions, properties, and boundary conditions as shown in Figure 90. From Figure 90a, there is a reduction in the observed solar cell temperature with the increase in the convective heat transfer coefficient, while the opposite has occurred when increasing the ambient temperature.

The maximum and minimum errors obtained from the comparison are 1.85% and 0.7% respectively. On the other hand, the change of the maximum solar cell temperature with an increase in the number of heat sink layers is presented in Figure 90b. A maximum error of 2.4% is obtained from this comparison which indicates that the results obtained are satisfactory. Another validation has been carried out with the experimental and simulation results of Chow et al. [263] and the present results in terms of the variation of the solar cell temperature with the concentration ratio with and without thermal paste as illustrated in Figure 91. The minimum observed deviation is 0.9%.

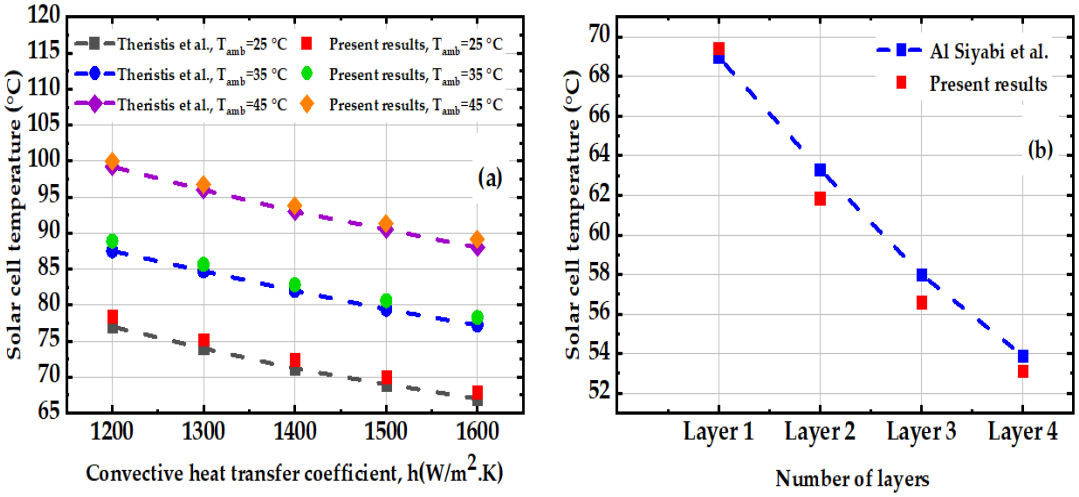

Figure 90 Variation of the solar cell temperature at different conditions for (a) Theristis et al. [75] *and (b) Al Siyabi et al.* [105] *and present results.*

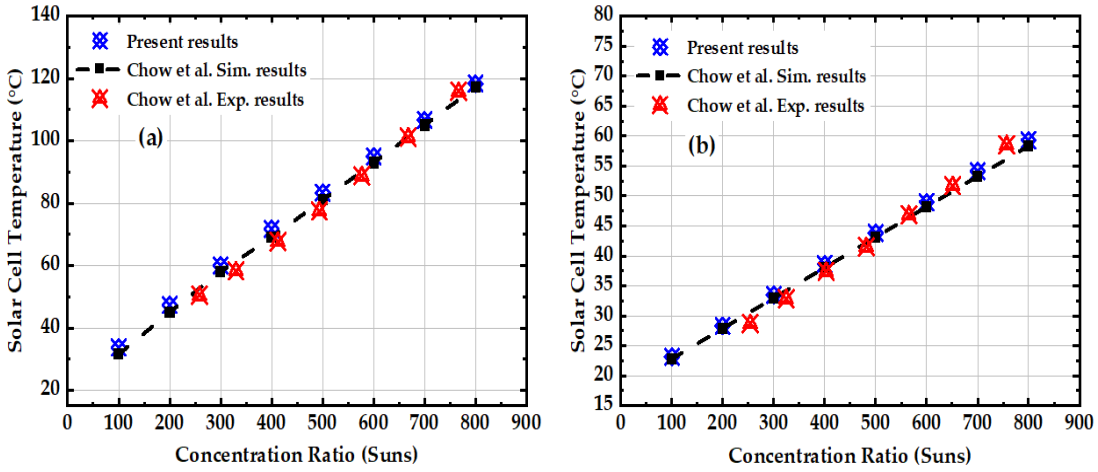

Figure 91 Variation of the solar cell temperature with concentration ratio for Chow et al. [263] *experimental and simulation results and the present results for cases: (a) without thermal paste, and (b) with thermal paste.*

5.4.2.2 Heat sink Validation

Secondly, verification of the current results and Wu et al. [264] heat sink model has been plotted in Figure 92a. The validation has been undertaken in terms of the maximum heat sink surface temperature for different substrate materials (Cu, Si, and AIN) and flow velocities. More details of the model design can be found in [264]. The maximum and minimum errors achieved are 0.92% and 0.27%, respectively. Figure 92b summarises the results of Xie et al. [265], empirical correlation of Kim and Kim [266] for the same model, and the present results. A maximum error of 1.14 % was attained by performing a comparison between Xie et al. [265] and the current results with a higher number of mesh elements. On the other hand, this error reached as low as 0.29% when comparing the same current results and Kim and Kim's [266] empirical equation which reveals that the present simulation solved the previously published model accurately.

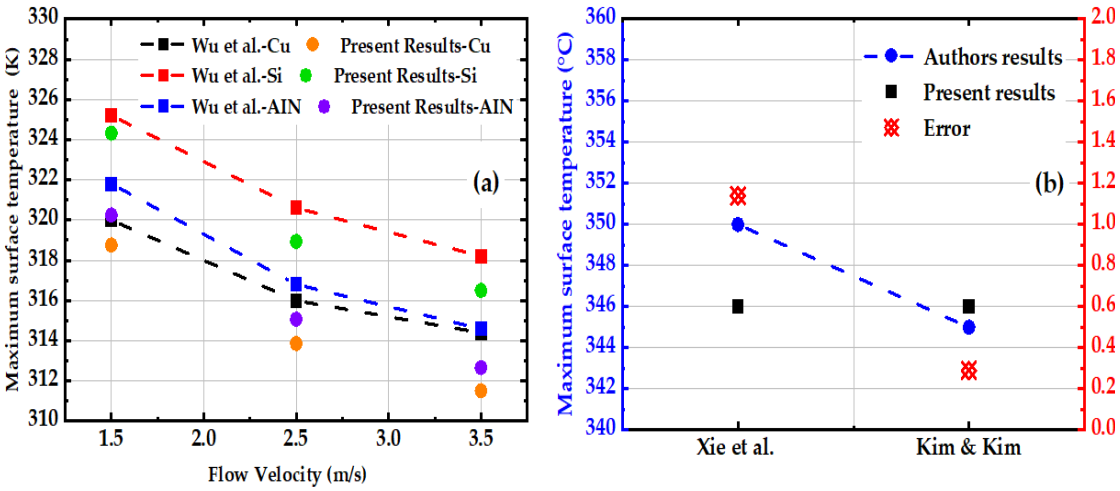

Figure 92 Variation of the maximum surface temperature at different conditions for (a) Wu et al. [264] *and present results. (b) Xie et al.* [265]*, Kim and Kim* [266]*, and present results.*

5.5 Conclusion

The mathematical approach used in this research was introduced in this chapter. Different heat sink configurations for HCPV applications with their dimensions and material properties were also presented. The theoretical analysis of the whole CPV system, including the performance parameters was explored and the exergy equations for the system were presented for more reliability. Furthermore, the thermophysical properties of different working media used in this research

were provided. The numerical solution procedure used through the investigation was introduced in detail including the grid independence test for each configuration. A considerable number of validation studies, including both numerical and experimental studies, were compared to verify the solution accuracy.

Chapter 6
Actively cooled high concentrator photovoltaics: Impact of using different working media and heat sink design

6.1 Introduction

This chapter provides a theoretical performance analysis of the HCPVT systems by using different heat transfer fluids and heat sink configurations through the theoretical approach provided in the previous chapter. The chapter discusses three different conditions. The first condition (6.2) examines the performance of the HCPVT system in the case of utilizing a finned minichannel heat sink with coolants: water, ethylene glycol, and water mixture, and syltherm oil 800. The second section (6.3) investigates the impact of using different types of nanofluids on the operation of the system using a finned minichannel heat sink. In the final part (6.4), a comparison between different heat sink configurations (straight channel, side inlet serpentine, and centre inlet serpentine) is introduced. The evaluation is presented in terms of solar cell temperature, temperature distribution, thermal resistance, energy, and exergy performance analyses.

6.2 Effect of using water, ethylene glycol/water mixture, and syltherm oil

This section investigates the impact of the concentration ratio and the mass flow rate of water, ethylene glycol and water mixture (60:40), syltherm-oil 800 on the maximum volumetric solar cell temperature, temperature distribution on the solar cell surface, outlet fluid temperature, and the thermal and electrical efficiency of the system. The heat sink used in this study is a finned minichannel heat sink as introduced in the previous chapter. The main aim of investigating the impact of these fluids on the HCPVT performance is they exhibit a stable performance and low potential for fouling in comparison with water.

6.2.1 Maximum solar cell temperature and temperature distribution over the surface of the solar cell

The impact of using water, ethylene-glycol mixture (60:40), syltherm oil 800 on the performance of the HCPVT system at different concentration ratios are presented in this section. Figure 93 compares the variation of the maximum volumetric solar cell temperature with the mass flow rate for water, ethylene glycol mixture, and syltherm oil. The highest temperature is observed by using oil (109.1 °C), while the lowest was by using water (93.5 °C) at the same mass flow rate and solar concentration ratio of 2000 suns. Increasing the mass flow rate had a positive effect on reducing the maximum volumetric solar cell temperature reaching 34.7 °C at a solar concentration ratio of 500 suns. In general, all the calculated maximum temperatures were lower than the recommended limit provided by the manufacturer. In addition, the temperature distribution for the different working media is presented in Figure 94. Water offers the most uniform temperature distribution followed by ethylene glycol and water mixture (60:40) the average temperature varying from 82.16 °C to 88.48 °C respectively.

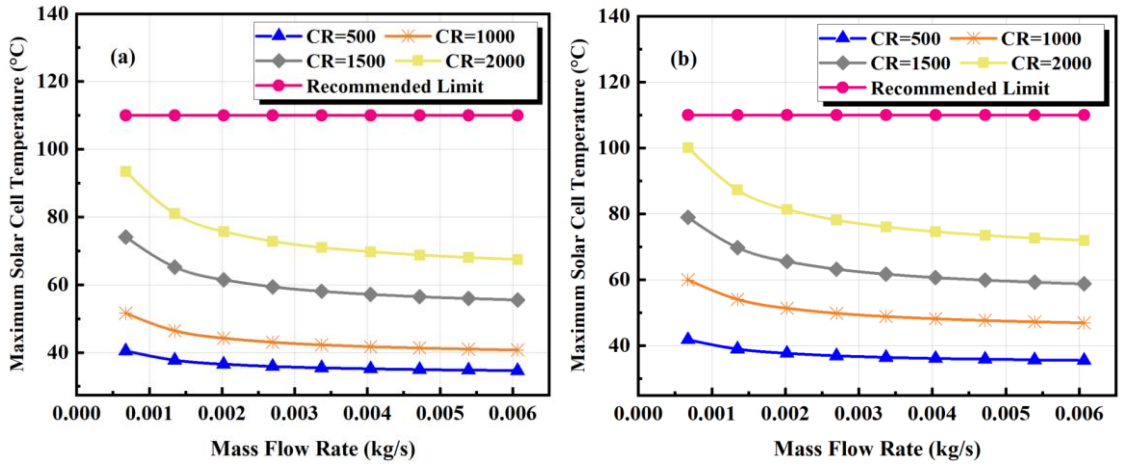

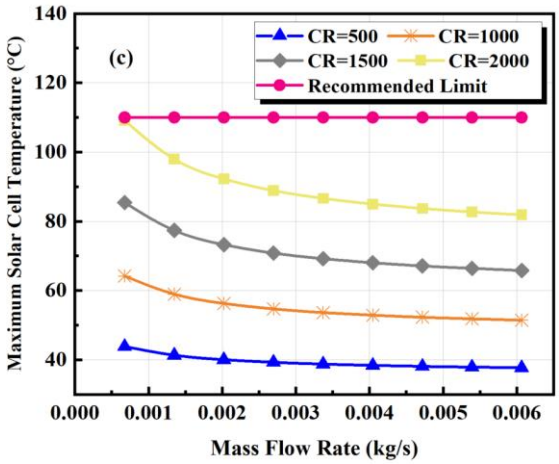

Figure 93 Variation of the maximum solar cell temperature with mass flow rates at different values of concentration ratios, (a) water, (b) ethylene-glycol mixture (60:40), and (c) syltherm oil 800.

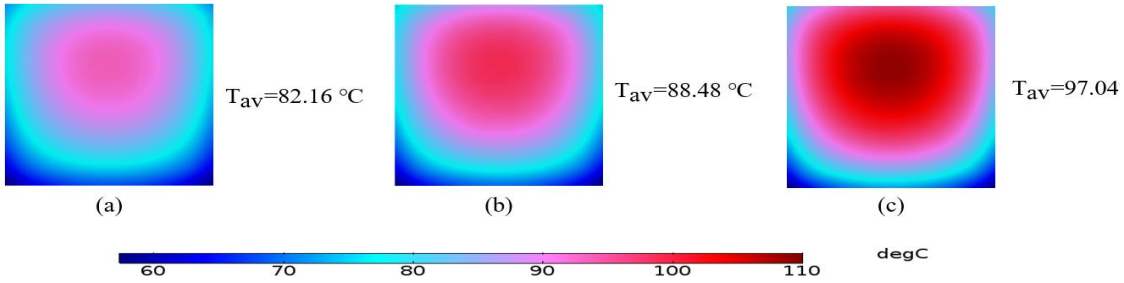

Figure 94 Solar cell surface temperature at 2000 suns and 6.74×10^{-4} kg/s for (a) water, (b) ethylene-glycol mixture (60:40), (c) syltherm oil 800.

6.2.2 Temperature non-uniformity

To predict how uniform the temperature is across the cell, temperature non-uniformity has been calculated. Figure 95 compares the temperature non-uniformity data by using water, ethylene glycol/water mixture, and oil at different concentration ratios. A reduction in temperature non-uniformity is achieved by increasing the mass flow rate. Also, the temperature non-uniformity is lower when using water rather than ethylene glycol/mixture and syltherm oil. At the lowest tested mass flow rate, the obtained temperature non-uniformity was 39 °C, 41 °C, and 42.5 °C. Similar values have been obtained at the highest mass flow rate due to the increase in the flow velocity which reduces the fluid viscosity especially with the reduction of the thermal load. The lowest temperature non-uniformity value by using water is 6.2 °C at a concentration ratio and mass flow rate of 500 suns and 0.0062 kg/s respectively.

6.2.3 Outlet fluid temperature

The Variation of the outlet temperatures of the fluids with the concentration ratio and mass flow rate are presented in Figure 96. The outlet temperature decreases with increasing the mass flow rate, while it increases with the concentration ratio. The highest outlet temperature observed in the case of using the sylltherm oil is 73.5 °C, while the lowest was in the case of using water 58.5 °C at a solar concentration of 2000 suns and a mass flow rate of 6.74×10^{-4} kg/s. Further, the outlet temperature by using ethylene-glycol mixture reached as high as 65 °C at the lowest tested mass flow rate at the concentration ratio of 2000 suns and 34 °C at a concentration ratio of 500 suns. Therefore, increasing the concentration ratio has a positive impact on the outlet temperature for all the tested fluids. Syltherm oil 800 offers the highest outlet fluid temperature in comparison with other fluids especially for a concentration ratio above 1000 suns. Overall, deciding which fluid to use depends mainly on the designed concentration ratio and the available heat recovery application.

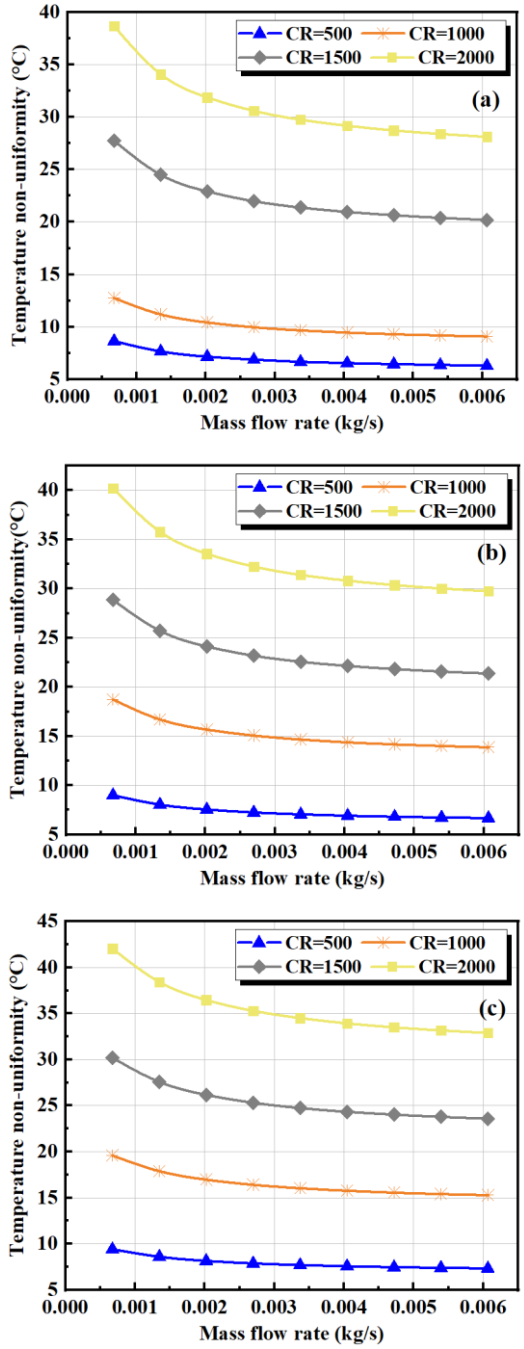

Figure 95 Variation of the temperature non-uniformity with the mass flow rate and concentration ratio for (a) water, (b) ethylene-glycol mixture (60:40) (c) syltherm oil 800.

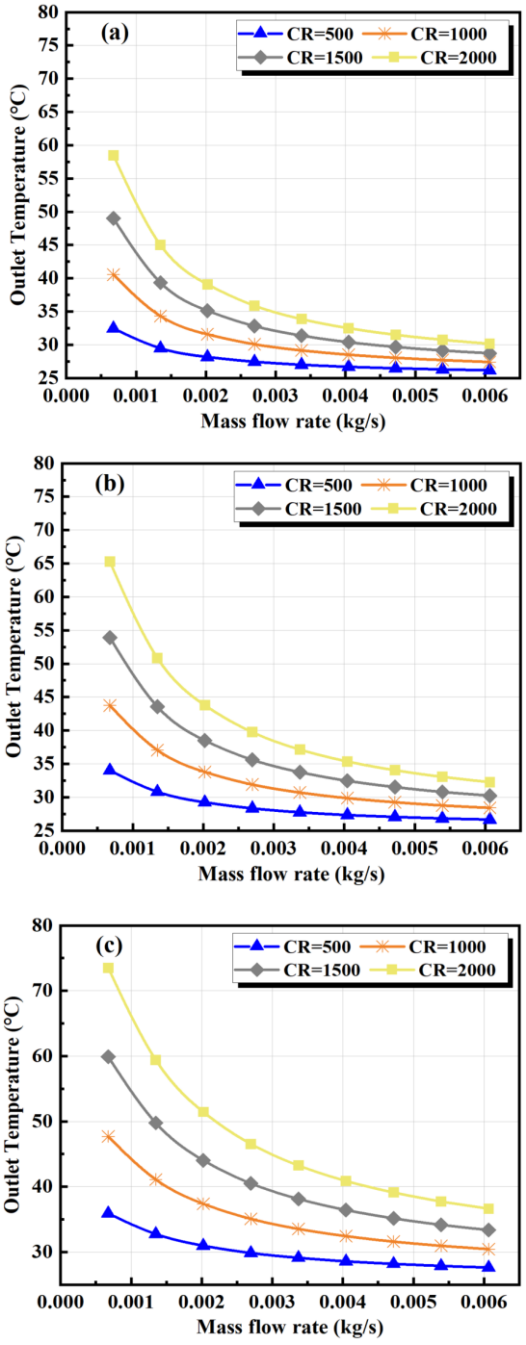

Figure 96 Variation of the outlet temperature with the mass flow rate and concentration ratio for (a) water, (b) ethylene-glycol mixture (60:40) (c) syltherm oil 800.

6.2.4 Heat sink thermal resistance and pumping power

Figure 97 a introduces the variation in the heat sink thermal resistance by using different working media with the mass flow rate. There is a notable decrease in the thermal resistance with an increase in the mass flow rate which can be attributed to the reduction in the heat sink surface temperature. Water, in contrast to syltherm oil, has achieved the lowest thermal resistance due to the highest degree of temperature uniformity. Pumping power variation with the mass flow rate is plotted in Figure 97 b. The required power to force the fluid to flow inside the heat sink channels increases by increasing of the mass flow rate to overcome the pressure drop resulted from raising the flow rate. Also, a growth in the required power reaching 750% is noticed by using syltherm oil in comparison with water at 0.0062 kg/s.

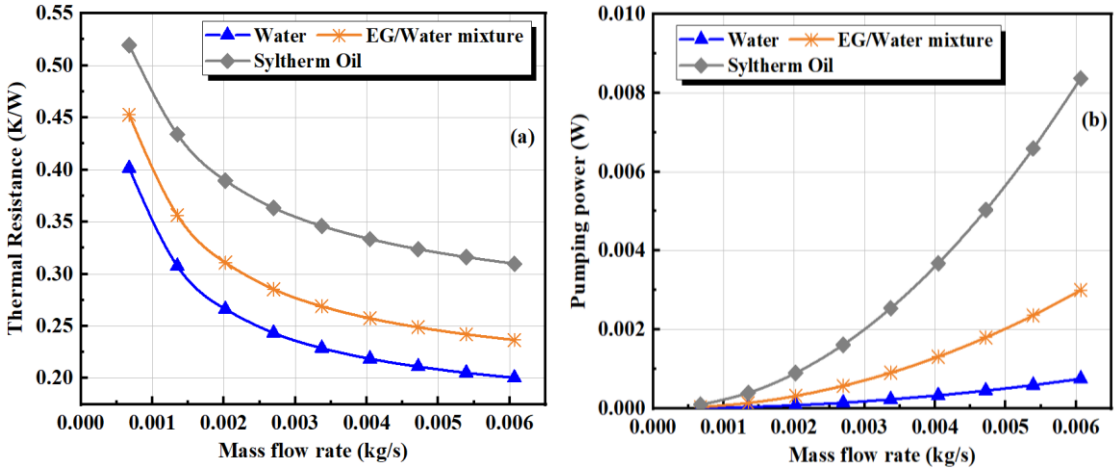

Figure 97 Variation of (a) thermal resistance, and (b) pumping power with mass flow rates for water, ethylene glycol and water mixture, and syltherm oil 800.

6.2.5 Electrical and thermal efficiencies

The solar cell temperature and the electrical efficiency were calculated by Eq. (5.1) using the trial and error method [105,246] by inputting the reference efficiency as provided by the manufacturer. Therefore, the electrical efficiency depends on the concentration ratio as well as the solar cell temperature. The electrical efficiency of the HCPVT system increased significantly with an increase in the mass flow rate of the working media as presented in Figure 98. Using syltherm oil decreased the electrical efficiency if compared with water by 2.2% at 6.74×10^{-4} kg/s especially at a concentration ratio of 2000 suns.

This can be attributed to the high surface temperature of the solar cell that is detected in the case of using the syltherm oil if compared with the other fluids at the same mass flow rates. The highest electrical efficiency was 40.8% in the case of using water and a concentration ratio of 500 suns and mass flow rate of 0.006 kg/s, while the lowest efficiency was 31.2% in the case of using syltherm oil and a concentration ratio of 2000 suns and mass flow rate of 6.74×10^{-4} kg/s.

Further, increasing the concentration ratio had a negative impact on the calculated electrical efficiency as a large portion of the concentrated solar irradiance was converted into heat. In total, among the tested fluids water showed the highest performance in terms of electrical efficiency especially at concentration ratios above 1000 suns. Figure 99 shows the effect of increasing the mass flow rate on the thermal efficiency of the HCPVT system at different concentration ratios.

The thermal efficiency of the HCPVT system increased with an increase in the mass flow rate and concentration ratio. The thermal efficiency varied from 42% to 65.4% for the concentration ratio between 500 suns and 2000 suns. The lowest values are observed in the case of using syltherm oil 800 due to its lower specific heat at constant pressure if compared with the other fluids. The thermal efficiency increased from 23.97% to 57.45% when using syltherm oil 800, while it varied from 34.65% to 62.8% when using the ethylene-glycol and water mixture. In the case of thermal efficiency, increasing the concentration ratio had a positive impact as shown in the results.

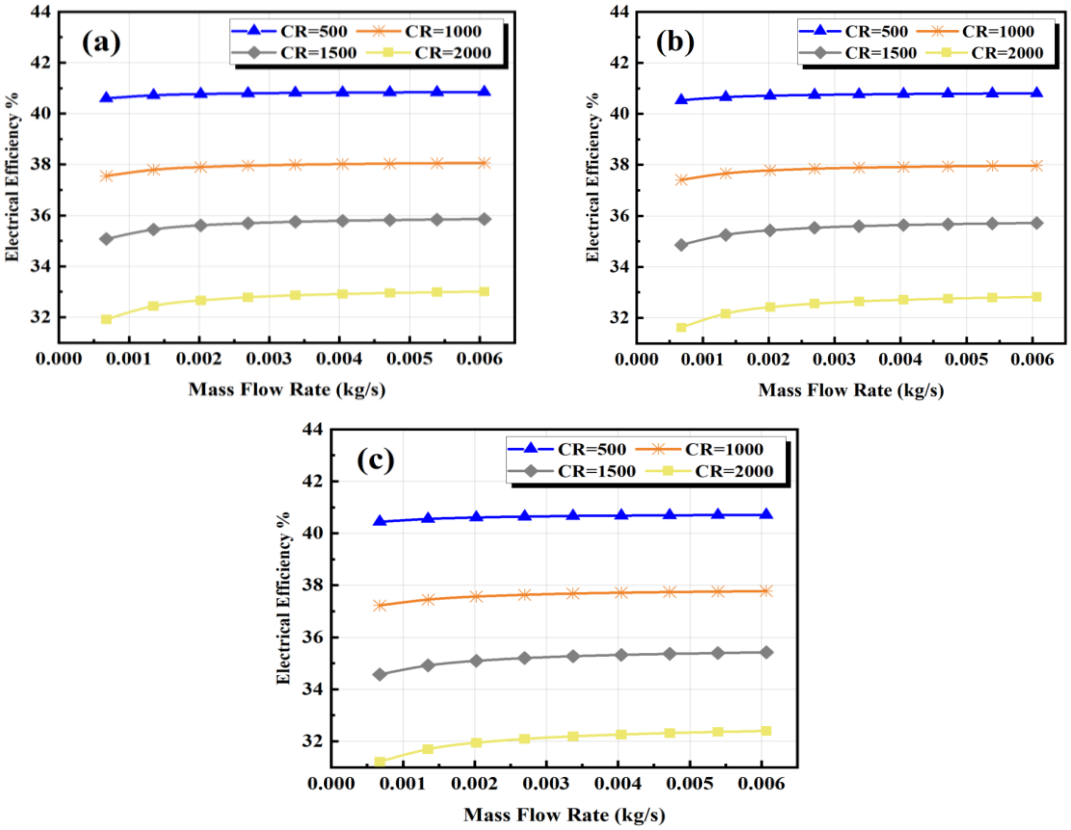

Figure 98 Variation of the electrical efficiency with the mass flow rate and concentration ratio for (a) water, (b) ethylene-glycol mixture (60:40) (c) syltherm oil 800.

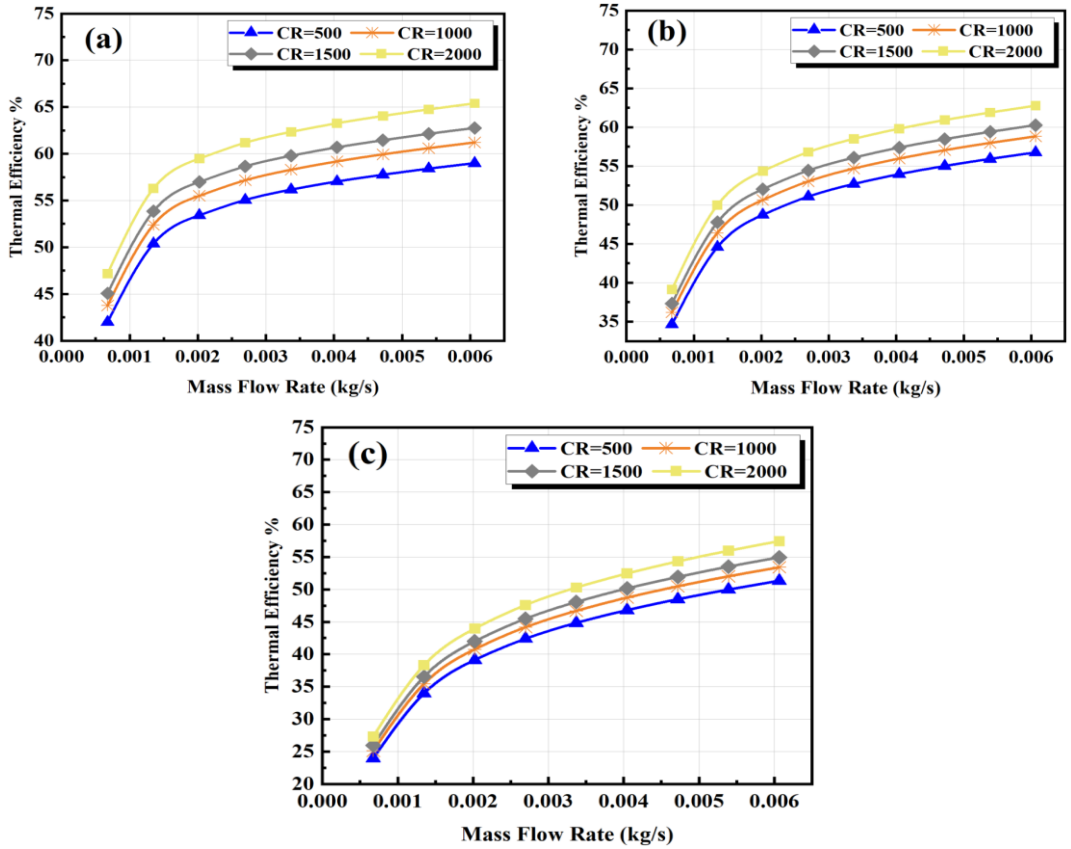

Figure 99 Variation of the thermal efficiency with the mass flow rate and concentration ratio for (a) water, (b) ethylene-glycol mixture (60:40) (c) syltherm oil 800.

6.3 Effect of using water, aluminium oxide/water, and silicon dioxide/water

In this section, the performance of the HCPVT system based on the finned mini-channel heat sink is investigated at different solar concentration ratios by using Al_2O_3/water and SiO_2/water at different volume fractions. A specific range of each parameter is defined and the results of two volume fractions are introduced as they showed a good thermal enhancement. Also, the results at the minimum and maximum studied Reynolds number are presented to show the performance limits for the system. The output parameters investigated here are heat transfer effectiveness factor, maximum solar cell temperature, electrical, thermal, and overall efficiencies, the pressure drop through the channels, the thermal resistance of the heat sink as well as the PEC.

6.3.1 Effectiveness of heat transfer

Figure 100a and b show the variation of the effectiveness factor with Reynolds number in the case of using Al_2O_3/water and SiO_2/water. There is a significant enhancement when using nanofluids as the factor is higher than 1. The effectiveness of the heat transfer process when using Al_2O_3/water at a different volume fractions outweighs the performance in the case of SiO_2/water. In addition, increasing the Reynolds number leads to noticeable enhancement in the heat transfer due to the increase in the flow velocity. The highest enhancement is observed for Al_2O_3/water and SiO_2/water at a volume fraction of 5% and a Reynolds number of 82.5 reaching 1.145 and 1.105 respectively. This can be attributed to the great enhancement in the measured thermal conductivity values if compared with water.

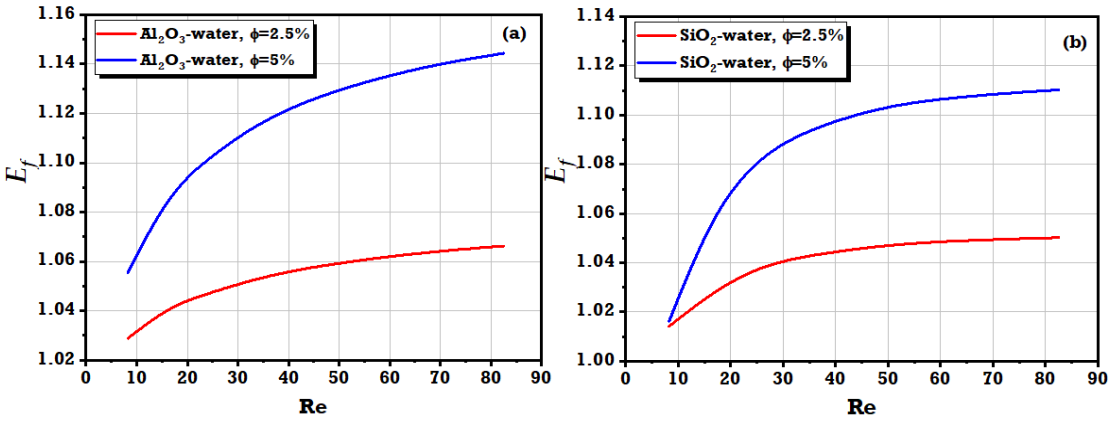

Figure 100 Variation of the effectiveness of heat transfer with Reynolds number for (a) Al_2O_3/water and (b) SiO_2/water at different volume fractions at a concentration ratio of 2000 suns.

6.3.2 Maximum temperature and temperature distribution of the MJ solar cell

Figure 101 and Figure 102 show the variation of the maximum temperature of the MJ solar cell with the volume fraction for both Al_2O_3/water and SiO_2/water from CR= 500 to 2000 suns. The maximum solar cell temperature clearly decreases with increasing the volume fraction at Re=8.25 and Re=82.5. The maximum observed temperature for different concentration ratios did not exceed the maximum recommended temperature by the manufacturer (110 °C). The temperature decreases significantly with the increase of the volume fraction of silicon dioxide and alumina nanoparticles within the water. This can be attributed to the enhanced thermal properties of the nanofluids used which improved the heat transfer process through the system allowing more heat to be extracted from the solar cell. The reduction in the maximum solar cell temperature varied from 3.6 °C to 0.97 °C by using SiO_2/water. In addition, from both graphs increasing the Reynolds number decreases the maximum volumetric solar cell temperature as it reached 67.2 °C. At a higher Reynolds number, the thermal boundary layer decreases (the thermal effect of adding nanoparticles to the fluids reduces) and the velocity becomes more dominant [267]. Therefore, Al_2O_3/water and SiO_2/water exhibited consistent performance at the highest tested Reynolds number of 82.5, while at the lowest tested Reynolds number SiO_2/water outperformed Al_2O_3/water in terms of volumetric solar cell temperature due to its higher thermal capacity.

Figure 103 explains the temperature distribution of the MJ solar cell at a concentration of 2000 suns and a Reynolds number of 8.25. Use of nanofluids enhances the temperature distribution on the surface of the solar cell as the hot spot decreases significantly at a volume fraction of 5% if compared to the case of using water only. In addition, the temperature distribution at the lowest concentration (500 suns) is better than in the case of the highest concentration as presented in Figure 104 due to the decrease in the heat generation through the solar cell.

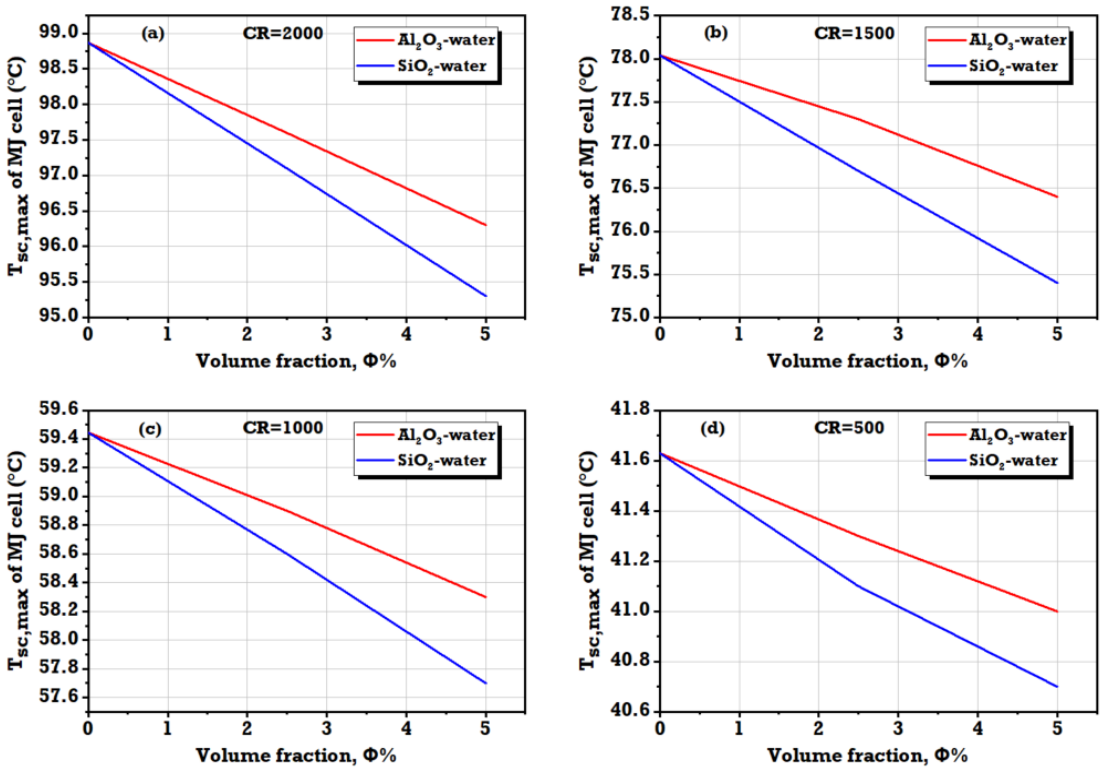

Figure 101 Variation of the maximum temperature of MJ solar cell with volume fraction at (a) 2000 suns, (b) 1500 suns, (c) 1000 suns, (d) 500 suns and Re=8.25.

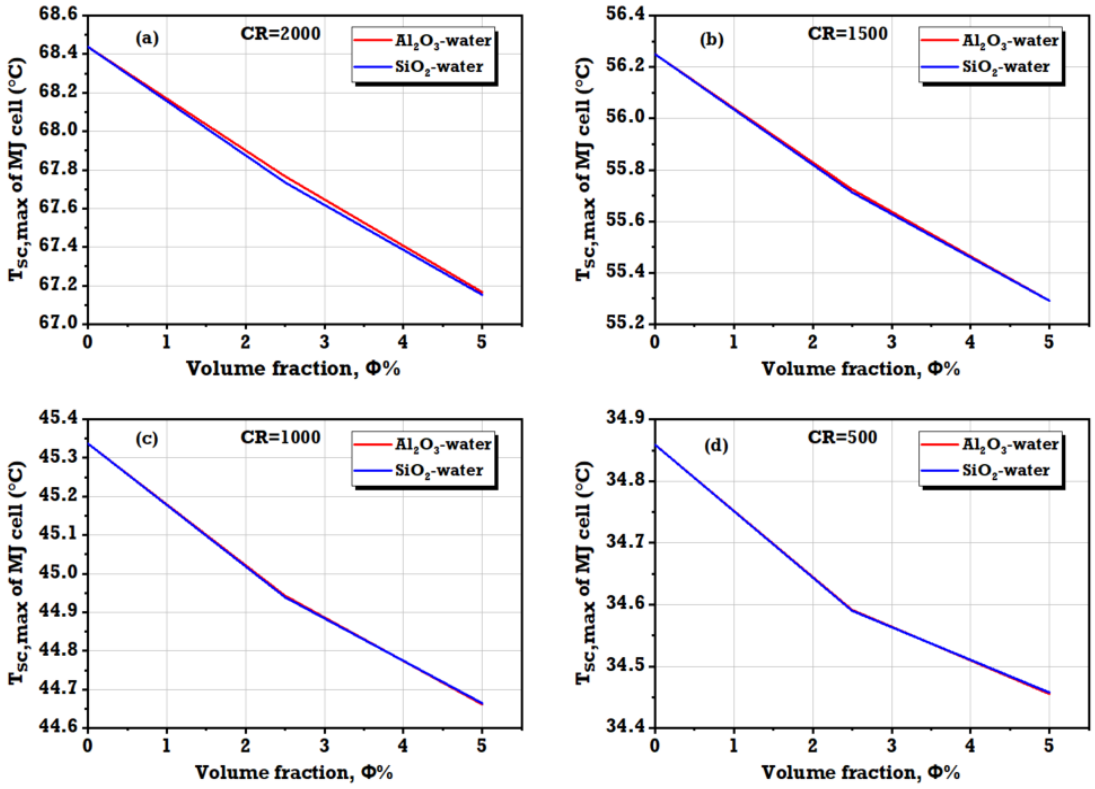

Figure 102 Variation of the maximum temperature of MJ solar cell with volume fraction at (a) 2000 suns, (b) 1500 suns, (c) 1000 suns, (d) 500 suns and Re=82.5.

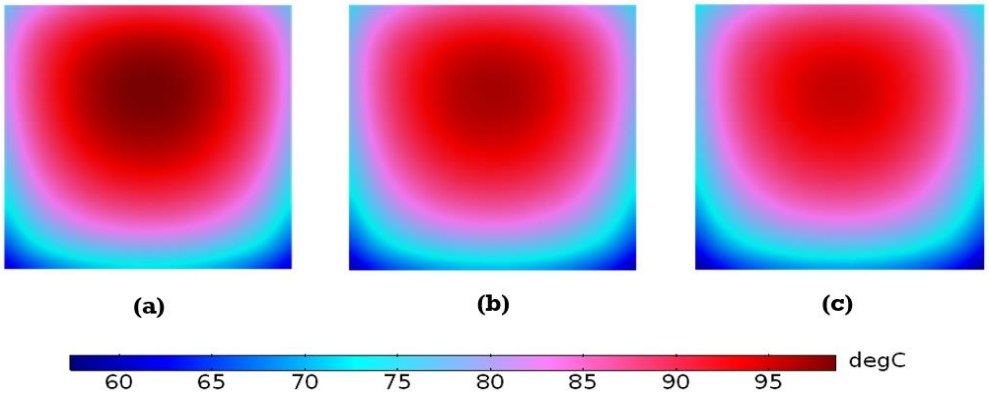

Figure 103 Temperature distribution of the MJ solar cell at CR= 2000 suns and Re=8.25 for (a) Water, (b) SiO_2/water, φ=2.5%,and (c) SiO_2/water, φ=5%.

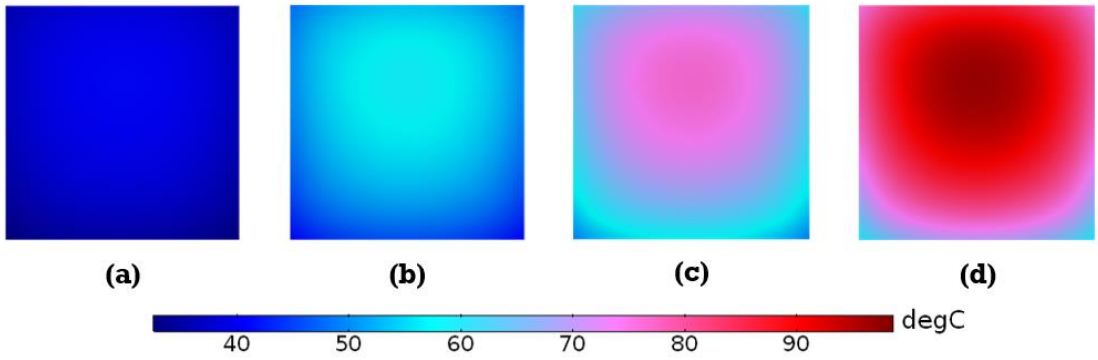

Figure 104 Temperature distribution of the MJ solar cell for (a) CR= 500 suns, (b) CR= 1000 suns, (c) CR= 1500 suns, and (d) CR= 2000 suns by using Al_2O_3/water, φ=5% at Re=8.25.

6.3.3 Solar cell temperature non-uniformity

Temperature non-uniformity can be defined as the difference between the maximum and minimum temperature of the solar cell. This term gives an indication of how uniform the temperature distribution is across the cell. The lower the value, the higher temperature uniformity (distribution). Figure 105 and Figure 106 present variation of the cell temperature non-uniformity with concentration ratios and volume fractions for Reynolds numbers of 8.25 and 82.5, respectively. From the graph, it can be seen that there is a clear reduction in the temperature non-uniformity as the volume fraction increases due to the enhancement in the fluid properties as discussed in the previous section. A reduction in temperature non-uniformity was obtained by decreasing the concentration ratio to 500 suns as it reached 8.8 °C by using SiO_2/water at 5% and Re=8.25. However, this enhancement is reduced as the Reynolds number increases due to the velocity augmentation. The lowest temperature non-uniformity is 6.38 °C at concentration of 500 suns by using 5% of SiO_2/water.

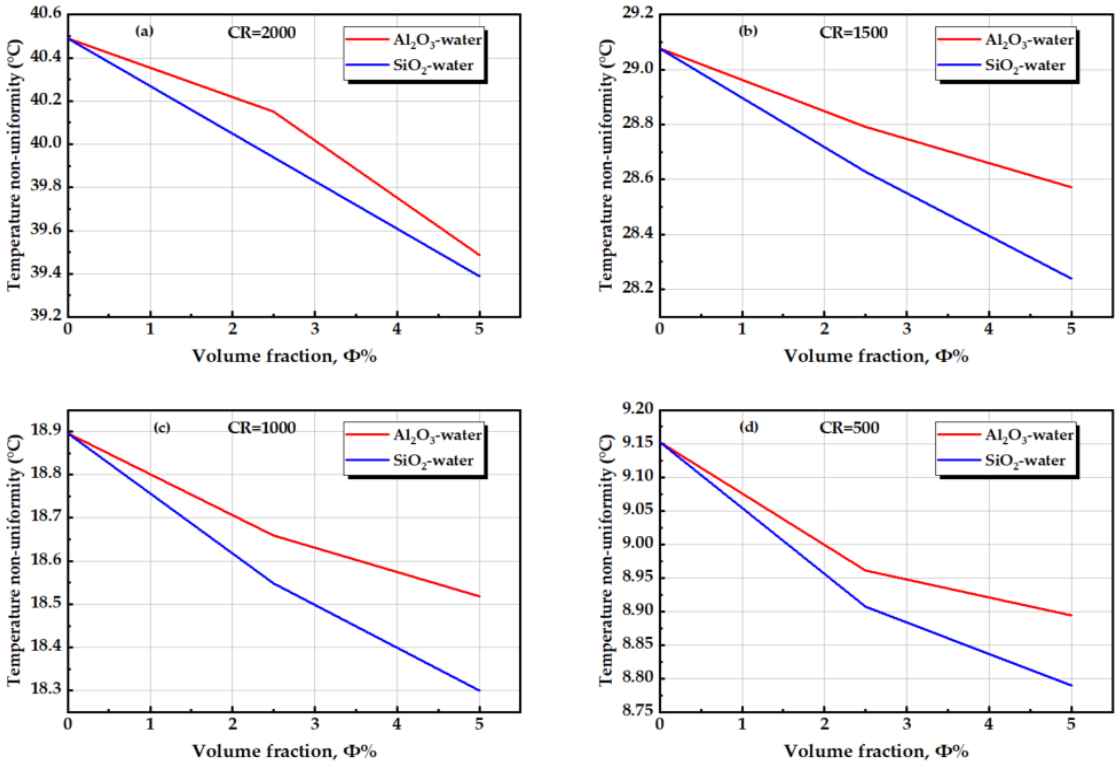

Figure 105 Variation of the cell temperature non-uniformity with volume fraction at (a) 2000 suns, (b) 1500 suns, (c) 1000 suns, (d) 500 suns and Re=8.25.

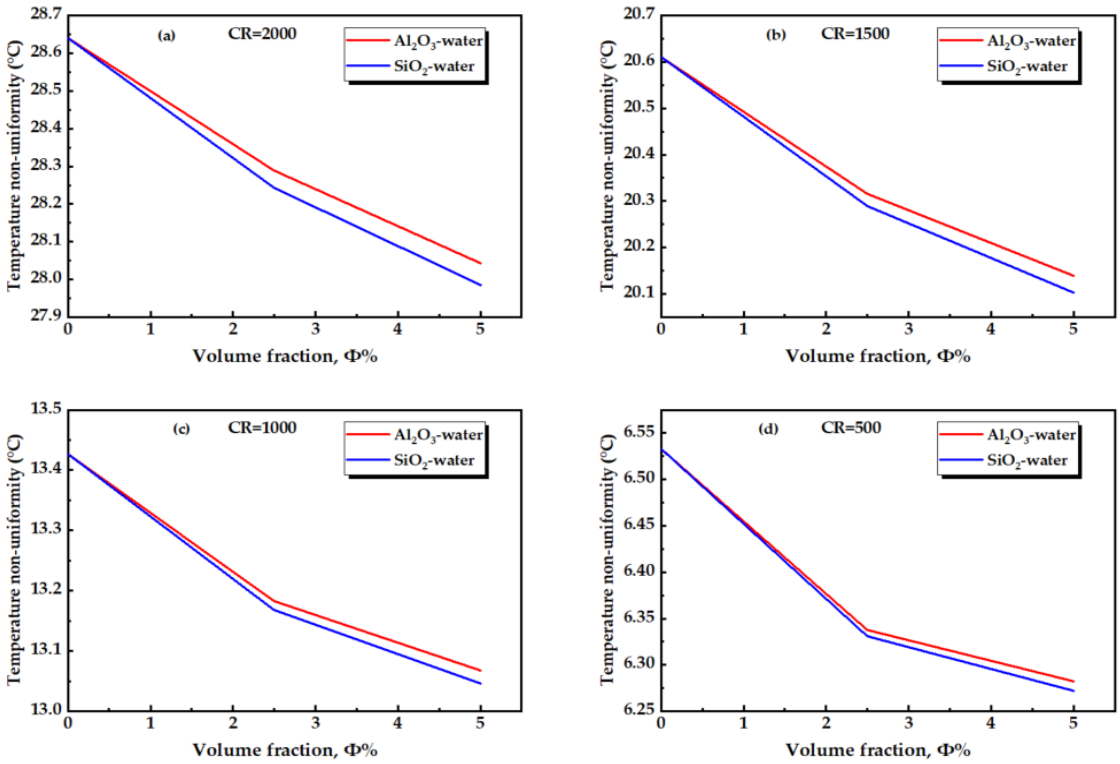

Figure 106 Variation of the cell temperature non-uniformity with volume fraction at (a) 2000 suns, (b) 1500 suns, (c) 1000 suns, (d) 500 suns and Re=82.5.

6.3.4 Heat sink thermal resistance and pressure drop

Thermal resistance is considered an important parameter to explore the performance of the heat sink and the working medium. Usually, lower values of thermal resistance indicate that the heat sink and the working medium are sufficiently effective to achieve a better temperature distribution for the solar cell. Also, a heat sink with a small thermal resistance prevents the solar cell from overheating. In addition, the pressure drop is an imperative factor to consider while using the nanofluids as it affects the net electrical power from the system as well as its electrical efficiency.

Figure 107 introduces the effect of the Reynolds number on both the heat sink thermal resistance and pressure drop for both types of nanofluids and pure water. From the two graphs, the pressure drop across the heat sink increases with the increase of the Reynolds number, while the opposite is observed in the case of heat sink thermal resistance. Also, as shown from the figures adding nanoparticles at a lower Reynolds number had a slight effect on the pressure drop. This effect increased as the Reynolds number increased. Besides that, the pressure drop of the nanofluids is more marked if compared with pure water due to the increase in the viscosity which is related to the existence of nanoparticles in the base fluid. For example, the maximum pressure drop (140 Pa) is observed by using SiO_2/water at φ=5%, while the lowest (100 Pa) occurred by using water at Re=82.5. On the other hand, the decrease in the thermal resistance using nanofluids can be attributed to the increase in the thermal conductivity and the decrease in the temperature difference between the inlet and maximum heat sink temperatures. The lowest achieved thermal resistance was 0.18 K/W at a volume fraction of 5% and Re=82.5.

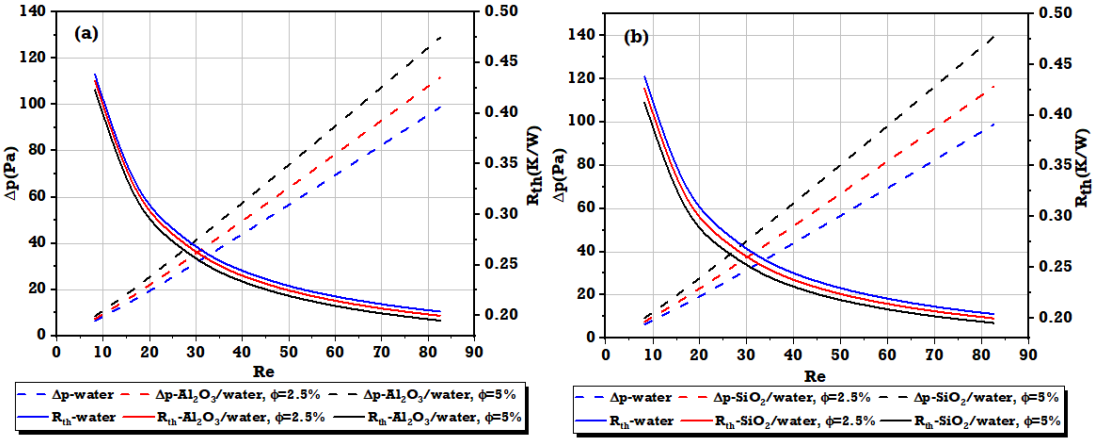

Figure 107 Variation of heat sink thermal resistance and pressure drop with Reynolds number for (a) Al_2O_3/water and (b) SiO_2/water at different concentrations.

6.3.5 Electrical, thermal, overall efficiencies

Table 14 concludes the performance limits of the HCPVT system at the minimum (CR=500 suns and Re=8.25) and maximum (CR=2000 suns and Re=82.5) working conditions using water and nanofluids. The table shows that the highest achieved electrical efficiency was 40.846% at Re=82.5, CR=500 suns and volume fraction of 5% . The electrical efficiency decreased by increasing the solar concentration, while it increased by increasing the volume fraction and Reynolds number. This can be attributed to the reduction in the reference solar cell efficiency while increasing the concentration ratio. Increasing the nanoparticles volume fraction had a positive impact on the electrical efficiency because of the reduction in the solar cell temperature as noticed in section 6.3.2.

Likewise, increasing the Reynolds number improved the electrical efficiency similarly because of the enhancement in the heat transfer process through the system which reduces the solar cell temperature. Overall, increasing the volume fraction of Al_2O_3/water to 5% at Re=8.25 improved the electrical efficiency by 0.067% and 0.29% at CR = 500 suns and 2000 suns respectively. However, at the same conditions SiO_2/water enhanced the efficiency by 0.36% and 0.47% respectively. This enhancement reduced by increasing the Reynolds number to reach 0.042% and 0.203% at the minimum and maximum concentration ratio respectively. This can be explained by the high reduction in the solar cell temperature caused by SiO_2/water if compared with Al_2O_3/water.

The thermal efficiency of the HCPVT system improved by increasing the solar concentration as a large portion of the concentrated solar irradiance is converted into heat through the solar cell. Further, it is noticed from the results that the thermal efficiency is enhanced by increasing both the Reynolds number and nanoparticles volume fraction. This is due to the enhanced heat capacity through the heat sink which increased the thermal energy carried by the fluid, thus leading to better thermal efficiency.

Besides, it is noted that the thermal efficiency enhancement by using SiO_2/water was higher than by using Al_2O_3/water. This is due to the high thermal capacity of SiO_2/water if compared with Al_2O_3/water. At 2000 suns, adding SiO_2 nanoparticles at 5% enhanced the thermal efficiency by 7.83% and 5.37% by using Al_2O_3 nanoparticles at the lowest Reynolds number. This improvement decreased to 1.36% and 0.8% by using SiO_2/water and Al_2O_3/water at the highest Reynolds number. This is because at a higher Reynolds number the velocity becomes effective which reduces the thermal effect of adding the nanoparticles.

Correspondingly the overall efficiency improved significantly due to the enhancement in the thermal and electrical power of the HCPVT system by adding the nanoparticles. The overall efficiency grows by adding nanoparticles to the base fluid and Reynolds number, while it declines by increasing the concentration ratio. The enhancement in the overall efficiency by adding nanoparticles was more noticeable at the lowest Reynolds number. The overall system efficiency increased by 4.68% and 3.82% by using SiO_2/water at 5% with CR=2000 suns and 500 suns respectively. Similarly, it improved by 3.2% and 2.68% by using Al_2O_3/water. Also, it is observed that the overall system efficiency enhanced slightly by using nanofluids at the highest Reynolds number. From the previous discussion, it can be clearly seen that implementing nanofluids with the HCPVT system leads to significant enhancement in the electrical, thermal, and overall efficiencies especially at the highest examined concentration ratio and the lowest Reynolds number.

Table 14 HCPVT system performance limits using water and nanofluids at different conditions.

			Al_2O_3/water			SiO_2/water				Al_2O_3/water			SiO_2/water		
CR	***φ***	**Min. Re**	η_{elec}	η_{th}	$\eta_{overall}$	η_{elec}	η_{th}	$\eta_{overall}$	**Max. Re**	η_{elec}	η_{th}	$\eta_{overall}$	η_{elec}	η_{th}	$\eta_{overall}$
suns	*%*		%	*%*	%	%	%	%		%	%	%	%	%	%
500	0	8.25	40.541	37.735	62.621	40.541	37.735	62.621	82.5	40.829	58.230	79.247	40.829	58.230	79.247
2000	0	8.25	31.686	42.453	59.311	31.686	42.453	59.311	82.5	32.955	64.555	78.008	32.955	64.555	78.008
500	2.5	8.25	40.556	38.630	63.349	40.563	39.125	63.750	82.5	40.841	58.454	79.435	40.841	58.618	79.567
2000	2.5	8.25	31.722	43.437	60.128	31.754	44.046	60.640	82.5	32.997	64.789	78.229	32.998	64.970	78.375
500	5	8.25	40.568	39.803	64.297	40.581	40.688	65.015	82.5	40.846	58.701	79.638	40.846	59.022	79.895
2000	5	8.25	31.778	44.732	61.208	31.834	45.775	62.087	82.5	33.022	65.050	78.458	33.022	65.407	78.744

6.3.6 Performance Evaluation Criterion

From the first law of thermodynamics perspective, if the ratio between the thermal energy and pumping power for a nanofluid is higher than that in the case of using the base fluid “water” it means that introducing nanofluid in the system is more efficient than using water. If the opposite occurs, it means that using a nanofluid has a negative effect on the performance of the system. Variation of PEC with the Reynolds number and volume fraction for both Al_2O_3/water and SiO_2/water is plotted in Figure 108. In general, PEC decreased with an increasing in the Reynolds number. In addition, water has better PEC values if compared with Al_2O_3/water and SiO_2/water at different concentrations.

This behaviour has been noticed before by Roy et al. [268] and Ferrouillat et al. [269]. Although SiO_2/water has shown better performance in the previous discussion in terms of thermal energy, it has the lowest PEC value. This can be interpreted by the large increase in the pressure drop (See Figure 107) in the case of the nanofluid if compared with the produced thermal energy. Therefore, although the nanofluids showed a better temperature distribution for the MJ solar cell, they had a negative impact on the pressure drop if compared with the produced thermal energy.

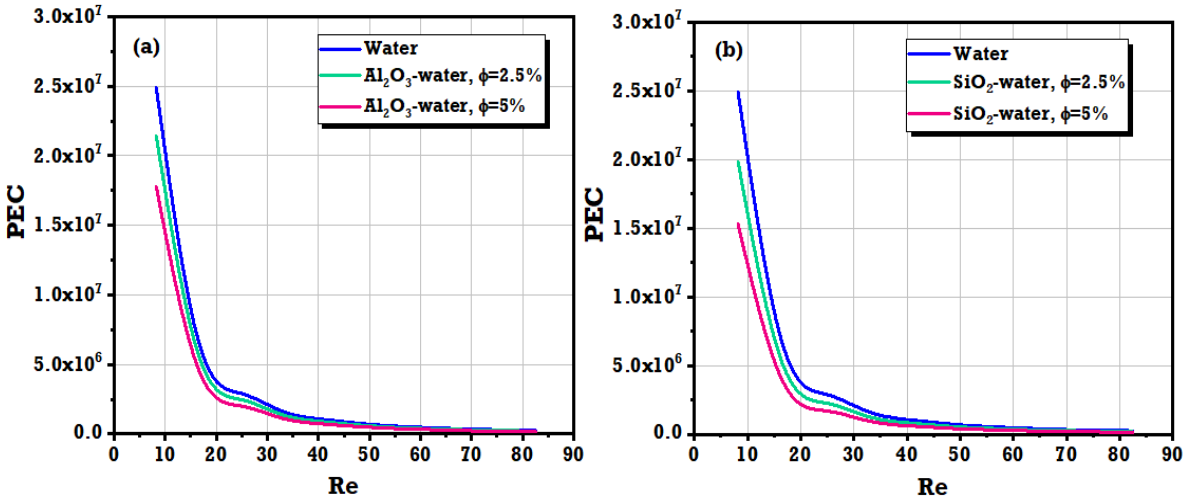

Figure 108 Variation of the Performance Evaluation Criterion with Reynolds number for (a) Al_2O_3/water and (b) SiO_2/water at different volume fractions.

6.4 Effect of using different configurations of heat sink: Straight channel, side inlet serpentine, centre inlet serpentine.

Performance analysis of different heat sink schemes (straight channel, side inlet serpentine, and centre inlet serpentine) for the HCPVT system is introduced in this section. This analysis includes the effect of different parameters (design of the heat sink, concentration ratio, and mass flow rate) on the temperature distribution and other system outputs.

6.4.1 MJ solar cell, outlet fluid temperature, and heat sink temperature distribution

The change in the volumetric maximum solar cell temperature with the mass flow rate and concentration ratio for different heat sink configurations are represented in Figure 109. At CR=2000 suns, the maximum solar cell temperature achieved by the SC arrangement exceeded the maximum recommended limit (MRL) at all the tested mass flow rates which makes it an inappropriate option in these conditions. In contrast, this configuration was able to maintain the solar cell temperature under the MRL for CR=1000 suns and 500 suns. This can be attributed to the low thermal energy released from the solar cell at these concentration ratios. In the CIS scheme, the fluid enters from the centre of the MJ solar cell and the heat is rejected from the side of the heat sink which guarantees a low solar cell temperature. This explains why the CIS configuration was able to reduce the solar cell temperature from 95.5 °C to 63 °C at CR=2000 suns with increasing the mass flow rate from 39 to 117 g/min. Also, using the SIS arrangement permitted more heat to be extracted from the system in comparison with the SC scheme due to the large heat transfer surface area offered by this configuration. For example, the SIS achieved a maximum solar cell temperature of 120 °C at $\dot{m}$=39 g/min and 39 °C at $\dot{m}$=117 g/min at CR=2000 suns and 500 suns, respectively. Hence, due to the sufficient level of mixing achieved using the CIS configuration, the outlet fluid temperature was high in comparison with the other arrangements as introduced in Figure 110a. The outlet fluid temperature reached as high as 74 °C at 2000 suns, while it decreased to 36 °C at 500 suns and mass flow rate of 39 g/min. On the other hand, increasing the mass flow rate decreased the outlet fluid temperature for all the configurations due to the increase in the fluid velocity.

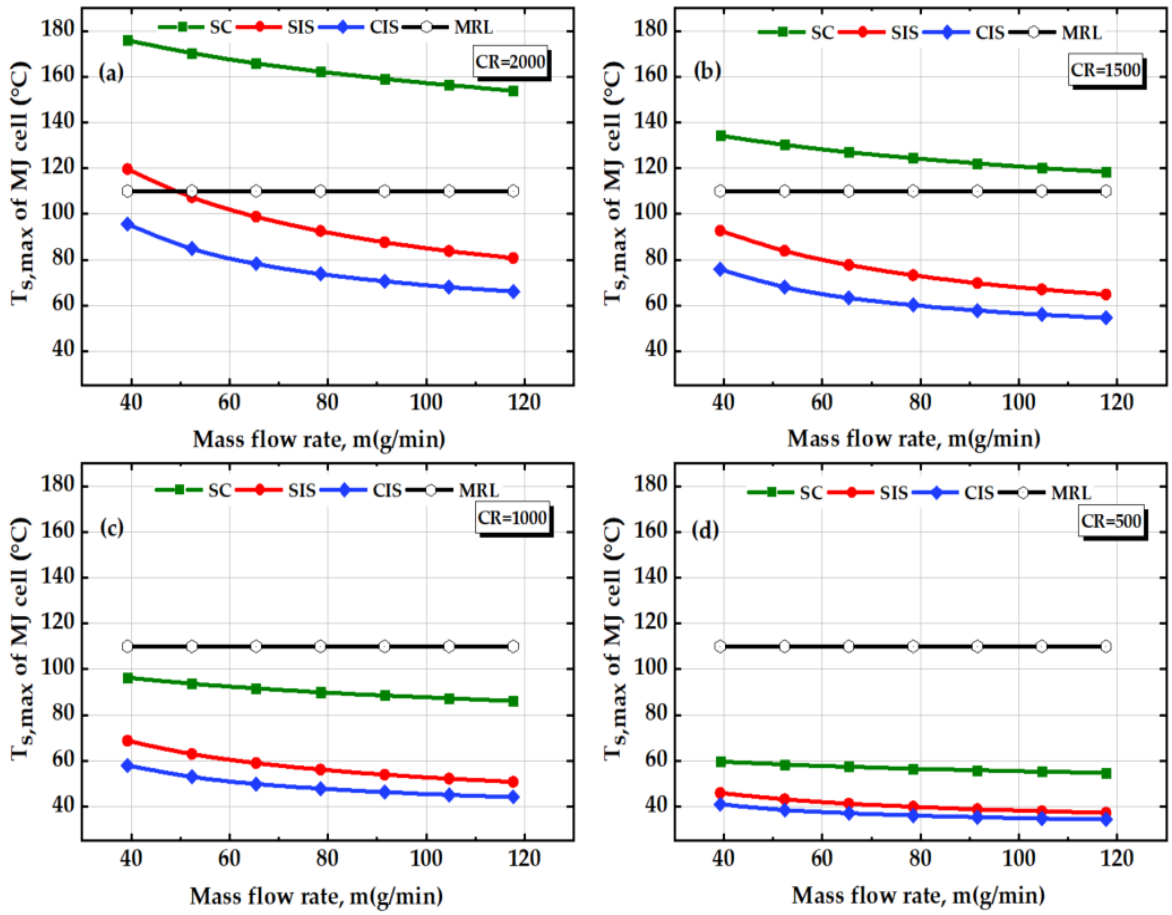

Figure 109 Variation of the MJ solar cell maximum temperature with mass flow rate for different cases and concentration ratios.

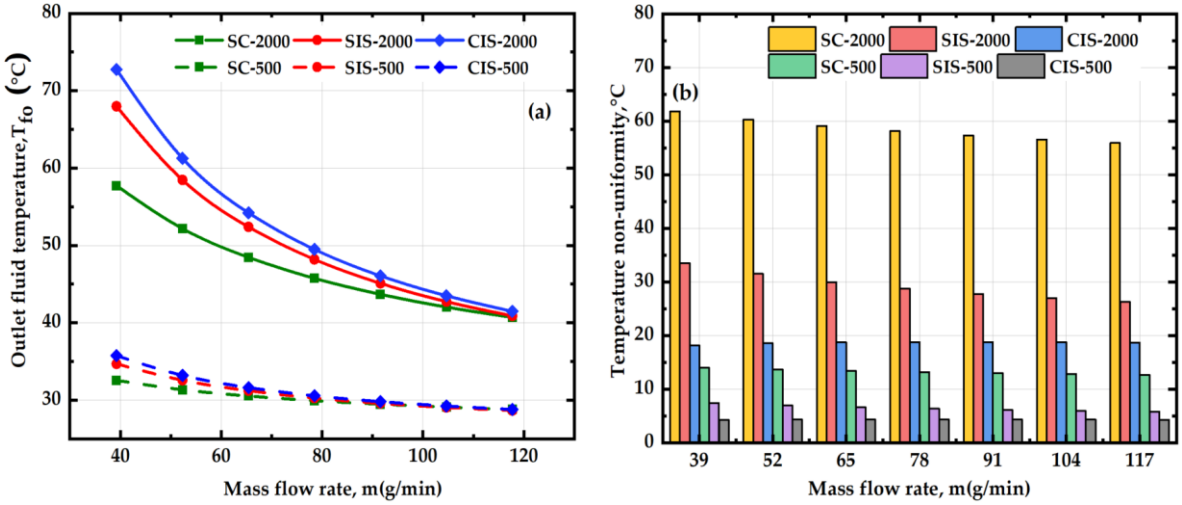

Figure 110 Variation of (a) outlet fluid temperature (b) temperature non-uniformity with mass flow rate for different cooling schemes at CR=2000 suns and 500 suns.

Temperature non-uniformity is defined as the difference between the maximum and minimum solar cell temperatures which measures how evenly the temperature is distributed on the surface of the solar cell. Figure 110b describes the change in the

solar cell temperature non-uniformity with the mass flow rate at the maximum and minimum studied concentration ratios. The worst temperature distribution is attained by the SC design due to the flow maldistribution at the surface of the solar cell, while a favourable effect has been achieved by using the CIS heat sink as the temperature non-uniformity reached as low as 18 °C and 4 °C at CR=2000 suns and 500 suns respectively.

In the case of the SIS arrangement, the distribution is enhanced in comparison with the SC as it reached 34 °C and 7 °C at $\dot{m}$=39 g/min and CR=2000 suns and 500 suns respectively. This can be ascribed to the formation of the fluid stagnation zones near the solar cell surfaces which allowed more thermal energy to be extracted in the case of the SIS and CIS schemes. The solar cell temperature distribution is represented in Figure 111. The formation of the hotspots is larger in the case of the SC, especially at the highest studied concentration ratio. This hotspot decreased as the mass flow rate increased and the concentration ratio decreased due to the low heat released from the solar cell as well as the increase in the flow velocity which enhanced the heat transfer process. As described in the graphs earlier, the formation of the temperature hotspot diminished by using the CIS configuration which helps to maintain the solar cell temperature under the recommended limit. Also, this design followed by the SIS allowed a uniform temperature distribution not only for the solar cell but also for the heat sink as illustrated in Figure 112. This graph shows the temperature contours at the midplane (section B-B) for different cases at $\dot{m}$=39 g/min and concentration ratio of 2000 suns.

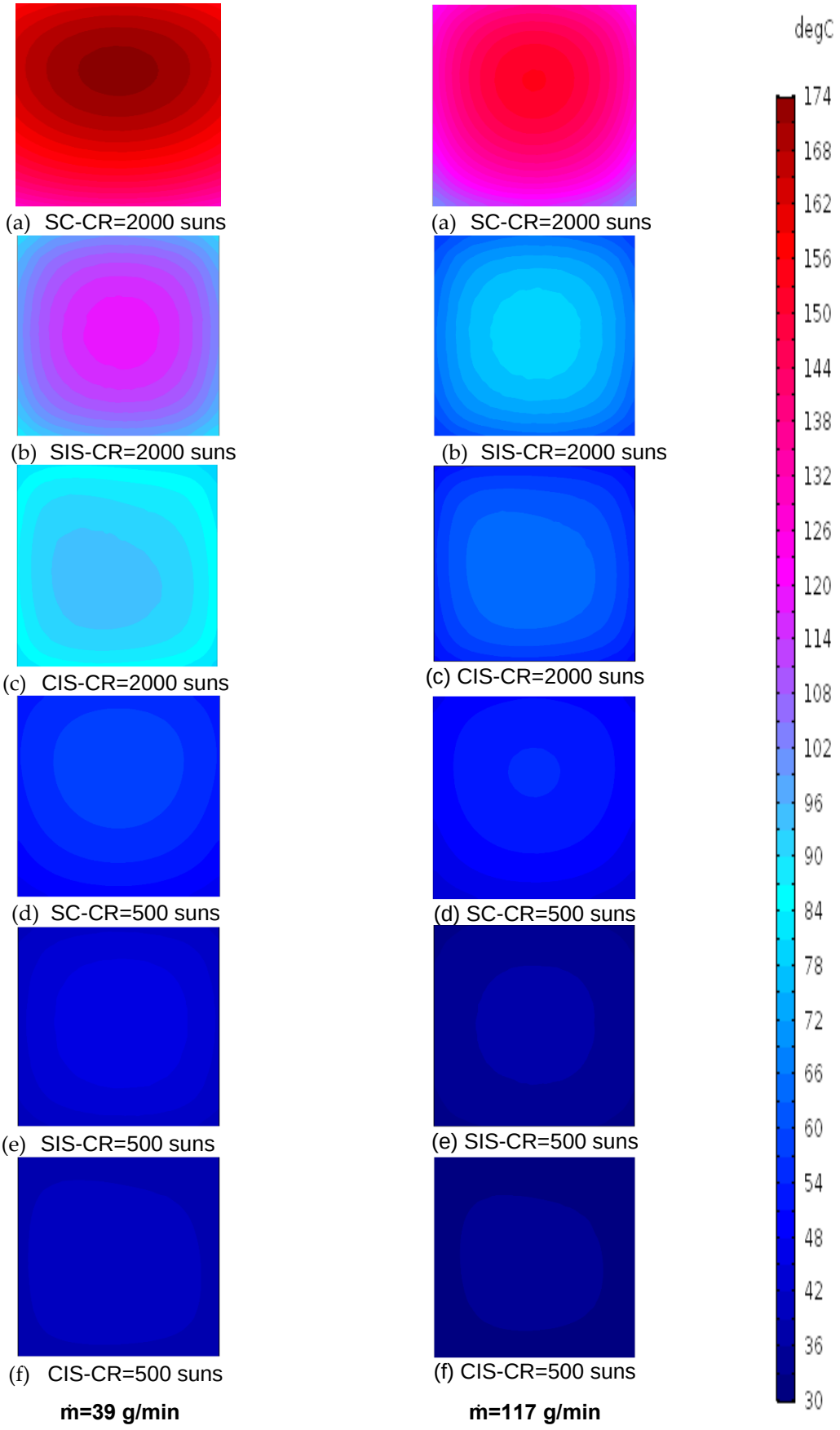

Figure 111 MJ solar cell temperature distribution for different configurations, mass flow rates, and concentration ratios.

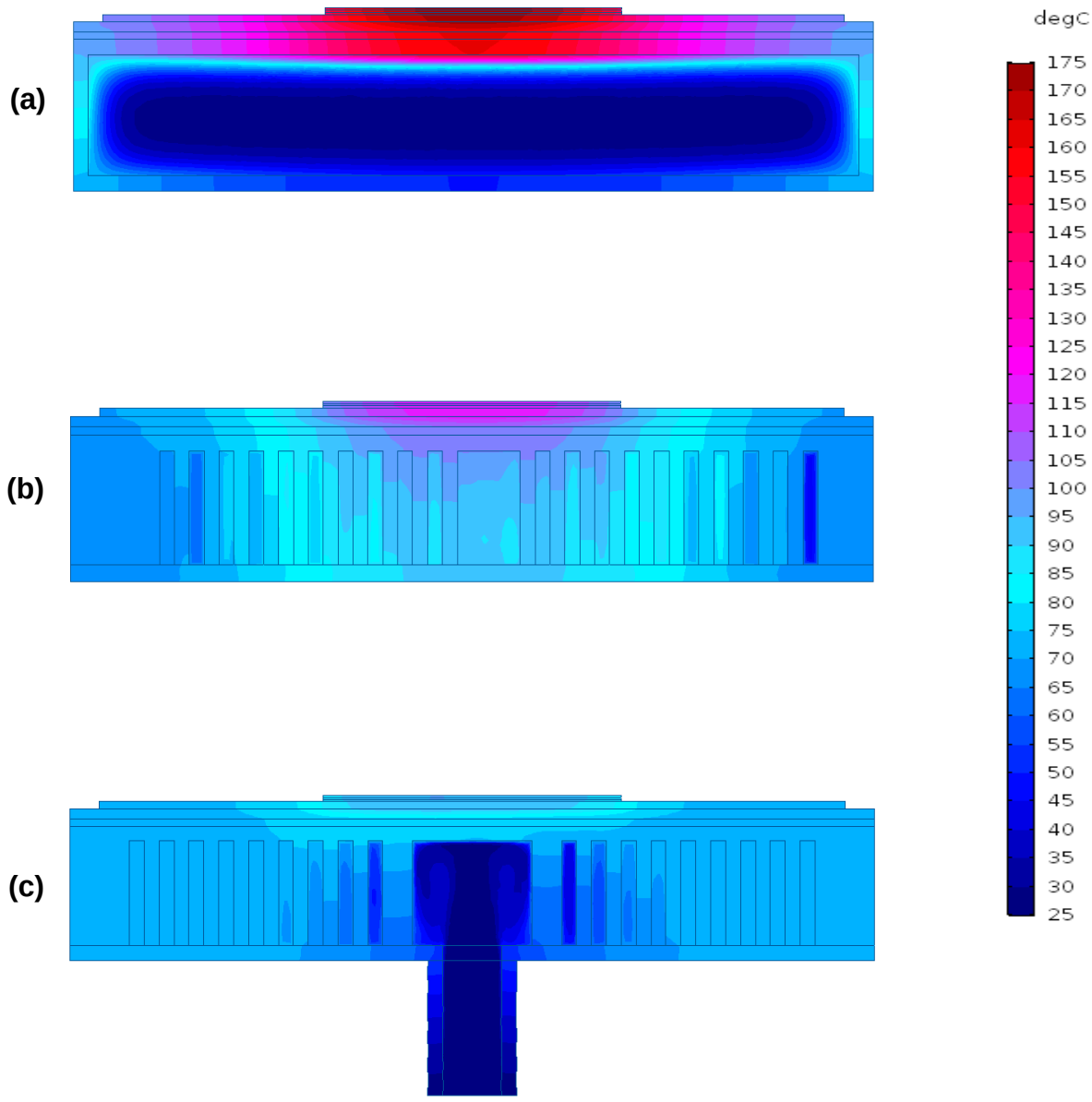

Figure 112 Temperature contour for the HCPVT system at section (B-B) at ṁ=39 g/min and CR=2000 suns for (a) SC, (b) SIS, (c) CIS.

6.4.2 HCPVT energy performance analysis

Pumping power is a measure of how much energy is required to overcome the pressure drop and allow fluid flow through the heat sink. Figure 113a compares the power consumption of the considered HCPVT systems. The comparison has been undertaken considering the change in the mass flow rate and the concentration ratio limits. In general, there is a gradual increase in the pumping power consumptions with an increase in the mass flow rate for both the SIS and CIS reaching 0.11 W and 0.1 W at ṁ=117 g/min, CR=500 suns, and 2000 suns, respectively. This can be assigned to the increase in the flow velocity that occurred with an increase in the mass flow rate.

Also, a slight increase in the pumping power is observed at a lower concentration ratio due to the increase in fluid viscosity with a decrease in the fluid temperature. To examine the heat sink efficiency, thermal resistance is considered as a key parameter.

Figure 113b shows the variation of the heat sink thermal resistance with water mass flow rate and concentration ratio limits. It can be noticed that the lowest thermal resistance is obtained by the CIS design varying from 0.4 to 0.18 K/W for ṁ=39 g/min and 117 g/min, respectively. Also, the thermal resistance changed from 0.58 to 0.28 K/W for the SIS and reached as high as 1.05 K/W for SC at ṁ=39 g/min. The enhancement observed by using the SIS and CIS is due to the improvement in the heat sink temperature distribution (as discussed earlier) which leads to a reduction in the difference between the maximum surface and fluid inlet temperatures.

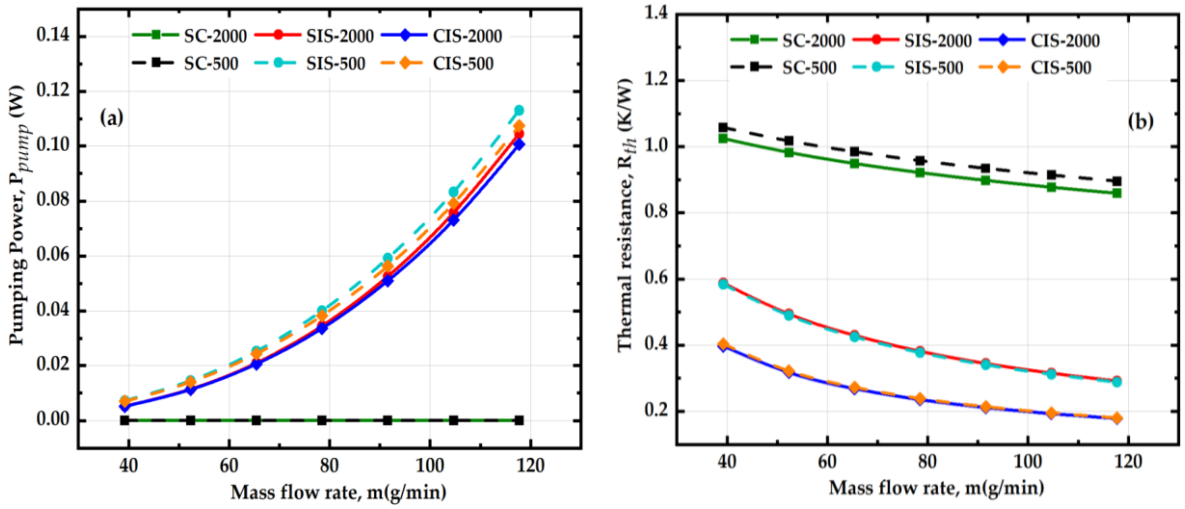

Figure 113 Variation of (a) Pumping power and (b) Thermal resistance of the HCPVT system with mass flow rates for the different studied configurations.

Figure 114 depicts the behaviour of the HCPVT electrical and thermal efficiencies at different conditions. This change is plotted against the mass flow rate and solar concentration ratios. The thermal efficiency varied from 65.23% to 67% for CIS at CR=2000 suns, while in the case of SIS and SC it fluctuated between 64% to 40% at ṁ=117 and 39 g/min and corresponding concentration ratio of 2000 suns and 500 suns respectively. In the case of the electrical efficiency, it reached as high as 40.8% by using the CIS at 500 suns and 117 g/min, whereas it dropped to 31% for SIS design at 2000 suns.

It is important to note that increasing the water mass flow rate enhanced thermal efficiency. This can be explained by increasing the thermal energy carried by the fluid

which leads to an improvement in thermal efficiency. The same behaviour is noticed for electrical efficiency because of the notable enhancement in the solar cell temperature with the mass flow rate as discussed in the previous section. Decreasing the solar concentration leads to a reduction in the thermal efficiency for different configurations as seen from the graph due to the reduction in the waste heat released from the solar cell. In contrast, a significant enhancement has been observed in electrical efficiency because of the decrease in the solar cell temperature. Moreover, it can be observed that both the electrical and thermal efficiencies achieved by using the CIS outperformed the SIS and SC designs due to the remarkable enhancement in the heat transfer process through the system.

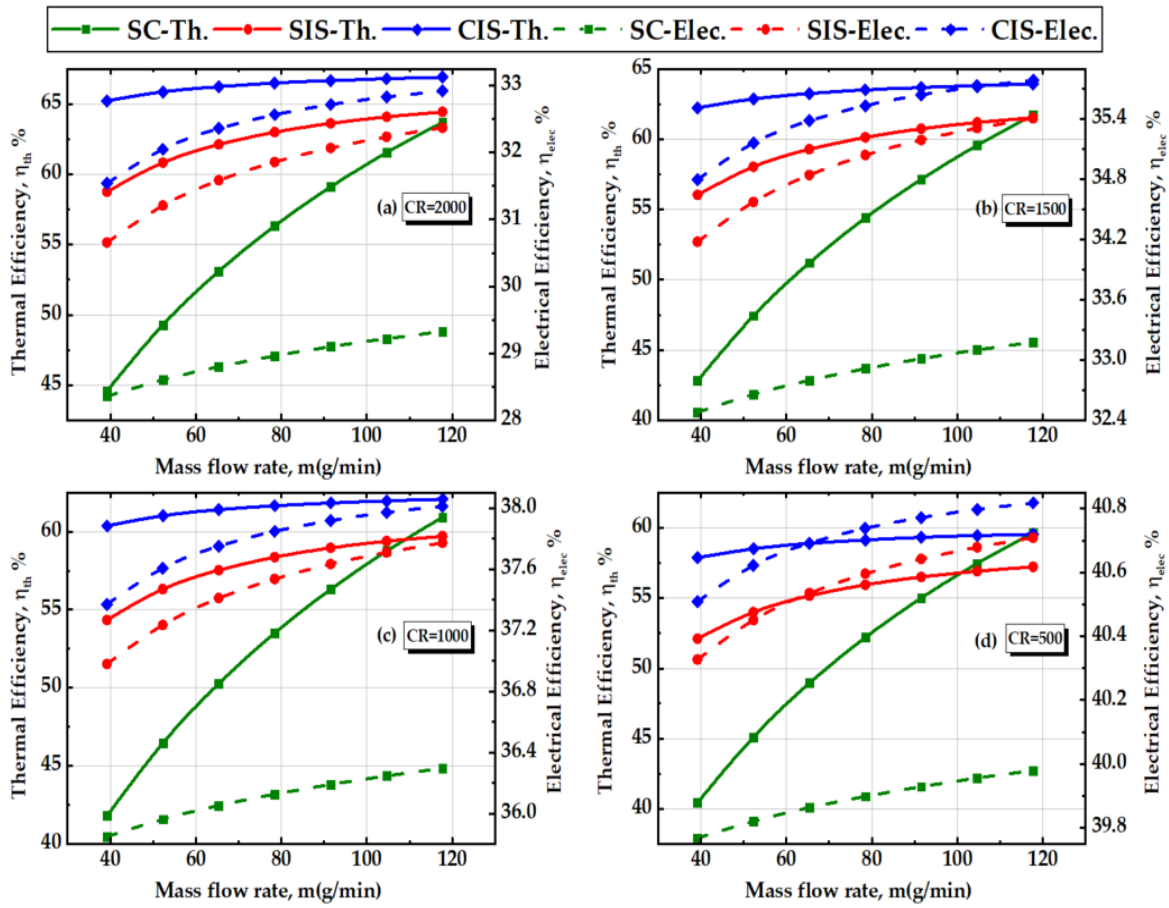

Figure 114 Variation of the thermal and electrical efficiencies for different heat sink configurations for the HCPVT systems for concentration ratios of (a) 2000 suns, (b) 1500 suns, (c) 1000 suns,(d) 500 suns and mass flow rates.

As a result of the significant improvement in both the electrical and thermal efficiencies using the CIS configurations, the overall efficiency of the HCPVT system has improved as introduced in Figure 115. Also, increasing the mass flow rate has a significant

impact on boosting overall efficiency. It has been raised to 80% at $\dot{m}$=117 g/min using the CIS at concentration ratio of 2000 suns, while it declined to 64% using the SC at 500 suns. Overall, the CIS overall performance was promising compared to the other configurations at the tested concentration ratios.

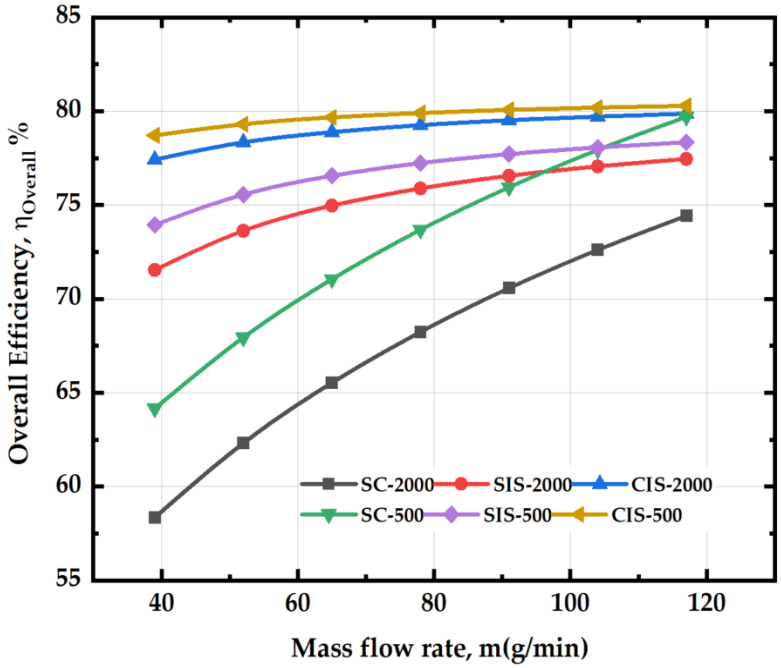

Figure 115 Variation of the HCPVT overall efficiency with mass flow rate for different heat sink configurations for CR=2000 suns and 500 suns.

6.4.3 HCPVT exergy performance analysis

A significant parameter to evaluate the performance of the system effectively and accurately is exergy analysis. Figure 116 represents the variation of thermal and electrical exergetic efficiencies with mass flow rate and concentration ratios. It is observed that the electrical exergy efficiency improved by increasing the mass flow rate, while the opposite has occurred in the case of the thermal exergy efficiency. This can be explained by increasing the mass flow rate reduces the difference between the fluid outlet and inlet temperatures which causes a low thermal exergy rate which is followed by a low thermal exergy efficiency. On the other hand, electrical exergy efficiency is enhanced because of the significant improvement in the electrical exergy rate. Also, from the graph, it can be seen that the effect of reducing the concentration ratio has a remarkable impact on both the electrical and thermal exergetic efficiencies which produced low thermal exergy content while more exergy became available as an electrical form. Therefore, the highest total exergetic efficiency (35.2%) was

obtained by the CIS followed by SIS (34.8%) at $\dot{m}$=39 g/min and CR=500 suns as illustrated in Figure 117. Also, at a concentration ratio of 2000 suns, the total exergetic efficiency reached 31.6% and 30% for the CIS and SIS respectively. These values are decreasing gradually with an increase in the mass flow rate. Therefore, for better total and thermal performances of the HCPVT system, it is preferred to run at low flow rate ranges.

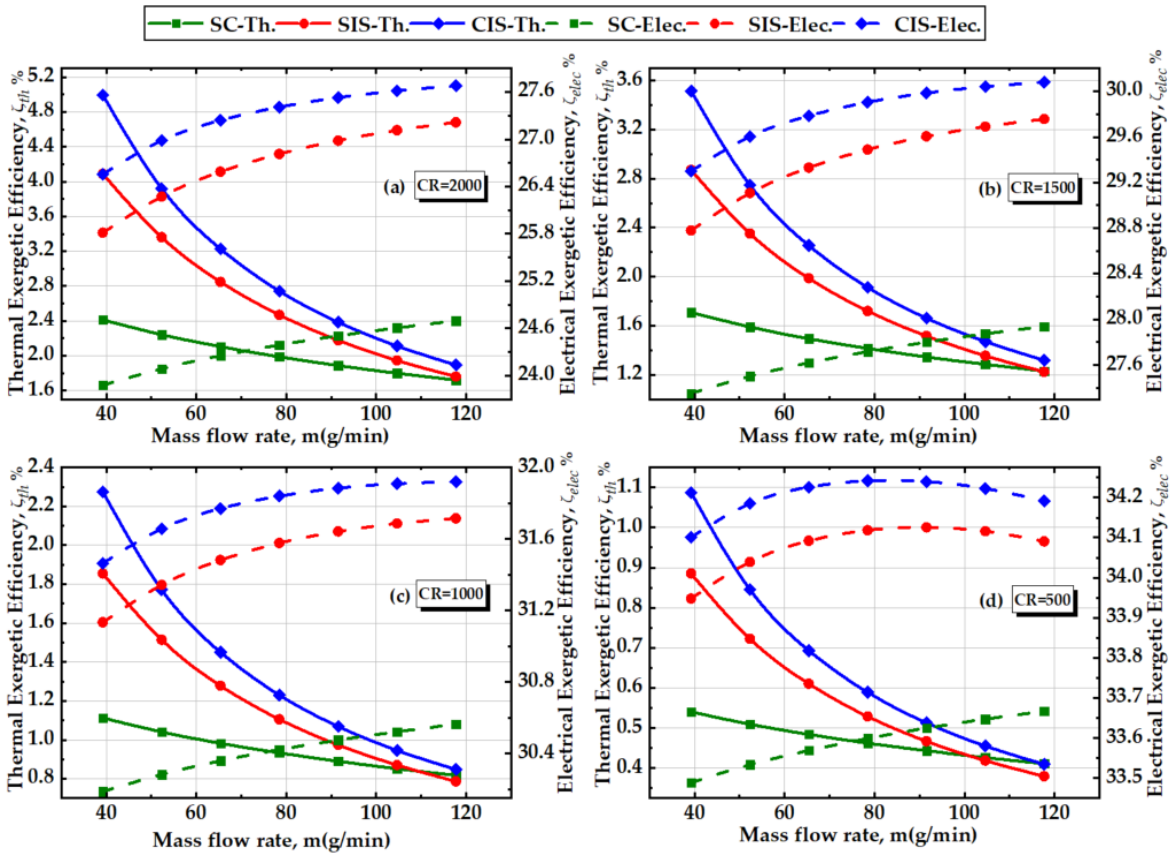

Figure 116 Variation of the thermal and electrical exergetic efficiencies with mass flow rate for different cooling schemes for (a) 2000 suns, (b) 1500 suns, (c) 1000 suns,(d) 500 suns.

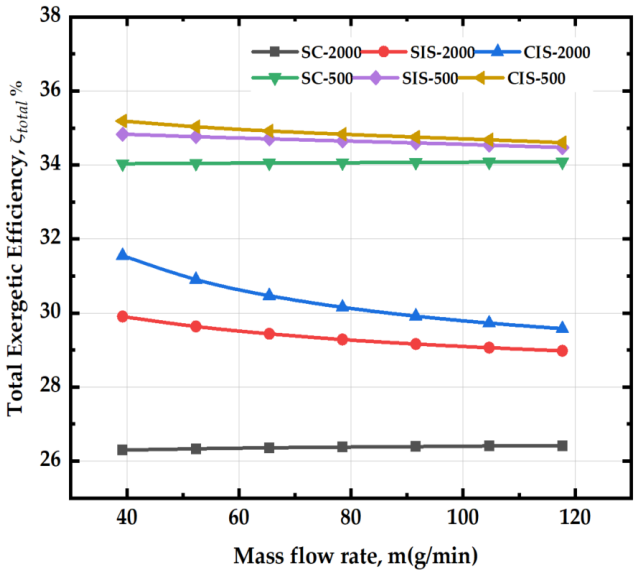

Figure 117 Variation of the total exergetic efficiency with mass flow rate for different heat sink configurations for CR=2000 suns and 500 suns.

6.4.4 Case study

To complete the analysis, the performance of the proposed configuration (CIS) is analysed by considering different real weather conditions that are available in the literature [270] of the city of Alexandria, Egypt (Longitude/Latitude: E 029°42'/N 30°55') on a clear day at 5th of May 2015 from 9:00 AM to 15:00 PM. These meteorological data include incident solar radiation, which was measured by a Pyranometer, while the ambient temperature and wind speed were obtained by Log weather station. Figure 118 shows the variation of the incident solar radiation, ambient temperature and windspeed. The highest values of solar radiation and ambient temperature obtained at the noon (12:00 PM) were about 955 W/m^2 and 34 °C , respectively, which represent a hot climate condition. The wind speed varied between 0.9 m/s to 1.7 m/s.

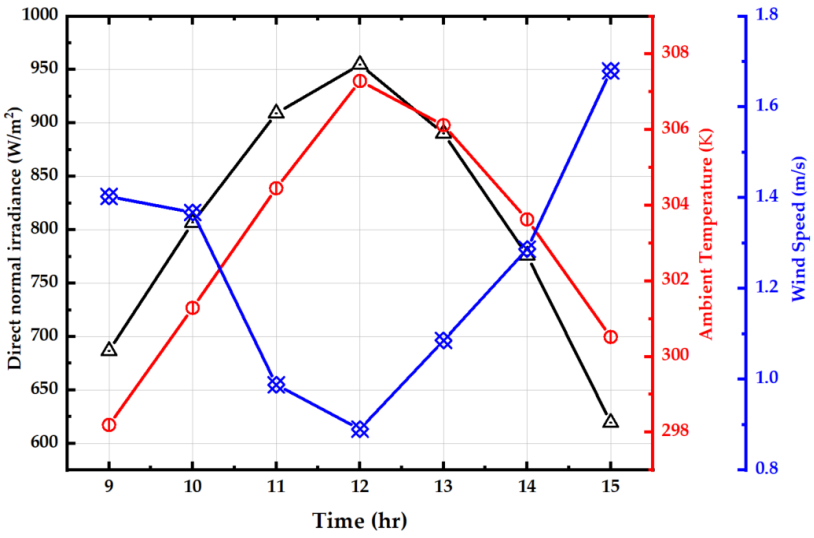

Figure 118 Hourly variation of direct normal irradiance, ambient temperature, and wind speed on 5th May 2015 in Alexandria, Egypt.

Figure 119 illustrates the change in the maximum solar cell temperature and power output based on the hourly real weather conditions for CR=2000 suns and 500 suns. The predicted maximum solar cell temperature of the system reached the peak at the solar noon when the solar radiation has its maximum value, and the wind speed is very low. For 2000 suns, the maximum calculated solar cell temperature reached 100 °C at $\dot{m}$=39 g/min, while it decreased with increasing the mass flow rate to 73 °C at $\dot{m}$=117 g/min at 12:00 PM. Using this configuration, the maximum solar cell temperature varied between 48 °C and 42 °C at $\dot{m}$=117 and 39 g/min, respectively. The estimated power output varied between 41 W, 12.5 W and 62 W, 19 W for CR=2000 suns and 500 suns as it is strongly dependent on the solar radiation.

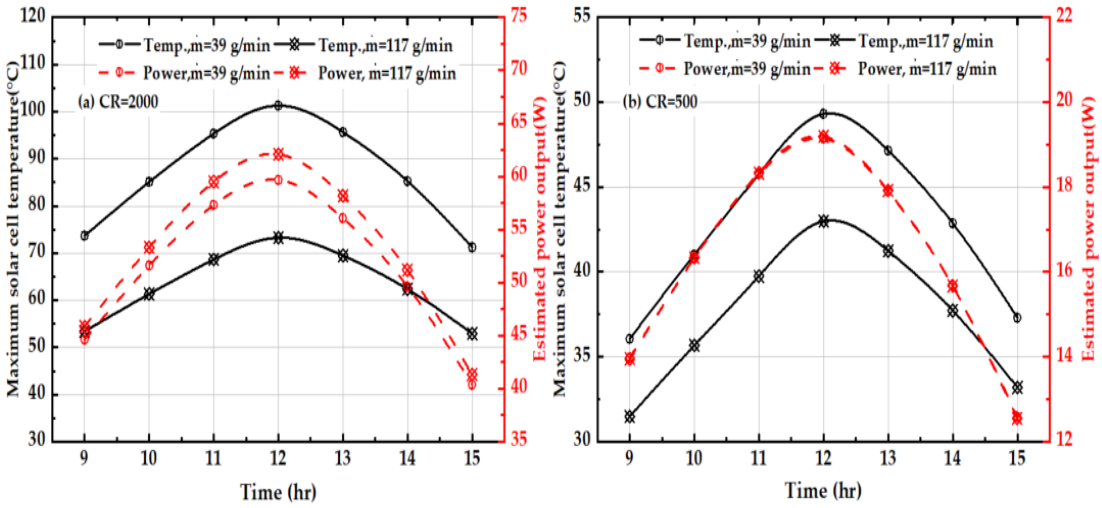

Figure 119 Hourly variation of the maximum solar cell temperature and estimated power output for mass flow rates of 39 g/min and 117 g/min at (a) CR=2000 suns, and (b) CR=500 suns.

6.5 Conclusion

This chapter investigated the performance of an actively cooled HCPVT system based on a single MJ solar cell using different coolants and heat sink arrangements. In the first section (condition 1), the performance of the HCPVT system was assessed using a finned minichannel heat sink with different coolants (water, ethylene glycol/water mixture, and syltherm oil). In terms of solar cell temperature, water offers the most uniform temperature distribution and the lowest volumetric temperature at the examined flow rates and concentration ratios. Further, in terms of the outlet temperature, syltherm oil 800 showed the highest fluid temperature especially for a concentration ratio above 1000 suns, which would be suitable for thermal applications that require a high temperature. At a high concentration ratio (above 1000 suns), using syltherm oil reduced the electrical efficiency by more than 1% when compared with water, while at lower concentration ratios the reduction was insignificant. Water achieved the highest thermal efficiency due to its high specific heat, followed by ethylene glycol mixture and then syltherm oil 800. Overall, deciding which fluid to be used depends mainly on the designed concentration ratio, the required outlet temperature, and thermal energy to be recovered.

In the second section (condition 2), the feasibility of using nanofluids as a heat transfer media using experimentally measured thermal conductivity values was considered with a finned mini-channel heat sink. The effectiveness of heat transfer increased from 1.058 to 1.15 in the case of Al_2O_3/water at 5%, reaching 1.11 using SiO_2/water. The maximum temperature of the MJ solar cell dropped by 3.6 °C by using nanofluids at a solar concentration ratio of 2000 suns. The nanofluids maintained a uniform temperature distribution on the surface of the MJ solar cell. In contrast, adding nanoparticles to the base fluid had a negative impact on increasing the pressure drop. Utilizing nanofluids had a considerable effect on the electrical, thermal, and overall efficiencies of the HCPVT as they increased by 0.47%, 7.83%, and 4.68% respectively at Re of 8.25 and concentration ratio of 2000 suns using SiO_2/water. Overall, the effect of using nanofluids was significant when the solar concentration had a high value. This impact weakened with decreasing the solar concentration and increasing the Reynolds number. Nanofluids may be more efficient in applications that have high heat flux and where temperature control is paramount [271,272]. Although introducing nanofluids to

the HCPVT system had a significant impact on the overall performance of the system, the performance evaluation criterion decreased by introducing these types of fluids.

The third section (condition 3) examined different heat sink configurations as heat extraction mechanisms for the MJ solar cell including straight channel, side inlet serpentine, and centre inlet serpentine. The centre inlet serpentine heat sink outperformed the other arrangements from energy and exergy perspectives as it achieved a lower solar cell temperature as well as uniform temperature distribution. For a concentration ratio higher than 1000 suns, the straight channel heat sink is not recommended as this can cause long-term degradation for the solar cell as the maximum temperature exceeded 110 °C. Employing the centre inlet serpentine at concentration of 2000 suns followed by the side inlet serpentine better protects the cell from deterioration. A centre inlet serpentine is an effective cooling method for the high concentrator photovoltaic system as it maintains the solar cell temperature below the maximum recommended limit for all the concentration ratio ranges in comparison with the other configurations.

Both the thermal and electrical energy efficiencies were improved at a higher mass flow rate resulting in higher overall efficiencies. In contrast, from the exergy analysis perspective, it is recommended that the system runs at a low flow rate range for better total and thermal performance. For that design, the maximum temperature, overall efficiency, and total exergy efficiency were 95.5 °C, 78%, and 31.6% at a mass flow rate 39 g/min and concentration 2000 suns, respectively. For the tested real weather conditions, the solar cell temperature and predicted power output reached 100 °C and 62 W and 48 °C and 19 W for 2000 suns and 500 suns, respectively at the solar noon. Table 15 summarises the studied cases included in this chapter and the obtained thermal, electrical, and overall efficiencies at concentration ratios of 500 suns and 2000 suns.

Table 15 Efficiencies' limits of different studied cases introduced in the chapter.

Conditions	**Type**	η_{elec}(%)		η_{th}(%)		$\eta_{overall}$(%)	
		500 suns	2000 suns	500 suns	2000 suns	500 suns	2000 suns
Condition 1 (section 6.2)	Water	40.829	32.955	58.230	64.555	79.247	78.008
	Ethylene glycol/water	40.799	32.820	56.753	62.767	78.043	76.469
	Syltherm oil	40.708	32.397	51.326	57.448	73.627	71.876
Condition 2 (section 6.3)	Water	40.829	32.955	58.230	64.555	79.247	78.008
	Al_2O_3/water, φ=2.5%	40.841	32.997	58.454	64.789	79.435	78.229
	Al_2O_3/water, φ=5%	40.846	33.022	58.701	65.050	79.638	78.458
	SiO_2/water, φ=2.5%	40.841	32.998	58.618	64.970	79.567	78.375
	SiO_2/water, φ=2.5%	40.846	33.022	59.022	65.407	79.895	78.744
Condition 3 (section 6.4)	Straight channel	39.979	29.327	59.641	63.698	79.697	74.421
	Side Inlet Serpentine	40.709	32.372	57.212	64.443	78.337	77.452
	Centre Inlet Serpentine	40.837	32.960	59.540	66.912	80.301	79.897

Chapter 7
Thermal management of a high concentrator photovoltaic system

7.1 Introduction

In this chapter, a number of investigation approaches of a Fresnel lens based HCPVT system are introduced. Indoor experimental investigations of the system under several scenarios are considered including optical, thermal, and electrical analyses. The first section (7.2) investigates the use of an optical filter to regulate the temperature of a silicon solar cell. Section 7.3 introduces a Fresnel lens focal spot analysis. Experimental investigation of the HCPVT system by using an electric resistance heater is presented in section 7.4 including the effect of heat sink configurations, working media and other important factors. In addition, a numerical model for this case is validated. Finally, an indoor study of the HCPVT system using the solar simulator and the Fresnel lens is analysed and the performance parameters are evaluated.

7.2 Effect of using an infrared filter on the performance of a silicon solar cell

The performance of a single junction silicon solar cell with an added IR filter subjected to solar irradiances of 400 and 1000 W/m^2 from a Fresnel lens is investigated. This is an experimental investigation into the effects of IR filters on cell performance. For high and ultrahigh concentrations there will be much higher cell efficiency losses due to the high concentration of harmful IR wavelengths and high cell temperatures. Although the HCPV system would utilize a multi-junction concentrator cell, the concentration ratios will still be beyond the cell's recommended working range, similar to the silicon cells used in these experiments. Also, these investigations were conducted with a single junction solar cell to avoid the damaging of the more expensive multi-junction concentrator. Figure 120 presents the caracks that occurred to the silicon solar cell during the test when no filter was used at solar intensity of 1000 W/m^2.

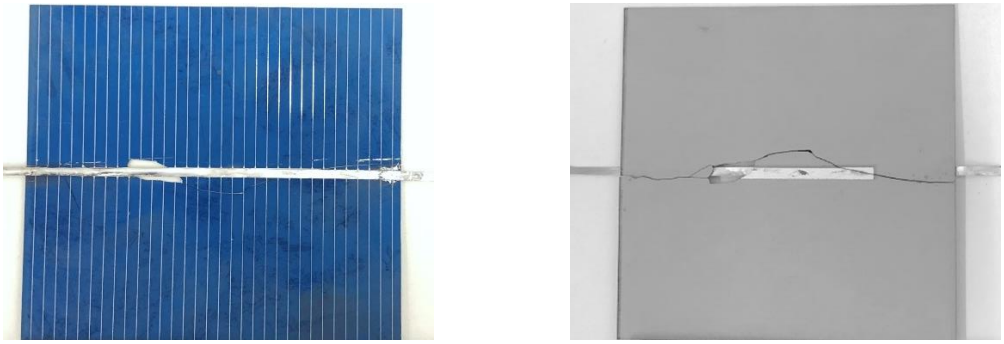

(a) **(b)**

Figure 120 Cracks occurred during the test without using the IR filter (a) top of the cell and (b) rear of the cell.

7.2.1 Experimental approach

The experimental setup used throughout the investigation is presented in Figure 121. The primary optical component of the HCPV system is a silicon on glass (SoG) Fresnel (FR) lens which is placed underneath a WACOM continuous solar simulator to simulate the solar irradiance from the sun. Also, it is connected to an I-V tracer for the measurements of solar cell electrical performance. An infrared filter is placed above the silicon solar cell to protect it from the harmful wavelengths as shown in Figure 121d. The lens is used to concentrate the light from the solar simulator on a single-junction silicon solar cell. Before recording any measurements, the Fresnel lens height was adjusted and measured along with the focal width for the maximum concentration and electrical output. The measured focal length and focal spot width are 42 cm and 2.8 cm respectively.

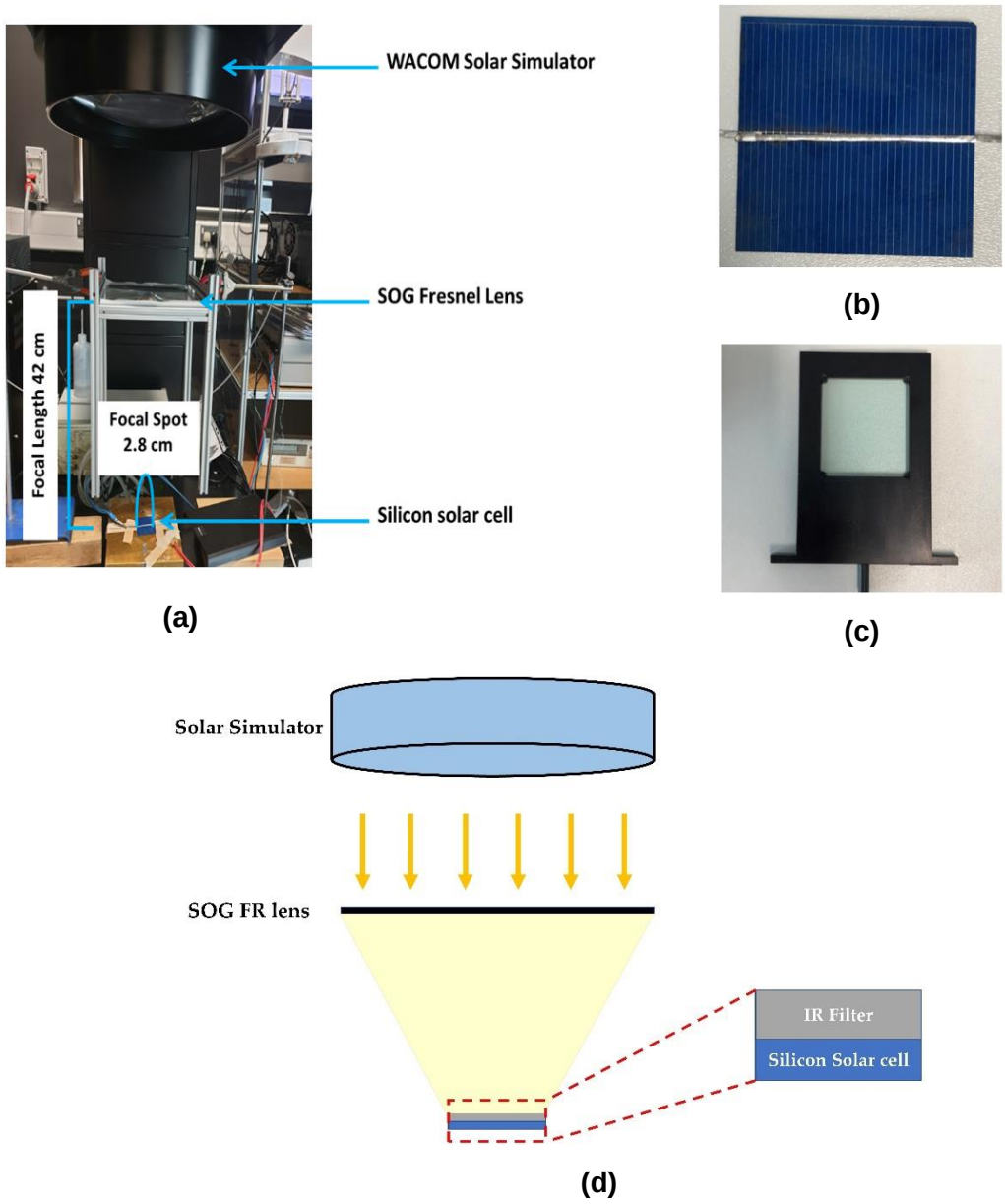

Figure 121 (a) The experimental setup used throughout the experiments, (b) silicon solar cell, (c) IR filter, (d) schematic diagram of the testing showing the IR filter is placed above the cell.

7.2.2 Theoretical approach

The concentration ratio (CR), 86 suns, is defined as the ratio between the Fresnel lens area (A_{lens}) to the focal spot area (A_{fo}):

$$CR = A_{lens} / A_{fo} \quad (7.1)$$

The geometrical cell concentration ratio (GCR), 20.3 suns, is calculated using the following relation:

$$GCR = A_{lens} / A_{cell} \quad (7.2)$$

The term A_{cell} is defined as the cell area. The effective solar irradiance, I_{eff}, can be defined as the actual incident solar irradiance on the surface of the solar cell after passing through the Fresnel lens:

$$I_{eff} = DNI\ \tau_{lens}\ \tau_{IR}\ CR \tag{7.3}$$

Where DNI, τ_{lens}, and τ_{IR} are the direct normal irradiance, average transmittance of the Fresnel lens, and average transmittance of the IR filter, respectively. The power incident on the cell can be calculated from the following relation:

$$P_{in} = DNI\ \tau_{lens}\ \tau_{IR}\ A_{cell}\ GCR \tag{7.4}$$

The cell conversion efficiency, η_{cell}, can be defined as the ratio between the experimental power output to the power incident on the cell.

$$\eta_{cell} = P_{out}/P_{in} \tag{7.5}$$

7.2.3 Impact of the IR filter on the performance parameters

The average transmittance of the Fresnel lens and IR filter is 92% and 19% respectively for the wavelengths between 350 nm and 1200 nm as illustrated in Figure 122. The performance of the silicon solar cell was first measured under the SoG Fresnel lens with solar simulator set to an output of 400 W/m^2. This means an effective irradiance of 31.3 kW/m^2, while after introducing the IR filter the effective solar irradiance decreased to 5.94 kW/m^2 due to the low transmittance of the IR filter.

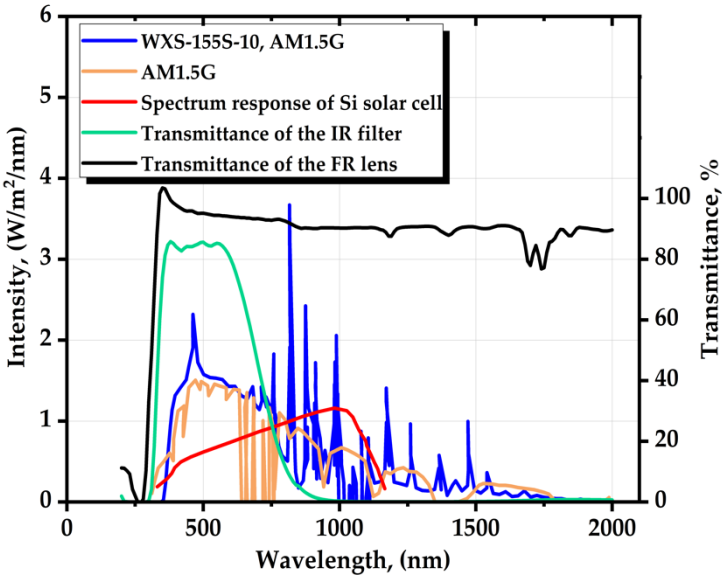

Figure 122 The solar spectrum of the silicon solar cell & transmittance of both the SoG lens and IR filter vs. wavelength.

The performance of the cell in both cases was measured in terms of current, voltage, and power as presented in Figure 123. From Figure 123a, the short

circuit current decreased from 4.005 A to 1.445 A (63.92% reduction) in the case of introducing the IR filter. In contrast, there is a slight decrease in the measured open-circuit voltage by roughly 0.88%. To compensate the energy difference between the two cases due to the IR filter's absorption spectra (Figure 122), the solar simulator was adjusted to 1000 W/m^2 which corresponds to an effective solar irradiance of 14.85 kW/m^2 and theoretical power incident on the cell of 9.15 W (Eq. 7.3).

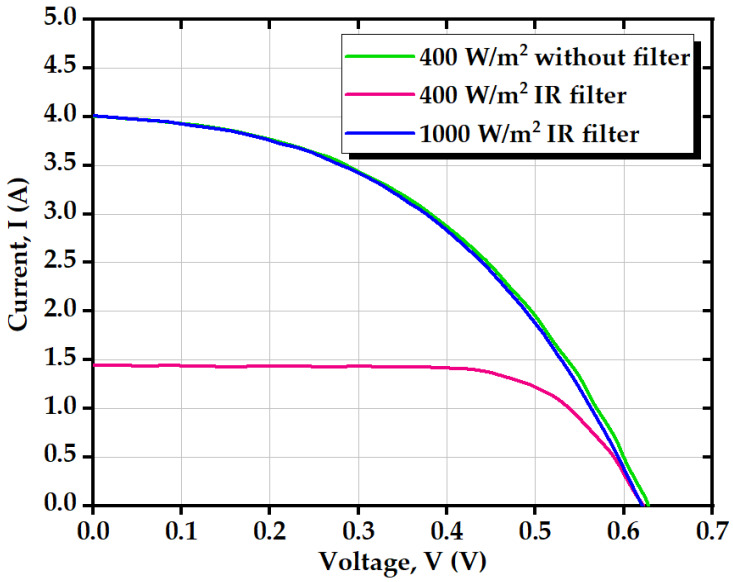

(a)

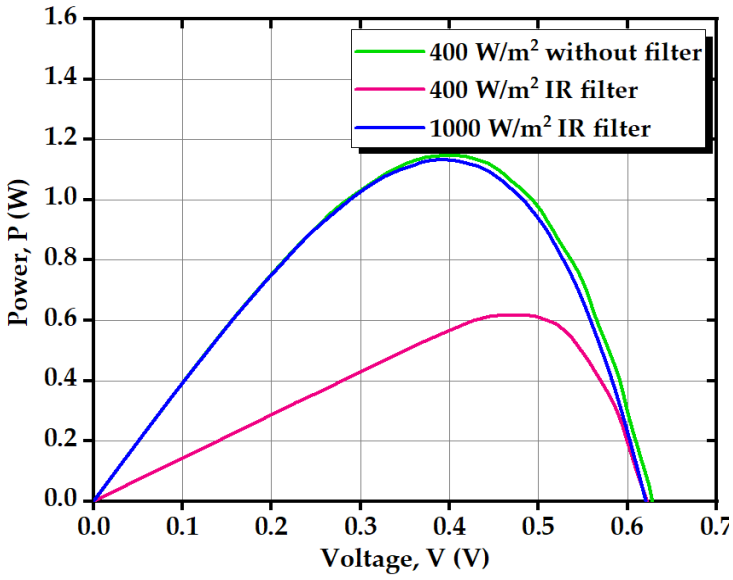

(b)

Figure 123 (a) Variation of the current with the voltage at different working conditions, and (b) Variation of the power with the voltage at different working conditions.

The short circuit current and open-circuit voltage for this case has been observed to increase again to 4.039 A and 0.6207 V, respectively, which are still slightly lower than the case when there is no filter (400 W/m^2). The maximum experimental power generated from the silicon solar cell at solar irradiance of 400 W/m^2 (effective solar irradiance of 31.3 kW/m^2 and theoretical power incident on the cell of 19.3 W) is 1.148 W without introducing the IR filter and decreased to about 0.619 W in the case of the IR filter (effective solar irradiance of 5.94 kW/m^2 and theoretical power incident on the cell of 3.66 W). This can be attributed to the absorption of some of the useful wavelengths for the silicon cell which occurred when using the IR filter.

When the solar irradiance raised to 1000 W/m^2 (effective solar irradiance of 14.85 kW/m^2 and theoretical power incident on the cell of 9.15 W), the experimental power increased again to almost 1.138 W which is still lower than the case without using the IR filter but utilizing more of the incident light on the cell. From the calculations, it can be understood that the cell efficiency (the ratio between the experimental power to theoretical power incident on the cell (Eq. 7.5) at solar irradiance of 400 W/m^2 increased from 6% to 17% (Figure 124) by using the IR filter which is equal to the maximum efficiency reported by the manufacturer. Besides that, the IR filter protected the solar cell from cracking near the tapping wire when it was exposed to 1000 W/m^2 with a cell efficiency reached 12% (Figure 124) and cell temperature of 52 °C.

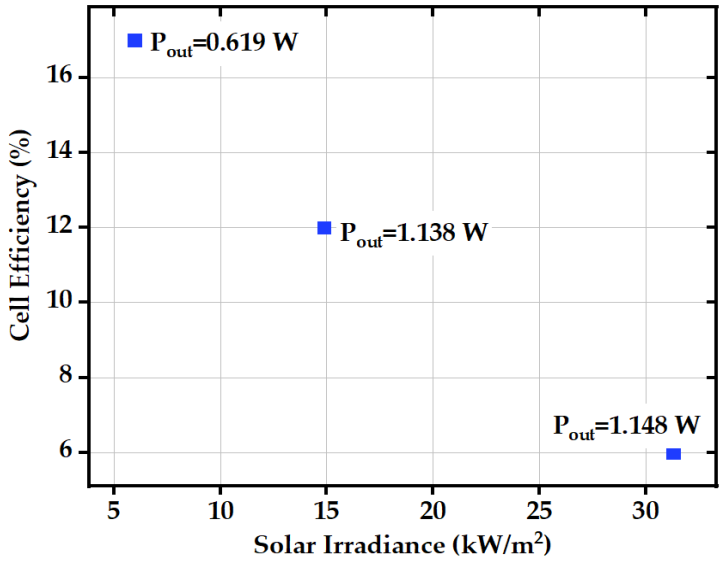

Figure 124 Variation of the solar cell efficiency with solar irradiance.

Although the IR filter caused a reduction in the experimental solar cell power output by 46.09% at a solar irradiance of 400 W/m^2 (Figure 125a), due to absorption losses,

solar cell efficiency increased by almost twice (180%) as illustrated in Figure 125b. This is important evidence towards utilizing IR filters for concentrator systems, especially if more precise filters matching the solar cell wavelength range are available. Further work into how these effects can be utilized for other solar concentration levels and solar cells is required to understand the full potential of the cell efficiency benefits for maximum power outputs.

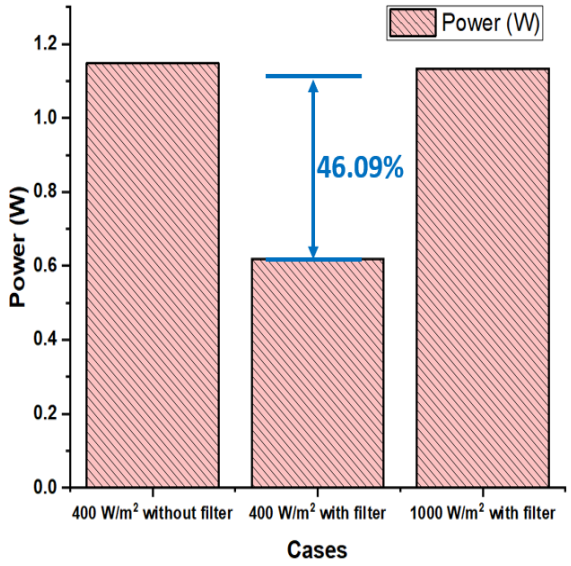

(a)

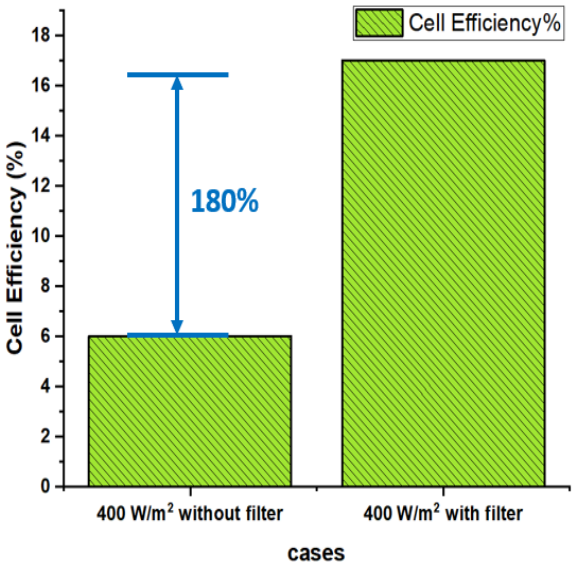

(b)

Figure 125 Representation of the gain and loss in both (a) power and (b) cell efficiency with and without the IR filter.

7.3 Primary optical component focal spot analysis

A better understanding of the focal area temperature and distribution, as well as the temperature of solar cells, is needed within the CPV designs to be able to expect the thermal behavior of the whole system and the maximum expected temperature of the solar cell. The methods to investigate the temperatures also needs to be evaluated. Consequently, two measuring methods have been compared here: thermocouples and infrared (IR) thermography.

In this section, a comprehensive indoor study of the temperature distribution at different locations in the focal spot as well as in the case of introducing the MJ solar cell is introduced. The temperature profiles expected for the receiving cells are described, including the effects of tabbed metal connections within the focal spot. The misalignment between the receiver and primary optical component that may be occurred which would affect the electrical performance parameters is introduced. In addition, the impact of changing solar irradiance on the solar cell temperature and its performance is presented.

7.3.1 Experimental approach

The experimental setup used throughout the investigation is presented in Figure 126a. The Fresnel lens is placed underneath a WACOM continuous solar simulator to simulate the solar irradiance from the sun. The multijunction solar cell is placed above Bentham cooling mount to study the effect of the cooling temperature on the performance of the system. An overview of the experiment components is presented in Figure 126b. Two methods are introduced in this research to measure the focal spot and the MJ cell temperatures. First, to measure the temperature distribution of the focal spot, thermocouples were soldered onto a metallic grid at different locations as in Figure 126c. Then, regarding the MJ solar cell temperature, the thermocouples (T_1, T_2, and T_3) were placed on the top surface of the solar cell assembly but without soldering to avoid damaging it except for the T_4 thermocouple that was placed underneath it as presented in Figure 126d. The temperature measurements of these methods were compared with the readings from the IR camera at different conditions. A clear sight from the IR camera to the cell was guaranteed with an angle of incident of 30° between the camera and the perpendicular to the measured surface. Before starting the measurement, both the thermocouples and the IR camera were calibrated with two points of temperatures; boiling water and liquid-ice water against a mercury thermometer which gave differences of ±0.2 °C and ±2.0 °C, respectively. Both the MJ solar cell as well as the focal spot were measured for their temperatures and electrical performance under the solar simulator for an exposure time of 3 min.

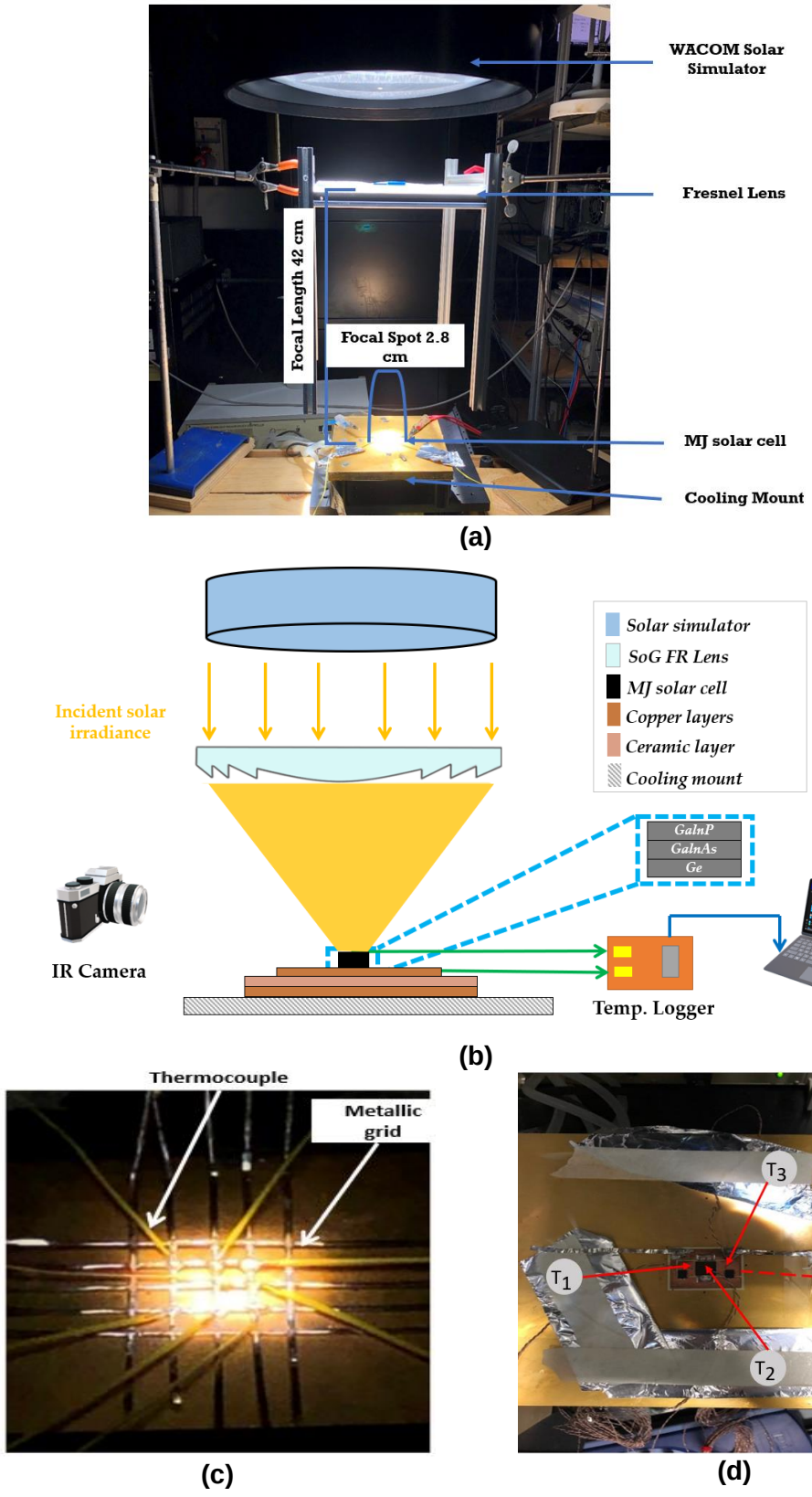

Figure 126 (a)The experimental setup, (b) schematic representation of the experimental setup showing both the thermocouples and IR camera, (c) metallic grid with the tapped thermocouples, and (d) for the MJ cell temperature measurement, the thermocouples T_1, T_2, T_3 are placed above the solar cell assembly, while T_4 thermocouple is underneath it.

7.3.2 Theoretical approach

The calculated geometrical concentration ratio for this case is 529 suns which is calculated using Eq. 7.2. All the system parameters and theoretical calculations are given in Table 16. Since the focal spot area is larger than the cell area, the geometrical loss (l) is calculated as follows:

$$l = (A_{fo} - A_{cell}) / A_{fo} \tag{7.6}$$

Then, the optical efficiency, η_{opt}, can be calculated from the following relation:

$$\eta_{opt} = (1 - l)\ \tau_{lens} \tag{7.7}$$

Therefore, the effective concentration ratio, ECR, will be:

$$ECR = GCR\ \eta_{opt} \tag{7.8}$$

Hence, the effective solar irradiance (I_{eff}) can be calculated as the following equation:

$$I_{eff} = \left(DNI\ \eta_{opt}\ A_{lens}\right) / A_{cell} \tag{7.9}$$

The theoretical power incident on the surface of the MJ solar cell and the cell efficiency are calculated using the following equations:

$$P_{in} = I_{eff}\ A_{cell} \tag{7.10}$$

Table 16 Summary of the systems parameters and theoretical calculations.

Parameter	**Symbol**	**Value**	**Unit**
Focal length	–	42	cm
Focal width	–	2.8	cm
Aperture area	A_{lens}	0.0529	cm^2
Solar cell area	A_{cell}	1	cm^2
Geometrical concentration ratio	GCR	529	suns
Geometrical loss	l	0.838	-
Optical efficiency	η_{opt}	14.5	%
Effective concentration ratio	ECR	76	suns
Focal spot area	A_{fo}	6.16	cm^2
Concentration ratio	CR	86	suns
Direct normal irradiance	DNI	700-1000	W/m^2

7.3.3 Focal spot temperature distribution

This section introduces the temperature distribution in the focal spot by using both thermocouples and the IR camera. After adjusting the FR lens position for the maximum concentration, the metallic grid has been introduced in the focal area as in Figure 126c. The thermocouples' locations are introduced in Figure 127 to allow predicting the maximum temperature in the focal spot.

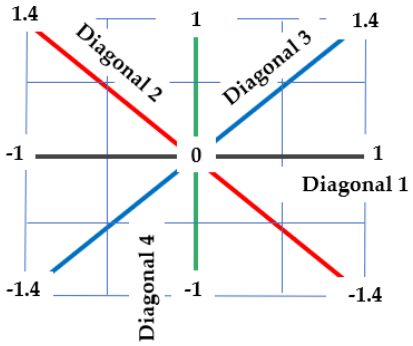

Figure 127 The positions of different thermocouples attached to the metallic grid.

Figure 128 shows the variation of different points temperature in the focal spot with the cooling mount temperature. It was observed that the maximum temperature in the focal spot reached 202 °C without introducing any cooling, while after introducing the cooling mount the temperature reduced significantly. In general, the highest recorded temperature is observed at the centre of the focal spot (0) where the maximum concentration is located. The temperature decreased significantly for the points far from the centre of the focal spot. This can be attributed to the Gaussian shape of the concentrated light. Both diagonals (1 and 4) and diagonals (2 and 3) showed similar performance on both sides of the curve despite the misalignment of the thermocouples on the left side of the grid which causes a small difference in the temperature readings.

At cooling mount of 25 °C and 10 °C, the maximum temperature at the focal spot centre reached 156.7 °C and 145.4 °C respectively. Also, the temperature distribution on the grid varied from 110 °C to 155 °C at both ends of diagonal 4 which are about 1 cm far from the centre (0) at cooling mount temperature of 10 °C and 25 °C respectively. Therefore, reducing the cooling mount temperature has a positive impact on decreasing the focal spot temperature. The thermal images of the focal spot at different cooling mount temperatures are introduced in Figure 129. The pictures show the maximum temperature is located at the centre of the focal spot. Also, it can be noticed that the readings from the IR

camera agree well with those by using the thermocouples at different conditions with a maximum difference of 0.48%.

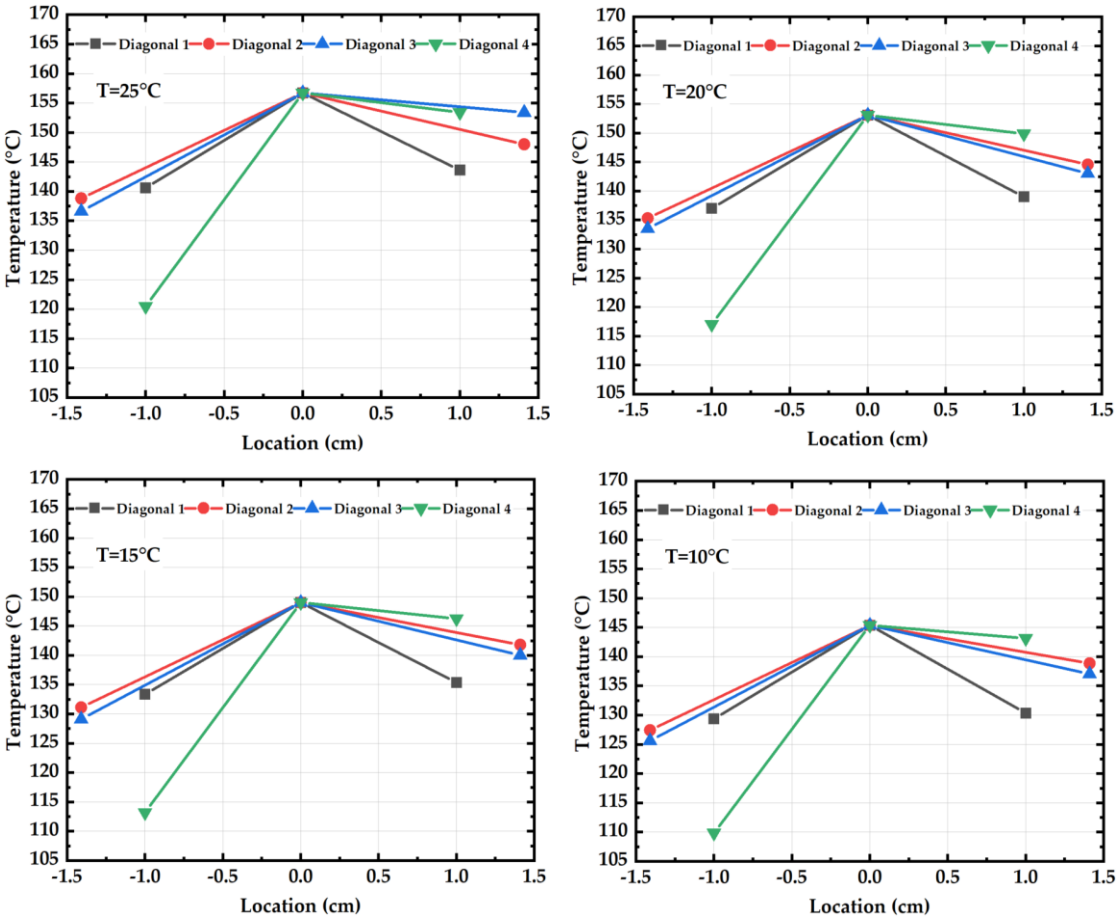

Figure 128 Variation of the focal spot temperature with different locations at cooling mount temperatures of (a) 25 °C, (b) 20 °C, (c) 15 °C, (a) 10 °C.

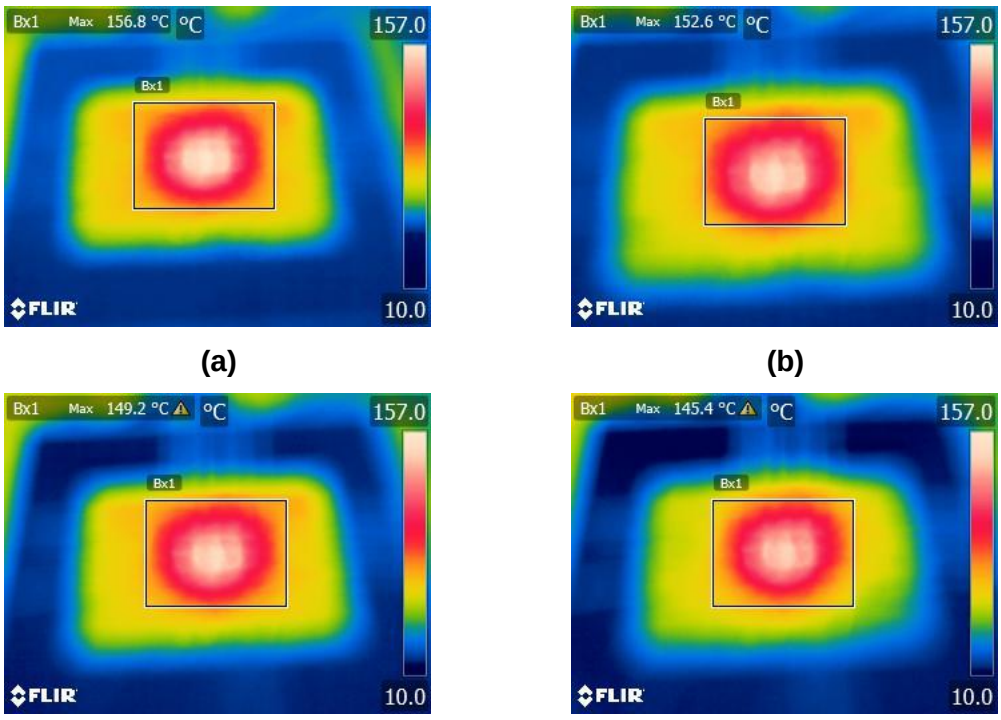

Figure 129 Focal spot thermal images at different cooling mount temperatures of (a) 25 °C, (b) 20 °C , (c) 15 °C, (a) 10 °C.

7.3.4 MJ solar cell thermal and electrical performance

Figure 126d displays the thermocouples' positions on the MJ solar cell where they are placed above the selected points. Solar cell temperature variation and electrical performance are plotted in Figure 130a to c. The centre of the solar cell did not vary significantly with the cooling mount temperature as it reduced by only 4 °C when the cooling mount temperature decreased from 25 °C to 10 °C. Also, it is worth mentioning that the solar cell temperature readings are lower than the focal spot temperatures from the previous section. This is because the MJ solar cell is attached to several layers composed of ceramic and copper which have high thermal conductivity and working as heat spreaders. These layers dissipate the heat effectively from the cell to the cooling mount.

Although the measured cell temperature is lower than the recommended working limit (110 °C), it is still high. This can be attributed to the absence of the thermal paste which is usually utilized for attaching the solar cell to the heat sink. Additionally, both the back surface of the CPV assembly and the cooling mount have different surface roughness. This may allow an air gap that has a low thermal conductivity causing an augmentation in the measured temperatures.

Figure 131 shows that the readings from the IR camera are in good agreement with the thermocouples as the maximum detected deviation is 1.81% which offered an alternative option for measuring the cell's temperature.

To investigate the MJ solar cell electrical performance, the I-V and power curves are plotted as illustrated in Figure 130b and c. A slight increase in the short circuit current with the increase of the cooling mount temperature is observed in Figure 130b. This is due to the increase of the electrons' energy with temperature [273]. On the other hand, the voltage dropped significantly due to the decrease in the bandgap energy [274]. This leads to a significant decrease in the maximum power as illustrated in Figure 130c as it reduced by about 3% at a cooling mount temperature of 25 °C.

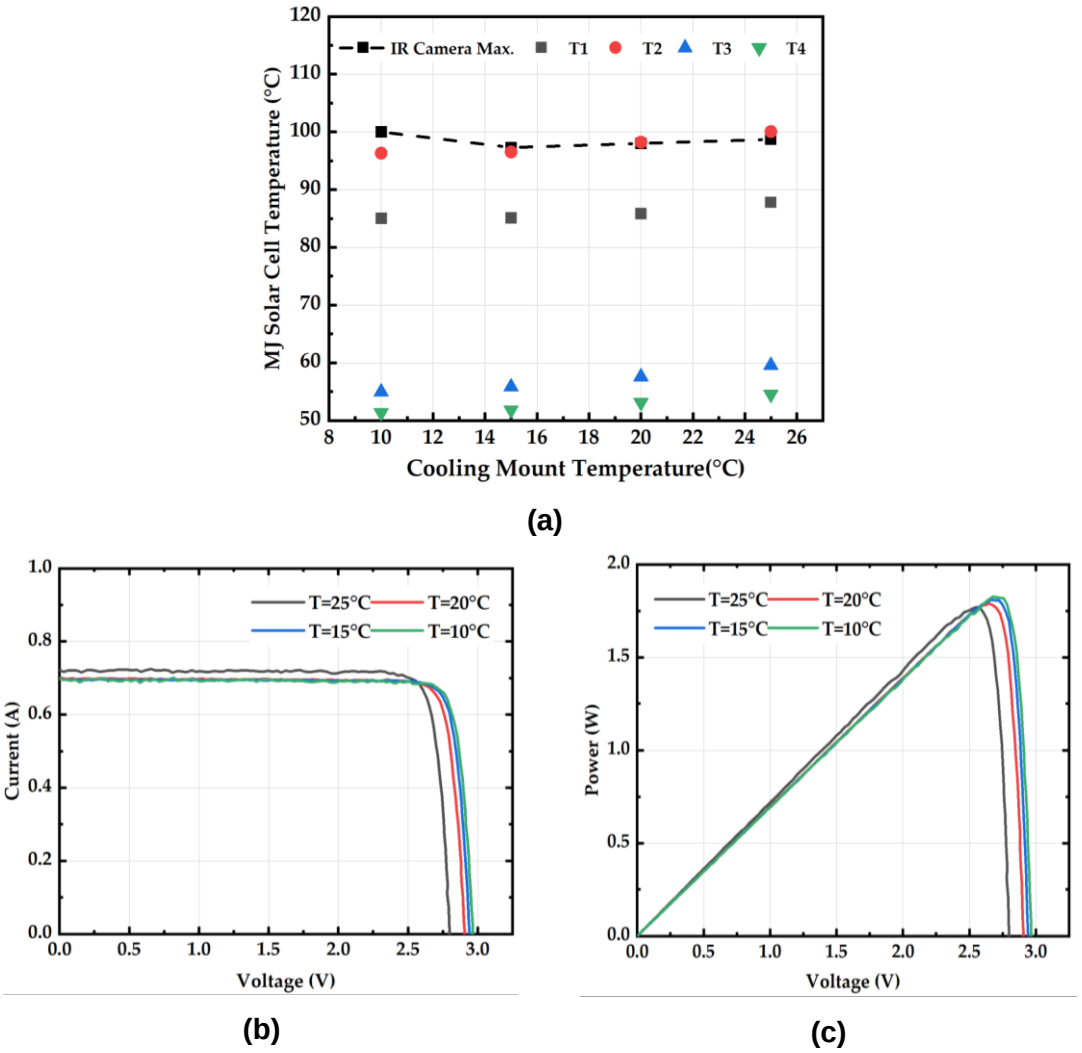

Figure 130 (a) Variation of the different point readings with cooling mount temperatures, (b) variation of the MJ solar cell current and voltage with cooling mount temperature (c) change of MJ solar cell power with the voltage at different cooling mount temperature.

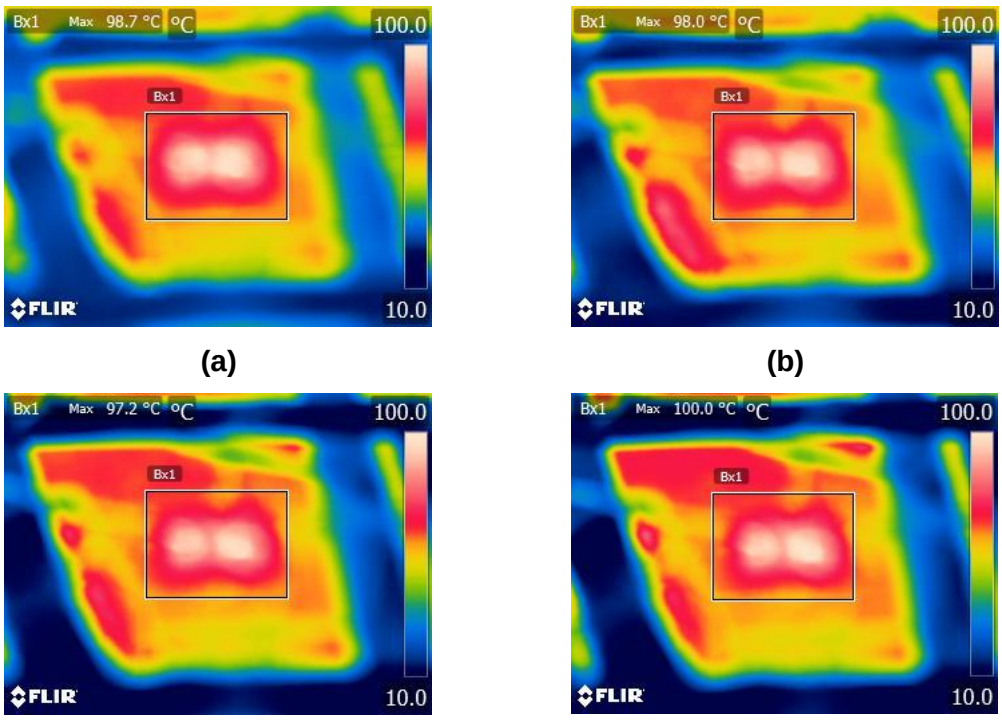

Figure 131 MJ solar cell thermal images at different cooling mount temperatures of (a) 25 °C, (b) 20 °C, (c) 15 °C, (d) 10 °C.

7.3.5 MJ solar cell thermal and electrical performance with location

In order to study the performance of the MJ solar cell if any misalignment occurred, the cell was allowed to move in predefined locations within the focal spot area as shown in Figure 132. The distance between each point is 0.5 cm in the horizontal (x) and vertical (y) directions. At each location, the solar cell temperature, current, voltage, and power have been recorded. The highest temperature is observed in the centre of the focal spot as it varied between 95 to 100 °C as presented in Figure 133a. Then the temperature started to decrease when moving far from the centre of the focal spot.

Higher temperatures have been noticed in the positive direction of the X-axis which may be attributed to the misalignment of the assembly that is holding the Fresnel lens. Similar distribution for the current and power output to the Gaussian shape of the concentrated light has been detected in Figure 133b and c. Obviously, there is a proportional relationship between the current and the generated power from the solar cell.

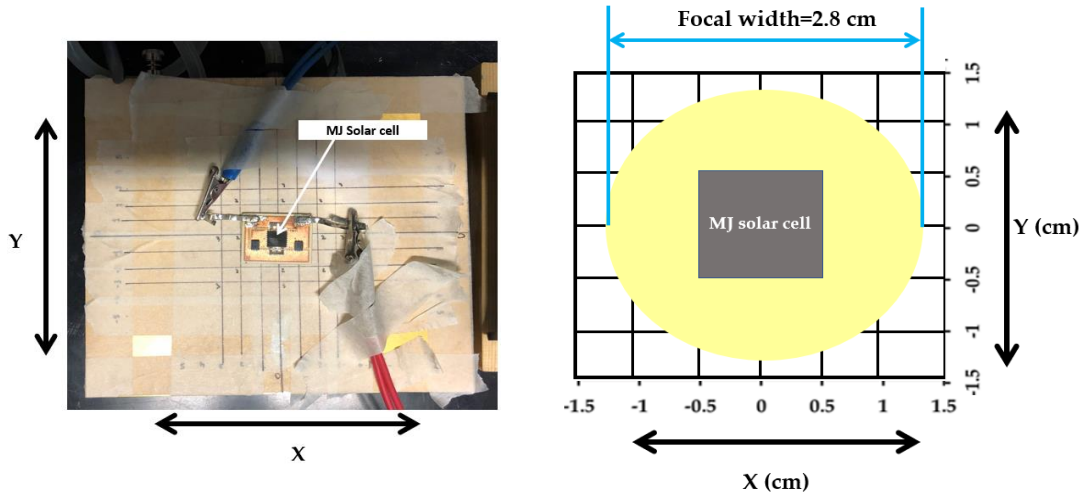

(a) **(b)**

Figure 132 (a) The tested MJ solar cell (b) Schematic figure for the tested locations of the MJ solar cell in X and Y directions.

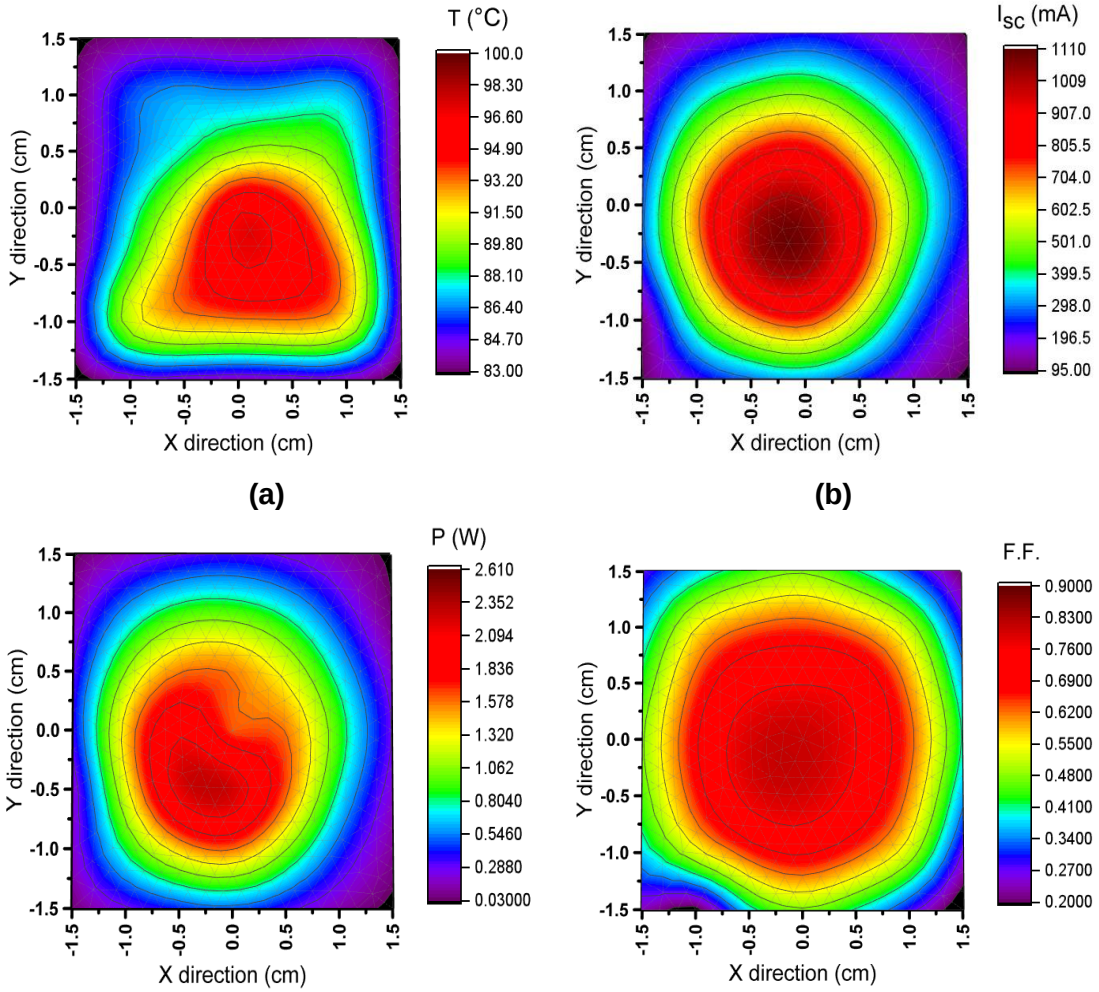

(a) **(b)**

(c) **(d)**

Figure 133 Distribution of (a) temperature, (b) current, (c) power, (d) Fill Factor at different locations at solar irradiance of 1000 W/m^2.

Therefore, the points that showed an increase in the current had an increase in the generated power. At the centre of the focal spot, the short circuit current changed between 900 and 1100 mA, while the maximum reported power in the same locations had values between 2 to 2.6 W. A reduction in the current and power values by almost 91% is observed at the focal spot boundaries due to the reduced values of the concentrated irradiance at these locations. The squareness of the I-V curve is defined as a Fill Factor (F.F.) which depends on the solar cell short circuit current and open-circuit voltage. When the solar cell was located at the centre, the fill factor changed from 0.83 to 0.9 which indicates a good irradiance uniformity across the cell, while it reduced when the solar cell moved far-off the centre because of the reduction in the power at these locations.

7.3.6 MJ solar cell thermal and electrical performance with irradiance

The effect of changing the solar irradiance on the current and power curves is introduced in Figure 134 a and b. It can be noticed that the short circuit current increases linearly with the increase of the effective solar irradiance as it improved from 0.7 A to 0.98 A at 53.9 kW/m^2 and 77 kW/m^2 respectively. This significant enhancement in the current can be attributed to the increase in the absorbed energy by the electrons which increases the short circuit current. On the other hand, the open-circuit voltage increases logarithmically with the incident light that explains the slight increase observed in the figure. Due to the improvement in the short circuit current with the solar irradiance, the maximum power output generated from the system increased as well. Figure 134c shows the effect of changing solar irradiance and the corresponding effective solar irradiance on the solar cell's maximum temperature and power. The power output from the MJ solar cell changed from 1.81 W to 2.5 W at effective solar irradiances of 53.9 and 77 kW/m^2 respectively. Therefore, it is expected that by increasing the effective solar irradiance by four times (for the whole system), the power output may reach up to 10 W.

The maximum temperature of the MJ solar cell was recorded using the thermocouple and IR camera. The thermal images of the MJ solar cell at different solar irradiances are presented in Figure 135a to d. The maximum temperature is located at the centre of the focal spot where the maximum concentration of the light is located. Also, increasing solar irradiance rises the effective solar

irradiance on the surface of the solar cell which augmented the maximum temperature of the solar cell. The temperature varied from 77.9 °C to 100.6 °C at effective solar irradiance of 53.9 and 77 kW/m^2, respectively. These high temperatures may be deceased to lower values when a thermal paste and efficient cooling system are introduced as mentioned before. A comparison between the maximum temperature readings of the thermocouples and IR camera is plotted in Figure 134c. The measured results are in good agreement with the readings from the IR thermal camera with a maximum difference of 1.46%.

Figure 134d represents the effect of increasing solar irradiance on the solar cell fill factor and cell efficiency. An increase in the fill factor with the solar irradiance is observed until 900 W/m^2. This increase was followed by a decrease when solar irradiance reached 1000 W/m^2. This can be attributed to the increase in the short circuit current at 1000 W/m^2 which was higher than the maximum power produced by the solar cell if compared with the values at lower solar intensities [275]. Regarding the cell efficiency, a reduction is noticed with the increase in solar intensity due to the increase in the solar cell temperature [276,277], and at the tested conditions further increase in the effective solar irradiance may lead to a larger drop in the conversion efficiency for the whole design.

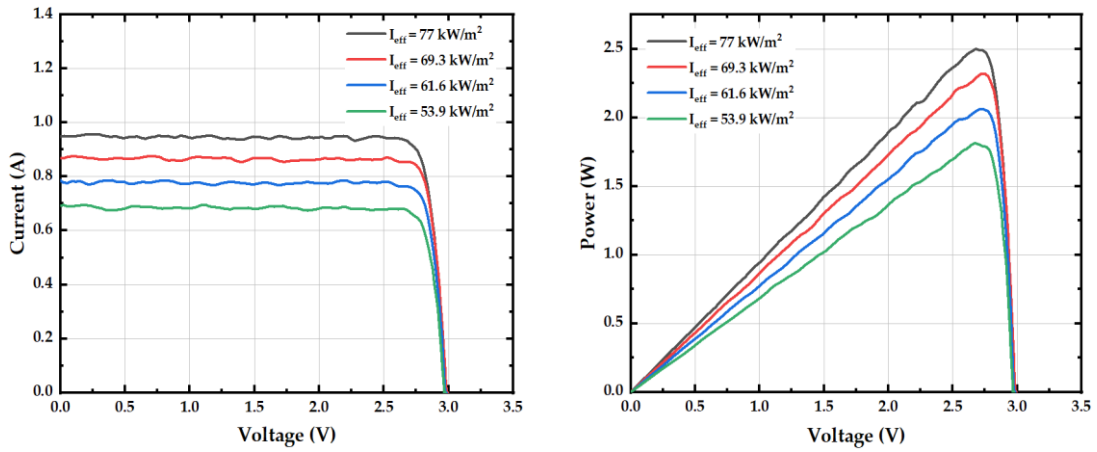

(a) **(b)**

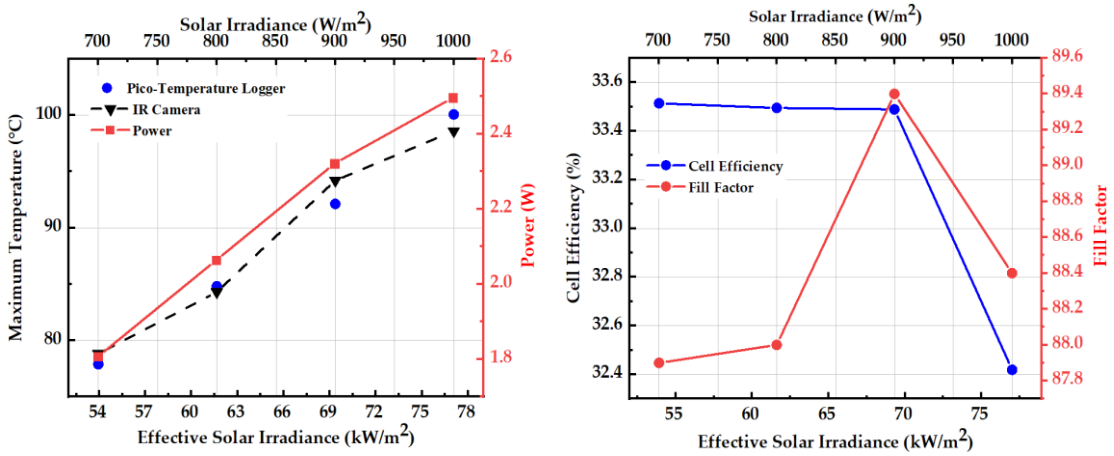

(c) **(d)**

Figure 134 (a) Variation of current with voltage, (b) change in power and voltage, (c) change of the maximum solar cell temperature and power (d) change of the cell efficiency and fill factor with solar irradiance.

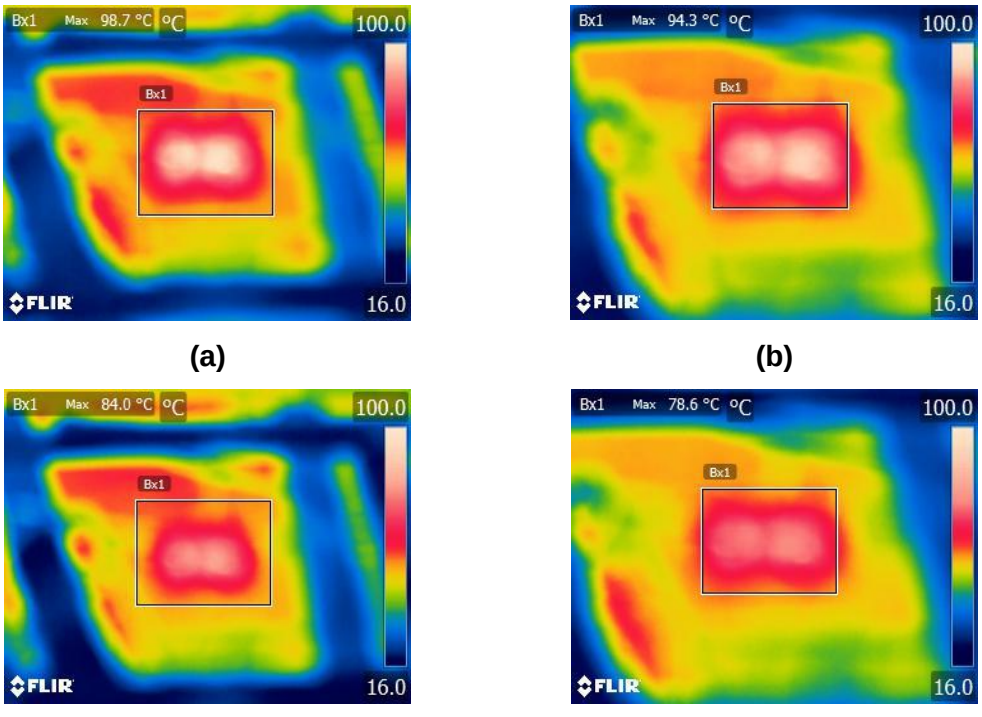

(a) **(b)**

(c) **(d)**

Figure 135 MJ solar cell thermal images at different solar irradiances of (a) 1000 W/m^2, (b) 900 W/m^2, (c) 800 W/m^2, (d) 700 W/m^2,respectively.

7.4 Thermal evaluation of the HCPVT system: the use of an electric resistance heater

A comprehensive experimental investigation of the thermal performance of a CPV system using an electric resistance heater to simulate the thermal load of the CPV is introduced in this section. The study includes both experimental and

numerical validation and the impact of heat sink configuration, working media, and flow rate is presented.

7.4.1 Experimental approach

Figure 136a presents the experimental setup used throughout the investigation. It consists of the heat sink test section, a peristaltic pump to circulate the flow inside the test section, water circulation bath, flow meter, DC power supply, Pico temperature logger with K-type thermocouples, and a laptop to record the temperature variation. A schematic diagram of the experiment is introduced in Figure 136b. The working medium is supplied at a fixed flow rate and temperature from an aluminium tank placed inside the water circulation bath. The inlet fluid temperature is kept at a constant temperature of 25 °C .

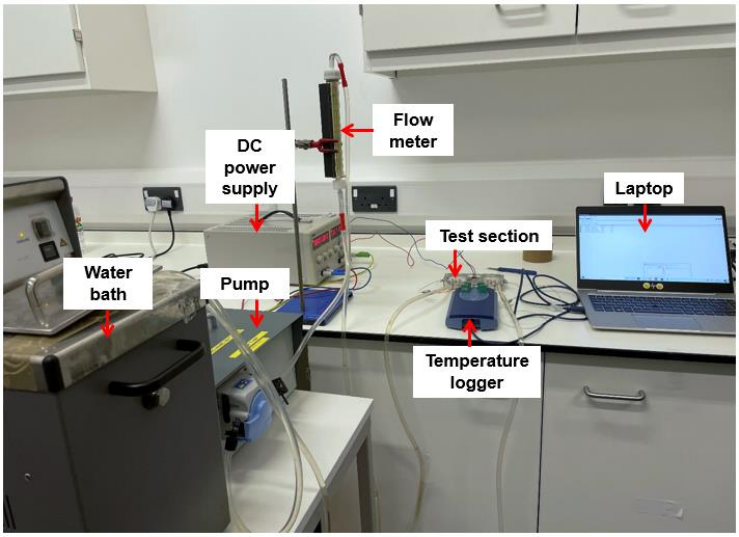

(a)

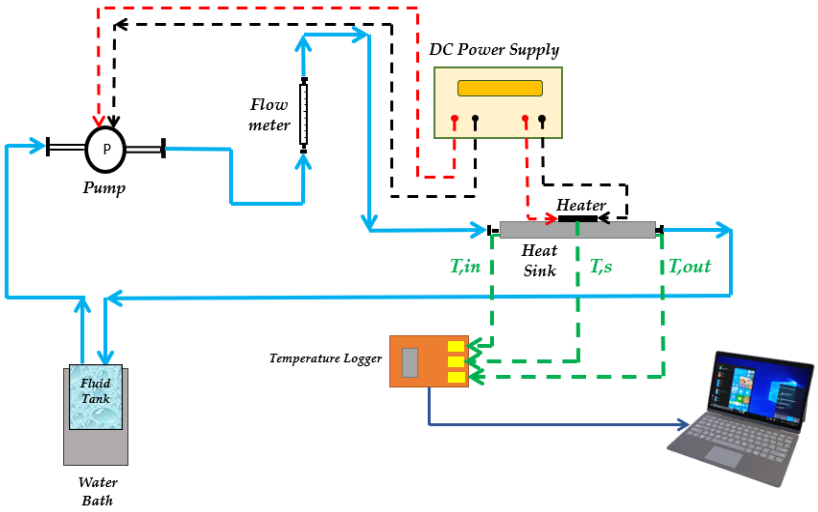

(b)

Figure 136 (a) A photograph of the experimental setup used throughout the investigation, (b) Schematic diagram of the experiment.

A thermocouple is placed at the inlet of the test section to monitor the temperature variation. Figure 137 shows the locations of the inlet and outlet fluid thermocouples in the test section. Also, a thermocouple is placed above the heat source to predict its temperature. The temperature is recorded at intervals of 1 second using the temperature logger and laptop. The fluid flow rate is measured using a variable area flow meter which is controlled by varying the current and voltage input to the pump.

7.4.1.1 Heat sink test section

The heat sink test section presented in Figure 137 is designed and fabricated in the ESI workshop to contain the aluminium mini-channel heat sink. The casing is made of two parts (top and bottom) of transparent acrylic plastic. The length, width, and thickness of each part are 150 mm, 60 mm, and 14 mm, respectively. M4 Nylon screws are used to join the top and bottom sections as displayed in Figure 137.

A piece of rubber is provided between the two parts to prevent any leakage due to the fluid force. 8 mm copper connectors are provided at one side of the acrylic casing for the fluid inlet and outlet. Two configurations of the aluminium mini-channel heat sinks which are the straight and finned mini-channel heat sinks as illustrated in Figure 138 a and b are investigated in this study. To fit the previously fabricated acrylic casing [278], the two tested configurations were fabricated in the ESI workshop with a length and width of 40 mm × 40 mm and fins thickness and height of 0.5 mm and 5 mm, respectively.

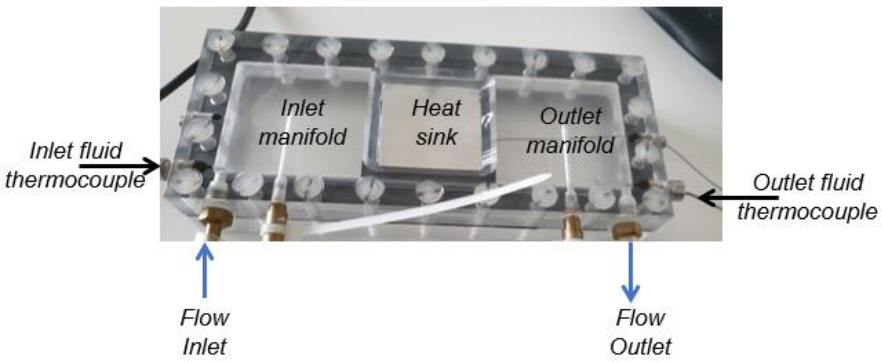

Figure 137 The heat sink test section with the attached thermocouples at the inlet and outlet.

During the investigation, the solar cell is replaced by a uniform heat source (electric resistance heater with a maximum power of 35 W) to model the thermal load generated by the HCPV as presented in Figure 139. The heater has the same width and length as the solar cell which is 10 mm × 10 mm, while the thickness is 4.5 mm. The heater is soldered into a copper layer which is attached to the heat sink, as shown in Figure 138 c, and d, using a thermal paste with thermal conductivity of 2.9 W/m.K with a thickness of 1 mm. The heat is transferred from the electric resistance heater to the heat sink and then to the coolant which dissipates the heat to the fluid tank. The input power to the electric resistance heater is controlled by varying the voltage and current input from the DC power supply until reaching the desired power supply.

After connecting all the instruments as illustrated in Figure 136 and before commencing any tests, the fluid was allowed to flow for 30 minutes through the test section to have a uniform temperature, ensure there is no leakage and remove any trapped air which may affect the recorded measurements. The experiment was started by switching on the water bath and the DC power supply to provide the pump with the needed power. The inlet fluid temperature was allowed to vary ±0.1 °C. Then, the power was supplied to the heater and the variation of the recorded temperatures was achieved by monitoring the data from the temperature logger and the laptop screen. After reaching the steady state, the experiment was stopped, and the recorded data was saved.

7.4.2 Numerical model

A 3D model of the casing, heat sink, and heater was built as presented in Figure 140. The partial differential equations of the heat transfer and fluid flow were solved using COMSOL Multiphysics software. The boundary conditions applied throughout the experiments were entered into the software. Two working media were tested through the experiments: distilled water and 2.5% SiO_2/water. The inlet temperature as stated earlier is kept at 25°C, while the boundary condition at the outlet was a pressure outlet. The heater is selected as the source of the heat. A thin layer of the paste with a thickness of 1 mm was applied between the copper layer and the heat sink surface. The studied domains were meshed, using free tetrahedral mesh, by varying the number of mesh elements to ensure that the solution is independent of the mesh size. Therefore, a total of 0.6×10^6

elements were selected as the change in the heater temperature was less than 0.1 °C.

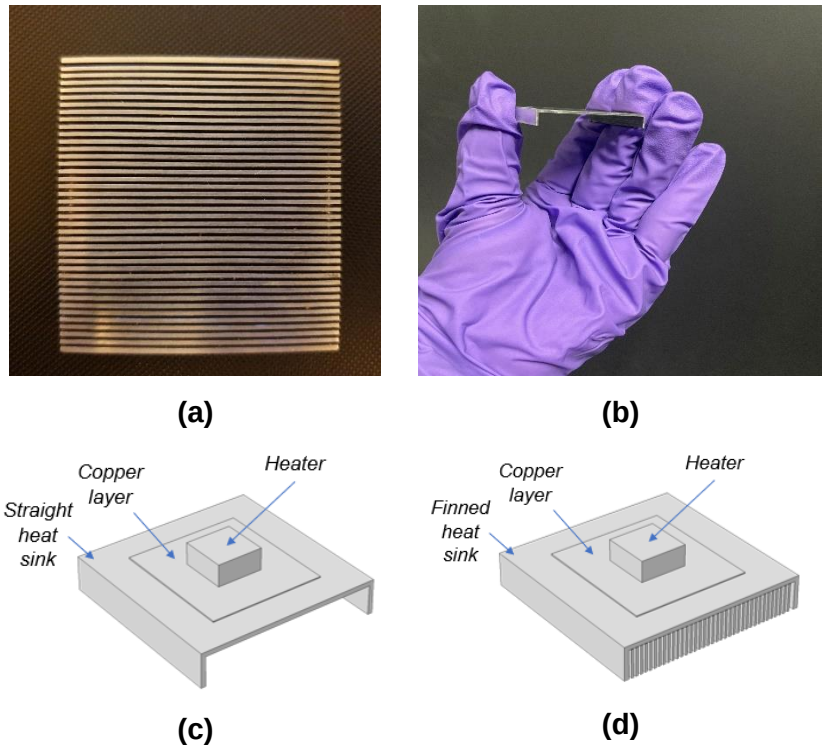

Figure 138 (a) A photograph of the finned mini-channel heat sink, (b) image of the straight mini-channel heat sink, the heater used throughout the experiments attached to the (c) straight channel heat sink, (d) finned heat sink

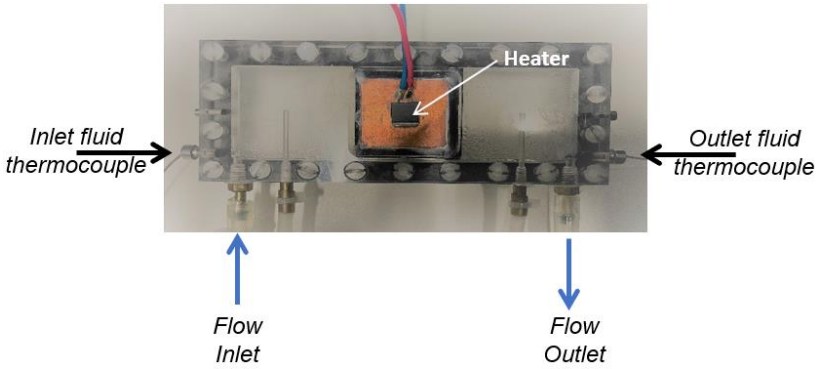

Figure 139 A photograph of the test section with electric resistance heater attached at the top of the heat sink.

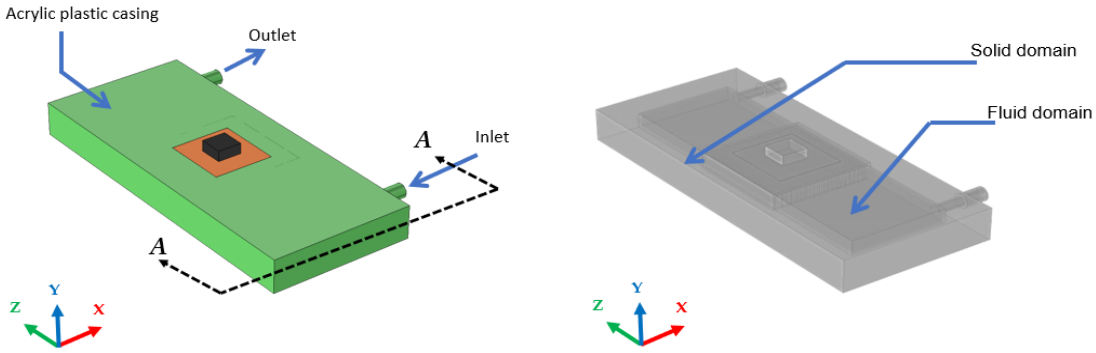

Figure 140 The 3D model of the acrylic casing which contains the heat sink.

7.4.3 Influence of heat sink configuration

Figure 141 compares the experimental and theoretical results of both the straight channel and finned channel heat sinks using distilled water at a flow rate of 0.3 L/min. It can be seen that for both the tested configurations, there is a linear relationship between the heater temperature and the input power obtained from theoretical and experimental results. Also, a good agreement is achieved between both results as the minimum and maximum differences are 0.18% and 10.8%. The maximum recorded heater temperature is 105 °C and 81 °C achieved at 35 W for the straight and finned heat sink, respectively. The finned channel heat sink outperformed the straight heat sink due to the high heat transfer area promoting the heat dissipation process from the heater. Although the recorded and the calculated temperature are still below the recommended working limit of the cell, using low thermal conductivity paste impedes the heat to be extracted efficiently by the heat sink.

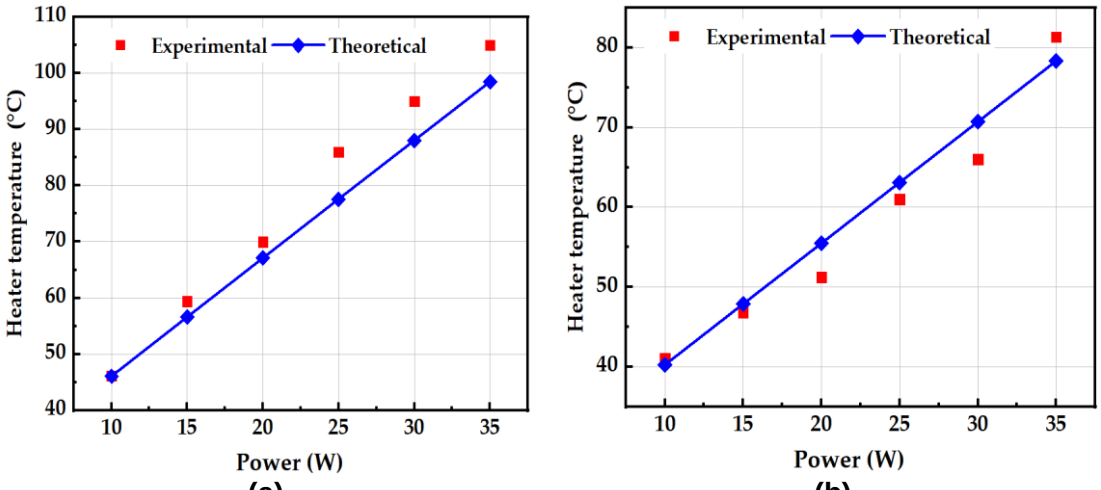

Figure 141 Comparison between the experimental and numerical results using distilled water at 0.3 L/min: variation of the heater temperature with the heater power for (a) straight heat sink, (b) finned heat sink.

The variation of the outlet fluid temperature with the heater power is plotted in Figure 142 for both configurations. The outlet water temperature increased by increasing the power input for the experimental and numerical results. A good agreement is obtained between both results as the maximum error is 1.29%. Figure 143 introduces the variation of the heat sink thermal resistance with the thermal load for the studied cases.

The thermal resistance values obtained by using the finned channel heat sink are much lower than those of by using the straight channel heat sink due to the uniform temperature distribution achieved on the surface of the heat sink as illustrated in Figure 144 at different power inputs. The observed temperature distribution obtained by using the finned channel is much lower than the other configuration due to the uniformity of the flow distribution offered by the fins as explained in Figure 145.

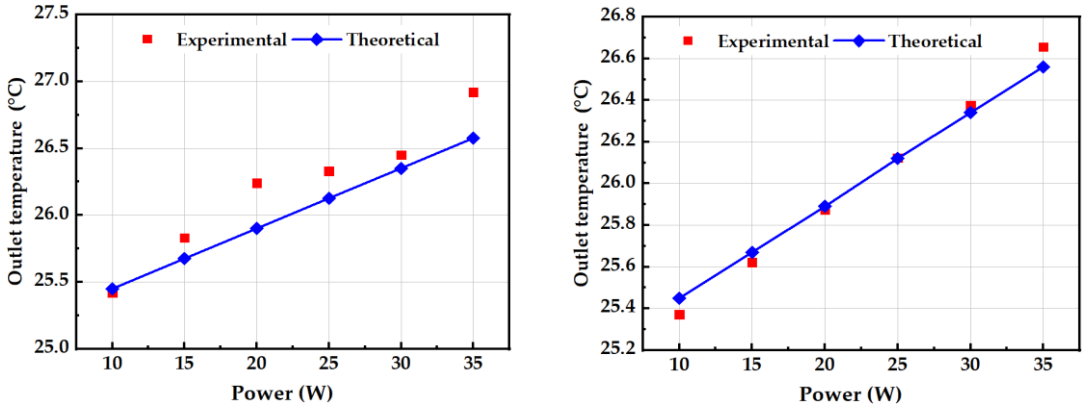

Figure 142 Comparison between the experimental and numerical results using distilled water at 0.3 L/min: variation of the outlet temperature with the heater power for (a) straight heat sink, (b) finned heat sink.

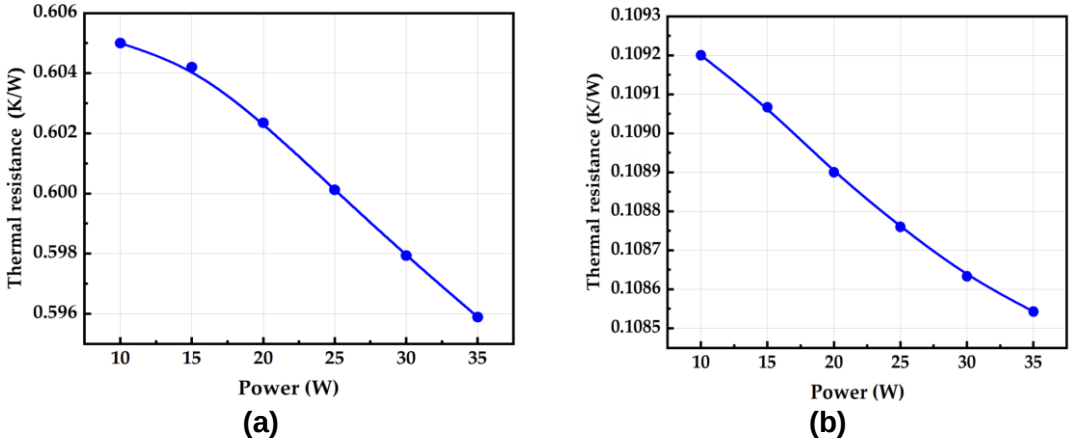

Figure 143 Comparison between the experimental and numerical results using distilled water at 0.3 L/min: variation of the thermal resistance with the heater power for (a) straight heat sink, (b) finned heat sink.

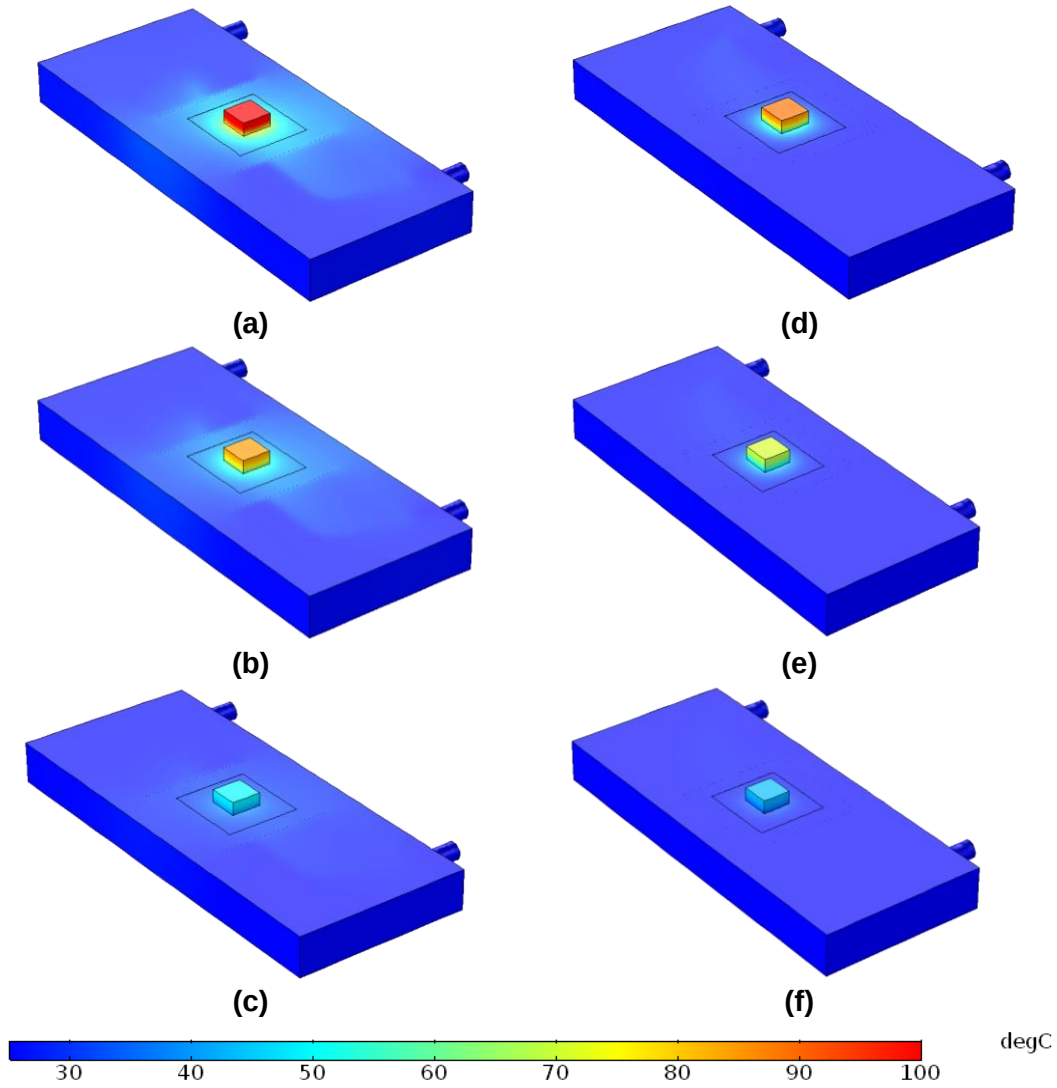

Figure 144 Temperature distribution of the test section by 1. straight channel heat sink at (a) 35 W, (b) 25 W, (c) 10 W and 2. finned channel heat sink at (d) 35 W, (e) 25 W, (f) 10 W.

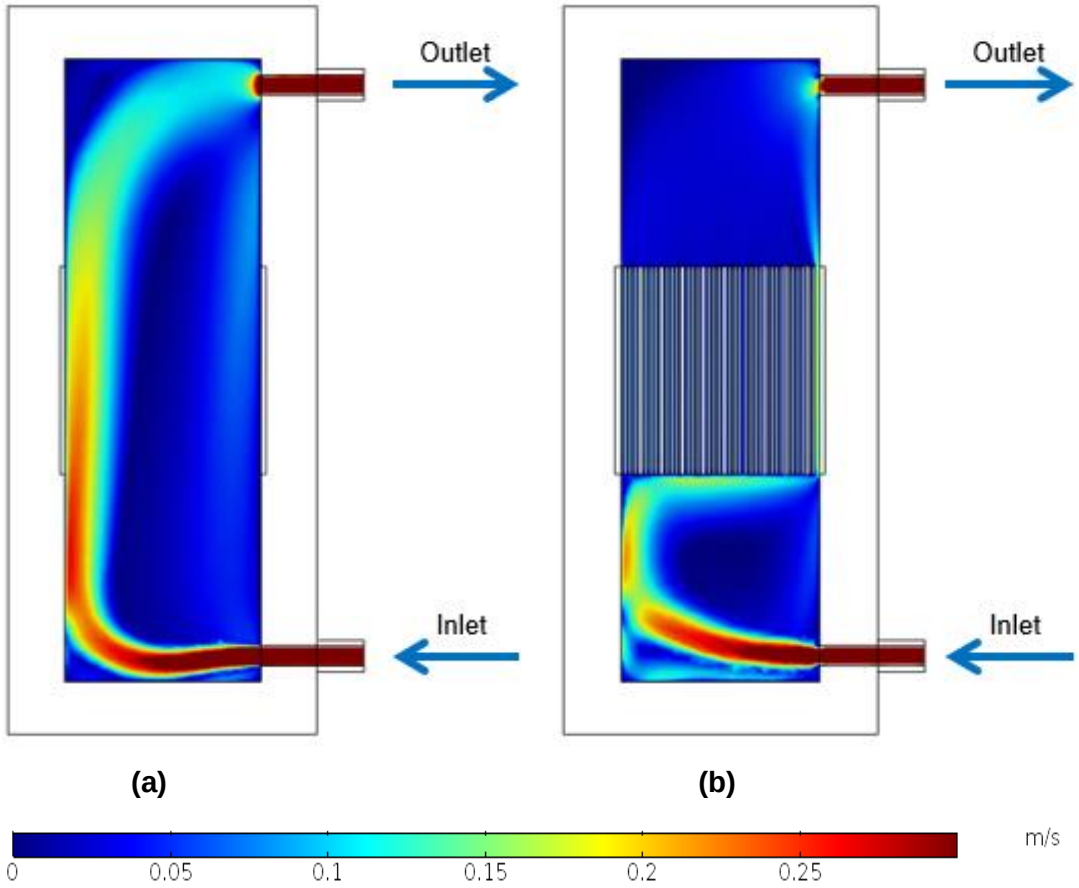

Figure 145 Velocity distribution at section (A-A) of (a) straight, and (b) finned channel heat sinks.

7.4.4 Influence of the working medium

Figure 146a compares both the numerical and experimental results of the heater temperature with the power input by using 2.5% SiO_2/ water. A good agreement is obtained from the comparison with minimum and maximum calculated differences of 0.4% and 7.68%, respectively. Although the difference is relatively small, this error may be reduced even further if all the fluid properties are experimentally measured. It can be noted that the heater temperature by using silica nanofluid decreased significantly in comparison with the results in Figure 141b due to the enhancement in the fluid properties. This improvement in the temperature is decreased with the reduction in the power input.

Both the numerical results of the outlet temperature are validated with the experimental values as shown in Figure 146b. A slight difference of 1.5% is obtained from the comparison, this error decreased by the reduction in the thermal load due to the dependence of the thermal properties on the temperature. The thermal resistance is a good parameter to measure the efficiency of the

coolant and the cooling system in dissipating the heat. From Figure 146c, it can be noticed that the maximum obtained thermal resistance by using silica nanofluid is 0.0973 K/W achieved at 10 W. By comparing the obtained results, it can be noted that by using nanofluid the thermal resistance was enhanced by 10.9% in comparison with water.

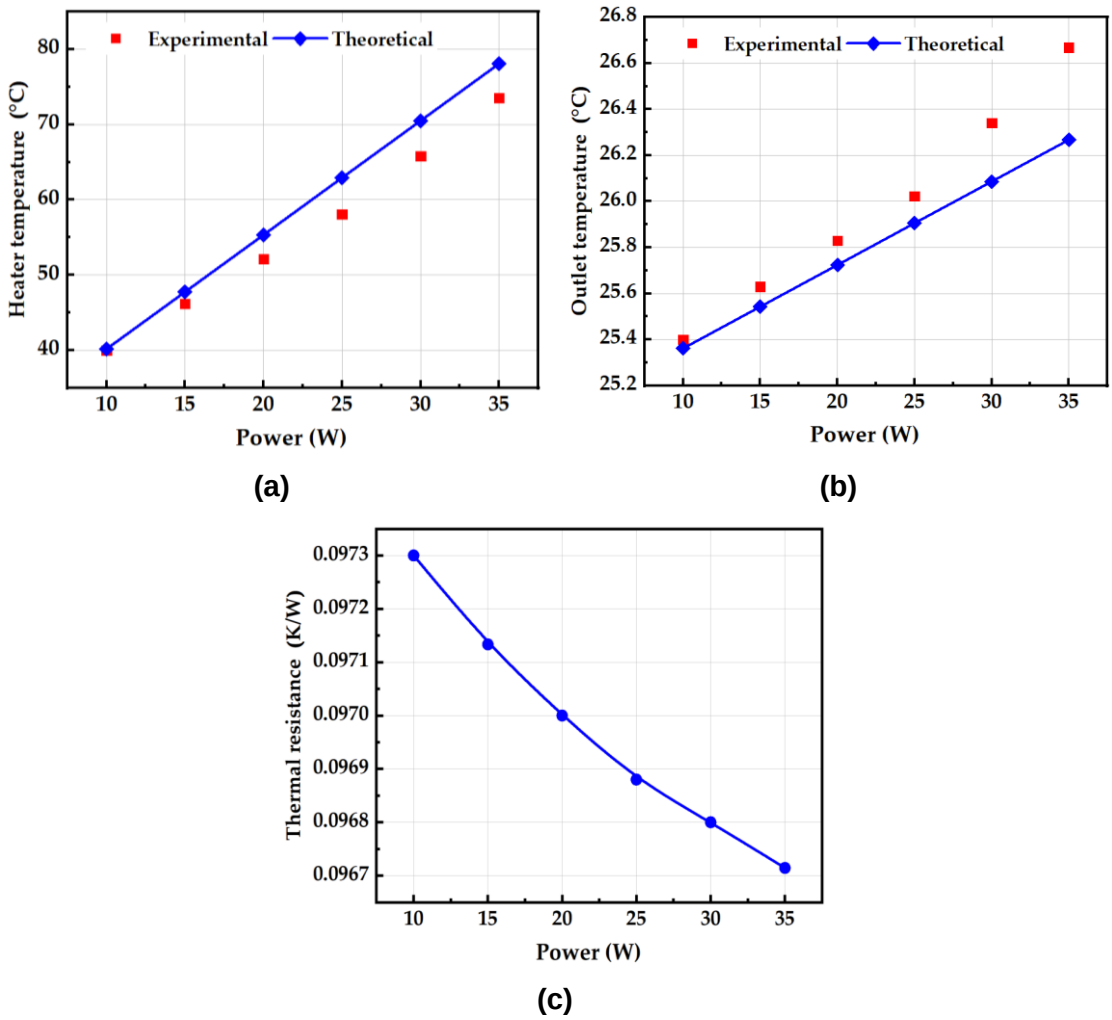

Figure 146 Comparison between the experimental and numerical results using 2.5% SiO_2/ water at 0.3 L/min (a) variation of the heater temperature with power input, (b) variation of the outlet temperature with power input, (c) variation of the thermal resistance with the power input for a finned channel heat sink.

7.4.5 Influence of the flow rate

The change in the heater temperature with the input power at a water flow rate of 0.2 L/min is displayed in Figure 147. From the comparison of the numerical and theoretical results, it can be seen that there is a small difference of 6.7% between both values. Also, in comparison with Figure 141b the heater temperature increased by 4 °C by decreasing the flow rate to 0.2 L/min, while an insignificant

increase in the temperature is noticed at lower power values. On the other hand, the water outlet temperature increased by 0.6 °C in comparison with Figure 142b at 35 W and by 0.15 °C at 10 W. The heater temperature and outlet fluid temperature were measured using 2.5% SiO_2/ water at a flow rate of 0.2 L/min as in Figure 148. An increase in the heater temperature reached 5 °C at a flow rate of 0.2 L/min in comparison with the results indicated at 0.3 L/min as in Figure 146. In terms of the silica nanofluid, a slight difference between the experimental and numerical results reached 5.6%. Also, an enhancement in the nanofluid outlet temperature was detected, especially at the maximum heater power as it reached 27.5 °C.

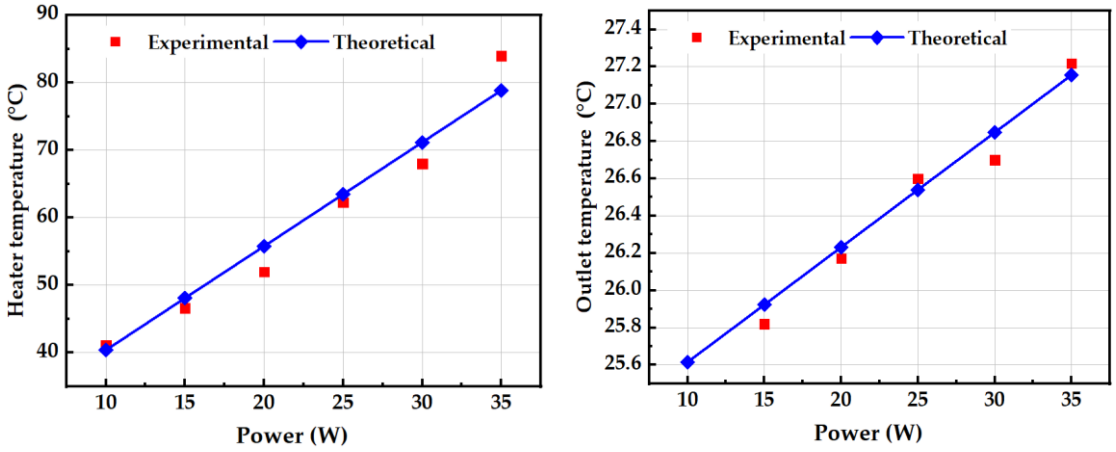

(a) **(b)**

Figure 147 Comparison between the experimental and numerical results using water at 0.2 L/min (a) variation of the heater temperature with power input, (b) variation of the outlet temperature with power input for a finned channel heat sink.

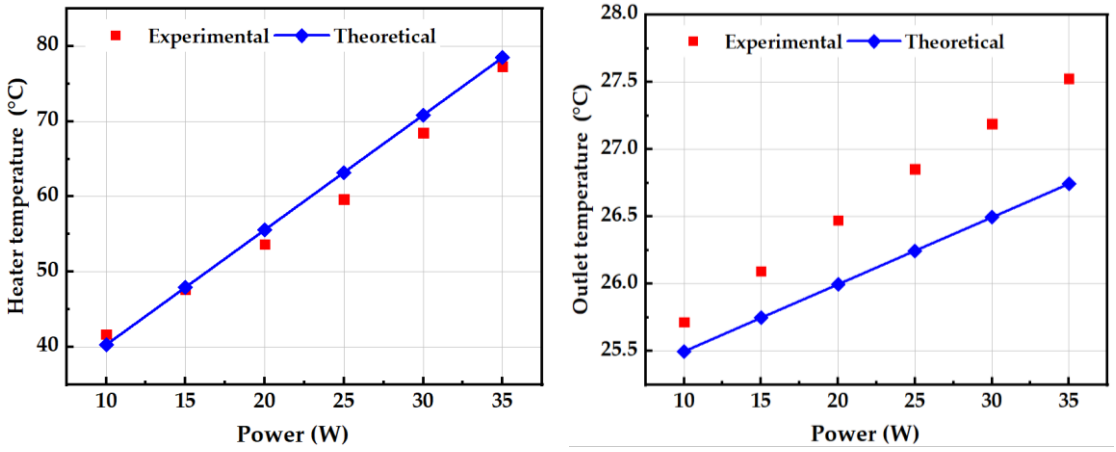

(a) **(b)**

Figure 148 Comparison between the experimental and numerical results using 2.5% SiO_2/ water at 0.2 L/min (a) variation of the heater temperature with power input, (b) variation of the outlet temperature with power input for a finned channel heat sink.

A comparison between the heat sink thermal resistance values detected at a flow rate of 0.2 L/min by using distilled water and silica nanofluid is illustrated in Figure 149. Both the thermal resistance values obtained by using water and nanofluids increased by an average of 20% due to the reduction in the flow rate. However, there is a significant enhancement in the heat sink thermal resistance by using silica nanofluid reaching 12.6% if compared with using distilled water only at 0.2 L/min.

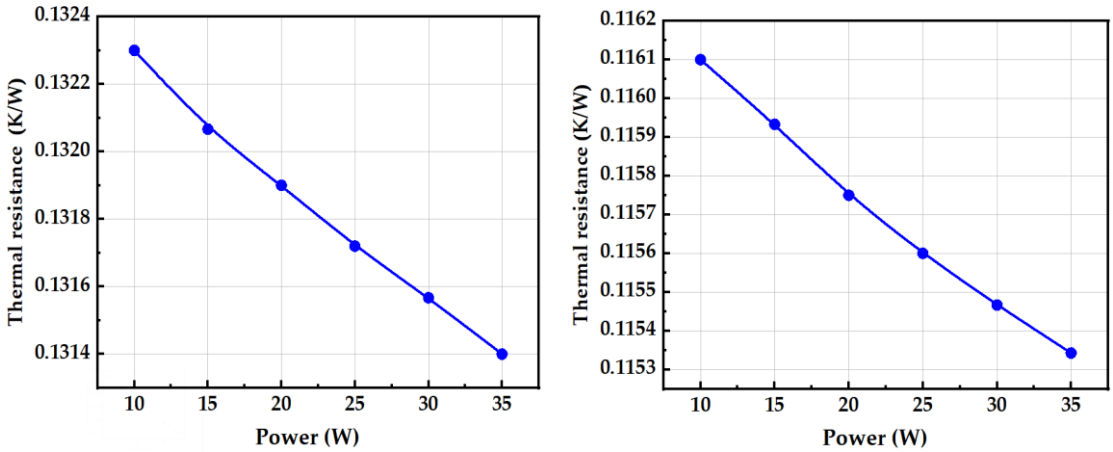

Figure 149 Variation of the heat sink thermal resistance with the input power at 0.2 L/min for (a) Water, (b) 2.5% SiO_2/water.

7.5 Performance evaluation of the HCPVT system: the use of an MJ solar cell

A detailed indoor experimental investigation of the HCPVT system based on a Fresnel lens and MJ solar cell is introduced. The study includes both experimental and theoretical comparisons. The influence of different operating parameters on the temperature distribution and system performance is presented.

7.5.1 Experimental approach

As shown in Figure 150a, the experimental setup is the same as the setup discussed in the previous section but in this case, the SoG Fresnel Lens was utilised to concentrate the incident light from the solar simulator onto the MJ solar cell. A schematic diagram of the indoor experimental investigation is displayed in Figure 150b. Thermocouples were attached at the inlet and outlet of the test section for the fluid temperature measurements. To measure the solar cell

temperature, thermocouples were placed above the cell. To attach the CPV assembly to the heat sink, a thin layer of 2 mm of the thermal paste was applied. To avoid the shadowing from the thermocouples, the cell temperature was measured firstly at the specified concentration without any electrical connections. After that, the cell was connected to the IV tracer for the electrical measurements.

Figure 151 presents a photograph of the heat sink test section showing the solar cell attached to the finned heat sink inside the acrylic casing. At the beginning of the experiment and after connecting all the instruments as shown in Figure 150b, the power unit of the solar simulator was turned on for warming up and the tested fluid was allowed to flow throughout the heat sink test section for 30 minutes using the pump to remove the trapped air from the circuit. The experiment was then started by turning on the solar simulator light, and the measuring data was monitored and recorded using the laptop and the I-V tracer.

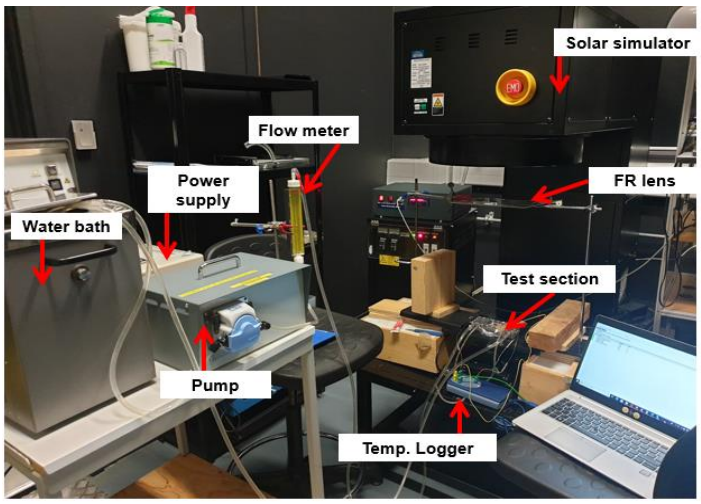

(a)

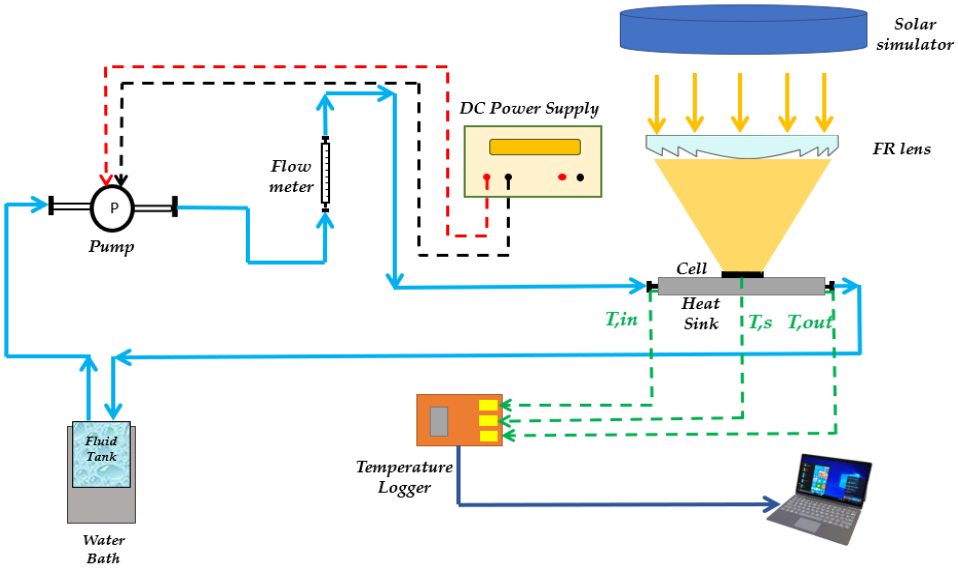

(b)

Figure 150 (a) A photograph of the experimental setup used throughout the indoor investigation, (b) schematic diagram of the indoor experiment.

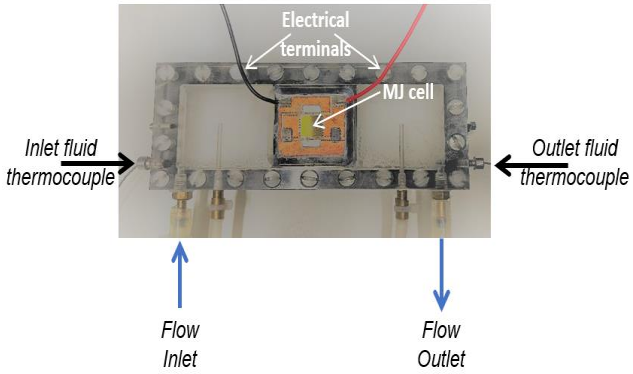

Figure 151 A photograph of the test section with the solar cell attached at the top of the heat sink.

7.5.2 Numerical model

A 3D model of the heat sink test section including the CPV assembly, the finned heat sink, and the acrylic casing was built as shown in Figure 152a. As discussed previously, the CPV assembly consists of MJ solar cell, copper layers, and a ceramic layer sandwiched between them. All the dimensions and thermophysical properties were mentioned in the previous sections. The computational model was meshed and solved using COMSOL-Multiphysics software.

The boundary conditions applied through the experiments were entered into the software to solve the partial differential equations of the heat transfer and fluid flow. The tested fluids were distilled water and 2.5% SiO_2/water. The solar cell is subjected to a uniform concentration ratio of 529 suns and the direct normal irradiance varied from 1000 W/m^2 to 400 W/m^2. The fluid flow rate changed between 0.35 L/min to 0.2 L/min. The inlet fluid temperature was kept constant at 25 °C and the outlet was a pressure outlet. A thin layer of 2 mm of the thermal paste was applied between the copper layer and the heat sink. A free tetrahedral mesh was selected to discretize the computational domain with a total number of elements of 0.95×10^6 being chosen.

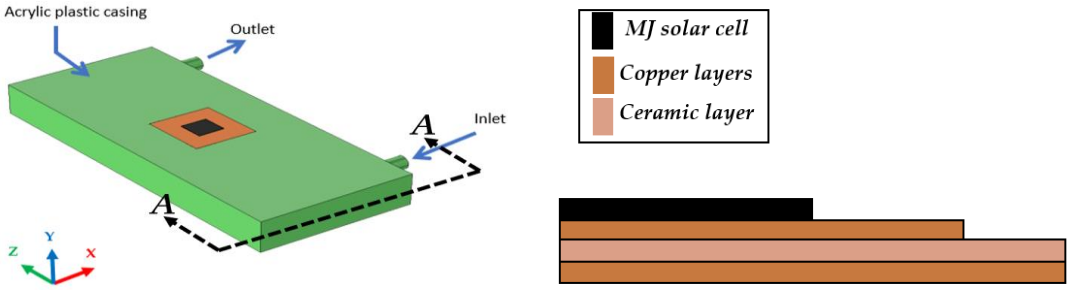

Figure 152 (a)The 3D model of the acrylic casing which contains the heat sink and solar cell, (b) The modelled CPV configuration

7.5.3 CPV system performance using distilled water

Figure 153a depicts the variation in the solar cell current with the voltage using water at different solar irradiances. An improvement in the current is noticed by increasing the solar irradiances from 400 W/m^2 to 1000 W/m^2 as the short circuit current increased by 131.38% due to the increase in the electrons' energy. On the other hand, a slight reduction in the open-circuit voltage reaching of 6% is

detected by increasing the solar irradiance. The change in the cell's power output with the solar irradiance and voltage is plotted as illustrated in Figure 153b. An improvement in the power output by increasing the solar irradiance is detected as the maximum power output reached 1400 mW at an irradiance of 1000 W/m^2 which decreased by 28.6% and 51% at 700 W/m^2 and 400 W/m^2, respectively.

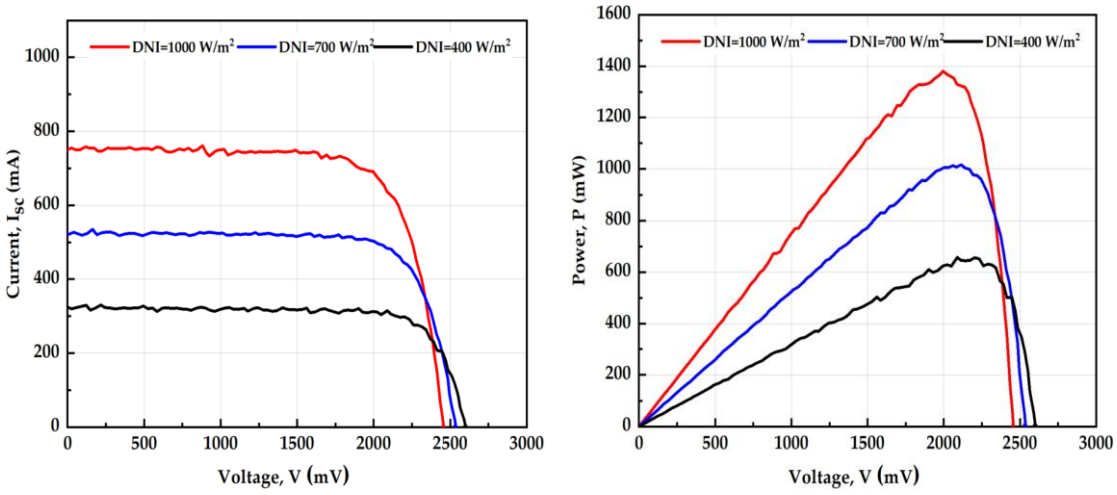

(a) **(b)**

Figure 153 (a) Variation of the cell current with voltage, (b) variation of the solar cell power output with voltage at different solar irradiances at a flow rate of 0.35 L/min.

Both the measured power output and fill factor are plotted against the solar irradiance as shown in Figure 154a. An enhancement in the cell's power output is observed with the increase in the solar irradiance in contrast to the fill factor as it reduced by 4.24% when the irradiance increased from 400 W/m^2 to 1000 W/m^2 due to the reduction in the cell voltage noticed at higher solar irradiances as presented in Figure 153.

A comparison between the measured and the theoretically calculated solar cell temperature at different working conditions is plotted in Figure 154. An increase in the cell's temperature with the increase in the solar irradiance is observed as the measured temperature increased from 55 °C to 86 °C using distilled water. Also, a good agreement is noticed from the comparison as the minimum and maximum calculated differences reached 4% and 9%, respectively.

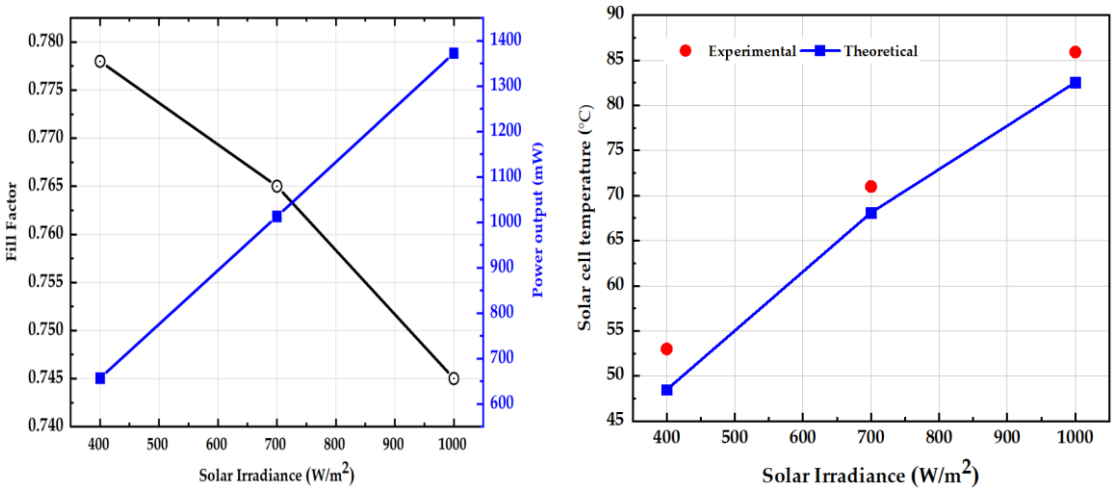

(a) **(b)**

Figure 154 (a) Change in the fill factor and power output with solar irradiance, (b) comparison between cell temperature's experimental and numerical results with solar irradiance using distilled water.

7.5.4 CPV system performance using nanofluid

In this section, the distilled water was replaced by 2.5% SiO_2/water as a working medium for the CPV system. The electrical performance of the system was measured in different working conditions which are the change in the solar irradiance and the flow rate. The obtained results are illustrated in Figure 155, Figure 156, and Figure 157 for solar irradiances of 1000 W/m^2, 700 W/m^2, and 400 W/m^2.

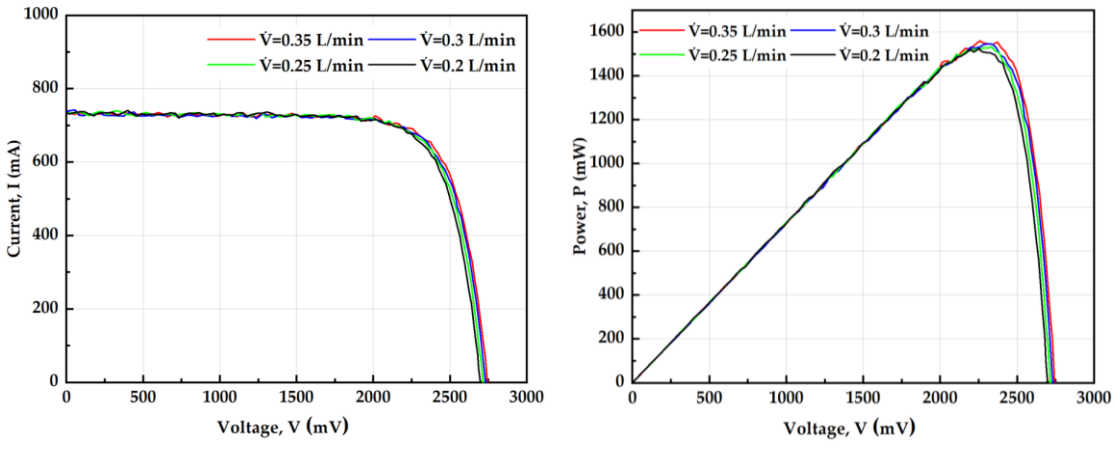

(a) **(b)**

Figure 155 (a) Change in the cell current and voltage, (b) change in power with voltage at different flow rates at solar irradiance of 1000 W/m^2.

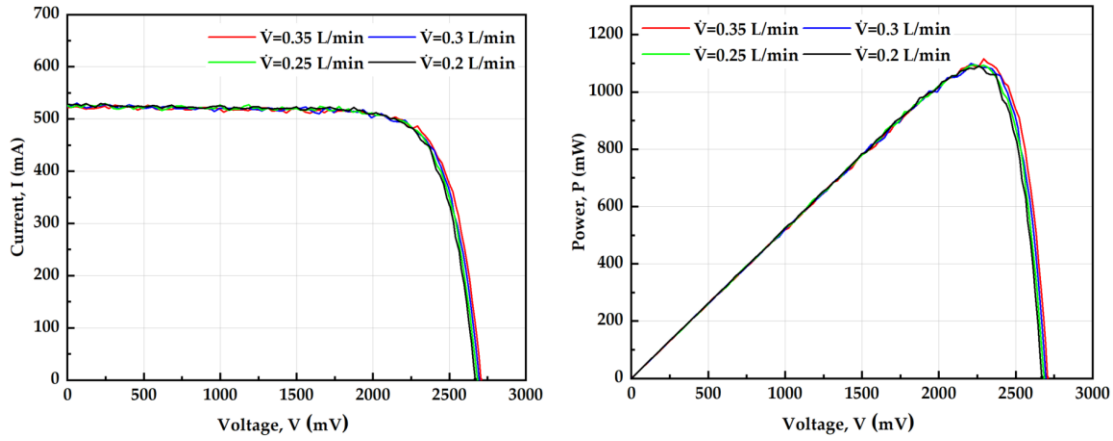

(a) **(b)**

Figure 156 (a) Change in the cell current and voltage, (b) change in power with voltage at different flow rates at solar irradiance of 700 W/m^2.

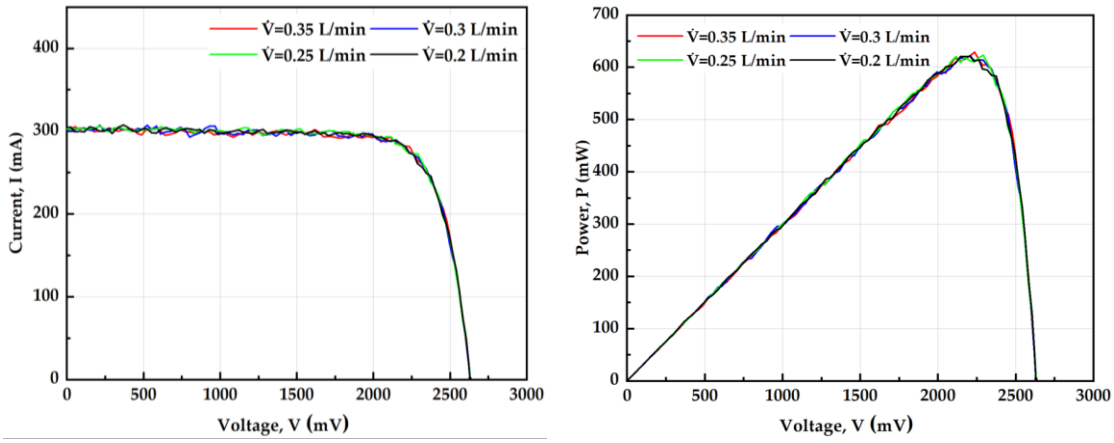

(a) **(b)**

Figure 157 (a) Change in the cell current and voltage, (b) change in power with voltage at different flow rates at solar irradiance of 400 W/m^2.

A slight change in the current and voltage was noticed with the tested flow rate, while an observed reduction in the power output is detected with a reduction in the flow rate due to the increase in the solar cell's temperature. On the other hand, the reduction of solar irradiance has a significant impact on the performance of the cell. The measured short circuit current values are 735.3 mA, 522.4 mA, and 301.5 mA at solar irradiances of 1000 W/m^2, 700 W/m^2, and 400 W/m^2, respectively at a flow rate of 0.35 L/min.

On the other hand, the measured open-circuit voltage increased to 2744 mV, 2708 mV, and 2631 mV at irradiances of 1000 W/m2, 700 W/m2, and 400 W/m2, respectively at a flow rate of 0.35 L/min. The variation of the solar cell's fill factor and power output with the flow rate and solar irradiance is illustrated in Figure 158.

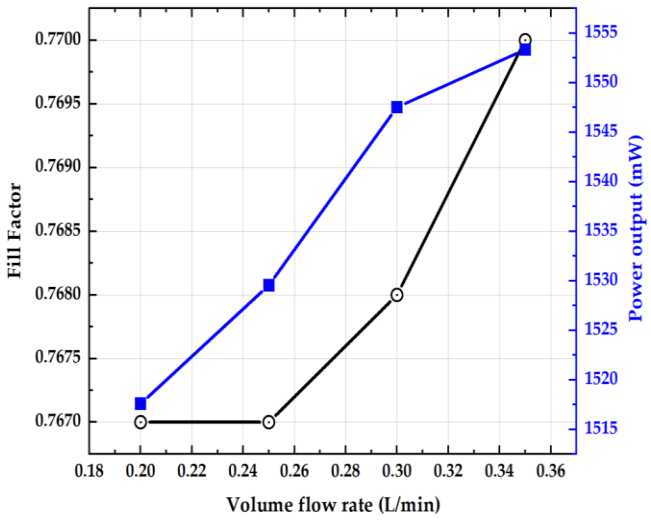

(a)

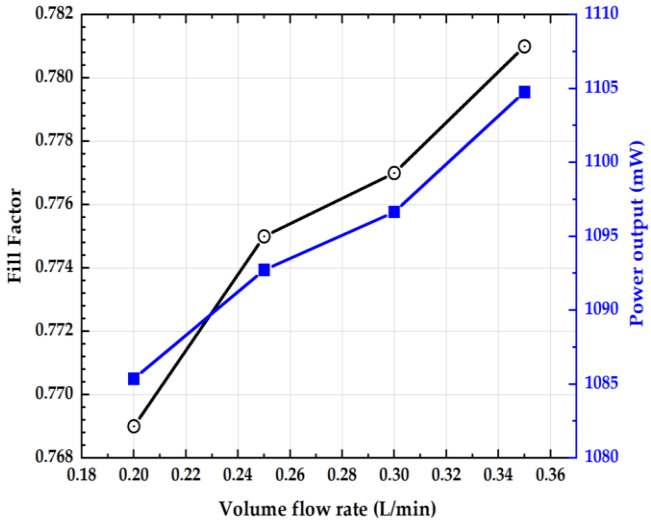

(b)

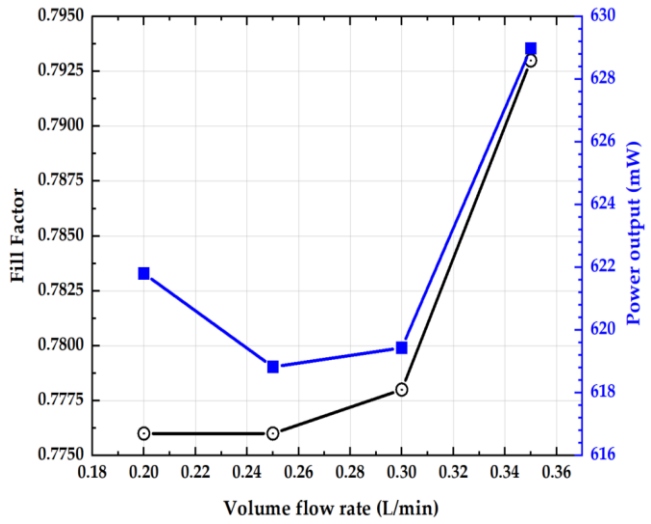

(c)

Figure 158 Change in the cell Fill Factor and power output at different values of flow rates and direct normal irradiances of (a) 1000 W/m^2, (b) 700 W/m^2, and (c) 400 W/m^2.

An enhancement in both the fill factor and power output is obtained by increasing the flow rate from 0.2 L/min to 0.35 L/min. The fill factor reached 0.77, 0.78, and 0.793 at solar irradiances of 1000 W/m^2, 700 W/m^2, and 400 W/m^2, respectively. On the other hand, the power output reached as high as 1553 mW at 1000 W/m^2 which is higher than the power output at 400 W/m^2 by almost 59%. Additionally, the performance parameters obtained by using distilled water and nanofluid are compared in terms of the cell's power output, fill factor, and cell efficiency at different solar irradiances as introduced in Figure 159. Using 2.5% SiO_2/water improved the cell's power output as shown in Figure 159a. Although utilizing water at 400 W/m^2 showed better power output, the enhancement increased by raising the solar irradiance reaching a maximum of 13.2 % at 1000 W/m^2.

In addition, the fill factor using the two working media is plotted against solar irradiance in Figure 159b. It can be seen that the fill factor shows a significant improvement by using SiO_2/water in comparison to water only. The average fill factor enhancement reached 2.5%. In terms of cell efficiency, utilizing SiO_2/water in the system showed significant results especially at higher solar irradiances as in Figure 159c the cell efficiency increasing by 3%. Nevertheless, the water showed a better efficiency value at 400 W/m^2 due to the increase in the power output shown in Figure 159a.

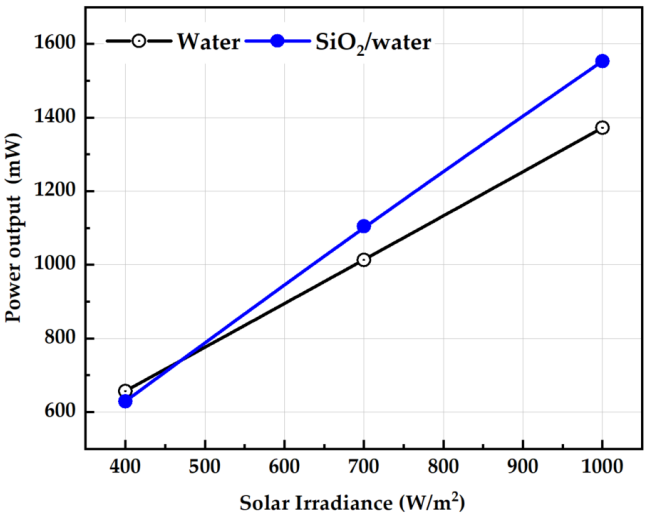

(a)

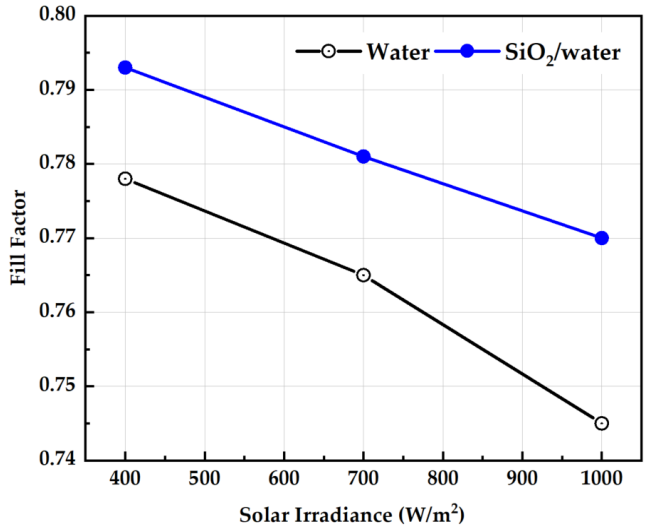

(b)

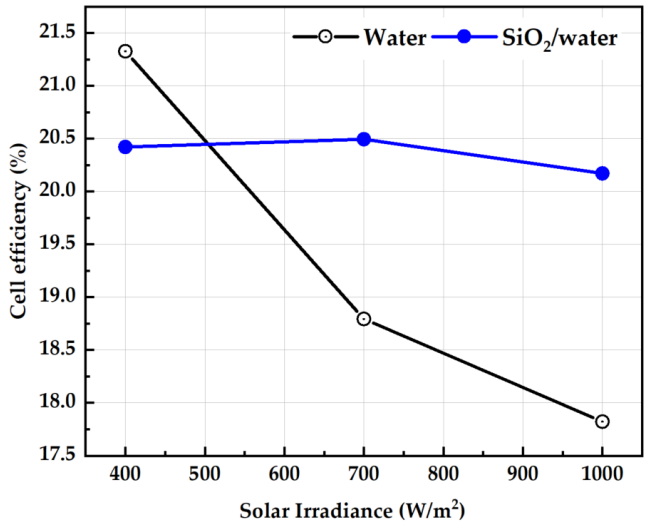

(c)

Figure 159 Comparison between using distilled water and SiO_2/water for (a) power output, (b) Fill Factor, and (c) cell efficiency.

Comparisons between the results obtained from the numerical modelling and the experimental measurements for both the solar cell and outlet temperatures at different values of flow rates and solar irradiances are plotted in Figure 160 a and b. An augmentation in the cell temperature is noticed by decreasing the flow rate reaching as high as 92 °C. Nevertheless, the cell temperature values are lower than the recommended limit. In addition, a reduction in the measured cell temperature by using nanofluid in comparison with using water reached 2.5 °C at 1000 W/m^2.

In terms of the outlet temperature, there is an increase in the temperature by decreasing the flow rate for all the tested solar irradiances the maximum temperature reaching 27.5 °C . Figure 161 shows the obtained temperature distribution contours for the solar cell and section A-A for the test section at different solar irradiances. Overall, a good agreement between the experimental and theoretical results is observed from the figures where the minimum and maximum differences in the cell temperatures reached 2% and 12%, respectively, while for the outlet temperature the error did not exceed 3.4%.

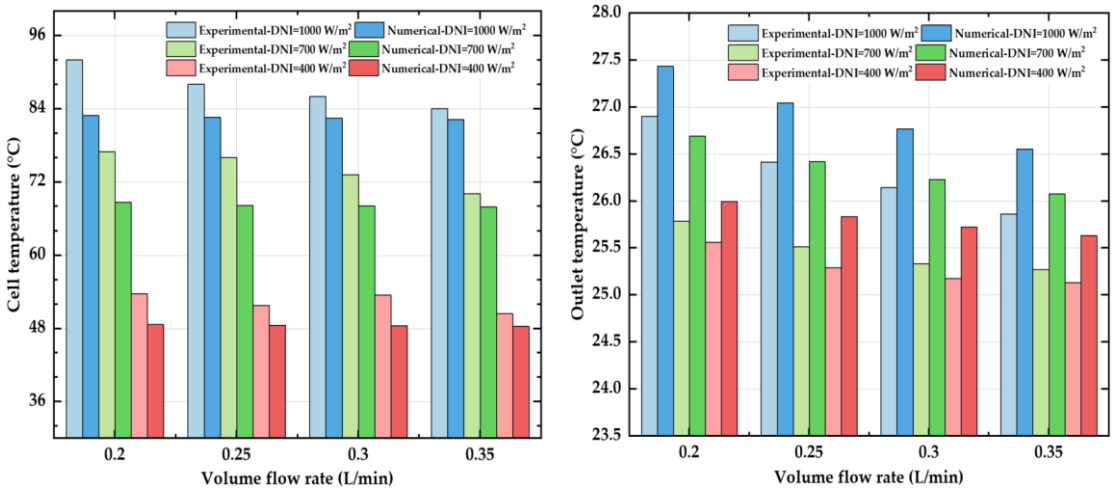

Figure 160 Comparison between the experimental and numerical results by using nanofluid for (a) cell temperature, and (b) outlet temperature.

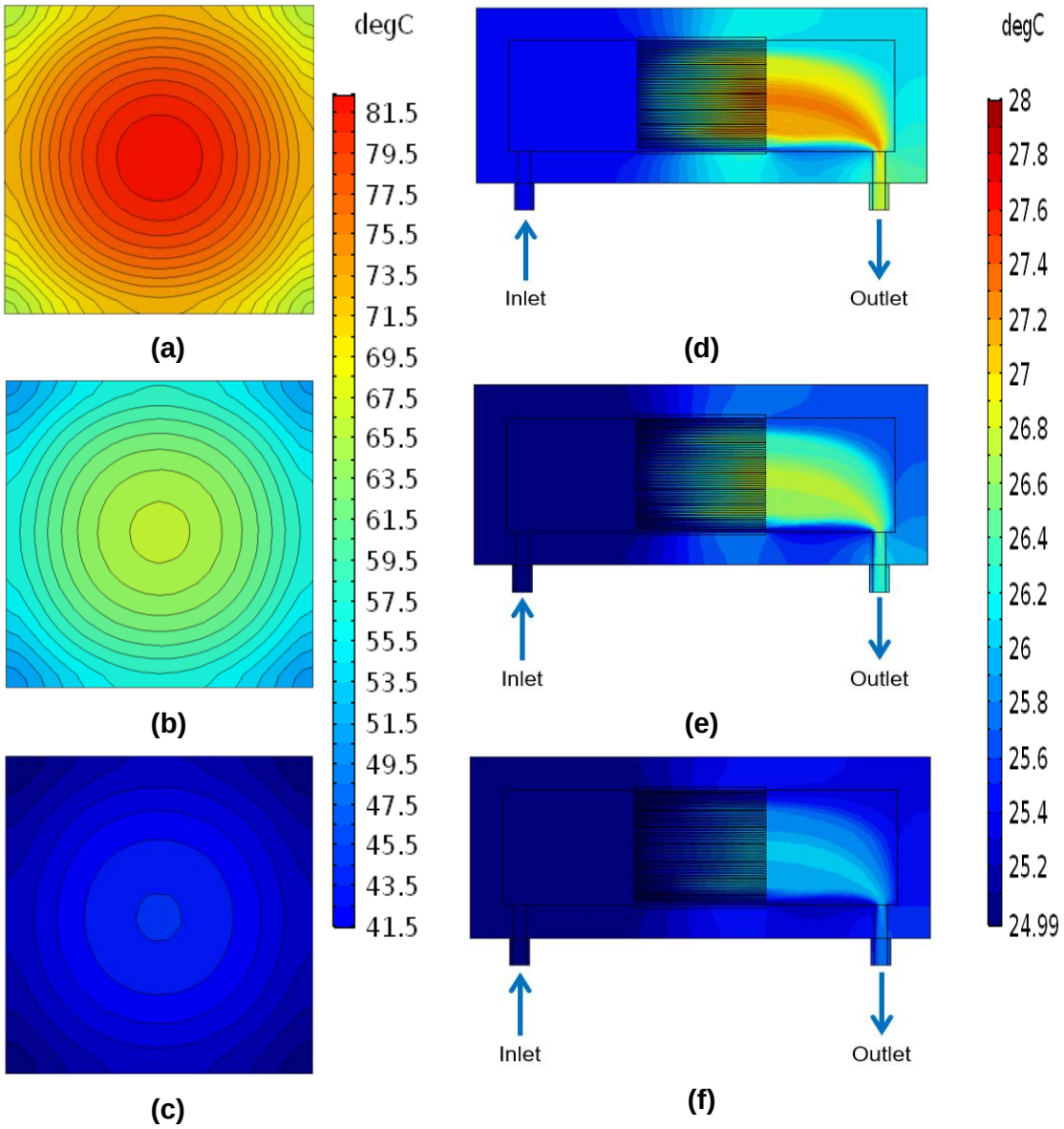

Figure 161 Temperature distribution of the solar cell at solar irradiances of (a) 1000 W/m^2, (b) 700 W/m^2, (c) 400 W/m^2 and temperature distribution at section (A-A) of the test section at solar irradiances of (d) 1000 W/m^2, (e) 700 W/m^2, (f) 400 W/m^2.

The performance parameters of the HCPVT system were calculated in terms of electrical, thermal, and total efficiency of the system as shown in Figure 162. A reduction in the electrical efficiency is observed with a decrease in the flow rate due to the increase in the cell temperature. Also, increasing the solar irradiance from 400 W/m^2 to 1000 W/m^2 reduces the electrical efficiency for all the tested flow rates. It can be seen that optimum cell performance of 20.5% is achieved at 700 W/m^2 and flow rate of 0.35 L/min. On the other hand, the thermal efficiency of the system is evaluated as presented in Figure 162b. From the graph, it can be seen that there is an improvement in the thermal efficiency using nanofluid

with a decrease in the flow rate as the fluid velocity is low which allows the fluid to absorb more heat from the cell.

Also, increasing the solar irradiance augmented the thermal efficiency due to the enhancement of the fluid thermal energy as more heat is absorbed by the heat sink. The maximum achieved thermal efficiency is 77% at 1000 W/m^2 and 0.2 L/min, while the lowest detected value is 20.6% at 400 W/m^2 and 0.35 L/min. The total efficiency of the system is evaluated and plotted in Figure 162c. Total efficiency is known as the summation of the thermal and electrical efficiencies. From Figure 162c, it can be observed that there is an increase in the total efficiency due to the large enhancement in the thermal efficiency noticed at higher solar irradiances and lower flow rates. A maximum of 97% of total efficiency is detected at 1000 W/m^2 and 0.2 L/min, while it decreased to 41% at 400 W/m^2 and 0.35 L/min.

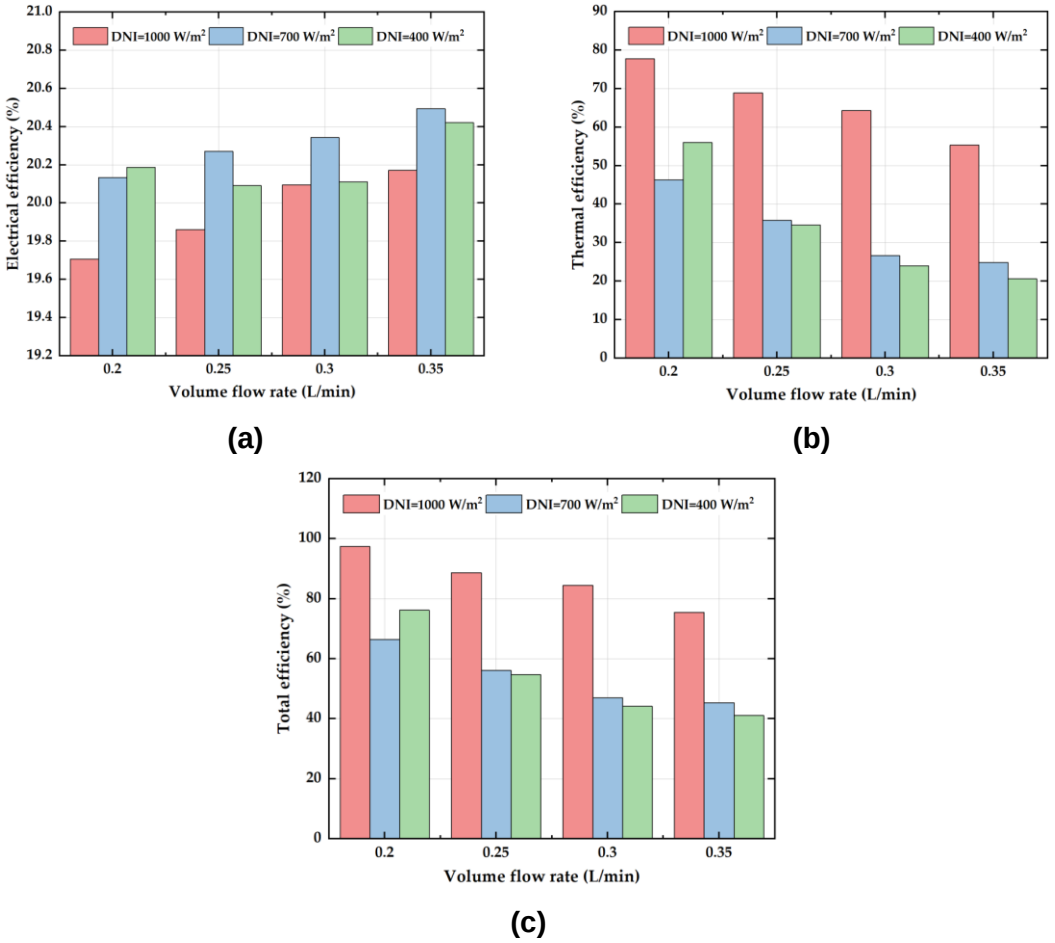

Figure 162 Variation of the (a) electrical efficiency, (b) thermal efficiency, (c) total efficiency with the nanofluid flow rate and solar irradiance.

7.6 Conclusion

This chapter evaluated the performance of the HCPVT system experimentally and numerically. The first section examined the possibility of using an IR filter with a silicon solar cell for a high concentrator photovoltaic system. The filter has been introduced to reduce the number of unwanted wavelengths which raise the temperature of the solar cell and decrease its efficiency. Investigations into the cell's performance with and without an IR filter have been described, including the contributing factors to its efficiency and stability under concentrated light. In one instance, the silicon cell cracked near the tabbing wire due to the difference in temperatures between the materials, but this did not occur when utilizing the filter even though the same effective concentrated light was incident on the cell. The IR filter, as expected, reduced the optical efficiency of the system due to its reduced transmittance spectra but when the irradiance was adjusted to compensate for this loss, the experimental power output was still slightly lower (1.133 W instead of 1.148 W). In comparison, the solar cell efficiency increased by 180% at solar irradiance of 400 W/m^2 when using the IR filter. Understanding the limits within which IR filtering is necessary or beneficial for increasingly high concentrating, and high-temperature CPV systems is, however, clearly important as the technology advances.

In the second section, a comprehensive investigation of the impact of using silicon on a glass Fresnel lens as a primary optical component for a high concentrator photovoltaic system has been introduced. Temperature distribution in the focal spot with/without introducing the MJ solar cell has been presented by using the thermocouples and IR camera. A good agreement has been observed between the two methods. The results showed that the focal spot temperature reached as high as 202 °C and after introducing the cooling mount the temperature reduce to 156 °C at the centre of the focal spot. Although the MJ solar cell had a good connection with the cooling mount via vacuum suction, the absence of a thermal paste and differing surface roughness augmented the cell temperature. The maximum recorded temperature for the cell was 100 °C while the lowest was 96.3 °C at a cooling temperature of 10 °C at the centre of the MJ solar cell. The results demonstrate the importance of even small heat-spreading mounting plates. The cell thermal and electrical performances were measured within the focal spot in case of any misalignment occurring between the lens and

the receiver. The results showed good thermal and electrical uniformity within the focal spot area.

In the third section, an experimental investigation on the impact of the heat sink configuration, working media, and flow rate on the CPV performance was presented. The solar cell was replaced by an electric resistance heater to model the thermal power of the cell. In addition, numerical validation of the test section was introduced. Two configurations of heat sinks were examined: straight and finned heat sinks, and two working media were studied: distilled water and 2.5% SiO_2/water. A good agreement was achieved between the experimental and numerical results with a maximum difference of 10.8%. This difference may be reduced even further if all the thermophysical properties of the fluids entered into the model were experimentally measured. Although the heater temperature was lower than the maximum recommended limit of the solar cell, the temperature may be decreased further if a high thermal conductivity thermal paste is utilised. The finned heat sink in combination with using 2.5% SiO_2/water offered the best temperature distribution for the system. The lowest heater temperature of 79 °C and thermal resistance of 0.0973 K/W were obtained at 0.3 L/min by using 2.5% SiO_2/water and finned channel heat sink.

In the last section, an indoor study of the HCPVT system performance using the MJ solar cell was carried out considering the influence of different experimental variables on the system behaviour. In addition, a numerical validation of the test section with the MJ solar cell was performed. The temperature distribution contours of different sections and cases were reported and the performance parameters of the HCPVT system were introduced. A good agreement was obtained between the experimental and numerical evaluations of the cell temperature with a maximum difference of 12%. This error may be decreased even further when considering the non-uniform illumination of the light on the surface of the solar cell and all the fluids' properties entered into the software are experimentally investigated. The solar cell temperature varied between 84 °C and 46 °C at a solar irradiance of 1000 W/m^2, while the total efficiency varied between 77% and 97% for flow rates 0.35 L/min and 0.2 L/min, respectively. Although the measured cell temperature was lower than the recommended maximum operating limit set by the manufacturer, it could be reduced further when a high thermal conductivity paste is utilised.

Chapter 8
Conclusions and recommendations for future work

8.1 Conclusions

This thesis has introduced theoretical and experimental investigations on innovative solutions for the advancement of the performance of high concentrator photovoltaic systems (HCPV). The research includes the following sections: a comprehensive literature review of concentrator photovoltaics from optical and thermal perspectives, the impact of different coolant types including the use of nanofluids, the impact of the heat sink design, an analysis of the focal spot area from thermal, optical, and electrical perspectives, the feasibility of using an infrared (IR) filter to enhance the system performance, and numerical and experimental validations for the HCPVT.

The first part of the thesis introduces a detailed review of the concentrator photovoltaic systems covering the solar cells and the integrated optics classifications. The existing designs of the primary and secondary optics have been also reviewed. The system challenges have been highlighted including the increase in the cell temperature related to the increase in the concentration ratio. Furthermore, the existing temperature regulating techniques have been reviewed suggesting that for higher concentration ratios, the active cooling method is considered a preferable technique. The optical filters, their working principles, and previous studies have also been addressed. Regarding the use of nanotechnology in solar thermal systems, a comprehensive review of this topic involving nanoparticle classifications and preparation methods, and parameters affecting the thermal conductivity have been highlighted.

In the second part of the thesis, detailed experimental investigations of the properties of a range of materials involving optical, thermal, and electrical studies have been introduced. The silicon on glass Fresnel lens has shown high transmittance values for the tested wavelengths. The average transmittance reached 92% for the whole wavelength range. In order to predict the effect of using the IR filter on the HCPV performance, the transmittance of the IR filter has

been identified. The filter average transmittance reached 19% through the whole wavelength range. After that, the thermal conductivity measurements of the distilled water, aluminium oxide/water, and silicon dioxide/water have been reported. These values have been validated with the thermal conductivity model. A significant enhancement in the tested nanofluids' thermal conductivity has been measured. A good agreement has been observed especially at lower temperatures. Furthermore, an electrical characterisation has been carried out for the single and multijunction solar cells.

The third part of the thesis has addressed the numerical modelling approach used throughout this research. The studied heat sink configurations and their dimensions have been introduced including the governing equations and boundary conditions to solve the three-dimensional modelling. Also, the theoretical equations used to analyse the system performance from energetic and exergetic perspectives have been reported. In addition, the thermophysical properties of different heat transfer fluids and nanofluids' single-phase model have been introduced. To ensure the solution accuracy, a number of grid-independent tests and validation studies have been conducted in the last section of this chapter.

In the fourth section, the HCPVT system performance using a single MJ solar cell and finned heat sink has been explored for a wide range of concentration ratios. Through this step, the feasibility of replacing water with an ethylene glycol and water mixture and syltherm oil has been investigated. Using water offered the most cell temperature uniformity in comparison with the other fluids. However, the highest outlet temperature has been achieved using syltherm oil 800 especially for a concentration ratio above 1000 suns which is suitable for heat recovery applications that require a high temperature. Overall, deciding the fluid suitability depends on several factors such as the designed concentration ratio, required outlet temperature and the thermal energy to be recovered.

The impact of using aluminium oxide/water and silicon dioxide/water nanofluids with a finned minichannel heat sink for the HCPVT system has been investigated. The heat transfer effectiveness of the nanofluids was enhanced at a higher Reynolds number as it reached 1.15 in the case of Al_2O_3/water at 5%, while in the case of using SiO_2/water reached 1.11. A uniform temperature distribution has been observed by using nanofluids especially at higher concentration ratios.

The maximum solar cell temperature decreased by 3.6 °C at a concentration of 2000 suns. Overall, utilising nanofluids for the HCPVT system enhanced the system performance significantly.

The impact of heat sink design on the system performance has been evaluated. The considered heat sink schemes were straight channel, centre inlet serpentine, and side inlet serpentine. The analysis includes several parameters such as concentration ratio and mass flow rate. The straight channel heat sink is not recommended for a concentration ratio higher than 1000 suns as the multijunction solar cell temperature exceeded 110 °C. The centre inlet serpentine showed the best performance until the concentration ratio of 2000 suns providing high-temperature uniformity and keeping the solar cell temperature below the recommended limit. Furthermore, from the exergy analysis perspective, it is recommended that the system runs at a low flow rate range for better total and thermal performance. A case study using the real weather conditions of Alexandria in Egypt has been performed, the solar cell temperature reaching 100 °C at a concentration ratio of 2000 suns.

In the fifth section, the feasibility of utilising the IR filter in the HCPV system based on a silicon solar cell has been examined experimentally. The investigation has been conducted using the silicon solar cell to avoid the damaging of the more expensive multijunction solar cell. The main aim of using this technique is to protect the solar cell from the cracking which appeared at the beginning of the experiment due to its fragility. A comparison between the performance parameters under different solar irradiance with and without the IR filter has been introduced. From the investigation, a number of relevant conclusions have been drawn. The IR filter successfully protects the cell from cracking reducing its temperature to 52 °C. Although the optical efficiency of the system dropped as expected by using the IR filter, the solar cell efficiency was enhanced by 180% at solar irradiance of 400 W/m^2.

A comprehensive analysis of the focal spot area of the Fresnel lens with and without utilising the solar cell has been conducted to determine the maximum temperature of the focal spot. Without any cooling, the focal spot temperature reached 202 °C under a geometrical concentration ratio of 529 suns. In order to predict the temperature distribution in the focal spot, a metallic grid of a tapped wires has been utilised. The focal spot temperature dropped to 156 °C at a

cooling mount temperature of 25 °C. After placing the MJ solar cell in the centre of the focal spot, the maximum temperature dropped significantly to 100 °C due to the attached layers (copper and ceramic) which worked as a heat spreader. Although the temperature was below the recommended operating temperature of the cell, it was still high which can be attributed to the absence of the thermal paste and differing surface roughness allowing an air gap between the copper layer and the surface of the cooling mount. Furthermore, to predict the electrical and thermal behaviour of the cell if a misalignment occurs between the lens and the receiver, the performance has been measured at different locations within the focal spot. Uniform electrical and thermal distribution has been detected within the focal spot showing the highest measured power at the centre of 2.5 W.

Detailed experimental and numerical validation have been carried out for the HCPVT system studying the impact of the heat sink configuration, working media, and flow rate. In this section, the solar cell has been replaced by a uniform heat source (electric resistance heater) to simulate its thermal load. A 3D model of the full test section has been built considering the experimental working conditions. A good agreement between the numerical and experimental results has been achieved with a maximum difference of 10.8%. Furthermore, using 2.5% SiO_2/water offers the best temperature distribution in comparison to distilled water.

Indoor experimental research has been conducted to evaluate the performance of the HCPVT system-based Fresnel lens. The effect of the working media, flow rate, and solar irradiance on the performance of the multijunction solar cell has been explored. A 3D numerical model of the test section including the solar cell has been built. The maximum reported solar cell temperature is 92 °C using 2.5% SiO_2/water. A good agreement between the experimental and numerical results has been obtained with a maximum difference of 12%. This error may be decreased even further if the non-uniformity of the light distribution is considered, and all the fluid properties are experimentally evaluated. Although the solar cell temperature was below the recommended limit, the temperature can be decreased even further if a high thermal conductivity thermal paste is utilised.

Finally, this thesis has introduced a number of solutions to thermally manage the temperature of the solar cells utilizing in HCPV applications starting from the heat sink design and choosing the most suitable cooling medium to the feasibility of

the IR filtering. In addition, a detailed analysis of the focal spot area aiming to build a solid base for additional research towards high and ultra-high concentration ratios has been performed.

8.2 Recommendations for future work

A further extension of the current research may be conducted including:

- A coupled optical, thermal, and electrical theoretical analysis of the HCPV system may be studied to evaluate the system output.
- Further investigation on the applicability of the IR filtering with the MJ solar cell.
- Detailed evaluation of the performance of the HCPV system after introducing a secondary optical component to minimize the non-uniformity of the incident light.
- The impact of other types of nanofluids could be investigated.
- The current heat sink casing was built as a prototype made from acrylic plastic which has a melting temperature of 160 °C which is not suitable for outdoor investigations, especially for higher concentration ratios. Therefore, the casing may be redesigned considering the improvement of the system performance, weight, and cost.
- Experimental investigation for different heat sink materials.
- Thermal cycling of the HCPV system components may be performed to predict the thermal deformation expected from the change in the temperature and other outdoor conditions.
- Levelized cost of energy (LCOE) may be performed for the HCPV system.

Bibliography

[1] NREL, Best Research-Cell Efficiency Chart, Natl. Renew. Energy Lab. (2019) 1. doi:http://www.nrel.gov/ncpv/images/efficiency_chart.jpg.

[2] International Renewable Energy Agency, Renewable energy technologies, 2020.

[3] International Renewable Energy Agency, Trends in Renewable Energy capacity, 2019. https://www.irena.org/solar.

[4] A.A. Hasan, J. Sarwar, A.A. Hasan, A.H. Shah, Concentrated photovoltaic: A review of thermal aspects, challenges and opportunities, Renew. Sustain. Energy Rev. 94 (2018) 835–852. doi:10.1016/j.rser.2018.06.014.

[5] M. Wiesenfarth, S.P. Philipps, A.W. Bett, K. Horowitz, S. Kurtz, Current Status of Concentrated Photovoltaic (CPV) Technology, 2017.

[6] K. Araki, H. Uozumi, M. Yamaguchi, A simple passive cooling structure and its heat analysis for 500× concentrator PV module, in: Conf. Rec. Twenty-Ninth IEEE Photovolt. Spec. Conf. 2002., IEEE, 2002: pp. 1568–1571. doi:10.1109/PVSC.2002.1190913.

[7] Azure Space Solar Power GMBH, AZUR space solar cell assembly 10x10mm^2, 2014. http://www.azurspace.com/images/products/DB_3987-00-00_3C42_AzurDesign_EFA_10x10_2014-03-27.pdf.

[8] X. Py, Y. Azoumah, R. Olives, Concentrated solar power: Current technologies, major innovative issues and applicability to West African countries, Renew. Sustain. Energy Rev. 18 (2013) 306–315. doi:10.1016/j.rser.2012.10.030.

[9] E.R. Shouman, H. Ezz, Forecasting transition electricity solar energy from Mena to Europe, ARPN J. Eng. Appl. Sci. 11 (2016) 3029–3040.

[10] Direct Normal Irradiation, (n.d.). https://solargis.com/maps-and-gis-data/download/world (accessed November 4, 2020).

[11] D. Barlev, R. Vidu, P. Stroeve, Innovation in concentrated solar power, Sol. Energy Mater. Sol. Cells. 95 (2011) 2703–2725. doi:10.1016/j.solmat.2011.05.020.

[12] S.B.S. GmbH, Solar Updraft Tower, Schlaich Bergermann Solar GmbH, 2011. http:%5C%5Cwww.solar-updraft-tower.com.

[13] P. Meisen, Solar-energy-and-technologies-2015-03-11, (2014) 1–40.

[14] C. Kost, T. Schlegl, J. Thomsen, S. Nold, J. Mayer, N. Hartmann, C.

Senkpiel, S. Philipps, S. Lude, N. Saad, Fraunhofer ISE: Levelized Cost of Electricity - Renewable Energy Technologies, March 2018, Fraunhofer ISE Levelized Cost Electr. - Renew. Energy Technol. (2018).

[15] S. Kurtz, Opportunities and Challenges for Development of a Mature Concentrating Photovoltaic Power Industry Opportunities and Challenges for Development of a Mature Concentrating Photovoltaic Power Industry, Natl. Renew. Energy Lab. (2012) 35. http://www.nrel.gov/docs/fy13osti/43208.pdf.

[16] A. Peled, J. Appelbaum, Minimizing the current mismatch resulting from different locations of solar cells within a PV module by proposing new interconnections, Sol. Energy. 135 (2016) 840–847. doi:10.1016/j.solener.2016.06.016.

[17] K. Shanks, J.P. Ferrer-Rodriguez, E.F. Fernàndez, F. Almonacid, P. Pérez-Higueras, S. Senthilarasu, T. Mallick, A >3000 suns high concentrator photovoltaic design based on multiple Fresnel lens primaries focusing to one central solar cell, Sol. Energy. 169 (2018) 457–467. doi:10.1016/j.solener.2018.05.016.

[18] K. Araki, K.H. Lee, M. Yamaguchi, Analysis of impact to optical environment of the land by CPV, AIP Conf. Proc. 1766 (2016). doi:10.1063/1.4962108.

[19] T. Zhang, H. Yang, High Efficiency Plants and Building Integrated Renewable Energy Systems, in: Handb. Energy Effic. Build., Elsevier, 2019: pp. 441–595. doi:10.1016/B978-0-12-812817-6.00040-1.

[20] T. Markvart, L. Castañer, Principles of Solar Cell Operation, in: McEvoy's Handb. Photovoltaics, Elsevier, 2018: pp. 3–28. doi:10.1016/B978-0-12-809921-6.00001-X.

[21] S. Sundaram, K. Shanks, H. Upadhyaya, Thin Film Photovoltaics, in: A Compr. Guid. to Sol. Energy Syst., Elsevier, 2018: pp. 361–370. doi:10.1016/B978-0-12-811479-7.00018-X.

[22] SOLOPOWER systems, SOLOPOWER, (n.d.). http://solopower.com.

[23] M. YAMAGUCHI, III–V compound multi-junction solar cells: present and future, Sol. Energy Mater. Sol. Cells. 75 (2003) 261–269. doi:10.1016/S0927-0248(02)00168-X.

[24] A.W. Bett, S.P. Philipps, S.S. Essig, S. Heckelmann, R. Kellenbenz, V. Klinger, M. Niemeyer, D. Lackner, F. Dimroth, Overview about technology

perspectives for high efficiency solar cells for space and terrestrial applications, 28th Eur. Photovolt. Sol. Energy Conf. Exhib. 0 (2013) 1–6. http://developzmi2.ise.fhg.de/isesite/de/veroeffentlichungen/konferenzbeitraege/konferenzbeitraege-2013/28th-eupvsec/bett.pdf.

[25] B. Burnett, The Basic Physics and Design of III-V Multijunction Solar Cells, Golden, Colorado, 2002. doi:10.1063/1.3658334.

[26] A. McEvoy, T. Markvart, L. Castaner, Practical Handbook of Photovoltaics - Fundamentals and Applications (2012), 2012.

[27] S.P. Philipps, A.W. Bett, III-V Multi-junction solar cells and concentrating photovoltaic (CPV) systems, Adv. Opt. Technol. 3 (2014) 469–478. doi:10.1515/aot-2014-0051.

[28] NREL, Best research-cell efficiencies, n.d. https://www.nrel.gov/pv/cell-efficiency.html.

[29] NREL, Champion Module Efficiencies, 2021. https://www.nrel.gov/pv/module-efficiency.html.

[30] A.W. Bett, F. Dimroth, G. Stollwerck, O. V. Sulima, III-V compounds for solar cell applications, Appl. Phys. A Mater. Sci. Process. 69 (1999) 119–129. doi:10.1007/s003390050983.

[31] A. Luque, V. Andreev, Concentrator Photovoltaics, Springer, Berlin, 2007.

[32] S. Sundaram, D. Benson, T.K. Mallick, Potential Environmental Impacts From Solar Energy Technologies, Sol. Photovolt. Technol. Prod. (2016) 23–45. doi:10.1016/b978-0-12-802953-4.00003-2.

[33] IEEE Std 1513-2001, IEEE Recommended Practice for Qualification of Concentrator Photovoltaic (PV) Receiver Sections, 2001. doi:10.1109/IEEESTD.2001.92764.

[34] M. Wiesenfarth, I. Anton, A.W. Bett, Challenges in the design of concentrator photovoltaic (CPV) modules to achieve highest efficiencies, Appl. Phys. Rev. 5 (2018). doi:10.1063/1.5046752.

[35] K. Shanks, S. Senthilarasu, T.K. Mallick, Optics for concentrating photovoltaics: Trends, limits and opportunities for materials and design, Renew. Sustain. Energy Rev. 60 (2016) 394–407. doi:10.1016/j.rser.2016.01.089.

[36] M. Bass, Handbook of Optics, 2nd ed., McGraw-Hill Education, 2010.

[37] R. Winston, L. Jiang, M. Ricketts, Nonimaging optics: a tutorial, Adv. Opt. Photonics. 10 (2018) 484. doi:10.1364/aop.10.000484.

[38] R. Winston, J.C. Miñano, P. Benitez, N. Shatz, J.C. Bortz, Nonimaging Optics, Nonimaging Opt. (2005). doi:10.1016/B978-0-12-759751-5.X5000-3.

[39] N. Gakkhar, M.S. Soni, S. Jakhar, Analysis of Water Cooling of CPV Cells Mounted on Absorber Tube of a Parabolic Trough Collector, Energy Procedia. 90 (2016) 78–88. doi:10.1016/j.egypro.2016.11.172.

[40] A. Ustaoglu, C. Kandilli, M. Cakmak, H. Torlaklı, Experimental and economical performance investigation of V-trough concentrator with different reflectance characteristic in photovoltaic applications, J. Clean. Prod. 272 (2020). doi:10.1016/j.jclepro.2020.123072.

[41] Q.C. Murphree, Point focusing double parabolic trough concentrator, Sol. Energy. 70 (2001) 85–94. doi:10.1016/S0038-092X(00)00138-9.

[42] K.J. Weber, V. Everett, P.N.K. Deenapanray, E. Franklin, A.W. Blakers, Modeling of static concentrator modules incorporating lambertian or v-groove rear reflectors, Sol. Energy Mater. Sol. Cells. 90 (2006) 1741–1749. doi:10.1016/j.solmat.2005.09.012.

[43] R. Tang, X. Liu, Optical performance and design optimization of V-trough concentrators for photovoltaic applications, Sol. Energy. 85 (2011) 2154–2166. doi:10.1016/j.solener.2011.06.001.

[44] S. Van Riesen, M. Neubauer, A. Boos, M.M. Rico, C. Gourdel, S. Wanka, R. Krause, P. Guernard, A. Gombert, New module design with 4-junction solar cells for high efficiencies, AIP Conf. Proc. 1679 (2015). doi:10.1063/1.4931553.

[45] T. Schult, M. Neubauer, Y. Bessler, P. Nitz, A. Gombert, Temperature Dependence of Fresnel Lenses for Concentrating Photovoltaics, ResearchGate. (2009) 2. https://www.researchgate.net/profile/Andreas_Gombert3/publication/267374113_Temperature_Dependence_of_Fresnel_Lenses_for_Concentrating_Photovoltaics/links/54b6625a0cf2e68eb27e832c.pdf.

[46] T. Hornung, M. Neubauer, A. Gombert, P. Nitz, Fresnel lens concentrator with improved thermal behavior, AIP Conf. Proc. 1407 (2011) 66–69. doi:10.1063/1.3658296.

[47] F. Languy, K. Fleury, C. Lenaerts, J. Loicq, D. Regaert, T. Thibert, S. Habraken, Flat Fresnel doublets made of PMMA and PC: combining low cost production and very high concentration ratio for CPV, Opt. Express.

19 (2011) A280. doi:10.1364/oe.19.00a280.

[48] F. Languy, C. Lenaerts, J. Loicq, T. Thibert, S. Habraken, Performance of solar concentrator made of an achromatic Fresnel doublet measured with a continuous solar simulator and comparison with a singlet, Sol. Energy Mater. Sol. Cells. 109 (2013) 70–76. doi:10.1016/j.solmat.2012.10.008.

[49] F. Languy, S. Habraken, Performance comparison of four kinds of flat nonimaging Fresnel lenses made of polycarbonates and polymethyl methacrylate for concentrated photovoltaics, Opt. Lett. 36 (2011) 2743. doi:10.1364/ol.36.002743.

[50] M. Victoria, C. Domínguez, N. Jost, G. Vallerotto, I. Antón, G. Sala, Spectrally-resolved optical efficiency using a multi-junction cell as light sensor: Application cases, AIP Conf. Proc. 1881 (2017). doi:10.1063/1.5001422.

[51] J. Jaus, A.W. Bett, H. Reinecke, E.R. Weber, Reflective secondary optical elements for fresnel lens based concentrator modules, Prog. Photovoltaics Res. Appl. 19 (2011) 580–590. doi:10.1002/pip.1065.

[52] K. Shanks, H. Baig, N.P. Singh, S. Senthilarasu, K.S. Reddy, T.K. Mallick, Prototype fabrication and experimental investigation of a conjugate refractive reflective homogeniser in a cassegrain concentrator, Sol. Energy. 142 (2017) 97–108. doi:10.1016/j.solener.2016.11.038.

[53] R. Herrero, M. Victoria, C. Domínguez, S. Askins, I. Antón, G. Sala, Understanding causes and effects of non-uniform light distributions on multi-junction solar cells: Procedures for estimating efficiency losses, AIP Conf. Proc. 1679 (2015). doi:10.1063/1.4931527.

[54] J. Jaus, P. Nitz, G. Perharz, G. Siefer, T. Schult, O. Wolf, M. Passig, T. Gand, A. Bett, SECOND STAGE REFLECTIVE AND REFRACTIVE OPTICS FOR CONCENTRATOR PHOTOVOLTAICS, Proc. 33rd IEEE Photovolt. Spec. Conf. (IEEE). (2008) 1–5.

[55] M. Victoria, S. Askins, I. Antón, G. Sala, G. Duggan, Temperature effects on two-stage optics made of silicone, AIP Conf. Proc. 1616 (2014) 92–96. doi:10.1063/1.4897036.

[56] N. Sellami, T.K. Mallick, Optical efficiency study of PV Crossed Compound Parabolic Concentrator, Appl. Energy. 102 (2013) 868–876. doi:10.1016/j.apenergy.2012.08.052.

[57] A. Ustaoglu, U. Ozbey, H. Torlaklı, Numerical investigation of concentrating

photovoltaic/thermal (CPV/T) system using compound hyperbolic – trumpet, V-trough and compound parabolic concentrators, Renew. Energy. 152 (2020) 1192–1208. doi:10.1016/j.renene.2020.01.094.

[58] Y. Su, S.B. Riffat, G. Pei, Comparative study on annual solar energy collection of a novel lens-walled compound parabolic concentrator (lens-walled CPC), Sustain. Cities Soc. 4 (2012) 35–40. doi:10.1016/j.scs.2012.05.001.

[59] Y. Su, G. Pei, S.B. Riffat, H. Huang, Radiance/Pmap simulation of a novel lens-walled compound parabolic concentrator (lens-walled CPC), Energy Procedia. 14 (2012) 572–577. doi:10.1016/j.egypro.2011.12.977.

[60] T. Cooper, F. Dähler, G. Ambrosetti, A. Pedretti, A. Steinfeld, Performance of compound parabolic concentrators with polygonal apertures, Sol. Energy. 95 (2013) 308–318. doi:10.1016/j.solener.2013.06.023.

[61] I.M. Saleh Ali, T. Srihari Vikram, T.S. O'Donovan, K.S. Reddy, T.K. Mallick, Design and experimental analysis of a static 3-D elliptical hyperboloid concentrator for process heat applications, Sol. Energy. 102 (2014) 257–266. doi:10.1016/j.solener.2014.01.031.

[62] L.C. Hirst, N.J. Ekins-Daukes, Fundamental losses in solar cells, Prog. Photovoltaics Res. Appl. 19 (2011) 286–293. doi:10.1002/pip.1024.

[63] M.K. Wong, K.Y. Wong, Investigation of the factors affecting the power conversion efficiency of all-solution-processed "bilayer" P3HT:PCBM solar cells, Synth. Met. 170 (2013) 1–6. doi:10.1016/j.synthmet.2013.02.021.

[64] K. Bücher, Site dependence of the energy collection of PV modules, Sol. Energy Mater. Sol. Cells. 47 (1997) 85–94. doi:10.1016/S0927-0248(97)00028-7.

[65] A. Royne, C.J. Dey, D.R. Mills, Cooling of photovoltaic cells under concentrated illumination: A critical review, Sol. Energy Mater. Sol. Cells. 86 (2005) 451–483. doi:10.1016/j.solmat.2004.09.003.

[66] A. Makki, S. Omer, H. Sabir, Advancements in hybrid photovoltaic systems for enhanced solar cells performance, Renew. Sustain. Energy Rev. 41 (2015) 658–684. doi:10.1016/j.rser.2014.08.069.

[67] Fundamentals Article, Photovoltaic Efficiency : The Temperature Effect, (2012) 1–4.

[68] M. Hasanuzzaman, A.B.M.A. Malek, M.M. Islam, A.K. Pandey, N.A. Rahim, Global advancement of cooling technologies for PV systems: A review, Sol.

Energy. 137 (2016) 25–45. doi:10.1016/j.solener.2016.07.010.

[69] S. Sargunanathan, A. Elango, S.T. Mohideen, Performance enhancement of solar photovoltaic cells using effective cooling methods: A review, Renew. Sustain. Energy Rev. 64 (2016) 382–393. doi:10.1016/j.rser.2016.06.024.

[70] F. Grubišić-Čabo, S. Nižetić, T.G. Marco, Photovoltaic panels: A review of the cooling techniques, Trans. Famena. 40 (2016) 63–74.

[71] H.M.S. Bahaidarah, A.A.B. Baloch, P. Gandhidasan, Uniform cooling of photovoltaic panels: A review, Renew. Sustain. Energy Rev. 57 (2016) 1520–1544. doi:10.1016/j.rser.2015.12.064.

[72] A. Ahmed, K. Shanks, S. Sundaram, T.K. Mallick, Theoretical investigation of the temperature limits of an actively cooled high concentration photovoltaic system, Energies. 13 (2020) 1902. doi:10.3390/en13081902.

[73] E.F. Fernández, D.L. Talavera, F.M. Almonacid, G.P. Smestad, Investigating the impact of weather variables on the energy yield and cost of energy of grid-connected solar concentrator systems, Energy. 106 (2016) 790–801. doi:10.1016/j.energy.2016.03.060.

[74] A. Valera, E.F. Fernández, P.M. Rodrigo, F. Almonacid, Feasibility of flat-plate heat-sinks using microscale solar cells up to 10,000 suns concentrations, Sol. Energy. 181 (2019) 361–371. doi:10.1016/j.solener.2019.02.013.

[75] M. Theristis, T.S. O'Donovan, Electrical-thermal analysis of III-V triple-junction solar cells under variable spectra and ambient temperatures, Sol. Energy. 118 (2015) 533–546. doi:10.1016/j.solener.2015.06.003.

[76] I. Mudawar, Assessment of high-heat-flux thermal management schemes, IEEE Trans. Components Packag. Technol. 24 (2001) 122–141. doi:10.1109/6144.926375.

[77] L. Micheli, E.F. Fernández, F. Almonacid, T.K. Mallick, G.P. Smestad, Performance, limits and economic perspectives for passive cooling of High Concentrator Photovoltaics, Sol. Energy Mater. Sol. Cells. 153 (2016) 164–178. doi:10.1016/j.solmat.2016.04.016.

[78] S. Hong, B. Zhang, C. Dang, E. Hihara, Development of two-phase flow microchannel heat sink applied to solar-tracking high-concentration photovoltaic thermal hybrid system, Energy. 212 (2020) 118739. doi:10.1016/j.energy.2020.118739.

[79] L. Micheli, S. Senthilarasu, K.S. Reddy, T.K. Mallick, Applicability of silicon micro-finned heat sinks for 500× concentrating photovoltaics systems, J. Mater. Sci. 50 (2015) 5378–5388. doi:10.1007/s10853-015-9065-2.

[80] A. Aldossary, S. Mahmoud, R. Al-Dadah, Technical feasibility study of passive and active cooling for concentrator PV in harsh environment, Appl. Therm. Eng. 100 (2016) 490–500. doi:10.1016/j.applthermaleng.2016.02.023.

[81] Y. Wu, P. Eames, T. Mallick, M. Sabry, Experimental characterisation of a Fresnel lens photovoltaic concentrating system, Sol. Energy. 86 (2012) 430–440. doi:10.1016/j.solener.2011.10.032.

[82] E.M. Abo-Zahhad, S. Ookawara, A. Radwan, A.H. El-Shazly, M.F. El-Kady, M.F.C. Esmail, Performance, limits, and thermal stress analysis of high concentrator multijunction solar cell under passive cooling conditions, Appl. Therm. Eng. 164 (2020) 114497. doi:10.1016/j.applthermaleng.2019.114497.

[83] S. Sharma, A. Tahir, K.S. Reddy, T.K. Mallick, Performance enhancement of a Building-Integrated Concentrating Photovoltaic system using phase change material, Sol. Energy Mater. Sol. Cells. 149 (2016) 29–39. doi:10.1016/j.solmat.2015.12.035.

[84] S. Sharma, L. Micheli, W. Chang, A.A. Tahir, K.S. Reddy, T.K. Mallick, Nano-enhanced Phase Change Material for thermal management of BICPV, Appl. Energy. 208 (2017) 719–733. doi:10.1016/j.apenergy.2017.09.076.

[85] S. Manikandan, C. Selvam, N. Poddar, K. Pranjyal, R. Lamba, S.C. Kaushik, Thermal management of low concentrated photovoltaic module with phase change material, J. Clean. Prod. 219 (2019) 359–367. doi:10.1016/j.jclepro.2019.02.086.

[86] I. Zarma, M. Ahmed, S. Ookawara, Enhancing the performance of concentrator photovoltaic systems using Nanoparticle-phase change material heat sinks, Energy Convers. Manag. 179 (2019) 229–242. doi:10.1016/j.enconman.2018.10.055.

[87] M. Emam, M. Ahmed, Performance analysis of a new concentrator photovoltaic system integrated with phase change material and water jacket, Sol. Energy. 173 (2018) 1158–1172. doi:10.1016/j.solener.2018.08.069.

[88] W.G. Anderson, S. Tamanna, D.B. Sarraf, P.M. Dussinger, Heat Pipe Cooling of Concentrating Photovoltaic Cells, 6th Int. Energy Convers. Eng. Conf. (2008). doi:https://doi.org/10.2514/6.2008-5672.

[89] A. Akbarzadeh, T. Wadowski, Heat pipe-based cooling systems for photovoltaic cells under concentrated solar radiation, Appl. Therm. Eng. 16 (1996) 81–87. doi:10.1016/1359-4311(95)00012-3.

[90] A. Cheknane, B. Benyoucef, A. Chaker, Performance of concentrator solar cells with passive cooling, Semicond. Sci. Technol. 21 (2006) 144–147. doi:10.1088/0268-1242/21/2/007.

[91] Y.A. Cengel, A.J. Ghajar, Heat Transfer: A practical approach, 3rd ed., Mc Graw Hill, 2006.

[92] L. Zhu, R.F. Boehm, Y. Wang, C. Halford, Y. Sun, Water immersion cooling of PV cells in a high concentration system, Sol. Energy Mater. Sol. Cells. 95 (2011) 538–545. doi:10.1016/j.solmat.2010.08.037.

[93] L. Zhu, Z. Fang, Y. Wang, Q. Huang, L. Han, Higher Performance of Silicon Solar Cells Immersed in Dielectric Liquid, Proc. ISES World Congr. 2007 (Vol. I – Vol. V). (2009) 1043–1047. doi:10.1007/978-3-540-75997-3_202.

[94] G. Xin, Y. Wang, Y. Sun, Q. Huang, L. Zhu, Experimental study of liquid-immersion III-V multi-junction solar cells with dimethyl silicon oil under high concentrations, Energy Convers. Manag. 94 (2015) 169–177. doi:10.1016/j.enconman.2015.01.063.

[95] X. Han, Y. Wang, L. Zhu, The performance and long-term stability of silicon concentrator solar cells immersed in dielectric liquids, Energy Convers. Manag. 66 (2013) 189–198. doi:10.1016/j.enconman.2012.10.009.

[96] X. Kang, Y. Wang, Q. Huang, Y. Cui, X. Shi, Y. Sun, Study on direct-contact phase-change liquid immersion cooling dense-array solar cells under high concentration ratios, Energy Convers. Manag. 128 (2016) 95–103. doi:10.1016/j.enconman.2016.09.073.

[97] F. Al-Amri, T.K. Mallick, Alleviating operating temperature of concentration solar cell by air active cooling and surface radiation, Appl. Therm. Eng. 59 (2013) 348–354. doi:10.1016/j.applthermaleng.2013.05.045.

[98] F. Al-Amri, T.K. Mallick, Effects of nonuniform incident illumination on the thermal performance of a concentrating triple junction solar cell, Int. J. Photoenergy. 2014 (2014). doi:10.1155/2014/642819.

[99] M. Sabry, Temperature optimization of high concentrated active cooled

solar cells, NRIAG J. Astron. Geophys. 5 (2016) 23–29. doi:10.1016/j.nrjag.2016.03.002.

[100] A. Radwan, S. Ookawara, M. Ahmed, Analysis and simulation of concentrating photovoltaic systems with a microchannel heat sink, Sol. Energy. 136 (2016) 35–48. doi:10.1016/j.solener.2016.06.070.

[101] K.S.S. Reddy, S. Lokeswaran, P. Agarwal, T.K. Mallick, Numerical investigation of micro-channel based active module cooling for solar CPV system, Energy Procedia. 54 (2014) 400–416. doi:10.1016/j.egypro.2014.07.283.

[102] I. Al Siyabi, S. Khanna, S. Sundaram, T. Mallick, Experimental and numerical thermal analysis of multi-layered microchannel heat sink for concentrating photovoltaic application, Energies. 12 (2019). doi:10.3390/en12010122.

[103] I. Al Siyabi, K. Shanks, T. Mallick, S. Sundaram, Indoor and outdoor characterization of concentrating photovoltaic attached to multi-layered microchannel heat sink, Sol. Energy. 202 (2020) 55–72. doi:10.1016/j.solener.2020.03.101.

[104] K. Yang, C. Zuo, A novel multi-layer manifold microchannel cooling system for concentrating photovoltaic cells, Energy Convers. Manag. 89 (2015) 214–221. doi:10.1016/j.enconman.2014.09.046.

[105] I. Al Siyabi, K. Shanks, T. Mallick, S. Sundaram, Thermal analysis of a multi-layer microchannel heat sink for cooling concentrator photovoltaic (CPV) cells, AIP Conf. Proc. 1881 (2017). doi:10.1063/1.5001434.

[106] A. Y. M. Ali, E.M. Abo-Zahhad, H.I. Elqady, M. Rabie, M.F. Elkady, S. Ookawara, A.H. El-Shazly, A. Radwan, Thermal Analysis of High Concentrator Photovoltaic Module Using Convergent-Divergent Microchannel Heat Sink Design, Appl. Therm. Eng. 183 (2020) 116201. doi:10.1016/j.applthermaleng.2020.116201.

[107] A.Y.M. Ali, E.M. Abo-Zahhad, M.F. Elkady, S. Ookawara, A.H. El-Shazly, A. Radwan, Temperature uniformity enhancement of densely packed high concentrator photovoltaic module using four quadrants microchannel heat sink, Sol. Energy. 202 (2020) 446–464. doi:10.1016/j.solener.2020.03.106.

[108] W.C. Tan, K.K. Chong, M.H. Tan, Performance study of water-cooled multiple-channel heat sinks in the application of ultra-high concentrator photovoltaic system, Sol. Energy. 147 (2017) 314–327.

doi:10.1016/j.solener.2017.03.040.

[109] M. Awad, A. Radwan, O. Abdelrehim, M. Emam, A.N. Shmroukh, M. Ahmed, Performance evaluation of concentrator photovoltaic systems integrated with a new jet impingement-microchannel heat sink and heat spreader, Sol. Energy. 199 (2020) 852–863. doi:10.1016/j.solener.2020.02.078.

[110] J. Barrau, A. Perona, A. Dollet, J. Rosell, Outdoor test of a hybrid jet impingement/micro-channel cooling device for densely packed concentrated photovoltaic cells, Sol. Energy. 107 (2014) 113–121. doi:10.1016/j.solener.2014.05.040.

[111] J. Barrau, J. Rosell, D. Chemisana, L. Tadrist, M. Ibañez, Effect of a hybrid jet impingement/micro-channel cooling device on the performance of densely packed PV cells under high concentration, Sol. Energy. 85 (2011) 2655–2665. doi:10.1016/j.solener.2011.08.004.

[112] E.M. Abo-Zahhad, S. Ookawara, A. Radwan, A.H. El-Shazly, M.F. Elkady, Numerical analyses of hybrid jet impingement/microchannel cooling device for thermal management of high concentrator triple-junction solar cell, Appl. Energy. 253 (2019) 113538. doi:10.1016/j.apenergy.2019.113538.

[113] Y. Sun, Y. Wang, L. Zhu, B. Yin, H. Xiang, Q. Huang, Direct liquid-immersion cooling of concentrator silicon solar cells in a linear concentrating photovoltaic receiver, Energy. 65 (2014) 264–271. doi:10.1016/j.energy.2013.11.063.

[114] X. Kang, Experiment and Simulation Study on Silicon Oil Immersion Cooling Densely-Packed Solar Cells Under High Concentration Ratio, Int. J. Energy Power Eng. 5 (2016) 90. doi:10.11648/j.ijepe.20160503.11.

[115] G. Huang, K. Wang, C.N. Markides, Efficiency limits of concentrating spectral-splitting hybrid photovoltaic-thermal (PV-T) solar collectors and systems, Light Sci. Appl. 10 (2021) 1–14. doi:10.1038/s41377-021-00465-1.

[116] Edmund Optics, Optical filters, (n.d.). https://www.edmundoptics.com/knowledge-center/application-notes/optics/optical-filters/.

[117] ABRISA Technologies, Wavelength selection filters, (n.d.). https://abrisatechnologies.com/products-services/coating-solutions/coatings-capabilities/wavelength-selection-filters/.

[118] J.H. Oh, S.J. Yang, Y.-G. Sung, Y.R. Do, Improved color coordinates of green monochromatic pc-LED capped with a band-pass filter, Opt. Express. 21 (2013) 4539. doi:10.1364/oe.21.004539.

[119] S. Jiang, P. Hu, S. Mo, Z. Chen, Optical modeling for a two-stage parabolic trough concentrating photovoltaic/thermal system using spectral beam splitting technology, Sol. Energy Mater. Sol. Cells. 94 (2010) 1686–1696. doi:10.1016/j.solmat.2010.05.029.

[120] P. Hu, Q. Zhang, Y. Liu, C. Sheng, X. Cheng, Z. Chen, Optical analysis of a hybrid solar concentrating Photovoltaic/Thermal (CPV/T) system with beam splitting technique, Sci. China Technol. Sci. 56 (2013) 1387–1394. doi:10.1007/s11431-013-5209-2.

[121] Y. Liu, P. Hu, Q. Zhang, Z. Chen, Thermodynamic and optical analysis for a CPV/T hybrid system with beam splitter and fully tracked linear Fresnel reflector concentrator utilizing sloped panels, Sol. Energy. 103 (2014) 191–199. doi:10.1016/j.solener.2014.01.047.

[122] L. Lane, M. Timmons, R. Venkatasubramanian, T. Colpitts, J. Hills, Close-packed cell arrays, (1994) 1938–1941.

[123] T.U. Ulavi, J.H. Davidson, T. Hebrink, Analysis of a hybrid PV/T concept based on wavelength selective mirror films, J. Sol. Energy Eng. Trans. ASME. 136 (2014) 1–9. doi:10.1115/1.4026678.

[124] V. Khoshdel, M. Joodaki, M. Shokooh-Saremi, UV and IR cut-off filters based on plasmonic crossed-shaped nano-antennas for solar cell applications, Opt. Commun. 433 (2019) 275–282. doi:10.1016/j.optcom.2018.10.005.

[125] K. Sudhakar, N. Jain, S. Bagga, Effect of color filter on the performance of solar photovoltaic module, Proc. 2013 Int. Conf. Power, Energy Control. ICPEC 2013. (2013) 35–38. doi:10.1109/ICPEC.2013.6527620.

[126] G. Huang, S.R. Curt, K. Wang, C.N. Markides, Challenges and opportunities for nanomaterials in spectral splitting for high-performance hybrid solar photovoltaic-thermal applications: A review, Nano Mater. Sci. 2 (2020) 183–203. doi:10.1016/j.nanoms.2020.03.008.

[127] R.A. Taylor, T.P. Otanicar, Y. Herukerrupu, F. Bremond, G. Rosengarten, E.R. Hawkes, X. Jiang, S. Coulombe, Feasibility of nanofluid-based optical filters, Appl. Opt. 52 (2013) 1413–1422. doi:10.1364/AO.52.001413.

[128] R.A. Taylor, T. Otanicar, G. Rosengarten, Nanofluid-based optical filter

optimization for PV/T systems, Light Sci. Appl. 1 (2012) 1–7. doi:10.1038/lsa.2012.34.

[129] D. Jing, Y. Hu, M. Liu, J. Wei, L. Guo, Preparation of highly dispersed nanofluid and CFD study of its utilization in a concentrating PV/T system, Sol. Energy. 112 (2015) 30–40. doi:10.1016/j.solener.2014.11.008.

[130] A. Mojiri, C. Stanley, R.A. Taylor, K. Kalantar-Zadeh, G. Rosengarten, A spectrally splitting photovoltaic-thermal hybrid receiver utilising direct absorption and wave interference light filtering, Sol. Energy Mater. Sol. Cells. 139 (2015) 71–80. doi:10.1016/j.solmat.2015.03.011.

[131] A. Mojiri, C. Stanley, G. Rosengarten, Spectrally splitting hybrid photovoltaic/thermal receiver design for a linear concentrator, Energy Procedia. 48 (2014) 618–627. doi:10.1016/j.egypro.2014.02.072.

[132] W. Nsengiyumva, S.G. Chen, L. Hu, X. Chen, Recent advancements and challenges in Solar Tracking Systems (STS): A review, Renew. Sustain. Energy Rev. 81 (2018) 250–279. doi:10.1016/j.rser.2017.06.085.

[133] R. Singh, S. Kumar, A. Gehlot, R. Pachauri, An imperative role of sun trackers in photovoltaic technology: A review, Renew. Sustain. Energy Rev. 82 (2018) 3263–3278. doi:10.1016/j.rser.2017.10.018.

[134] Official website of the United States National Nanotechnology Initiative, (n.d.). https://www.nano.gov (accessed January 17, 2019).

[135] S.K. Das, S.U.S. Choi, H.E. Patel, Heat transfer in nanofluids - A review, Heat Transf. Eng. 27 (2006) 3–19. doi:10.1080/01457630600904593.

[136] A.S. Abdelrazik, F.A. Al-Sulaiman, R. Saidur, R. Ben-Mansour, A review on recent development for the design and packaging of hybrid photovoltaic/thermal (PV/T) solar systems, Renew. Sustain. Energy Rev. 95 (2018) 110–129. doi:10.1016/j.rser.2018.07.013.

[137] F. Yazdanifard, M. Ameri, E. Ebrahimnia-Bajestan, Performance of nanofluid-based photovoltaic/thermal systems: A review, Renew. Sustain. Energy Rev. 76 (2017) 323–352. doi:10.1016/j.rser.2017.03.025.

[138] E. Bellos, Z. Said, C. Tzivanidis, The use of nanofluids in solar concentrating technologies: A comprehensive review, J. Clean. Prod. 196 (2018) 84–99. doi:10.1016/j.jclepro.2018.06.048.

[139] K. Khanafer, K. Vafai, A review on the applications of nanofluids in solar energy field, Renew. Energy. 123 (2018) 398–406. doi:10.1016/j.renene.2018.01.097.

[140] K. V. Wong, O. De Leon, Applications of nanofluids: Current and future, Adv. Mech. Eng. 2010 (2010). doi:10.1155/2010/519659.

[141] V. Trisaksri, S. Wongwises, Critical review of heat transfer characteristics of nanofluids, Renew. Sustain. Energy Rev. 11 (2007) 512–523. doi:10.1016/j.rser.2005.01.010.

[142] I.M. Mahbubul, Introduction to Nanofluid, in: William Andrew (Ed.), Prep. Charact. Prop. Appl. Nanofluid, 1st ed., Elsevier Inc., Saudia Arabia, 2019: p. 374. doi:10.1016/B978-0-12-813245-6.00001-0.

[143] P.K. Nagarajan, J. Subramani, S. Suyambazhahan, R. Sathyamurthy, Nanofluids for solar collector applications: A review, Energy Procedia. 61 (2014) 2416–2434. doi:10.1016/j.egypro.2014.12.017.

[144] O. Zaytseva, G. Neumann, Carbon nanomaterials: Production, impact on plant development, agricultural and environmental applications, Chem. Biol. Technol. Agric. 3 (2016) 1–26. doi:10.1186/s40538-016-0070-8.

[145] S. Oh, J. Lee, T. Sekino, K. Niihara, Fabrication of Cu dispersed Al2O3 Nanocomposites using Al2O3 a, 44 (2001) 2117–2120.

[146] A. Kasaeian, S. Daviran, R.D. Azarian, A. Rashidi, Performance evaluation and nanofluid using capability study of a solar parabolic trough collector, Energy Convers. Manag. 89 (2015) 368–375. doi:10.1016/j.enconman.2014.09.056.

[147] O. Arthur, M.A. Karim, An investigation into the thermophysical and rheological properties of nanofluids for solar thermal applications, Renew. Sustain. Energy Rev. 55 (2016) 739–755. doi:10.1016/j.rser.2015.10.065.

[148] W.I.A. Aly, Numerical study on turbulent heat transfer and pressure drop of nanofluid in coiled tube-in-tube heat exchangers, Energy Convers. Manag. 79 (2014) 304–316. doi:10.1016/j.enconman.2013.12.031.

[149] N.E. Hjerrild, S. Mesgari, F. Crisostomo, J.A. Scott, R. Amal, R.A. Taylor, Hybrid PV/T enhancement using selectively absorbing Ag-SiO2/carbon nanofluids, Sol. Energy Mater. Sol. Cells. 147 (2016) 281–287. doi:10.1016/j.solmat.2015.12.010.

[150] R. Saidur, K.Y. Leong, H.A. Mohammad, A review on applications and challenges of nanofluids, Renew. Sustain. Energy Rev. 15 (2011) 1646–1668. doi:10.1016/j.rser.2010.11.035.

[151] J. Lee, I. Mudawar, Assessment of the effectiveness of nanofluids for single-phase and two-phase heat transfer in micro-channels, Int. J. Heat

Mass Transf. 50 (2007) 452–463. doi:10.1016/j.ijheatmasstransfer.2006.08.001.

[152] P. Razi, M.A. Akhavan-Behabadi, M. Saeedinia, Pressure drop and thermal characteristics of CuO-base oil nanofluid laminar flow in flattened tubes under constant heat flux, Int. Commun. Heat Mass Transf. 38 (2011) 964–971. doi:10.1016/j.icheatmasstransfer.2011.04.010.

[153] J.L. Routbort, D. Singh, E. V. Timofeeva, W. Yu, D.M. France, Pumping power of nanofluids in a flowing system, J. Nanoparticle Res. 13 (2011) 931–937. doi:10.1007/s11051-010-0197-7.

[154] R.A. Taylor, P.E. Phelan, R.J. Adrian, A. Gunawan, T.P. Otanicar, Characterization of light-induced, volumetric steam generation in nanofluids, Int. J. Therm. Sci. 56 (2012) 1–11. doi:10.1016/j.ijthermalsci.2012.01.012.

[155] S. Dagher, Y. Haik, A.I. Ayesh, N. Tit, Synthesis and optical properties of colloidal CuO nanoparticles, J. Lumin. 151 (2014) 149–154. doi:10.1016/j.jlumin.2014.02.015.

[156] S.U. Ilyas, R. Pendyala, N. Marneni, Preparation, sedimentation, and agglomeration of nanofluids, Chem. Eng. Technol. 37 (2014) 2011–2021. doi:10.1002/ceat.201400268.

[157] Y. Yang, A. Oztekin, S. Neti, S. Mohapatra, Particle agglomeration and properties of nanofluids, J. Nanoparticle Res. 14 (2012). doi:10.1007/s11051-012-0852-2.

[158] G.P. Celata, F. D'Annibale, A. Mariani, S. Sau, E. Serra, R. Bubbico, C. Menale, H. Poth, Experimental results of nanofluids flow effects on metal surfaces, Chem. Eng. Res. Des. 92 (2014) 1616–1628. doi:10.1016/j.cherd.2013.12.003.

[159] M.J. Mashock, T. Zanon, A.D. Kappell, L.N. Petrella, E.C. Andersen, K.R. Hristova, Copper oxide nanoparticles impact several toxicological endpoints and cause neurodegeneration in caenorhabditis elegans, PLoS One. 11 (2016) 1–19. doi:10.1371/journal.pone.0167613.

[160] A.M. Schrand, M.F. Rahman, S.M. Hussain, J.J. Schlager, D.A. Smith, A.F. Syed, Metal-based nanoparticles and their toxicity assessment, Wiley Interdiscip. Rev. Nanomedicine Nanobiotechnology. 2 (2010) 544–568. doi:10.1002/wnan.103.

[161] S.U. Ilyas, R. Pendyala, N. Marneni, Preparation, sedimentation, and

agglomeration of nanofluids, Chem. Eng. Technol. 37 (2014) 2011–2021. doi:10.1002/ceat.201400268.

[162] H.A. Mohammed, A.A. Al-Aswadi, N.H. Shuaib, R. Saidur, Convective heat transfer and fluid flow study over a step using nanofluids: A review, Renew. Sustain. Energy Rev. 15 (2011) 2921–2939. doi:10.1016/j.rser.2011.02.019.

[163] H. Chang, C.S. Jwo, P.S. Fan, S.H. Pai, Process optimization and material properties for nanofluid manufacturing, Int. J. Adv. Manuf. Technol. 34 (2007) 300–306. doi:10.1007/s00170-006-0597-0.

[164] I.M. Mahbubul, Preparation, Characterization, Properties and Application of Nanofluid, 2019. doi:10.1016/B978-0-12-813245-6.00008-3.

[165] I.M. Mahbubul, E.B. Elcioglu, R. Saidur, M.A. Amalina, Optimization of ultrasonication period for better dispersion and stability of TiO2–water nanofluid, Ultrason. Sonochem. 37 (2017) 360–367. doi:10.1016/j.ultsonch.2017.01.024.

[166] Y. Hwang, J.K. Lee, J.K. Lee, Y.M. Jeong, S. ir Cheong, Y.C. Ahn, S.H. Kim, Production and dispersion stability of nanoparticles in nanofluids, Powder Technol. 186 (2008) 145–153. doi:10.1016/j.powtec.2007.11.020.

[167] Y. Li, S. Tung, E. Schneider, S. Xi, A review on development of nano fluid preparation and characterization, Powder Technol. 196 (2009) 89–101. doi:10.1016/j.powtec.2009.07.025.

[168] W. Yu, H. Xie, A review on Nanofluids: Preparation, Stability Mechanisms, and Applications, J. Nanomater. 2012 (2012) 17. doi:10.1155/2012/435873.

[169] S. Manikandan, K.S. Rajan, Sand-propylene glycol-water nanofluids for improved solar energy collection, Energy. 113 (2016) 917–929. doi:10.1016/j.energy.2016.07.120.

[170] A.H.A. Al-Waeli, K. Sopian, M.T. Chaichan, H.A. Kazem, H.A. Hasan, A.N. Al-Shamani, An experimental investigation of SiC nanofluid as a base-fluid for a photovoltaic thermal PV/T system, Energy Convers. Manag. 142 (2017) 547–558. doi:10.1016/j.enconman.2017.03.076.

[171] A.H.A. Al-Waeli, K. Sopian, H.A. Kazem, J.H. Yousif, M.T. Chaichan, A. Ibrahim, S. Mat, M.H. Ruslan, Comparison of prediction methods of PV/T nanofluid and nano-PCM system using a measured dataset and artificial neural network, Sol. Energy. 162 (2018) 378–396.

doi:10.1016/j.solener.2018.01.026.

[172] M. Sardarabadi, M. Passandideh-Fard, Experimental and numerical study of metal-oxides/water nanofluids as coolant in photovoltaic thermal systems (PVT), Sol. Energy Mater. Sol. Cells. 157 (2016) 533–542. doi:10.1016/j.solmat.2016.07.008.

[173] Y. Khanjari, F. Pourfayaz, A.B. Kasaeian, Numerical investigation on using of nanofluid in a water-cooled photovoltaic thermal system, Energy Convers. Manag. 122 (2016) 263–278. doi:10.1016/j.enconman.2016.05.083.

[174] A.R.A. Hashim A.Hussien, Ali H. Noman, Indoor Investigation for Improving the Hybrid Photovoltaic / Thermal System Performance Using Nanofluid (AL2O3-Water), Eng. &Tech.Journal. 33 (2015) 889–901.

[175] M. Elmir, R. Mehdaoui, A. Mojtabi, Numerical simulation of cooling a solar cell by forced convection in the presence of a nanofluid, Energy Procedia. 18 (2012) 594–603. doi:10.1016/j.egypro.2012.05.072.

[176] O. Rejeb, M. Sardarabadi, C. Ménézo, M. Passandideh-Fard, M.H. Dhaou, A. Jemni, Numerical and model validation of uncovered nanofluid sheet and tube type photovoltaic thermal solar system, Energy Convers. Manag. 110 (2016) 367–377. doi:10.1016/j.enconman.2015.11.063.

[177] S.A.Nada, D.H.El-Nagar, H.M.S.Hussein, Improving the thermal regulation and efficiency enhancement of PCM-Integrated PV modules using nano particles, Energy Convers. Manag. 166 (2018) 735–743. doi:10.1016/j.enconman.2018.04.035.

[178] M. Sardarabadi, M. Passandideh-Fard, S. Zeinali Heris, Experimental investigation of the effects of silica/water nanofluid onPV/T (photovoltaic thermal units), Energy. 66 (2014) 264–272. doi:10.1016/j.energy.2014.01.102.

[179] J.J. Michael, S. Iniyan, Performance analysis of a copper sheet laminated photovoltaic thermal collector using copper oxide - water nanofluid, Sol. Energy. 119 (2015) 439–451. doi:10.1016/j.solener.2015.06.028.

[180] M. Ghadiri, M. Sardarabadi, M. Pasandideh-Fard, A.J. Moghadam, Experimental investigation of a PVT system performance using nano ferrofluids, Energy Convers. Manag. 103 (2015) 468–476. doi:10.1016/j.enconman.2015.06.077.

[181] A.N. Al-Shamani, K. Sopian, S. Mat, H.A. Hasan, A.M. Abed, M.H. Ruslan,

Experimental studies of rectangular tube absorber photovoltaic thermal collector with various types of nanofluids under the tropical climate conditions, Energy Convers. Manag. 124 (2016) 528–542. doi:10.1016/j.enconman.2016.07.052.

[182] S. Hassani, R.A. Taylor, S. Mekhilef, R. Saidur, A cascade nanofluid-based PV/T system with optimized optical and thermal properties, Energy. 112 (2016) 963–975. doi:10.1016/j.energy.2016.06.142.

[183] K. Rahbar, A. Riasi, H. Khatam Bolouri Sangjoeei, N. Razmjoo, Heat recovery of nano-fluid based concentrating Photovoltaic Thermal (CPV/T) Collector with Organic Rankine Cycle, Energy Convers. Manag. 179 (2019) 373–396. doi:10.1016/j.enconman.2018.10.066.

[184] Z. Xu, C. Kleinstreuer, Concentration photovoltaic-thermal energy co-generation system using nanofluids for cooling and heating, Energy Convers. Manag. 87 (2014) 504–512. doi:10.1016/j.enconman.2014.07.047.

[185] Z. Xu, C. Kleinstreuer, Computational Analysis of Nanofluid Cooling of High Concentration Photovoltaic Cells, J. Therm. Sci. Eng. Appl. 6 (2014) 031009. doi:10.1115/1.4026355.

[186] S. Srivastava, K.S. Reddy, Simulation studies of thermal and electrical performance of solar linear parabolic trough concentrating photovoltaic system, Sol. Energy. 149 (2017) 195–213. doi:10.1016/j.solener.2017.04.004.

[187] D. Lelea, D.G. Calinoiu, G. Trif-Tordai, A.E. Cioabla, I. Laza, F. Popescu, The hybrid nanofluid/microchannel cooling solution for concentrated photovoltaic cells, 122 (2015) 122–128. doi:10.1063/1.4908592.

[188] F. Yazdanifard, E. Ebrahimnia-Bajestan, M. Ameri, Performance of a parabolic trough concentrating photovoltaic/thermal system: Effects of flow regime, design parameters, and using nanofluids, Energy Convers. Manag. 148 (2017) 1265–1277. doi:10.1016/j.enconman.2017.06.075.

[189] A. Menbari, A.A. Alemrajabi, A. Rezaei, Heat transfer analysis and the effect of CuO/Water nanofluid on direct absorption concentrating solar collector, Appl. Therm. Eng. 104 (2016) 176–183. doi:10.1016/j.applthermaleng.2016.05.064.

[190] E. Bellos, C. Tzivanidis, Investigation of a nanofluid-based concentrating thermal photovoltaic with a parabolic reflector, Energy Convers. Manag.

180 (2019) 171–182. doi:10.1016/j.enconman.2018.11.008.

[191] W. An, J. Wu, T. Zhu, Q. Zhu, Experimental investigation of a concentrating PV/T collector with Cu9S5nanofluid spectral splitting filter, Appl. Energy. 184 (2016) 197–206. doi:10.1016/j.apenergy.2016.10.004.

[192] A. Radwan, M. Ahmed, S. Ookawara, Performance enhancement of concentrated photovoltaic systems using a microchannel heat sink with nanofluids, Energy Convers. Manag. 119 (2016) 289–303. doi:10.1016/j.enconman.2016.04.045.

[193] A. Radwan, M. Ahmed, Thermal management of concentrator photovoltaic systems using microchannel heat sink with nanofluids, Sol. Energy. 171 (2018) 229–246. doi:10.1016/j.solener.2018.06.083.

[194] T.P. Otanicar, P.E. Phelan, R.S. Prasher, G. Rosengarten, R.A. Taylor, Nanofluid-based direct absorption solar collector, J. Renew. Sustain. Energy. 2 (2010). doi:10.1063/1.3429737.

[195] W. Kang, Y. Shin, H. Cho, Economic analysis of flat-plate and U-tube solar collectors using an Al2O3nanofluid, Energies. 10 (2017). doi:10.3390/en10111911.

[196] T. Yousefi, F. Veysi, E. Shojaeizadeh, S. Zinadini, An experimental investigation on the effect of Al2O3-H2O nanofluid on the efficiency of flat-plate solar collectors, Renew. Energy. 39 (2012) 293–298. doi:10.1016/j.renene.2011.08.056.

[197] F. Kiliç, T. Menlik, A. Sözen, Effect of titanium dioxide/water nanofluid use on thermal performance of the flat plate solar collector, Sol. Energy. 164 (2018) 101–108. doi:10.1016/j.solener.2018.02.002.

[198] S.K. Verma, A.K. Tiwari, S. Tiwari, D.S. Chauhan, Performance analysis of hybrid nanofluids in flat plate solar collector as an advanced working fluid, Sol. Energy. 167 (2018) 231–241. doi:10.1016/j.solener.2018.04.017.

[199] S.S. Chougule, A.T. Pise, P.A. Madane, Performance of nanofluid-charged solar water heater by solar tracking system, Int. Conf. Adv. Eng. Sci. Manag. (2012) 247–253.

[200] J. Ghaderian, N.A.C. Sidik, An experimental investigation on the effect of Al2O3/distilled water nanofluid on the energy efficiency of evacuated tube solar collector, Int. J. Heat Mass Transf. 108 (2017) 972–987. doi:10.1016/j.ijheatmasstransfer.2016.12.101.

[201] S. Iranmanesh, H.C. Ong, B.C. Ang, E. Sadeghinezhad, A. Esmaeilzadeh,

M. Mehrali, Thermal performance enhancement of an evacuated tube solar collector using graphene nanoplatelets nanofluid, J. Clean. Prod. 162 (2017) 121–129. doi:10.1016/j.jclepro.2017.05.175.

[202] Z.H. Liu, R.L. Hu, L. Lu, F. Zhao, H.S. Xiao, Thermal performance of an open thermosyphon using nanofluid for evacuated tubular high temperature air solar collector, Energy Convers. Manag. 73 (2013) 135–143. doi:10.1016/j.enconman.2013.04.010.

[203] M. Mahendran, G.C. Lee, K.V. Sharma, A. Shahrani, R.A. Bakar, Performance of Evacuated Tube Solar Collector Using Water-Based Titanium Oxide Nanofluid, J. Mech. Eng. Sci. 3 (2012) 301–310. doi:10.1017/CBO9781107415324.004.

[204] A.H. Hussain, Q. Jawad, K.F. Sultan, Experimental analysis on thermal efficiency of evacuated tube solar collector by using nanofluids 2 . Preparation of Silver and Zirconium, Internatonal J. Sustain. Green Energy. 4 (2015) 19–28. doi:10.11648/j.ijrse.s.2015040301.14.

[205] H. Kaya, K. Arslan, N. Eltugral, Experimental investigation of thermal performance of an evacuated U-Tube solar collector with ZnO/Etylene glycol-pure water nanofluids, Renew. Energy. 122 (2018) 329–338. doi:10.1016/j.renene.2018.01.115.

[206] Y. Tong, J. Kim, H. Cho, Effects of thermal performance of enclosed-type evacuated U-tube solar collector with multi-walled carbon nanotube/water nanofluid, Renew. Energy. 83 (2015) 463–473. doi:10.1016/j.renene.2015.04.042.

[207] A. Ozsoy, V. Corumlu, Thermal performance of a thermosyphon heat pipe evacuated tube solar collector using silver-water nanofluid for commercial applications, Renew. Energy. 122 (2018) 26–34. doi:10.1016/j.renene.2018.01.031.

[208] L.Q. Tang, Q.Z. Zhu, Performance study of flowing-over PV/T system with different working fluid, Appl Mech Mater Trans Tech Publ. 489 (2014) 1173–1176. doi:10.4028/www.scientific.net/AMM.488-489.1173.

[209] M. Faizal, R. Saidur, S. Mekhilef, M.A. Alim, Energy , economic and environmental analysis of metal oxides nanofluid for flat-plate solar collector, ENERGY Convers. Manag. 76 (2013) 162–168. doi:10.1016/j.enconman.2013.07.038.

[210] A. Kamyar, R. Saidur, M. Hasanuzzaman, Application of Computational

Fluid Dynamics (CFD) for nanofluids, Int. J. Heat Mass Transf. 55 (2012) 4104–4115. doi:10.1016/j.ijheatmasstransfer.2012.03.052.

[211] O. Bait, M. Si-Ameur, Enhanced heat and mass transfer in solar stills using nanofluids: A review, Sol. Energy. 170 (2018) 694–722. doi:10.1016/j.solener.2018.06.020.

[212] Y. Vermahmoudi, S.M. Peyghambarzadeh, S.H. Hashemabadi, M. Naraki, Experimental investigation on heat transfer performance of Fe 2 O 3 / water nanofluid in an air-finned heat exchanger, Eur. J. Mech. B/Fluids. 44 (2014) 32–41. doi:10.1016/j.euromechflu.2013.10.002.

[213] M.A. Sabiha, R. Saidur, S. Hassani, Z. Said, S. Mekhilef, Energy performance of an evacuated tube solar collector using single walled carbon nanotubes nanofluids, Energy Convers. Manag. 105 (2015) 1377–1388. doi:10.1016/j.enconman.2015.09.009.

[214] L.S. Sundar, M.K. Singh, A.C.M. Sousa, Enhanced heat transfer and friction factor of MWCNT-Fe3O4/water hybrid nanofluids, Int. Commun. Heat Mass Transf. 52 (2014) 73–83. doi:10.1016/j.icheatmasstransfer.2014.01.012.

[215] M. Hemmat Esfe, A.A. Abbasian Arani, M. Rezaie, W.M. Yan, A. Karimipour, Experimental determination of thermal conductivity and dynamic viscosity of Ag-MgO/water hybrid nanofluid, Int. Commun. Heat Mass Transf. 66 (2015) 189–195. doi:10.1016/j.icheatmasstransfer.2015.06.003.

[216] L.S. Sundar, M.K. Singh, M.C. Ferro, A.C.M. Sousa, Experimental investigation of the thermal transport properties of graphene oxide / Co 3 O 4 hybrid nano fl uids, Int. Commun. Heat Mass Transf. 84 (2017) 1–10. doi:10.1016/j.icheatmasstransfer.2017.03.001.

[217] A.F. Al-alawy, A Numerical Analysis of Cu – Engine Oil Nanofluid Forced Convection in Annular Tubes, Int. J. Sci. Technol. 6 (2017) 705–713.

[218] S. Lee, S. Choi, S. Li, J. Eastman, Measuring Thermal Conductivity of Fluids Containing Oxide Nanoparticles, Heat Transf. 121 (2013).

[219] A. Ahmed, G. Zhang, K. Shanks, S. Sundaram, Y. Ding, T. Mallick, Performance evaluation of single multi-junction solar cell for high concentrator photovoltaics using minichannel heat sink with nanofluids, Appl. Therm. Eng. 182 (2021) 115868. doi:10.1016/j.applthermaleng.2020.115868.

[220] H. Xie, J. Wang, X. Tonggeng, Y. Liu, F. Ai, Dependence of the thermal conductivity of nanoparticle-fluid mixture on the base fluid, J. Mater. Sci. Lett. 21 (2002) 1469–1471.

[221] E. Timofeeva, J. Routbort, D. Singh, Particle shape effects on thermophysical properties of alumina nanofluids, Appl. Phys. 106 (2009). doi:10.1063/1.3155999.

[222] S.M.S. Murshed, K.C. Leong, C. Yang, Enhanced thermal conductivity of TiO 2 — water based nanofluids, 44 (2005) 367–373. doi:10.1016/j.ijthermalsci.2004.12.005.

[223] Babita, S.K. Sharma, S.M. Gupta, Preparation and evaluation of stable nanofluids for heat transfer application: A review, Exp. Therm. Fluid Sci. 79 (2016) 202–212. doi:10.1016/j.expthermflusci.2016.06.029.

[224] P. Elmer, LAMBDA 1050+ UV/Vis/NIR Spectrophotometer specification, 2019. (2019). https://www.perkinelmer.com/uk/product/lambda-1050-2d-system-l6020056.

[225] M. Schaufler, Super solar simulator specification, (2013). https://vosselectronic.de/58-voss.

[226] G. Voss electronic, HelioCon product specification, (2017). https://www.vosselectronic.de/62-heliocon/114-heliocon.

[227] I-V curve tracer, (n.d.). https://eko-eu.com/products/solar-energy/iv-measurements.

[228] LAMBDA 01/L thermal conductivity meter, (n.d.). https://flucon.de/en/products/thermal-conductivity-system-lambda/.

[229] Water bath, (n.d.). http://www.promix.ru/manuf/ge/electrophoresis/b_prib/Multitemp_III.pdf.

[230] DC power supply, (n.d.). https://uk.farnell.com.

[231] Stuart magnetic stirrer, (n.d.). https://uk.rs-online.com/web/p/hot-plate-stirrers.

[232] VERDERFLEX peristaltic pump, (n.d.). https://uk.rs-online.com/web/p/positive-displacement-pumps/7056653/.

[233] Blue-White, (n.d.). https://www.blue-white.com/educational/peristaltic-pump-wear-factors/.

[234] Variable area flow meter, (n.d.). https://uk.rs-online.com/web/p/products/1859998/.

[235] R. Usamentiaga, P. Venegas, J. Guerediaga, L. Vega, J. Molleda, F.G.

Bulnes, Infrared thermography for temperature measurement and non-destructive testing, Sensors (Switzerland). 14 (2014) 12305–12348. doi:10.3390/s140712305.

[236] Pico-temperature logger, (n.d.). https://uk.rs-online.com/web/p/data-loggers/4925105/.

[237] EXTECH-temperature meter, (n.d.). http://www.extech.com/products/SDL200.

[238] FLIR thermal camera, (n.d.). https://www.flir.com.

[239] AZURE Space 3C40 data sheet, n.d. http://www.azurspace.com.

[240] SUNYIMA, Silicon solar cell data sheet, n.d.

[241] Bourns, Power Resistor data sheet, n.d. www.Bourns.com.

[242] R. Component, RS Thermal paste, (n.d.). uk.rs-online.com/web/p/thermal-grease.

[243] Sigma-Aldrich, Aluminum Oxide, n.d.

[244] Sigma-Aldrich, LUDOX® HS-40 colloidal silica, n.d.

[245] R.L. Hamilton, O.K. Crosser, Thermal conductivity of heterogeneous two-component systems, Ind. Eng. Chem. Fundam. 1 (1962) 187–191. doi:10.1021/i160003a005.

[246] J. Zhou, Q. Yi, Y. Wang, Z. Ye, Temperature distribution of photovoltaic module based on finite element simulation, Sol. Energy. 111 (2015) 97–103. doi:10.1016/j.solener.2014.10.040.

[247] A. Ahmed, H. Baig, S. Sundaram, T.K. Mallick, Use of Nanofluids in Solar PV/Thermal Systems, Int. J. Photoenergy. 2019 (2019) 1–17. doi:10.1155/2019/8039129.

[248] COMSOL-Multiphysics, (n.d.). https://uk.comsol.com (accessed January 5, 2019).

[249] O. Mahian, L. Kolsi, M. Amani, P. Estellé, G. Ahmadi, C. Kleinstreuer, J.S. Marshall, M. Siavashi, R.A. Taylor, H. Niazmand, S. Wongwises, T. Hayat, A. Kolanjiyil, A. Kasaeian, I. Pop, E. Abu-nada, S. Rashidi, H. Niazmand, S. Wongwises, T. Hayat, A. Kasaeian, I. Pop, Recent advances in modeling and simulation of nanofluid flows — Part I : Fundamentals and theory, Phys. Rep. 790 (2019) 1–48. doi:10.1016/j.physrep.2018.11.004.

[250] M. Keshavarz Moraveji, E. Esmaeili, Comparison between single-phase and two-phases CFD modeling of laminar forced convection flow of nanofluids in a circular tube under constant heat flux, Int. Commun. Heat

Mass Transf. 39 (2012) 1297–1302. doi:10.1016/j.icheatmasstransfer.2012.07.012.

[251] C.J. Ho, J.C. Liao, C.H. Li, W.M. Yan, M. Amani, Experimental study of cooling characteristics of water-based alumina nanofluid in a minichannel heat sink, Case Stud. Therm. Eng. 14 (2019) 1–9. doi:10.1016/j.csite.2019.100418.

[252] M. Theristis, T.S. O'Donovan, An Integrated Thermal Electrical Model for Single Cell Photovoltaic Receivers Under Concentration, in: Int. Heat Transf. Conf., 2014. doi:10.1615/ihtc15.sol.009239.

[253] T.L. Chou, Z.H. Shih, H.F. Hong, C.N. Han, K.N. Chiang, Thermal performance assessment and validation of high-concentration photovoltaic solar cell module, IEEE Trans. Components, Packag. Manuf. Technol. 2 (2012) 578–586. doi:10.1109/TCPMT.2011.2181165.

[254] I. Dincer, M.A. Rosen, Exergy, 2nd ed., Elsevier Ltd., 2013. doi:10.1016/C2010-0-68369-6.

[255] G. Evola, L. Marletta, Exergy and thermoeconomic optimization of a water-cooled glazed hybrid photovoltaic/thermal (PVT) collector, Sol. Energy. 107 (2014) 12–25. doi:10.1016/j.solener.2014.05.041.

[256] G.N. Tiwari, M. Meraj, M.E. Khan, Exergy analysis of N-photovoltaic thermal-compound parabolic concentrator (N-PVT-CPC) collector for constant collection temperature for vapor absorption refrigeration (VAR) system, Sol. Energy. 173 (2018) 1032–1042. doi:10.1016/j.solener.2018.08.031.

[257] D. Atheaya, A. Tiwari, G.N. Tiwari, Exergy analysis of photovoltaic thermal (PVT) compound parabolic concentrator (CPC) for constant collection temperature mode, Sol. Energy. 135 (2016) 222–231. doi:10.1016/j.solener.2016.05.055.

[258] R.S. Vajjha, D.K. Das, A review and analysis on influence of temperature and concentration of nanofluids on thermophysical properties, heat transfer and pumping power, Int. J. Heat Mass Transf. 55 (2012) 4063–4078. doi:10.1016/j.ijheatmasstransfer.2012.03.048.

[259] Loikits, Syltherm 800, (n.d.). http://www.loikitsdistribution.com/files/syltherm-800-technical-data-sheet.pdf (accessed January 1, 2019).

[260] S.K. Das, S.U.S. Choi, W. Yu, T. Pradeep, Nanofluids: Science and

Technology, John Wiley& Sons, Hoboken, New Jersey, New Jersey, 2007. doi:10.1192/bjp.111.479.1009-a.

[261] K. Khanafer, K. Vafai, A critical synthesis of thermophysical characteristics of nanofluids, Int. J. Heat Mass Transf. 54 (2011) 4410–4428. doi:10.1016/j.ijheatmasstransfer.2011.04.048.

[262] H.C. Brinkman, The viscosity of concentrated suspensions and solutions, J. Chem. Phys. 20 (1952) 571. doi:10.1063/1.1700493.

[263] S. Chow, C.E. Valdivia, J.F. Wheeldon, R. Ares, O.J. Arenas, V. Aimez, D. McMeekin, S. Fafard, K. Hinzer, Thermal test and simulation of alumina receiver with high efficiency multi-junction solar cell for concentrator systems, Photonics North 2010. 7750 (2010) 775035. doi:10.1117/12.872894.

[264] J. Wu, J. Zhao, J. Lei, B. Liu, Effectiveness of nanofluid on improving the performance of microchannel heat sink, Appl. Therm. Eng. 101 (2016) 402–412. doi:10.1016/j.applthermaleng.2016.01.114.

[265] X.L. Xie, Z.J. Liu, Y.L. He, W.Q. Tao, Numerical study of laminar heat transfer and pressure drop characteristics in a water-cooled minichannel heat sink, Appl. Therm. Eng. 29 (2009) 64–74. doi:10.1016/j.applthermaleng.2008.02.002.

[266] S.J. Kim, D. Kim, Forced convection in microstructures for electronic equipment cooling, J. Heat Transfer. 121 (1999) 639–645. doi:10.1115/1.2826027.

[267] M. Sheikholeslami, Application of Control Volume Based Finite Element Method (CVFEM) for Nanofluid Flow and Heat Transfer, 1st ed., Elsevier, 2019. doi:10.1016/C2017-0-01264-8.

[268] G. Roy, I. Gherasim, F. Nadeau, G. Poitras, C.T. Nguyen, Heat transfer performance and hydrodynamic behavior of turbulent nanofluid radial flows, Int. J. Therm. Sci. 58 (2012) 120–129. doi:10.1016/j.ijthermalsci.2012.03.009.

[269] S. Ferrouillat, A. Bontemps, J.P. Ribeiro, J.A. Gruss, O. Soriano, Hydraulic and heat transfer study of SiO2/water nanofluids in horizontal tubes with imposed wall temperature boundary conditions, Int. J. Heat Fluid Flow. 32 (2011) 424–439. doi:10.1016/j.ijheatfluidflow.2011.01.003.

[270] M.S. Yousef, A.K. Abdel Rahman, S. Ookawara, Performance investigation of low – Concentration photovoltaic systems under hot and arid conditions:

Experimental and numerical results, Energy Convers. Manag. 128 (2016) 82–94. doi:10.1016/j.enconman.2016.09.061.

[271] V. Bianco, A. Marchitto, F. Scarpa, L.A. Tagliafico, Computational fluid dynamics modeling of developing forced laminar convection flow of Al2O3-Water nanofluid in a two-dimensional rectangular section channel, J. Enhanc. Heat Transf. 25 (2018) 387–398. doi:10.1615/JEnhHeatTransf.2018021380.

[272] V. Bianco, F. Scarpa, L.A. Tagliafico, Numerical analysis of the Al2O3-water nanofluid forced laminar convection in an asymmetric heated channel for application in flat plate PV/T collector, Renew. Energy. 116 (2018) 9–21. doi:10.1016/j.renene.2017.09.067.

[273] M. Chegaar, A. Hamzaoui, A. Namoda, P. Petit, M. Aillerie, A. Herguth, Effect of illumination intensity on solar cells parameters, Energy Procedia. 36 (2013) 722–729. doi:10.1016/j.egypro.2013.07.084.

[274] H. Helmers, M. Schachtner, A.W. Bett, Influence of temperature and irradiance on triple-junction solar subcells, Sol. Energy Mater. Sol. Cells. 116 (2013) 144–152. doi:10.1016/j.solmat.2013.03.039.

[275] G. Siefer, A.W. Bett, Analysis of temperature coefficients for III-V multi-junction concentrator cells, Prog. Photovoltaics Res. Appl. 22 (2014) 515–524. doi:10.1002/pip.2285.

[276] C. Xiao, X. Yu, D. Yang, D. Que, Impact of solar irradiance intensity and temperature on the performance of compensated crystalline silicon solar cells, Sol. Energy Mater. Sol. Cells. 128 (2014) 427–434. doi:10.1016/j.solmat.2014.06.018.

[277] G. Bonsignore, A.A. Gallitto, S. Agnello, M. Barbera, R. Candia, M. Cannas, A. Collura, I. Dentici, F.M. Gelardi, U. Lo Cicero, F.M. Montagnino, F. Paredes, L. Sciortino, Electrical-optical characterization of multijunction solar cells under 2000X concentration, AIP Conf. Proc. 1616 (2014) 102–105. doi:10.1063/1.4897038.

[278] I. Al Siyabi, Enhancing the performance of concentrating photovoltaics through multi-layered microchannel heat sink and phase change materials, University of Exeter, 2018.